

TIME-LAPSE SEISMIC IMAGING BY LINEARIZED JOINT  
INVERSION

A DISSERTATION  
SUBMITTED TO THE DEPARTMENT OF GEOPHYSICS  
AND THE COMMITTEE ON GRADUATE STUDIES  
OF STANFORD UNIVERSITY  
IN PARTIAL FULFILLMENT OF THE REQUIREMENTS  
FOR THE DEGREE OF  
DOCTOR OF PHILOSOPHY

Gboyega Ayeni

April 2012





# Abstract

This dissertation presents methods that overcome some limitations in the application of time-lapse seismic imaging to subsurface reservoir monitoring. These methods attenuate artifacts and distortions in time-lapse seismic images that are caused by differences in survey acquisition geometries, presence of obstructions, complex overburden and man-made noise. Unless these artifacts are attenuated, it is impossible to make reliable deductions about changes in subsurface reservoir properties from time-lapse seismic images.

Improvements to two conventional post-imaging seismic cross-equalization methods are considered. Multi-dimensional warping of baseline and monitor images is implemented as sequential one-dimensional cross-correlations and interpolations. This method avoids the cost of full three-dimensional warping, and it avoids errors caused by considering only vertical apparent displacements between images. After warping, matched filters are derived using optimal parameters derived using an Evolutionary Programming algorithm. Applications to four North Sea data sets show that a combination of these two methods provides an efficient and robust cross-equalization scheme. Importantly, the warping method is a key preprocessing tool for linearized joint inversion.

Linearized joint inversion of time-lapse data sets is an extension of least-squares migration/inversion of seismic data sets. Linearized inversion improves both structural and amplitude information in seismic images. Joint inversion allows incorporation spatial and temporal regularizations/constraints, which stabilize the inversion and ensure that results are geologically plausible. Implementations of regularized

joint inversion in both the data-domain and image-domain are considered. Joint data-domain inversion minimizes a global least-squares objective function, whereas joint image-domain inversion utilizes combinations of target-oriented approximations of the Hessian of the least-squares objective function. Applications to synthetic data sets show that, compared to migration or separate inversion, linearized joint inversion provides time-lapse seismic images that are less sensitive to geometry differences between surveys and to the overburden complexity. An important advantage of an image-domain inversion is that it can be solved efficiently for a small target around the reservoir.

Joint image-domain inversion requires careful preprocessing to ensure that the data contain only primary reflections, and that the migrated images are aligned. The importances of various preprocessing steps are demonstrated using two-dimensional time-lapse data subsets from the Norne field. Applications of regularized image-domain joint inversion to the Valhall Life-of-Field Seismic (LoFS) data sets show that it provides improved time-lapse images compared to migration. These applications show that regularized joint image-domain inversion attenuates obstruction artifacts in time-lapse seismic images and that it can be applied to several data sets. Furthermore, because it is computationally efficient, joint image-domain inversion can be repeated quickly using various a priori information.

# Preface

The electronic version of this report<sup>1</sup> makes the included programs and applications available to the reader. The markings **ER**, **CR**, and **NR** are promises by the author about the reproducibility of each figure result. Reproducibility is a way of organizing computational research that allows both the author and the reader of a publication to verify the reported results. Reproducibility facilitates the transfer of knowledge within SEP and between SEP and its sponsors.

**ER** denotes Easily Reproducible and are the results of processing described in the paper. The author claims that you can reproduce such a figure from the programs, parameters, and makefiles included in the electronic document. The data must either be included in the electronic distribution, be easily available to all researchers (e.g., SEG-EAGE data sets), or be available in the SEP data library<sup>2</sup>. We assume you have a UNIX workstation with Fortran, Fortran90, C, X-Windows system and the software downloadable from our website (SEP makerules, SEPScons, SEPlib, and the SEP latex package), or other free software such as SU. Before the publication of the electronic document, someone other than the author tests the author's claim by destroying and rebuilding all ER figures. Some ER figures may not be reproducible by outsiders because they depend on data sets that are too large to distribute, or data that we do not have permission to redistribute but are in the SEP data library, or that the rules depend on commercial packages such as Matlab or Mathematica.

---

<sup>1</sup><http://sepwww.stanford.edu/private/docs/sep14X>

<sup>2</sup><http://sepwww.stanford.edu/public/docs/sepdata/lib/toc.html>

**CR** denotes Conditional Reproducibility. The author certifies that the commands are in place to reproduce the figure if certain resources are available. The primary reasons for the CR designation is that the processing requires 20 minutes or more.

**NR** denotes Non-Reproducible figures. SEP discourages authors from flagging their figures as NR except for figures that are used solely for motivation, comparison, or illustration of the theory, such as: artist drawings, scannings, or figures taken from SEP reports not by the authors or from non-SEP publications.

Our testing is currently limited to LINUX 2.6 (using the Intel Fortran90 compiler) and the SEPlib-6.4.6 distribution, but the code should be portable to other architectures. Reader's suggestions are welcome. For more information on reproducing SEP's electronic documents, please visit <http://sepwww.stanford.edu/research/redoc/>.

# Acknowledgments

Several advances in the field of exploration seismology would have been impossible without the important contributions from the Stanford Exploration Project (SEP). I thank Biondo Biondi for giving me the opportunity to be a part of this unique and innovative group. In addition, I thank Biondo for his advice and guidance throughout my time at Stanford.

Jon Claerbout's vision and continued passion for teaching and research continues to shape the directions of student research in SEP. Jon's class—Geophysical Estimation by Example (GEE)—provided the most important tools for my research.

The Geophysics department Staff provided excellent support throughout my time at Stanford. Diane Lau, the SEP administrator, ensured all research, travel and tuition related issues are promptly dealt with. Tara Ilich, the Student Services Manager, ensured that everything I needed to be successful student was taken care of. Dennis Michael, the CEES Systems Administrator, provided superb support throughout my use of the cluster computers.

Statoil, through the Norwegian University of Science and Technology IO Center and Stanford Smart Fields project, provided the migrated time-lapse data sets used in chapter two of this dissertation. Bard Osdal of Statoil provided the raw time-lapse data sets used in chapter five. I thank Olav Barkved of BP for his assistance in the release of the Valhall time-lapse data sets used in chapter six.

Past and present SEP students made my time at Stanford enjoyable and my research productive. Many aspects of my research were built on previous work by Alejandro Valenciano and Yaxun Tang. Adam Halpert, my office mate for several years, proofread parts of my dissertation. Yi Shen brought sunshine to our office. I would miss current SEP students: Xukai Shen, Sjoerd de Ridder, Mandy Wong, Elita Li, Yang Zhang, Ohad Barak, Chris Leader, Ali Almomin, Qiang Fu, Noha Farghal, Musa Maharramov, and Jason Chang. I cherish times spent with and lessons learnt from previous students: Daniel Rosales, Brad Artman, Gabriel Alvarez, Guojian Shan, Bill Curry, Jeff Shragge, Abdullah Al Theyab, Mohammad Maysami, and Kittinat Taweessintananon. I would miss SEP seminars.

My years at Stanford were pleasant because of great friends like Tope Akinbehinje, Hiroki Sone and Evan Um. I learned a lot about geophysics from Roland Gunther and Otunba Claudio Cardoso, who started at SEP the same year I did. I thank Otunba Adeyemi Arogunmati for being a good friend and colleague throughout my time at Stanford.

My parents, Joseph and Mary Ayeni, have been supportive throughout my time at Stanford. Thank you for your prayers and patience. I thank my siblings, Kayode, Kunle and Dupe for their love and encouragement. I dedicate this research to the memory of my brother and mentor, Ayodeji Ayeni (1977-2008).

I am lucky to be married to a woman that is smarter than I am. Taiwo has thought me more about life in two and a half years than I have learned before meeting her. Thank you for your love, your patience and your support throughout our time at Stanford.

# Contents

Abstract	v
Preface	vii
Acknowledgments	ix
1 Introduction	1
2 Time-lapse seismic cross-equalization	17
3 Joint least-squares migration/inversion: theory	55
4 Synthetic examples	81
5 2D field data applications	119
6 3D field data applications	143
7 Conclusions	191
A Inverting for the monitor image at the baseline position	193

<b>B Joint inversion formulations for multiple surveys</b>	<b>196</b>
<b>Bibliography</b>	<b>201</b>

# List of Tables

2.1 Matched filter parameters . . . . . 37

# List of Figures

1.1	Comparison between migrated baseline and monitor seismic traces along a producing reservoir section (a). The superposed traces (left) and the difference (right) are shown before (b), and after (c) time-lapse cross-equalization. Note that before cross-equalization, small amplitude and phase differences contaminate the interesting time-lapse amplitude change between the traces (b). After careful cross-equalization, we obtain production-related amplitude change—indicated by the arrow X in (c)—which can then be transformed into reservoir property changes. . . . .	4
1.2	Cartoon illustrating a typical marine seismic acquisition geometry. The migrated baseline, monitor and time-lapse images for the boxed region (target area), obtained using the same geometry for both the baseline and monitor data sets, are shown in Figure 1.3. <b>[NR]</b> . . . . .	5
1.3	Migrated baseline image (a), monitor image (b), and time-lapse image (c) for the target area indicated in the numerical model in Figure 1.2. Note that in this ideal case, where acquisition geometries are repeated for both the baseline and monitor data sets, the amplitude difference in the time-lapse image is related only to changes within the reservoir. <b>[CR]</b> . . . . .	7

1.4	Cartoon illustrating how an obstruction in marine seismic acquisition affects data recording. Compare this cartoon to Figure 1.2. The time-lapse image for the target area, between the baseline image in Figure 1.3(a) and a monitor image with a gap caused by an obstruction, is shown in Figure 1.5. <b>[NR]</b> . . . . .	8
1.5	Time-lapse image obtained from a complete baseline data set (Figure 1.2) and an incomplete monitor data set (Figure 1.4). Note that, compared to the ideal time-lapse image in Figure 1.3(c), this image is highly contaminated with artifacts resulting from gap in the monitor acquisition geometry. To explain these artifacts, the impulse responses (point spread functions) at point Z for the complete and incomplete geometries are studied later in this chapter. <b>[CR]</b> . . . . .	8
1.6	Cartoon illustrating a typical marine acquisition geometry over a complex earth model. Comparing this cartoon to Figure 1.2, note that in this subsurface model, the reservoir is located under a complex salt body. The time-lapse image for the target area, computed as the image difference between the baseline and monitor data sets, is shown in Figure 1.7. <b>[NR]</b> . . . . .	10
1.7	Time-lapse image between perfectly repeated baseline and monitor data sets from the numerical model in Figure 1.6. Note that, compared to the ideal time-lapse image in Figure 1.3(c), this image is distorted. These distortions in time-lapse amplitudes are caused by the uneven/irregular subsurface illumination associated with the complex overburden (Figure 1.9). To explain these distortions, the impulse responses (point spread functions) at points X, Y, and Z are studied later in this chapter. <b>[CR]</b> . . . . .	10

1.8	PSFs at point Z in Figure 1.5 in the spatial domain (top) and wavenumber domain (bottom). The left and middle panels are the PSFs for the baseline and monitor geometries respectively. The right panels show the differences between the baseline and monitor PSFs resulting from differences in their geometries. [CR]. . . . .	11
1.9	Point spread functions (PSFs) at points X, Y, and Z in Figure 1.7 in the spatial domain (top) and wavenumber domain (bottom). Although these points are located close to each other, because of the complex overburden, they differ significantly in the range of illuminated wavenumbers—hence the difference in the spreading. [CR]. . .	12
2.1	Synthetic seismic images (a) and (b), and components of the apparent displacements between them along the horizontal (c) and vertical (d) axes. The image differences before, and after different kinds of warping are shown in Figure 2.2. The evolution of apparent displacement components derived from sequential 1D warping are presented in Figures 2.3 and 2.4. [CR]. . . . .	23
2.2	Differences between the seismic images in Figures 2.1(a) and 2.1(b) before warping (a), after one iteration of vertical warping (b), after 10 iterations of vertical warping (c), and after 10 iterations of sequential one-dimensional warping. All images are clipped to similar amplitude levels. Although iterative vertical warping provides improved match compared to one iteration of <i>conventional</i> vertical warping (b), there are still significant differences between the two images (c). Sequential 1D warping provides the best results with negligible amplitude differences between the warped images (d). [CR]. . . . .	24

2.3	Evolution of the horizontal displacement components between Figures 2.1(a) and 2.1(b) obtained via sequential 1D warping. These panels show the estimated displacements after one, two, four, six, eight and ten iterations, respectively. As a function of iterations, these displacements converge towards the actual values in Figure 2.1(c). [CR].	26
2.4	Evolution of the vertical displacement components between Figures 2.1(a) and 2.1(b) obtained via sequential 1D warping. These panels show the estimated displacements after one, two, four, six, eight and ten iterations, respectively. As a function of iterations, these displacements converge towards the actual values in Figure 2.1(d). [CR]. . . . .	27
2.5	Migrated images of the Norne field obtained from the 2001 baseline (a), and 2006 Monitor (b) data sets. The data processing steps are discussed by Osdal et al. (2006). [CR]. . . . .	32
2.6	Vertical displacement components (time-shifts) between the 2006 monitor image and the baseline after one (a), two (b) and three (c) iterations. Note that the first iteration captures main features of the displacement field, whereas later iterations capture the higher-frequency details, thereby improving the resolution. The top of the producing segments between 2.5 s and 2.6 s can be mapped easily using these displacement components. [CR]. . . . .	34
2.7	Horizontal displacement components between the 2006 monitor and the baseline in the inline (a), and crossline (b) directions; Time-shift errors (c) that are caused by neglecting horizontal displacements. [CR].	35
2.8	Absolute vertical and lateral displacements at the top of the reservoir between the baseline and the 2003 (a), 2004 (b), and 2006 (c) monitor images. In (c), the box indicates the location of the zoomed panel (d). The arrows indicate the displacement direction. [CR]. . . . .	36

2.9	Fractional velocity change between the baseline and the 2003 (a), 2004 (b) and 2006 (c) monitor images. Note that in general, due to depletion, velocity within the reservoir decreases with time. The velocity change along the horizon (top of the reservoir) for these three cases are shown in Figure 2.11. [CR]. . . . .	38
2.10	Velocity errors caused by neglecting horizontal displacements between the baseline and the 2003 (a), 2004 (b) and 2006 (c) monitor images. Note that the error in velocity increases with time. The errors in velocity change along the horizon (top of the reservoir) are shown in Figure 2.12. [CR]. . . . .	39
2.11	Maps of fractional velocity change at the top of the reservoir (Figure 2.9) between the baseline and the 2003 (a), 2004 (b) and 2006 (c) monitor images. Note that in general, due to depletion, velocity within the reservoir decreases with time. [CR]. . . . .	40
2.12	Maps of errors in fractional velocity change at the top of the reservoir (Figure 2.10) between the baseline and the 2003 (a), 2004 (b) and 2006 (c) monitor images. Note that the errors are greatest in parts of the field with the largest change (Figure 2.11). Furthermore, note how the errors increase with time. [CR]. . . . .	41
2.13	Maps of selected optimized matched filtering parameters. The panels show the damping parameter $\epsilon$ (a), the filter length, and perturbations to the upper boundary of the estimation window. [CR]. . . . .	42
2.14	Time-lapse images between the 2006 monitor and the baseline after different processing steps. The panels show the time-lapse image before warping (a), after warping (b), and after optimized matched filtering. The time-lapse amplitudes of interest are located around the time-slice position. Note the improvements in quality of the time-lapse image after different processing steps. [CR]. . . . .	43

2.15	<p>Comparison between time-lapse images after different processing steps. The panels show inline sections through the time-lapse image after warping (a), after matched filtering with a single set of parameters (b), and after matched filtering with optimized parameters (c). The time-lapse amplitudes of interest are indicated by label <i>A</i>. In the oval, note that whereas the time-lapse image from filtering with a single set of parameters (b) contains artifacts that are not present in the original time-lapse image (a), these artifacts are attenuated by filtering with optimized parameters (c). [CR]. . . . .</p>	45
2.16	<p>Maps of average time-lapse amplitudes between the baseline image and the 2006 monitor image within a 0.6 s window around the reservoir. The panels show amplitude difference after warping (a), after matched filtering with a single set of parameters (b), and after optimized matched filtering (c). As shown in Figures 2.17 and 2.18, amplitudes within oval B are artifacts. The most significant production-related changes are expected only within ovals A and C. These artifacts are better attenuated by optimized filtering (c). Note that the time-lapse amplitudes within oval A in (b) are corrupted by filtering artifacts. [CR]. . . . .</p>	47
2.17	<p>Maps of average time-lapse amplitudes between the baseline image and the 2006 monitor image within a 0.5 s window located above the reservoir, where no production-related amplitude change is expected. The panels show amplitude differences after warping (a), after matched filtering with a single set of parameters (b), and after optimized matched filtering (c). In (b), note that matched filtering with a single set of parameters attenuate many of the non-repeatability artifacts (e.g., oval B) but also introduces undesirable artifacts (e.g., oval A). Note in (c) that optimized matched filtering provides satisfactory attenuation of the artifacts without introducing new undesirable artifacts. [CR]. . .</p>	48

2.18	Maps of average time-lapse amplitudes between the baseline image and the 2006 monitor image within a 0.5 s window located below the reservoir, where no production-related amplitude change is expected. The panels show amplitude differences after warping (a), after matched filtering with a single set of parameters (b), and after optimized matched filtering (c). Note that matched filtering with provides satisfactory attenuation of the high amplitude artifacts in the (e.g., oval B). Furthermore, note that at several locations (e.g., oval A) the result from optimized filtering contain fewer artifacts. <b>[CR]</b> . . . . .	49
2.19	Maps showing errors in time-lapse amplitudes within the reservoir caused by considering only vertical displacements versus considering multidimensional displacements. The panels show amplitude differences between the baseline and the 2003 (a), 2004 (b), and 2006 (c) monitor surveys. These amplitude differences represent errors in time-lapse amplitudes caused by approximating multidimensional warping by vertical warping. <b>[CR]</b> . . . . .	50
3.1	Two-dimensional slices through 3D impulse responses derived by cascaded two-dimensional filtering (a) and full 3D factorization (b)-(d). Note that the impulse responses derived from full factorization are more isotropic than the one derived from cascaded two-dimensional filtering. Furthermore, note that the filters in (b), (c), and (d) have large, medium and small ranges. <b>[ER]</b> . . . . .	76
3.2	Impulse response for two different dip combinations derived from full factorization. The filter in (a) has a positive inline dip and negative crossline dip, whereas the filter in (b) has a negative inline dip and positive crossline dip. Furthermore, note that the filter in (a) has a smaller range than the filter in (b). <b>[ER]</b> . . . . .	77

4.1	Wavefields from multiple randomized simultaneous sources (a), and from two continuously shooting seismic sources (b). In each figure, the blue line indicates intersecting positions of the the three slices that are displayed. In Panel (a), the geometry and relative shot-timing are different for all surveys, whereas in Panel (b), only the acquisition geometry differs between surveys. The third dimension denotes survey/recording time. <b>[CR]</b> . . . . .	87
4.2	Baseline velocity model of the modified Marmousi model. The only changes between surveys are reflectivity changes within the reservoir. <b>[CR]</b> . . . . .	88
4.3	Synthetic data from multiple asynchronous sources. In (a) and (b), the front panels show the encoded data for two different surveys. In addition to varying the relative shot time, the source positions are also different for each survey (Figure 4.4). Note that, whereas the first dimension denote two-way travel time, the third dimension denotes survey/recording time. <b>[CR]</b> . . . . .	89
4.4	Plots of relative time-delays (left) and shot-displacements for seven out of the fifteen numerical models that were used to generate the data in Figure 4.3. In all plots, the horizontal axis indicates shot position. The relative shooting times are referenced to the earliest shot in each survey, whereas shot-displacements are referenced to the baseline shot positions. <b>[CR]</b> . . . . .	90
4.5	Migrated images (a) and corresponding time-lapse estimates (b) obtained from perfectly repeated conventional (single-source) data sets. In these (and in similar Figures), the side panel (third axis) shows the seismic properties (a) and time-lapse changes (b) at a fixed spatial position, whereas the top panel shows the spatial-temporal distribution seismic properties. <b>[CR]</b> . . . . .	92

4.6	Images (a) and corresponding time-lapse estimates (b) obtained from migrating the data sets in Figure 4.3. In both Figures, note the numerous artifacts caused by geometry and shot-timing non-repeatability and crosstalk artifacts. Without attenuating these artifacts, it would be difficult to accurately interpret the time-lapse information. [CR]. . . . .	93
4.7	Dips derived from the migrated baseline image. These dips are used to construct the spatial regularization operator for the inversion. Note that the faults in the dip field are picked manually from the baseline image. [CR]. . . . .	94
4.8	Dip-contrast computed based on how rapidly the dips change in the model. To obtain this image, the picked faults are smoothed to obtain variances based on the distance from the faults. By changing the filter range according to these variances, the faults are preserved during regularized inversion. [CR]. . . . .	94
4.9	Images (a) and corresponding time-lapse estimates (b) obtained from inversion of the simultaneous-source data sets in Figure 4.3. These results are obtained after fifty-six conjugate gradients iterations. Note that the non-repeatability and crosstalk artifacts in the migrated images (Figure 4.6) have been attenuated by inversion. Also, note the improved resolution of the inverted images compared to the migrated single-source data (Figure 4.5). [CR]. . . . .	96
4.10	Time-lapse seismic images obtained after two and five conjugate gradient iterations (a) and (b), respectively. Note the gradual reduction in the artifacts compared to the time-lapse images from migration (Figure 4.6(b)). Furthermore, note that the artifacts have decreased in (b) compared to (a). [CR]. . . . .	97

4.11	Time-lapse seismic images obtained after fifteen and fifty conjugate gradient iterations (a) and (b), respectively. Note the reduction in the artifacts compared to the time-lapse images from migration (Figure 4.6(b)). Furthermore, note that the artifacts have further decreased in (b) compared to (a) and compare to Figures 4.10(a) and 4.10(b). [CR]. . . . .	98
4.12	Numerical two-dimensional velocity model used in Example II. The box indicates the location of the target-area around the crest of the folded reservoir (top-and base indicated by the red horizon). [CR] . .	101
4.13	Numerical two-dimensional velocity model used to generate the reference images in Figure 4.14 and in Example III. The box indicates the location of the target-area around the crest of the folded reservoir (top-and base indicated by the red horizon). [CR] . . . . .	101
4.14	Migrated monitor (a) and time-lapse (b) images, and subsurface illumination (c) for the target area shown in Figure 4.13. In (c), red indicates high illumination, whereas blue indicates low illumination. Compare these images to those in Figures 4.15 and 4.18. [CR] . . .	102
4.15	Migrated monitor (a) and time-lapse (b) images, and subsurface illumination (c) for the target area shown in Figure 4.12 At points $X$ , $Y$ , and $Z$ along the reservoir, note that the illumination is highly irregular, the migrated image is distorted, and compared to Figure 4.15(b), the time-lapse image is distorted. Recall that point-spread-functions at points $X$ , $Y$ , and $Z$ are shown in Figure 1.9. [CR] . . . . .	103
4.16	Inverted monitor (a) and time-lapse (b) images for the target area shown in Figure 4.13. Note that these images show improved resolution over the migrated images (Figure 4.14). Compare these to the inverted images in Figures 4.17 and 4.19. [CR] . . . . .	104

4.17	Inverted monitor (a) and time-lapse (b) images for the target area shown in Figure 4.12. Note that these images are comparable to those in Figure 4.16. Importantly, at points $X$ , $Y$ , and $Z$ , note that distortions in the migrated time-lapse image (Figure 4.15(b)) have been corrected by inversion. The salt body in these images has been cropped for clarity. [CR] . . . . .	105
4.18	Migrated monitor image (a), time-lapse image (b), and subsurface illumination (c) for the target area shown in Figure 4.13, where an a simulated obstruction causes a gap in the monitor data. Note that, compared to the reference time-lapse image (Figure 4.14(b)), the time-lapse image (b) is contaminated by obstruction artifacts. The difference in the point-spread-functions for the baseline and monitor geometries at point $Z$ is shown in Figure 1.8. [CR] . . . . .	107
4.19	Inverted monitor (a) and time-lapse (b) images for the target area shown in Figure 4.13 with a simulated obstruction in the monitor data. Note that these images are comparable to those in Figure 4.16. [CR] . . . . .	108
4.20	Band-limited reference reflectivity models for the first (a), and second (b) monitors. The baseline model is similar to these but with constant reflectivity along each horizontal reflector. The reference time-lapse models computed as the differences between (a) and (b), and the baseline reflectivity model are shown in Figure 4.21. [CR]. . . . .	110
4.21	Reference time-lapse images between the first (a), and second (b) monitor models (Figure 4.20) and the baseline model (not shown). Not that reflectivity changes increase in amplitude and size with time. [CR]. . . . .	111
4.22	Migrated time-lapse images between the first (a), and second (b) synthesized monitor images and the baseline. Note that, compared to the reference time-lapse images (Figure 4.21), the time-lapse amplitudes are contaminated by obstruction artifacts. [CR]. . . . .	112

4.23	Inverted time-lapse images between the first (a), and second (b) monitor and the baseline, derived from weakly-coupled joint inversion between the baseline and monitor images. Note that, although most of the obstruction artifacts in Figure 4.22 have been attenuated, the time-lapse amplitudes are still contaminated by numerous artifacts not present in the reference time-lapse images (Figure 4.21). . . . .	114
4.24	Inverted time-lapse images between the first (a), and second (b) monitor and the baseline derived from strongly-coupled joint inversion between the baseline and monitor images. Note that, although the artifacts in Figures 4.23 and 4.22 have been attenuated, compared to the reference time-lapse images (Figure 4.21), the time-lapse amplitudes have been destroyed. . . . .	115
4.25	Inverted time-lapse images between the first (a), and second (b) monitor and the baseline, derived from satisfactorily coupled joint inversion of the baseline and monitor images. Note that the obstruction artifacts are sufficiently attenuated, whereas the time-lapse amplitudes are preserved. These results are comparable in quality to the reference time-lapse images (Figure 4.21). . . . .	116
5.1	A portion of the raw two-dimensional streamer data from the Norne 2004 (baseline) data set. [CR] . . . . .	121
5.2	Raw baseline (a) and monitor (b) stacked images. Note that, along this section, the geology is relatively simple, with predominantly horizontal reflectors. The reservoir is located at approximately 2600 m depth. [CR]	122

5.3	Raw pre-stack baseline (a) and monitor (b) images of the target area. In these images, the horizontal events are primaries, which have been adequately imaged. The dominant artifacts in both images are multiples, which show significant curvature across angles. If they are not adequately attenuated, these multiples will contaminate the time-lapse difference between these images. [CR] . . . . .	124
5.4	Pre-stack baseline image (a) and monitor image (b) of the target area obtained from the preprocessed data sets. Note that the artifacts in the raw image (Figure 5.3) have been attenuated. In addition, note that the monitor image has been warped (using apparent displacements in Figures 5.5) to the baseline image. [CR] . . . . .	125
5.5	Pre-stack apparent vertical displacements between the baseline and monitor images (Figures 5.4(a) and 5.4(b)). Red, blue and green denote positive, negative and zero displacements, respectively. Note that the maximum apparent displacements correspond to the reservoir location in the horizontal range between 2000 m and 3000 m. Also, note that the apparent displacement varies with opening angle. [CR] . . . . .	127
5.6	Hessian diagonal (subsurface illumination) for the target area. Red indicates regions with high illumination, whereas blue indicates regions with low illumination. [CR] . . . . .	128
5.7	Dips derived from the stacked baseline image. Red indicates positive dips, whereas blue indicates negative dips. These dips are used to construct the spatial regularization operator used in the inversion. [CR]	129
5.8	Time-lapse images obtained from the raw data (a), after multiple attenuation by parabolic Radon demultiple (b), and after amplitude correction (c). Note the incremental improvements in the time-lapse image from (a) to (c). [CR] . . . . .	130

5.9	Time-lapse images obtained after pre-stack warping (a), after residual post-stack warping (b), and after image-domain inversion (c). Note the incremental improvements in the time-lapse image from (a) to (c). [CR] . . . . .	131
5.10	Gapped monitor data. Note that sources and receivers are missing within the simulated obstruction. [CR] . . . . .	133
5.11	Pre-stack apparent vertical displacements between the complete baseline image and the image from interpolated monitor data sets. Comparing this to Figure 5.5, note that estimates of the apparent displacements are similar to those from the complete data case. [CR] . . . .	134
5.12	Illumination ratio between the baseline and monitor. Red indicates regions with equal illumination (i.e., ratio equals unity) whereas blue indicates unequal illumination (i.e., ratio less than unity). [CR] . . .	135
5.13	PSFs at point $x = 2600$ m and $z = 2600$ m for the baseline (a) and (c), and the monitor (b) and (d). The panels show the PSFs in the spatial domain (a) and (b), and in the wavenumber domain (c) and (d). The differences between these PSFs are shown in Figures 5.14. [CR] . . .	136
5.14	Differences between the baseline and monitor PSFs at $x = 2600$ m and $z = 2600$ m in the spatial domain (a) and wavenumber domain (b). In (a), note that there are significant differences between PSFs away from the central point (i.e., in the off-diagonal elements of the Hessian matrices). Likewise, in (b), there are significant differences in wavenumber illumination for the two geometries. [CR] . . . . .	136
5.15	Time-lapse images obtained from the raw data (a), after conventional time-lapse processing (b), and after image-domain inversion (c). Because of artifacts introduced by the incomplete monitor data, conventional methods fail to provide results of comparable quality to the complete data example (Figure 5.9(b)). As shown in (c), regularized joint inversion provides satisfactory results. [CR] . . . . .	137

5.16	Time-lapse image obtained after weighting the baseline and monitor images by the diagonal of the Hessian matrices. Because the diagonal of the Hessian does not contain full information about subsurface illumination discrepancies, it only provides limited improvements compared to conventional methods (Figure 5.15(b)). As shown in Figure 5.15(c), regularized joint inversion provides a time-lapse image that is more comparable in quality to the complete data example (Figure 5.9(b)).	138
	<b>[CR]</b> . . . . .	
6.1	Baseline migration velocity obtained by full waveform inversion (see Sirgue et al. (2010)). This velocity model was used to image all data sets in this study. The target area—indicated by the box—is restricted to a small area of interest around the reservoir. The gas cloud, located outside the study area, does not cause significant imaging challenges in the target area. <b>[NR]</b> . . . . .	145
6.2	Full LoFS acquisition geometry showing locations of all shots and receivers. The purple box indicates the location of the study area, shown in detail in Figure 6.3. The coordinate axes in these figures (and in all figures) are distances in meters. <b>[ER]</b> . . . . .	147
6.3	Acquisition geometry showing locations of all shots and receivers for the data subsets used in this study. Apart from the introduction of gaps in some examples, the source-receiver geometry is closely repeated for all data sets. The gap is located at the center of the study area (see Figure 6.6). An enlarged view of the study area is presented in Figure 6.4. <b>[ER]</b> . . . . .	148
6.4	An enlarged view of the study area (Figure 6.3) showing the complete source-receiver geometry. The shot spacing is 50 m in both the inline and crossline directions, while the receiver spacing is 50 m in the inline direction and 300 m in the crossline direction. <b>[ER]</b> . . . . .	149

6.5	Sample receiver gathers acquired at the same location for the first (a), and ninth (b) LoFS surveys. Note in both gathers the full azimuth of the recording geometry. In both panels, the second and third dimensions are the inline and crossline offsets, respectively. <b>[ER]</b> . . . . .	150
6.6	An enlarged view of the study area (Figure 6.3) showing the shot and receiver locations within the study area, and the location of the simulated obstruction in the monitor geometry. There are not sources and receivers within the gap. Compare this to Figure 6.4, which shows the complete geometry of the baseline survey. <b>[ER]</b> . . . . .	153
6.7	Surface (CMP) fold for the baseline (a) and monitor (b). Red indicates high fold, whereas blue indicates low fold. Note that whereas the baseline fold is mostly uniform within the study area, the gapped monitor geometry causes significant non-uniformity of fold. The box indicates the same study area shown in Figures 6.3. <b>[ER]</b> . . . . .	154
6.8	Hessian diagonal for the complete baseline (a) and incomplete monitor (b) geometries. In these (and similar) displays throughout this chapter, the top panel is a depth slice and the side panels are the inline and crossline slices. The crosshairs show the position of the slices in the image cube. The depth slices show the illumination at the ocean bottom (a) and (b). Red indicates high illumination, whereas cyan indicates low illumination. <b>[CR]</b> . . . . .	156
6.9	Hessian diagonal for the complete baseline (a) and incomplete monitor (b). The depth slices show the illumination at a depth the above the reservoir. Red indicates high illumination, whereas cyan indicates low illumination. <b>[CR]</b> . . . . .	157
6.10	Hessian diagonal for the complete baseline (a) and incomplete monitor (b). The depth slices show the illumination within the reservoir. Red indicates high illumination, whereas cyan indicates low illumination. <b>[CR]</b> . . . . .	158

6.11	Illumination ratio between the baseline and monitor at the ocean bottom (a) and at the reservoir depth (b). Note that the simple rectangular illumination disparity at the ocean bottom becomes more complex at the reservoir depth. [CR] . . . . .	159
6.12	Point spread function (row of the baseline Hessian matrix) at subsurface point inline 6,600 m, crossline 6,475 m and depth 2,580 m in the spatial domain (a), and in the wavenumber domain (b) for the complete (baseline) geometry. [CR] . . . . .	160
6.13	Difference between the baseline point spread function at subsurface point inline 6,600 m, crossline 6,475 m and depth 2,580 m (Figure 6.12) and the monitor point spread function at the same point in the spatial domain (a), and in the wavenumber domain (b). [CR] . . . . .	161
6.14	Migrated images showing depth slices at the ocean bottom. The box indicates the target area in the baseline image (a) and in the monitor image (b). Note the location of the gap in the monitor. [CR] . . . . .	163
6.15	Migrated images showing depth slices at 50 m. The box indicates the target area in the baseline image (a) and in the monitor image (b). The shallow faults at this depth are clearly imaged. [CR] . . . . .	164
6.16	Migrated images showing depth slices above the reservoir at 1,750 m. The box indicates the target area in the baseline image (a) and in the monitor image (b). The well-imaged unconformity show evidence of faulting and channelization. [CR] . . . . .	165
6.17	Migrated images showing depth slices at the reservoir depth. The box indicates the target area in the baseline image (a) and in the monitor image (b). In (a) and (b), the flanks of the Valhall structure are imaged clearly. [CR] . . . . .	166

6.18	Migrated images of the target area obtained from the complete baseline data (a), and the incomplete monitor data (b). The time-lapse image between these images is shown in Figure 6.19. Compare these images to the inverted images in Figure 6.25. [CR]	168
6.19	Time-lapse image obtained as the difference between the migrated baseline and monitor images (Figure 6.18) prior to warping. Compare this to the time-lapse image difference between the warped images (Figure 6.22(a)), and between the inverted images (Figure 6.24(a)). [CR]	169
6.20	Vertical (a) components of apparent displacement vectors between the baseline and monitor images within the target area. Red indicates downward displacements, whereas blue indicates upward displacements. The inline and crossline components of these displacement vectors are presented in Figure 6.21. [CR]	169
6.21	Inline (a) and crossline (b) components of apparent displacement vectors between the baseline and monitor images within the target area. In these figures, Red indicates rightward displacements, whereas blue indicates leftward displacements. The corresponding vertical (depth) components are shown in Figure 6.20. [CR]	170
6.22	Migrated time-lapse images of the target area obtained after warping the monitor image to the baseline image. Panel (a) shows the time-lapse image derived from the complete baseline and incomplete monitor, whereas panel (b) shows the time-lapse image derived from complete baseline and complete monitor data sets. In (a), artifacts caused by misalignments due to velocity and compaction have been removed, leaving only differences due to production-induced reflectivity changes and difference in geometry between the baseline and monitor data. The differences between (a) and (b) are caused by the incomplete monitor geometry in (a). [CR]	171

6.23	Inline (a) and crossline (b) dips estimated from the baseline image (Figure 6.18(a)) using the plane-wave destruction method (see Fomel (2002)). These dips are used to construct the spatial regularization operator for the inversion. <b>[CR]</b> . . . . .	173
6.24	Time-lapse images of the target area obtained from regularized image-domain inversion of the incomplete (a) and complete (b) data sets. Note that these inverted time-lapse images are comparable. In (a), obstruction artifacts in the migrated time-lapse image (Figure 6.22(a)) have been attenuated by inversion. In addition, this inverted time-lapse image shows improved resolution over the migrated time-lapse image. A comparison of the time-lapse amplitudes along the reservoir is presented in Figure 6.26. <b>[CR]</b> . . . . .	175
6.25	Inverted baseline image (a), and monitor image (b) of the target area obtained from the complete baseline and incomplete monitor data sets. The difference between these images, which are obtained by regularized joint image-domain inversion, is presented in Figure 6.24(a). Compared to the migrated images in Figure 6.18, these images show improved resolution of the subsurface reflectivity. <b>[CR]</b> . . . . .	176
6.26	Average time-lapse amplitudes within a 60 m window around the reservoir obtained from migration (a) and (b), and from regularized image-domain inversion (c) and (d). Figures (a) and (c) are the reference amplitudes obtained from the complete data, whereas (b) and (d) are obtained from the incomplete data. These amplitude maps are presented at the same clip level relative to the respective baseline and monitor images. Note the discrepancies in the time-lapse amplitude distribution obtained via migration of the complete (a), and incomplete (b) data. This discrepancy has been attenuated via inversion of the same data sets (c) and (d). <b>[CR]</b> . . . . .	177

6.27	An enlarged view of the study area (Figure 6.3) showing the shot and receiver locations within the study area, and the location of the simulated obstruction in the geometry the first monitor (LoFS 5). Note that the gap in the source locations is bigger than the gap in the receiver locations. There are not sources and receivers within the overlap area. Compare this to Figures 6.4 and 6.6, which show the complete baseline geometry and the incomplete geometry of the second monitor. [ER] . . . . .	179
6.28	Subsurface illumination ratio between the complete baseline survey and the incomplete <i>first</i> monitor survey, showing a depth slice through the reservoir. Compare this figure to the illumination ratio between the baseline and the second monitor survey (Figure 6.11(b)). The illumination ratio between the baseline and the two monitor geometries along the reservoir are shown in Figure 6.29. [CR] . . . . .	180
6.29	Illumination ratio between the baseline and the first monitor (a), and between the baseline and the second monitor (b). In these maps, red indicates regions with the largest illumination disparity, whereas blue indicates regions with the smallest illumination disparity. In both examples, although the geometry difference is caused by a rectangular gap in the monitor geometries, the illumination disparities are complex at depth. [CR] . . . . .	181
6.30	Average time-lapse amplitudes within a 60 m window around the reservoir obtained from migration. Panels (a) and (c) are the difference maps between the complete baseline, and the complete first and second monitor, respectively. Panels (b) and (d) are the corresponding results from the complete baseline and the incomplete monitor data. These amplitude maps are presented at the same clip relative to the respective baseline and monitor images. Note that there are large discrepancies in the time-lapse amplitude distribution obtained via migration of the complete and incomplete data sets. [CR] . . . . .	182

6.31 Average time-lapse amplitudes within a 60 m window around the reservoir obtained from from regularized joint image-domain inversion. Panels (a) and (c) are the difference maps between the complete baseline, and the complete first and second monitor, respectively. Panels (b) and (d) are the corresponding results from the complete baseline and the incomplete monitor data. These amplitude maps are presented at the same clip relative to the respective baseline and monitor images. Note that discrepancies in the time-lapse amplitude distribution in the migrated results (Figure 6.30) have been reduced. [CR] . . . . . 183

6.32 Scaled residual for six different regularization parameters. Each graph corresponds to a different temporal regularization parameter, expressed as a percentage of the RMS energy in the migrated baseline image. All the graphs are obtained with the same spatial regularization parameter but different temporal constraints. As expected, large temporal constraints lead to higher residuals. These graphs correspond to the residuals for the amplitude maps in Figure 6.33. [CR]. . . . . 185

6.33 Average time-lapse amplitudes within a 60 m window around the reservoir obtained from using different regularization parameters in the image-domain inversion of the complete baseline and monitor data. In these maps, which are presented at the same clip relative to the baseline and monitor images, the temporal (coupling) regularization parameter increases from (a) to (f). These amplitude maps are obtained with the same spatial regularization parameter. Especially within the ovals (labeled A, B and C), note the systematic changes in the time-lapse amplitudes as a function of the coupling strength. [CR] . . . . . 186

B.1 Concatenated truncated target-oriented Hessian matrices for three surveys. The matrix dimension is  $N_s \times N_{mod}$ , where  $N_s$  is the number of surveys and  $N_{mod}$  is the number of model points in the target area.  $S_i$  denotes the Hessian corresponding to survey  $i$ . Note that because this matrix is sparse and that the absolute values of its coefficients decrease away from its diagonal. As shown, the point-spread-function (PSF) refer to a row of the Hessian matrix, whereas the illumination refers to its diagonal. [CR]. . . . . 199



# Chapter 1

## Introduction

Time-lapse (4D) seismic imaging has become an established technology for monitoring changes in subsurface reservoir properties. In general, time-lapse seismic imaging involves repetition of similar seismic experiments over an evolving subsurface reservoir. Changes in the measured seismic reflection amplitudes and travel-times are then used to estimate changes in reservoir rock and fluid properties.

Over the past decade, the most important applications of time-lapse imaging have been in hydrocarbon reservoir monitoring. Widespread adoption of this technology as a reliable hydrocarbon reservoir monitoring tool can be attributed to improvements in seismic acquisition and imaging methods and to an improved understanding of the seismic responses of changing subsurface properties. Today, time-lapse seismic imaging is used to monitor changes in fluid flow, deformation, pressure, and saturation that are associated with hydrocarbon production and fluid injection. By providing information about changes within and around hydrocarbon reservoirs, time-lapse seismic imaging makes effective exploitation and management of hydrocarbon reserves possible. In addition, time-lapse seismic imaging has been widely applied to (and continues to be developed for) environmental investigations, such as monitoring the flow of carbon dioxide sequestered in subsurface reservoirs.

Although time-lapse seismic imaging technology is now almost fully matured,

several challenges still remain. In this dissertation, I explore some of these challenges and propose novel techniques to overcome them. Importantly, these techniques can attenuate artifacts in time-lapse images<sup>1</sup> that are caused by differences in acquisition parameters, obstructions, complex overburden and man-made noise. Therefore, even in the most difficult circumstances, we can obtain good-quality time-lapse images from which we can make reliable deductions about changes in subsurface reservoir properties.

## TIME-LAPSE SEISMIC IMAGING CHALLENGES

Reservoir rock and fluid property changes can be obtained from seismic amplitude and/or travel-time changes. There is a wide range of published work on the most important considerations for time-lapse seismic imaging. For example, Batzle and Wang (1992) and Mavko et al. (2003) outline important rock and fluid relationships; Lumley (1995), Calvert (2005), and Johnston (2005) discuss important processing and practical considerations; and Landro et al. (1999), Lefeuvre et al. (2003), Whitcombe et al. (2004), Zou et al. (2006), and Helgerud et al. (2011a) present several successful case studies. Because of the recorded successes in its applications, time-lapse seismic imaging has become an integral part of many hydrocarbon reservoir management projects.

In practice, differences in time-lapse seismic images caused by hydrocarbon production or fluid injection can be masked by non-repeatability artifacts (e.g., differences in acquisition geometry and ambient noise) or by uneven illumination due to complex overburden (e.g., a rugose salt canopy). Therefore, to correctly interpret time-lapse seismic images, such artifacts must be attenuated—a process commonly called seismic cross-equalization or cross-matching (Rickett and Lumley, 2001; Hall et al., 2005). Unless these artifacts are attenuated, it is impossible to accurately relate seismic image differences to changes in reservoir properties.

---

<sup>1</sup>Note that throughout this dissertation, unless otherwise stated, a time-lapse image refers to the difference in reflectivity between a baseline image and a monitor image.

Although conventional seismic cross-equalization methods are well developed and give reliable results in many practical applications, they fail where there are large inconsistencies between data sets or where the reservoir overburden is complex. In such scenarios, the inversion methods developed in this dissertation provide a way to attenuate artifacts that degrade time-lapse seismic images. Therefore, these methods improve our ability to estimate actual changes in reservoir properties from differences between seismic images. In addition, this dissertation discusses two common conventional time-lapse cross-equalization methods and shows how they can be improved. In the following sections, I outline some aspects of time-lapse seismic imaging that are considered in this dissertation.

### **Time-lapse *post-imaging* cross-equalization**

Even where the acquisition parameters have been closely repeated for seismic baseline and monitor data sets, production-related image differences between them can still be masked by unwanted differences. These masking differences may be caused by factors such as changes in water velocity due to salinity or temperature changes, tidal differences, changes in source depth and/or source waveform, and uncorrelated ambient noise and multiples. In many cases, these differences may be strong enough to completely mask differences in time-lapse seismic images that are related to hydrocarbon production or fluid injection. As discussed above, in conventional time-lapse seismic processing, the process of attenuating these masking artifacts in time-lapse images is called seismic cross-equalization. In practice, depending on the data quality, seismic cross-equalization is applied at different stages during the processing sequence—before and/or after imaging.

Figure 1.1 shows the seismic baseline, monitor and time-lapse traces extracted from raw and cross-equalized data sets from a producing North Sea field. In this example, both the baseline and monitor data sets were acquired using state-of-the-art marine seismic acquisition technology, with the geometries repeated as closely as possible. However, small acquisition differences generate undesirable artifacts that

mask production-related amplitude differences in the raw data (Figure 1.1(b)). In Figure 1.1(b), note that because of these undesirable artifacts, it is impossible to relate amplitudes in the time-lapse trace to production-related changes in the reservoir. Through seismic cross-equalization, these artifacts have been attenuated and production-related amplitude differences have been preserved (Figure 1.1(c)).

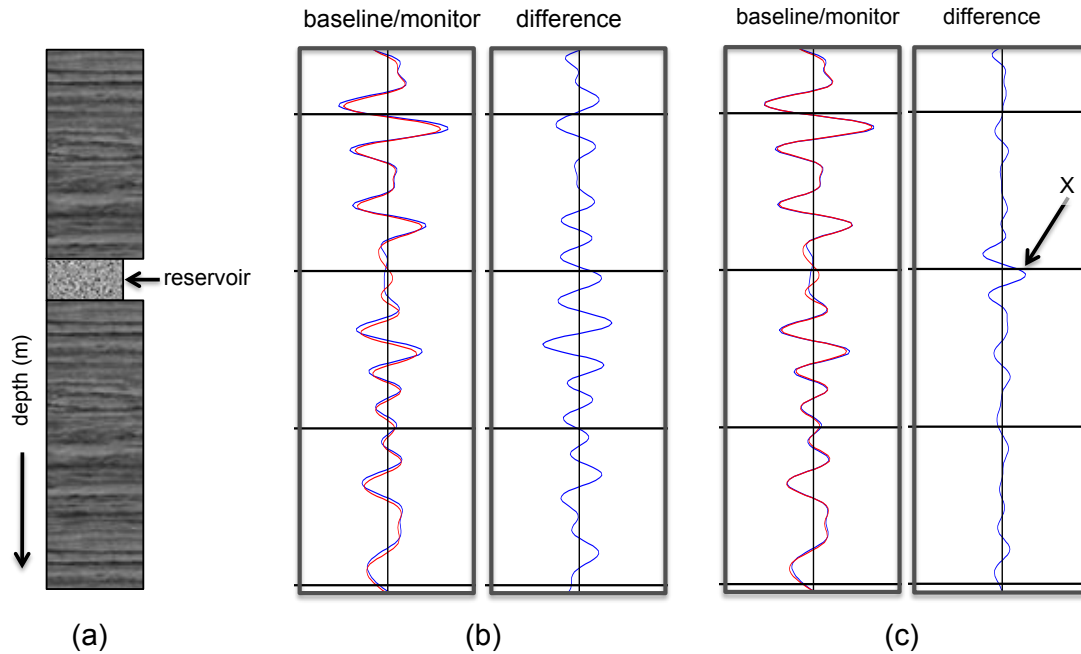


Figure 1.1: Comparison between migrated baseline and monitor seismic traces along a producing reservoir section (a). The superposed traces (left) and the difference (right) are shown before (b), and after (c) time-lapse cross-equalization. Note that before cross-equalization, small amplitude and phase differences contaminate the interesting time-lapse amplitude change between the traces (b). After careful cross-equalization, we obtain production-related amplitude change—indicated by the arrow X in (c)—which can then be transformed into reservoir property changes. chap1/. itr-4d

In this dissertation, I discuss how two widely used post-imaging cross-equalization methods—warping and match-filtering—can be improved. In addition, I show the processing steps applied to the raw data to obtain the result in Figure 1.1. Furthermore, I show practical scenarios where such processing steps become inadequate.

## Geometry differences

In principle, if the acquisition and environmental conditions are perfectly repeated between surveys, the time-lapse seismic image can provide accurate information about production-induced changes in reservoir properties. For example, Figure 1.2 shows a typical marine acquisition geometry for a seismic baseline survey. In Figure 1.2, and throughout this dissertation, the target area is a region of interest around the reservoir, where production- or injection-induced changes are expected. Assuming a baseline data set was acquired prior to production, by acquiring the monitor data at a later date after production using the same geometry, the image difference between the baseline and monitor can provide a reliable measure of production-induced changes reservoir properties.

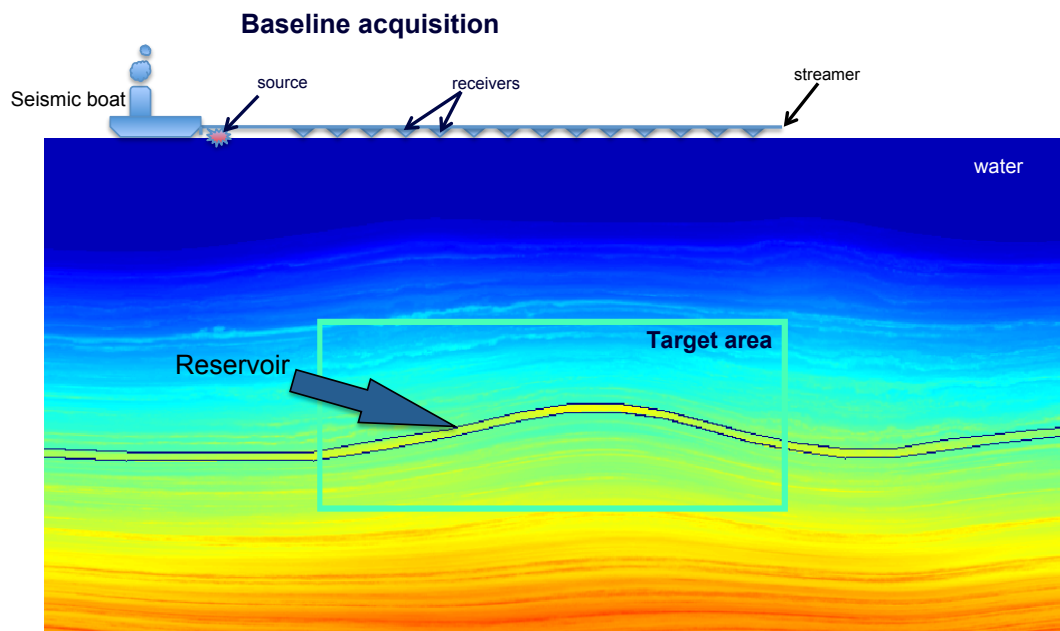


Figure 1.2: Cartoon illustrating a typical marine seismic acquisition geometry. The migrated baseline, monitor and time-lapse images for the boxed region (target area), obtained using the same geometry for both the baseline and monitor data sets, are shown in Figure 1.3. [NR] `chap1/. acq-base`

Figure 1.3 shows the migrated baseline and monitor images, and the time-lapse image (monitor minus baseline) for the target area indicated in Figure 1.2. For this ideal case, amplitudes in the time-lapse image (Figure 1.3(c)) can be related directly to changes within the reservoir.

As noted earlier, where differences in the acquisition parameters are small, conventional time-lapse seismic processing methods (i.e., seismic cross-equalization methods) are sufficient to obtain reliable time-lapse images. However, these methods are usually unable to perfectly reconcile large differences in acquisition geometry between time-lapse data sets. Such large geometry differences can be caused by changes in acquisition systems, obstructions due to new production or drilling facilities, or natural environmental changes.

Figure 1.4 shows a practical time-lapse imaging problem in many oil and gas fields, where obstructions due to new production or drilling facilities prevent data recording in parts of the field. In many cases, these obstructions are absent during the baseline acquisition. As shown in Figure 1.5, the time-lapse image obtained in this scenario is different from the one derived in the ideal case (Figure 1.3(c)). In this example, artifacts caused by acquisition geometry difference have masked the true reflectivity change, making it impossible to relate this time-lapse image difference to actual changes within the reservoir. Although new acquisition methods attempt to overcome this kind of problem, such methods are usually expensive (Stopin et al., 2011). In addition, whereas careful data regularization and processing methods can improve the information derivable from data acquired with different geometries, these methods will fail where the geometry difference is large.

Artifacts exist in the time-lapse image (Figure 1.5) because the conventional imaging operator does not account fully for geometry differences between surveys. As described later in this chapter, linearized joint inversion provides a way to correct for such geometry differences. In chapter 4, I show that by applying the linearized joint inversion methods developed in this dissertation to the data sets that produce the contaminated time-lapse image in Figure 1.5, we can obtain a time-lapse image similar in quality to that in Figure 1.3(c).

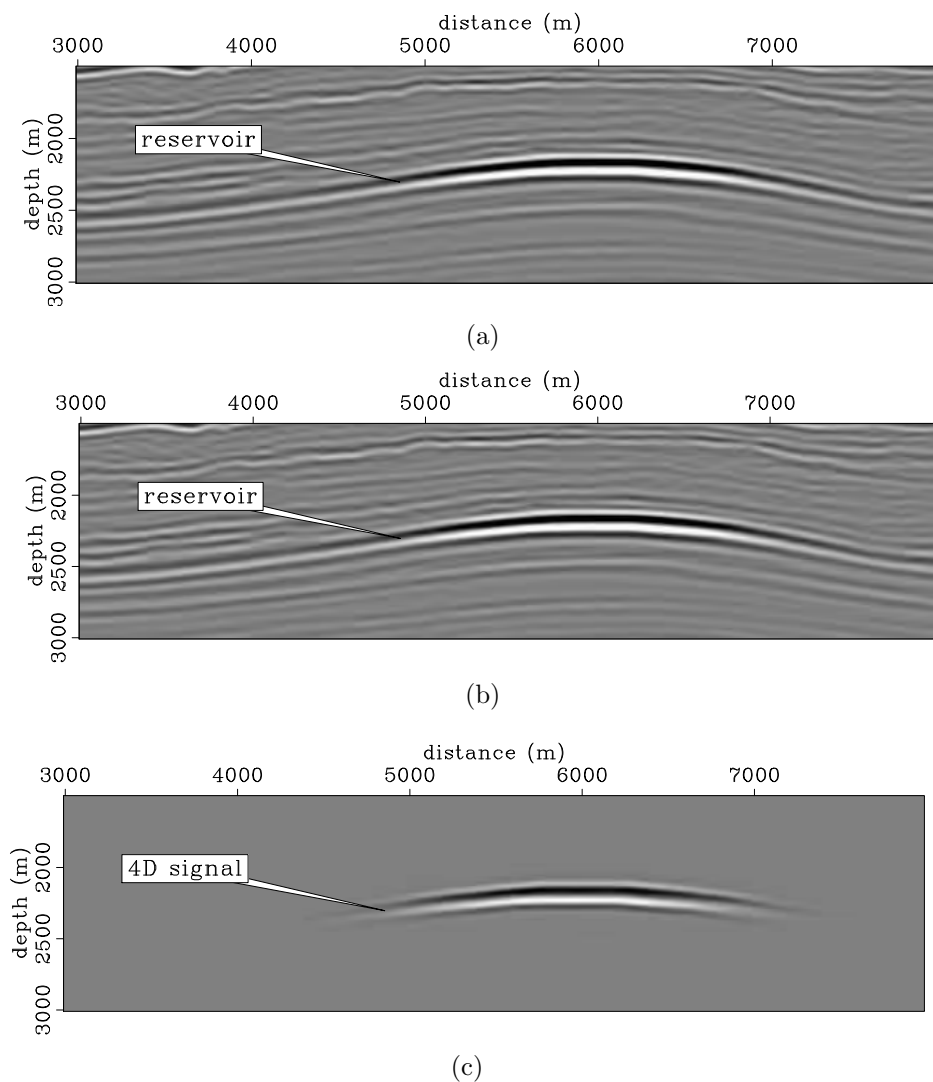


Figure 1.3: Migrated baseline image (a), monitor image (b), and time-lapse image (c) for the target area indicated in the numerical model in Figure 1.2. Note that in this ideal case, where acquisition geometries are repeated for both the baseline and monitor data sets, the amplitude difference in the time-lapse image is related only to changes within the reservoir. [CR] chap1/. s-mig-1l,s-mig-2l,s-mig-dl

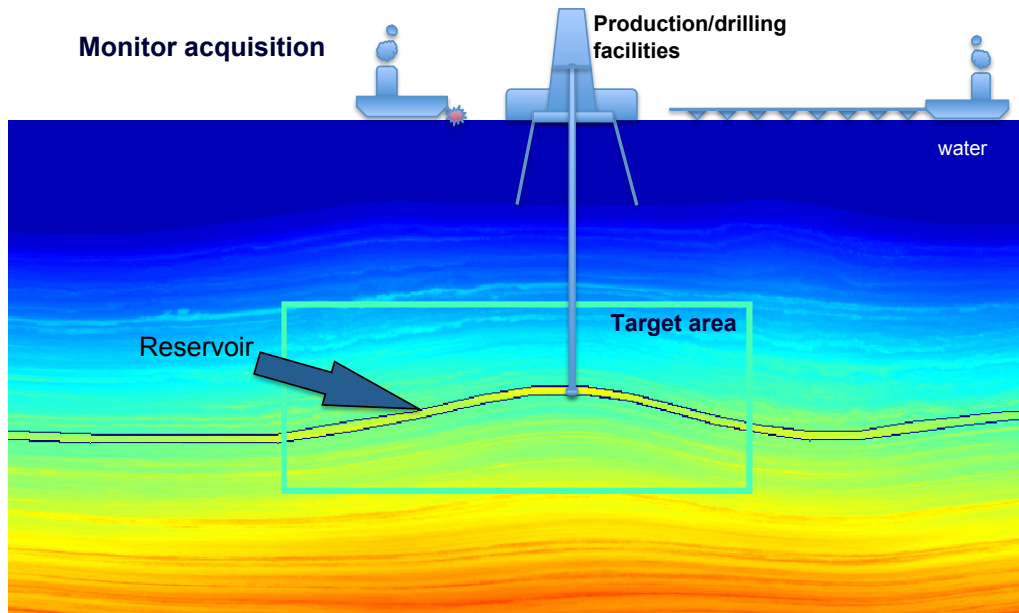


Figure 1.4: Cartoon illustrating how an obstruction in marine seismic acquisition affects data recording. Compare this cartoon to Figure 1.2. The time-lapse image for the target area, between the baseline image in Figure 1.3(a) and a monitor image with a gap caused by an obstruction, is shown in Figure 1.5. [NR] `chap1/. acq-moni`

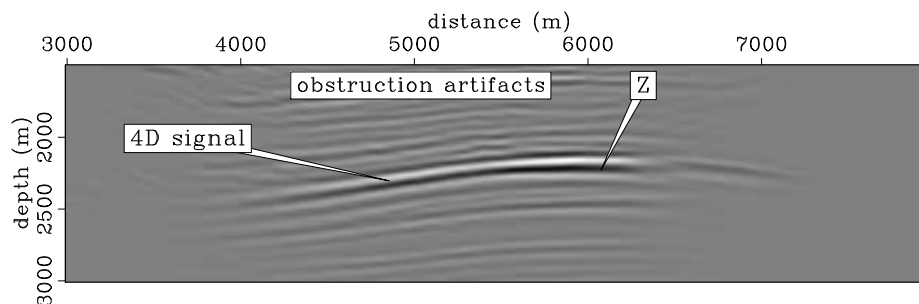


Figure 1.5: Time-lapse image obtained from a complete baseline data set (Figure 1.2) and an incomplete monitor data set (Figure 1.4). Note that, compared to the ideal time-lapse image in Figure 1.3(c), this image is highly contaminated with artifacts resulting from gap in the monitor acquisition geometry. To explain these artifacts, the impulse responses (point spread functions) at point Z for the complete and incomplete geometries are studied later in this chapter. [CR] `chap1/. s-mig-gap-dl`

## Overburden complexity

Conventional time-lapse seismic processing methods are adequate in areas with fairly simple geology—where, for example, simple migration methods (e.g., pre-stack time migration) image the targets with sufficient accuracy. However, hydrocarbon exploration and production have shifted from relatively simple to complex geological environments (e.g., sub-salt reservoirs), where many of these methods are not adequate. Although recent advances in seismic acquisition have improved seismic imaging in these areas, seismic reservoir monitoring remains difficult in complex geological environments.

Figure 1.6 shows an illustration of a reservoir located under a complex salt body. Because of the large contrasts in seismic velocities between the salt body and surrounding sediments, unlike in the simple overburden example (Figure 1.2), only limited amount of seismic energy illuminates this sub-salt reservoir. Furthermore, such large contrasts in seismic velocities and the rugosity (of the top and especially the base) of the salt body cause uneven illumination of the reservoir.

Figure 1.7 shows the time-lapse image for the target area in Figure 1.6, obtained from baseline and monitor data sets that are modeled with the same acquisition geometry. Compared to the simple overburden example (Figure 1.3(c)), even with perfectly repeated acquisition geometries, the time-lapse image in this example is distorted. Because the conventional imaging operator does not account for these non-stationary distortions, it is difficult to accurately relate the observed reflectivity change to changes in reservoir properties. As described in the next section, linearized inversion provides a way to correct for these distortions in time-lapse seismic images caused by complex overburden.

In chapter 4, I show that by applying the linearized joint inversion methods developed in this dissertation to the data sets that produce the distorted time-lapse image in Figure 1.7, we can obtain a time-lapse image similar in quality to that in Figure 1.3(c).

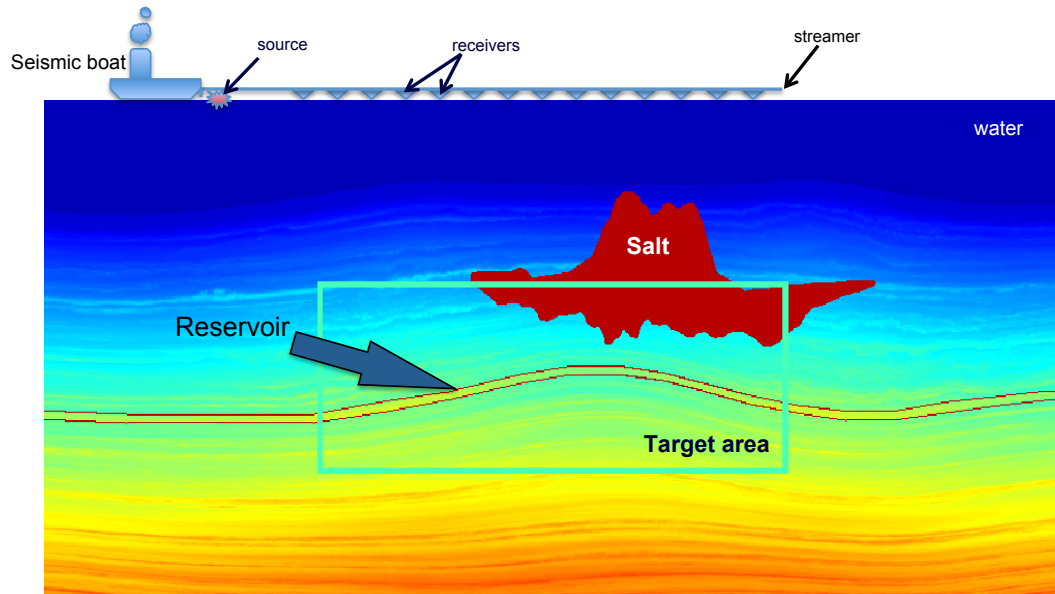


Figure 1.6: Cartoon illustrating a typical marine acquisition geometry over a complex earth model. Comparing this cartoon to Figure 1.2, note that in this subsurface model, the reservoir is located under a complex salt body. The time-lapse image for the target area, computed as the image difference between the baseline and monitor data sets, is shown in Figure 1.7. [NR]. `chap1/. acq-moni-salt`

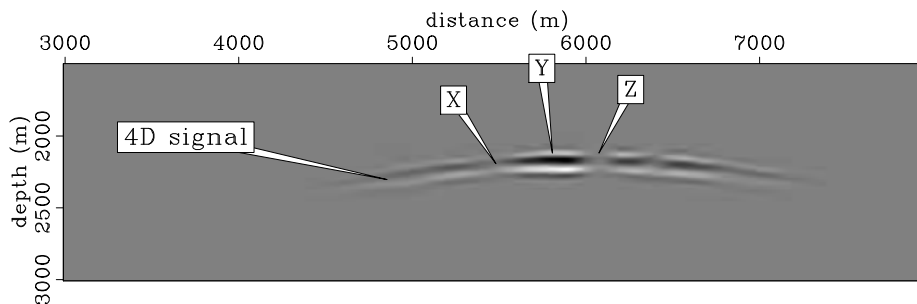


Figure 1.7: Time-lapse image between perfectly repeated baseline and monitor data sets from the numerical model in Figure 1.6. Note that, compared to the ideal time-lapse image in Figure 1.3(c), this image is distorted. These distortions in time-lapse amplitudes are caused by the uneven/irregular subsurface illumination associated with the complex overburden (Figure 1.9). To explain these distortions, the impulse responses (point spread functions) at points X, Y, and Z are studied later in this chapter. [CR] `chap1/. s-mig-salt-dl`

## Time-lapse imaging by inversion

The conventional imaging (migration) operator is an adjoint approximation of the inverse of the linearized seismic modeling experiment. However, in many practical cases—where the target is illuminated by limited (or variable) ranges of angles and azimuths—the adjoint is a poor approximation of the inverse. Such poor approximation cause artifacts and distortions in time-lapse images, such as those observed in Figures 1.5 and 1.7. Linearized inversion provides a way to correct for these artifacts and distortions. To understand why artifacts exist in the migrated time-lapse images (Figures 1.5 and 1.7) and how linearized inversion corrects them, let us consider briefly the point spread functions (PSFs) at selected image points. A PSF describes the response of an imaging system to a subsurface spike.

Figure 1.8 shows the PSFs at point  $Z$  in Figure 1.5. As shown, at this image point,

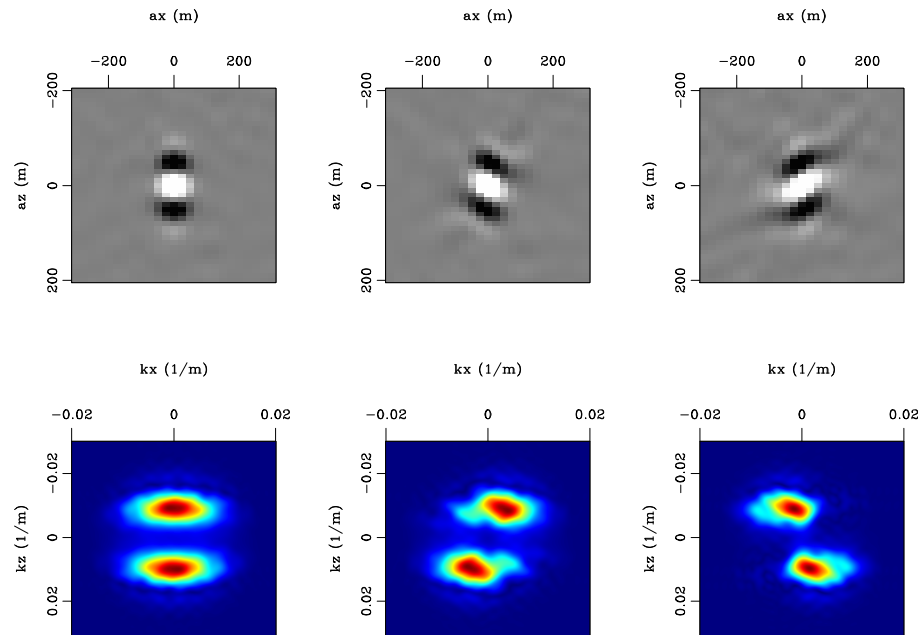


Figure 1.8: PSFs at point  $Z$  in Figure 1.5 in the spatial domain (top) and wavenumber domain (bottom). The left and middle panels are the PSFs for the baseline and monitor geometries respectively. The right panels show the differences between the baseline and monitor PSFs resulting from differences in their geometries. [CR].

chap1/. sm-psf-gap-a

because different acquisition geometries illuminate different ranges of wavenumbers, the spatial impulse response differ for the baseline and monitor. These differences in the impulse responses (or PSFs) caused by the geometry differences explain the artifacts observed in Figure 1.5. By removing the effects of the different PSFs at each image point, linearized inversion attenuates the associated geometry artifacts.

Figure 1.9 shows the PSFs at points X, Y, and Z in Figure 1.7. As shown, because of the complex overburden, even for these closely-spaced points, there are significant differences in spatial impulse responses (and hence in the range of illuminated wavenumbers). Large differences in the PSFs cause varying amounts of distortions in the time-lapse (Figure 1.7). Because inversion removes the effects of these non-stationary PSFs, it can attenuate distortions observed in time-lapse images.

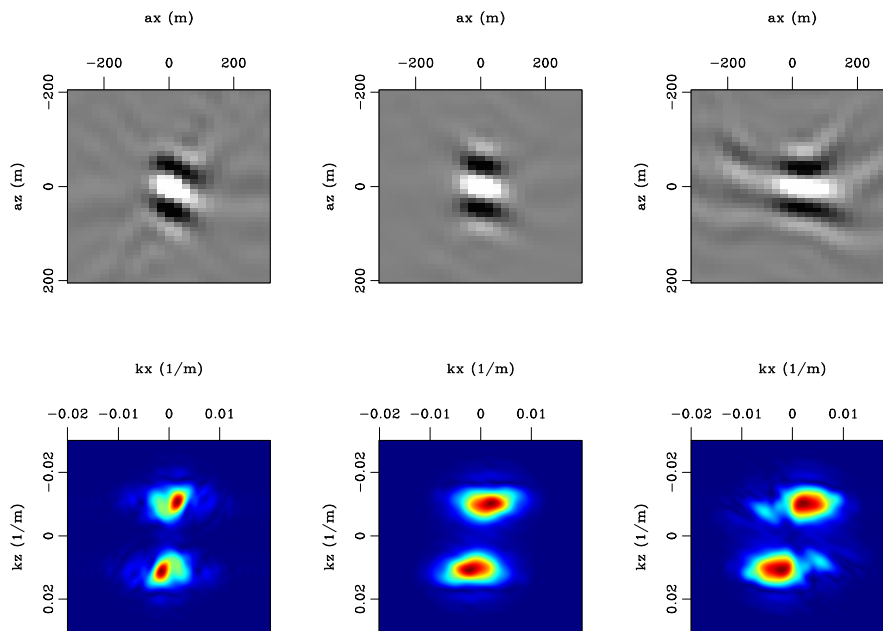


Figure 1.9: Point spread functions (PSFs) at points X, Y, and Z in Figure 1.7 in the spatial domain (top) and wavenumber domain (bottom). Although these points are located close to each other, because of the complex overburden, they differ significantly in the range of illuminated wavenumbers—hence the difference in the spreading. [CR]. `chap1/. sm-psf-salt-a`

As described above, linearized inversion can attenuate artifacts in time-lapse seismic images caused by differences in acquisition geometries and by wave-propagation through complex overburden. However, because it is ill-posed, linearized inversion of seismic data can be unstable. Therefore, in practice, unconstrained linearized inversion may lead to unsatisfactory results. However, for the time-lapse imaging problem, there are useful information about the subsurface geology, reservoir location and parts of the subsurface where production- or injection-related changes are expected. In this dissertation, I show that including these a priori information as spatial and temporal constraints in the inversion provides stable and reliable time-lapse images. Whereas spatial constraints introduce a priori information about subsurface earth structure into the inversion, temporal constraints/coupling limit the difference between images from different surveys.

## DISSERTATION OVERVIEW AND CONTRIBUTIONS

The remaining chapters in this dissertation are organized according to the following outline:

**Chapter 2 *Time-lapse seismic cross-equalization*:** Before introducing inversion methods in later chapters, it is important to understand conventional methods, their limitations, and how they can be improved. In this chapter, I focus on two post-imaging time-lapse seismic cross-equalization methods. First, I describe an efficient implementation of multidimensional warping of time-lapse seismic images, which is based on a method adapted from Hale (2009). This method utilizes sequential one-dimensional cross-correlations and interpolations. Multidimensional warping is also an important prerequisite for the inversion methods developed in later chapters. Then, using the method developed in Ayeni (2011), I show that selecting matched filtering parameters with an evolutionary algorithm leads to an improved match between time-lapse data sets. I apply these proposed methods to four time-lapse data sets from the Norne field.

**Chapter 3 *Joint least-squares wave-equation migration/inversion:*** In this chapter, I discuss the theory of linear least-squares migration/inversion of seismic data (Nemeth et al., 1999; Clapp and Biondi, 2002; Köhl and Sacchi, 2003; Clapp, 2005; Valenciano, 2008; Tang, 2011), and how it can be extended to joint inversion of time-lapse data sets. One important advantage of solving a joint least-squares problem is that it allows the introduction of both spatial and temporal constraints. First, because seismic inversion is inherently ill-posed, these constraints help to stabilize the inversion. In addition, spatial and temporal constraints ensure that inverted the time-lapse images are geologically plausible. Therefore, compared to migration and separate inversion, joint least-squares inversion provides more reliable time-lapse images. I describe formulations of the regularized joint inversion in both the data and image domains. In general, the data-domain and image-domain inversion provide equivalent ways to solve the joint least-squares problem. However, one important advantage of image-domain inversion is that the problem can be efficiently solved for a small target around the reservoir.

**Chapter 4 *Synthetic examples:*** In this chapter, I apply the regularized joint inversion methods developed in chapter 3 to various synthetic examples. First, I demonstrate how data-domain inversion can be used to obtain high-quality time-lapse images in non-repeated simultaneous-source data sets. Second, I show how image-domain inversion can be used to correct for distortions in time-lapse images caused by complex overburden effects. Third, I show that image-domain inversion can be used to attenuate artifacts in time-lapse images caused by obstructions in acquisition geometries. Finally, I demonstrate how different regularization parameters in joint image-domain inversion affect the quality of time-lapse images. Because image-domain is relatively computationally inexpensive, it is possible to efficiently test different realistic regularization parameters. These examples show that compared to conventional imaging by migration or separately regularized inversion, spatio-temporally regularized joint inversion provides more reliable time-lapse images.

**Chapter 5 *2D field data examples*:** In this chapter, I apply the joint image-domain inversion method developed in chapter 3 to subsets of a streamer time-lapse data set from the Norne field. As noted in the next section, the inversion method developed in this dissertation assumes that the data contain only primary reflections. Therefore, prior to inversion, careful preprocessing is necessary to ensure that as much as possible, the data satisfy this and other assumptions made in chapter 3. Using the Norne data sets, I demonstrate how different preprocessing steps improve the time-lapse amplitude information and condition the data for inversion. In addition, I show that that linearized inversion can improve time-lapse images obtained from conventional closely-repeated seismic acquisition geometries. Furthermore, I demonstrate that this method can be used to attenuate obstruction artifacts in time-lapse seismic images.

**Chapter 6 *3D field data examples*:** In this chapter, I apply the joint image-domain inversion method developed in chapter 3 to full-azimuth ocean-bottom-cable (OBC) data sets from the Valhall Life of Field Seismic (LoFS) project. First, as in the 2D field data example in chapter 5, I demonstrate that joint image-domain inversion can be used to attenuate obstruction artifacts in time-lapse images between two and three surveys. In addition, I show that compared to migration, joint image-domain inversion provides results with improved resolution and more reliable information about production-related seismic amplitude changes. Finally, I demonstrate that because joint image-domain inversion is computationally inexpensive, we can use different regularization parameters to obtain several plausible time-lapse images of reservoir changes. This means that it is possible to introduce realistic constraints or prior knowledge in the computation of the time-lapse image difference.

**Chapter 7 *Conclusions*:** In this chapter, I first summarize the most important results in this dissertation. I then discuss some possible directions for future research.

## ASSUMPTIONS AND LIMITATIONS

The joint least-squares formulations developed in this dissertation are subject to several assumptions and limitations. Below, I summarize the most important of these.

- **Velocity and compaction:** I assume that the background baseline velocity is accurate. Also, I assume that between surveys, velocity change relative to the background, and compaction relative to the reservoir size and depth are small. Where the velocity change and compaction are unavailable (or are not of interest), I assume that errors introduced by imaging all data sets with the baseline velocity can be removed by post-imaging warping/alignment.
- **Noise:** In deriving the inversion formulations in this dissertation, I assume a linear *primaries-only* approximation to the wave-equation. Therefore, prior to inversion, all data sets must be pre-processed to remove correlated and uncorrelated noise. I assume that residual noise in the data sets is of smaller magnitude than the time-lapse signal of interest.
- **Reservoir property changes:** Throughout this dissertation, inversion is limited to the estimation of changes in reflectivity amplitudes. Changes in actual rock properties (e.g., saturation and permeability) can be obtained from the inverted time-lapse amplitudes. One possible direction of future research is an extension of the formulations developed in this dissertation to direct inversion of reservoir property changes without this intermediate step of reflectivity inversion.

## Chapter 2

# Time-lapse seismic cross-equalization

Time-lapse (4D) seismic images provide important information about production- or injection-related changes in reservoir properties. However, in practice, imperfect repetition of survey geometries, non-repeatable ambient noise, changes in natural environmental conditions, and other discrepancies generate artifacts that contaminate production-related amplitude differences between seismic images. Before reservoir property changes can be extracted from time-lapse seismic images, these artifacts must be attenuated, while production-related differences must be preserved.

In conventional time-lapse seismic imaging, the process of attenuating unwanted differences between seismic data sets is called cross-equalization or cross-matching (Rickett and Lumley, 2001; Hall et al., 2005). Together with better-quality data derived from improved acquisition technology, in many cases, seismic cross-equalization makes it possible to extract reliable information about reservoir property changes from time-lapse seismic images. However, as discussed in later chapters, seismic cross-equalization methods are inapplicable or inadequate in several practical scenarios. Before introducing new methods that overcome some limitations of seismic

cross-equalization in later chapters, it is important to first consider conventional processing methods and how they can be improved.

Depending on the monitoring goals and the data quality, seismic cross-equalization methods can be applied at different stages of the processing sequence—before and/or after imaging. In general, it is desired that throughout the processing sequence, identical parameters and steps are applied to individual data sets. Prior to imaging, some key preprocessing steps include data regularization, noise and multiple attenuation, amplitude and phase corrections, and trace selection (4D-binning). These preprocessing steps are well developed and are applied in routine time-lapse processing (Helgerud et al., 2011b; Sharma et al., 2011). As discussed in later chapters, careful data preprocessing is also important for the inversion methods developed in this dissertation.

In this chapter, I consider two common post-imaging cross-equalization steps: warping and matched filtering. Warping involves estimating the apparent displacements (misalignments) between images, which are caused by production-induced velocity changes and deformation. Such apparent displacements can be used to estimate velocity and geomechanical changes between surveys (Hatchell and Bourne, 2005b; Røste et al., 2006; Hawkins et al., 2007). In addition, prior to computing the amplitude difference between baseline and monitor images, the computed apparent displacements are used to align the images, thereby correcting for compaction and velocity errors.

Using a method adapted from Hale (2009), I show how multidimensional warping can be performed efficiently with a sequential one-dimensional (1D) approach. This approach prevents errors in time-lapse images commonly caused by approximating multidimensional warping by a 1D vertical warping; it also avoids the computational expense of full multidimensional cross-correlation, search and interpolation. To obtain accurate information about production-related changes from time-lapse seismic images, all displacement components must be considered. Importantly, this warping method will be applied in later chapters as a preprocessing step for the inversion methods developed in this chapter.

Matched filtering removes residual amplitude and phase differences between the aligned images. First, matched filters are designed in a region outside the reservoir, where no change is expected. These matched filters are then applied to the full data, including the reservoir. I show how optimal matched filters can be estimated with evolutionary programming and that matched filters estimated this way provide more reliable time-lapse images than conventional methods. Combining this matched filtering method with the sequential warping method described above provides an efficient and robust cross-equalization tool.

In the following sections, I first discuss the sequential warping and optimized matched filtering methods. I then apply these methods to two time-lapse seismic data sets from the Norne field. I show that these cross-equalization methods provide a robust way to obtain good quality time-lapse images.

## **MULTIDIMENSIONAL WARPING BY SEQUENTIAL 1D CROSS-CORRELATION**

Reservoir depletion and fluid injection cause stress-induced compaction and stretching in and around a producing reservoir, which in turn cause changes in seismic travel times and path lengths between surveys. However, relative to the background velocity and reflector depth, the resulting velocity and geomechanical changes between surveys are typically small. Furthermore, because these velocity and geomechanical changes are coupled, it is often difficult to estimate accurate migration velocities for individual data sets without introducing additional errors that may mask the production-induced changes of interest. Therefore, in practice, baseline and monitor data sets are usually imaged with a single (baseline) velocity model, leading to amplitude and kinematic differences between the baseline and monitor images. It is assumed that relative to amplitude differences caused by reservoir fluid and rock property changes, small errors introduced by imaging the monitor data with the baseline velocity are negligible.

To correctly estimate production- or injection-related time-lapse amplitudes, kinematic differences, which show up as *apparent* displacements between the images, can

be corrected by multidimensional warping (Rickett and Lumley, 2001; Hall et al., 2005). However, because it is expensive to estimate all components of the apparent displacement field, and because of the generally horizontal layering of sedimentary units, it is common practice to consider only vertical components. Instead of this *vertical-only* approximation, it is possible to efficiently estimate all displacement components using a sequential 1D warping approach (Hale, 2009). As shown by Hale (2009), this sequential 1D warping approach produces components of apparent displacement vectors that are equivalent to results from full multidimensional warping. Other approaches to solving the multidimensional warping problem as a combination of several sequential 1D warping problems have been published by other authors (Aarre, 2008). In order to obtain accurate estimates of reservoir property changes, all displacement components must be taken into account.

Here, to implement a multidimensional warping operator, I follow the approach of Hale (2009). This method, which only requires sequential 1D searches for cross-correlation peaks along different axes, is summarized in Algorithm 1. Given two seismic traces  $b$  and  $m$ , the normalized correlation coefficient  $C_{bm}$ , computed within a sliding window of half-width  $h$  around sample point  $k$ , is given by

$$C_{bm}(l) = \frac{\sum_{i=k-h}^{k+h} b(i) \cdot m(i+l)}{\sqrt{\sum_{i=k-h}^{k+h} b(i)^2} \cdot \sqrt{\sum_{i=k-h}^{k+h} m(i+l)^2}}, \quad (2.1)$$

where  $l$  denotes the correlation lag between samples in the traces. For the time-lapse problem,  $b$  and  $m$  represent baseline and monitor data, respectively. The cross-correlation at each sample point is localized by a Gaussian taper  $W$  given by

$$W(j) = e^{-\frac{j^2}{2r^2}}, \quad (2.2)$$

where  $q$  is the sample distance relative to point  $k$ , and  $r$  is the Gaussian width. In this dissertation, after testing different values of  $r$ , I find that 1/4 the half-width of the correlation window gives a satisfactory result.

---

**Algorithm 1** Apparent displacements by cyclic 1D search
 

---

```

 $b \leftarrow preprocess(b_o)$ 
 $m \leftarrow preprocess(m_o)$ 
while  $s^{ia=1:3} \geq s_{stop}^{ia=1:3}; j = 1 : niter$  do
  for  $axis = 1:3$  do
    if  $axis = 1$  then
       $s^1 = s[xcorr_{peak}(m_j|b)]$  !compute displacement components along axis 1
       $z^1 \leftarrow s^1 < z^1 > + s^1$  !interpolate/accumulate components along axis 1
       $z^2 \leftarrow s^1 < z^2 >$  !interpolate along components along axis 2
       $z^3 \leftarrow s^1 < z^3 >$  !interpolate along components along axis 3
       $m_j^1 \leftarrow s^1 < m_j >$  !interpolate monitor along components along axis 1
    else if  $axis = 2$  then
       $s^2 = s[xcorr_{peak}(m_j^1|b)]$ 
       $z^1 \leftarrow s^2 < z^1 >$ 
       $z^2 \leftarrow s^2 < z^2 > + s^2$ 
       $z^3 \leftarrow s^2 < z^3 >$ 
       $m_j^2 \leftarrow s^2 < m_j^1 >$ 
    else if  $axis = 3$  then
       $s^3 = s[xcorr_{peak}(m_j^2|b)]$ 
       $z^1 \leftarrow s^3 < z^1 >$ 
       $z^2 \leftarrow s^3 < z^2 >$ 
       $z^3 \leftarrow s^3 < z^3 > + s^3$ 
       $m_j^3 \leftarrow s^3 < m_j^2 >$ 
       $m_{j+1} \leftarrow m_j^3$ 
    end if
  end for
end while
 $m_o \leftarrow z^{1:3} < m_o >$ 

```

$j$  – iteration;

$ia$  – axis;

$b_o$  – original baseline data

$m_o$  – original monitor data

$b$  – preprocessed baseline data

$m$  – preprocessed monitor data

$xcorr_{peak}$ : correlation peak

$s^{ia}$  – apparent displacement along axis  $ia$

$z^{ia}$  – cumulative displacements along axis  $ia$

$w < m >$ : interpolation of  $m$  with displacements  $w$

---

Although this implementation closely follows the method proposed in Hale (2009), I introduce several additional constraints that further improve the method. The most important changes are summarized below:

- To improve the resolution of the correlation peaks along the horizontal axes, I preprocess the input images by removing near-zero wavenumber components along these axes. Along any axis, if the data within a cross-correlation window are dominated by near-zero wavenumbers, it becomes impossible to reliably estimate the apparent displacements between them.
- To first capture the lower-frequency apparent displacement components, this iterative procedure starts with large correlation gates and lags. Then, to capture higher-frequency components, the correlation gates and lags are systematically decreased as a function of iteration.
- To improve the accuracy of the estimated displacements, prior to searching for the cross-correlation peaks, I smooth the correlation coefficients by averaging the values from neighboring traces. In addition, I define an acceptance criterion based on the relative cross-correlation peaks and apparent displacements such that outliers are discarded. For example, at points in the image volume where the peak cross-correlation values are relatively small and the estimated apparent displacements relatively large, the displacement components are rejected and then replaced by values interpolated from neighboring points.

As shown in Algorithm 1, for each iteration, the results (accumulated displacement components and warped images) along one axis (e.g., vertical) serve as inputs for computation along the next axis (e.g., in-line). For each axis, displacement components are accumulated after interpolating the image and displacement components from the previous step. This accumulation procedure is explained in detail by Hale (2009). In this dissertation, I perform all interpolations with a cubic spline algorithm (Press et al., 1996).

Figure 2.1 shows two synthetic seismic images and the horizontal and vertical displacement components between them. These displacement components represent vertical downward and horizontal outward apparent displacements of image points in Figure 2.1(b) relative to those in Figure 2.1(a). The only difference between these two images is misalignments of image points described by these displacements (Figures 2.1(c) and 2.1(d)). To align these images, I apply the sequential 1D warping

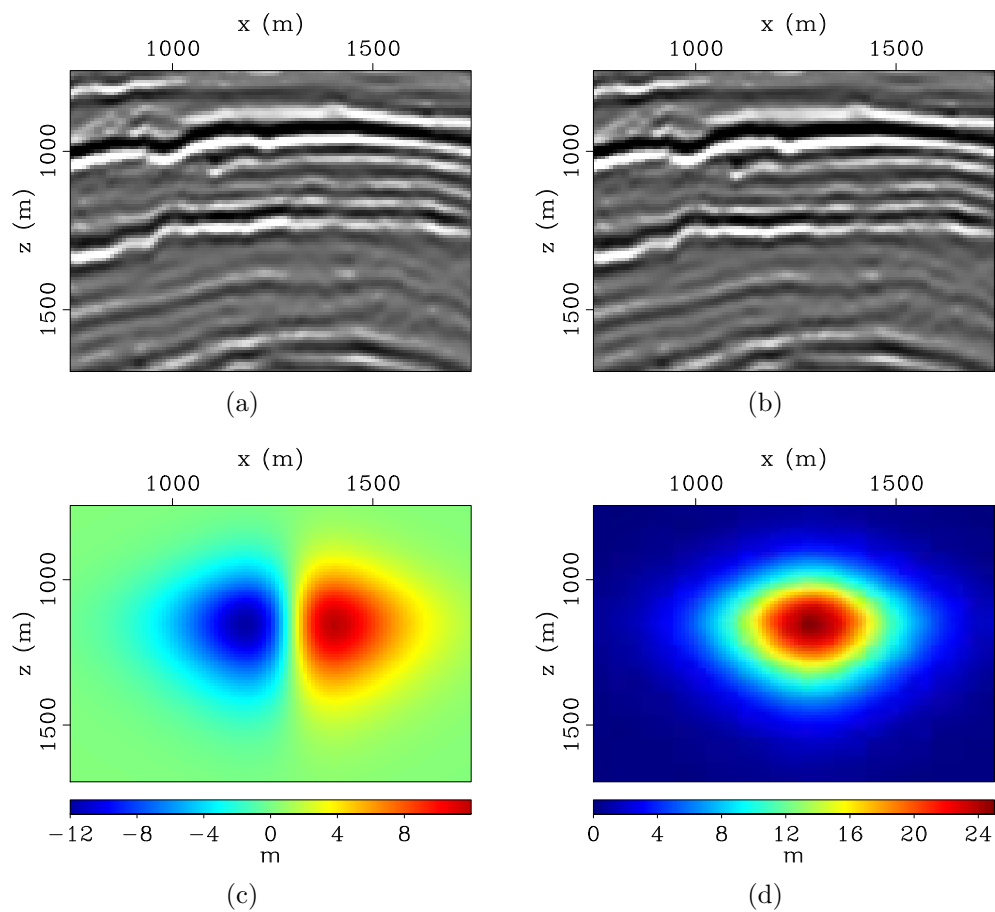


Figure 2.1: Synthetic seismic images (a) and (b), and components of the apparent displacements between them along the horizontal (c) and vertical (d) axes. The image differences before, and after different kinds of warping are shown in Figure 2.2. The evolution of apparent displacement components derived from sequential 1D warping are presented in Figures 2.3 and 2.4. [CR].

chap2/. s-warp-1,s-warp-2,s-warp-x,s-warp-z

method described above to them. For comparison, I also align these images using one iteration of vertical warping (neglecting all horizontal components), and ten iterations of vertical warping. The image differences before and after warping are presented in Figure 2.2.

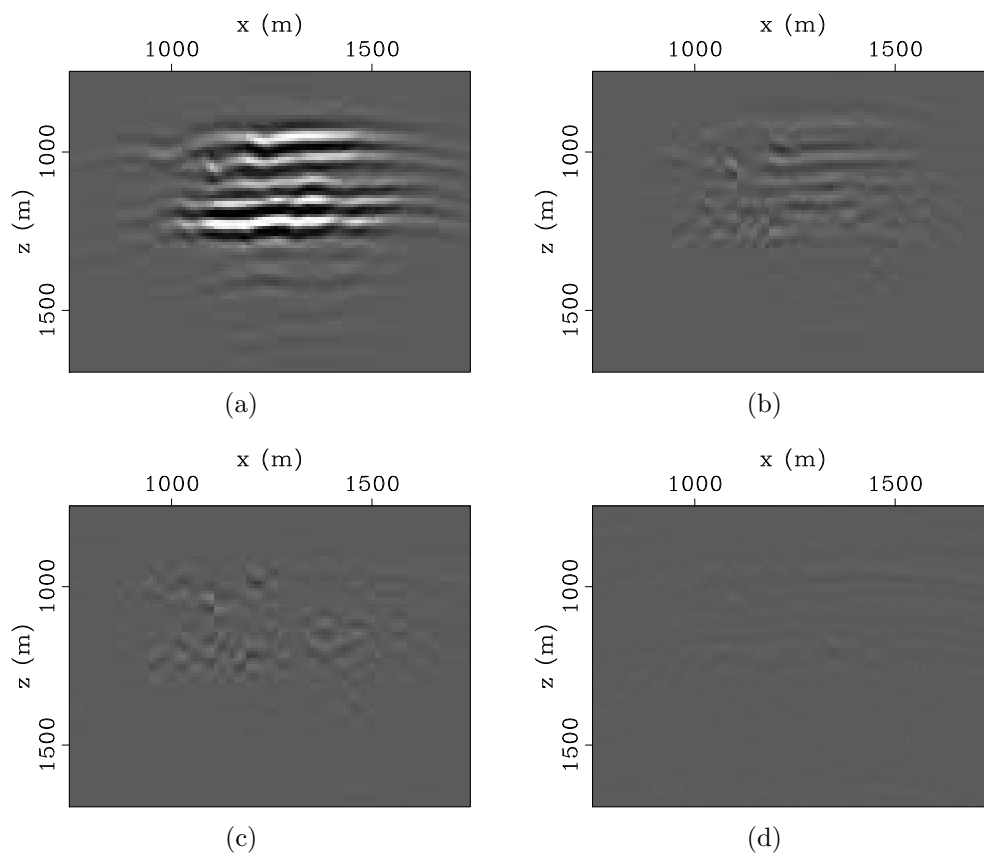


Figure 2.2: Differences between the seismic images in Figures 2.1(a) and 2.1(b) before warping (a), after one iteration of vertical warping (b), after 10 iterations of vertical warping (c), and after 10 iterations of sequential one-dimensional warping. All images are clipped to similar amplitude levels. Although iterative vertical warping provides improved match compared to one iteration of *conventional* vertical warping (b), there are still significant differences between the two images (c). Sequential 1D warping provides the best results with negligible amplitude differences between the warped images (d). [CR]. chap2/. s-warp-d-b4,s-warp-d-afO,s-warp-d-afz,s-warp-d-af

In Figure 2.2, because one iteration of vertical warping is a poor approximation to the multidimensional displacements between the images, it provides poor alignment of these images—hence the large residual differences between them (Figure 2.2(b)). In addition, although iterative vertical warping provides an improved alignment of the images, there are still large residual differences between the aligned images (Figure 2.2(c)). However, using the sequential 1D warping method, residual amplitude differences between the aligned images are negligible (Figure 2.2(d)). Negligible amplitude differences in Figure 2.2(d) suggests that this sequential 1D warping method can sufficiently resolve multidimensional apparent displacements between images. Figures 2.3 and 2.4 show how the two components of the apparent displacement vectors evolve with iterations. Note that as a function of iterations, estimates of the displacement components converge toward the actual displacements (Figures 2.1(c) and 2.1(d)).

As previously stated, the computed apparent displacements serve two general purposes. First, prior to computing the amplitude difference between the baseline and monitor images, these displacements are used to align the images, thereby ensuring that all events are collated. Furthermore, it is possible to obtain important information about changes within and around the reservoir from these apparent displacements. For example, the fractional velocity change  $\frac{\delta v}{v}$  and vertical strain  $\epsilon_{zz}$  can be computed as follows (Hatchell and Bourne, 2005a; Hale, 2009):

$$\frac{\delta v}{v} = -\frac{R}{1+R} \frac{d(\delta t)}{dt}, \quad (2.3)$$

$$\epsilon_{zz} = -\frac{1}{R} \frac{\delta v}{v}, \quad (2.4)$$

where  $v$  is the baseline velocity,  $\delta v$  is the change in velocity between the baseline and monitor surveys,  $d(\delta t)$  is the corresponding vertical displacement (time-shift), and  $R$  is the dilation factor. For the examples considered in this chapter, I assume a constant dilation factor,  $R = 5$ , a value within the range measured for North Sea reservoirs (Hatchell and Bourne, 2005a).

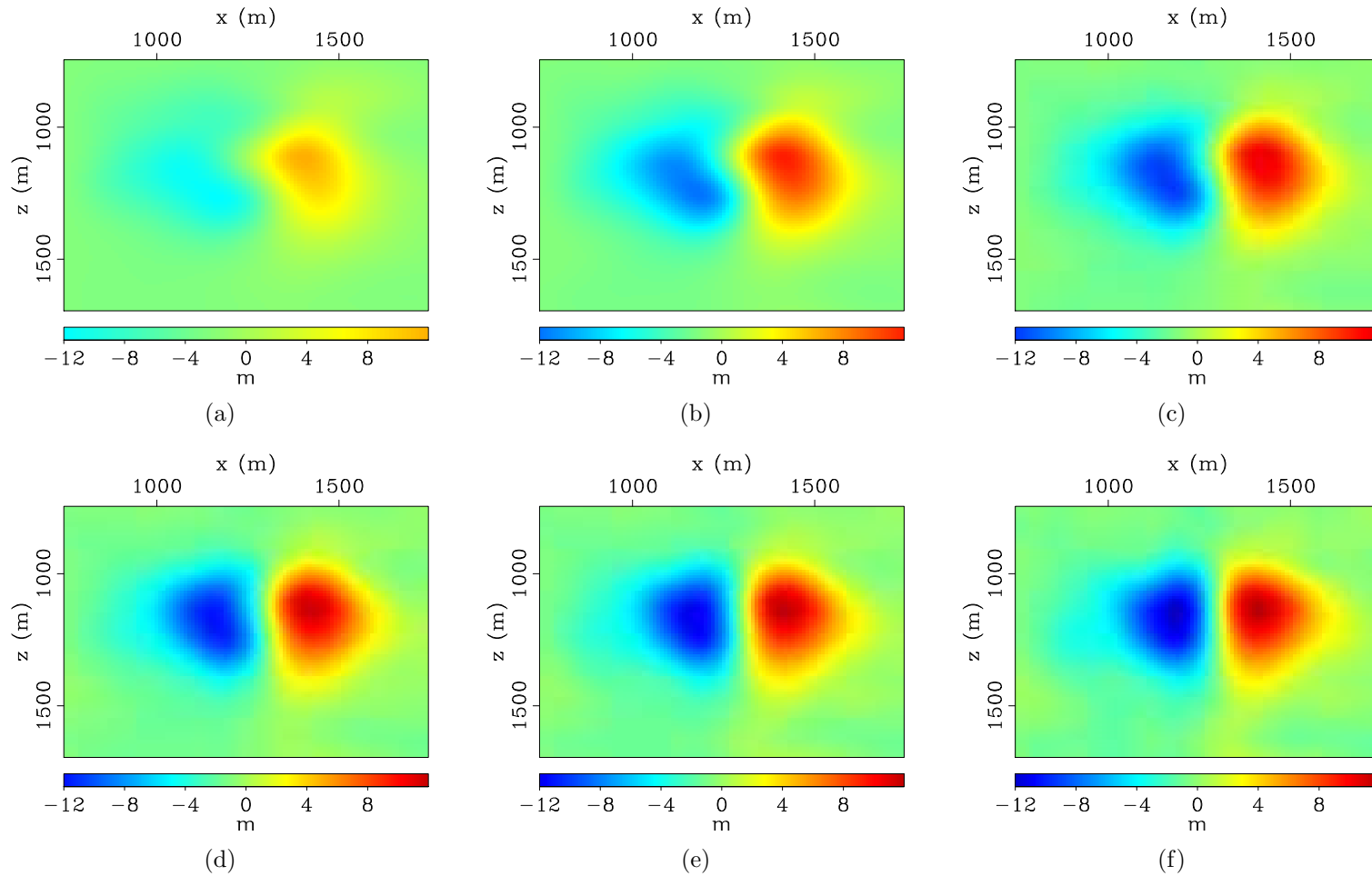


Figure 2.3: Evolution of the horizontal displacement components between Figures 2.1(a) and 2.1(b) obtained via sequential 1D warping. These panels show the estimated displacements after one, two, four, six, eight and ten iterations, respectively. As a function of iterations, these displacements converge towards the actual values in Figure 2.1(c). [CR]. `chap2/. s-warp-x1,s-warp-x2,s-warp-x3,s-warp-x4,s-warp-x5,s-warp-x6`

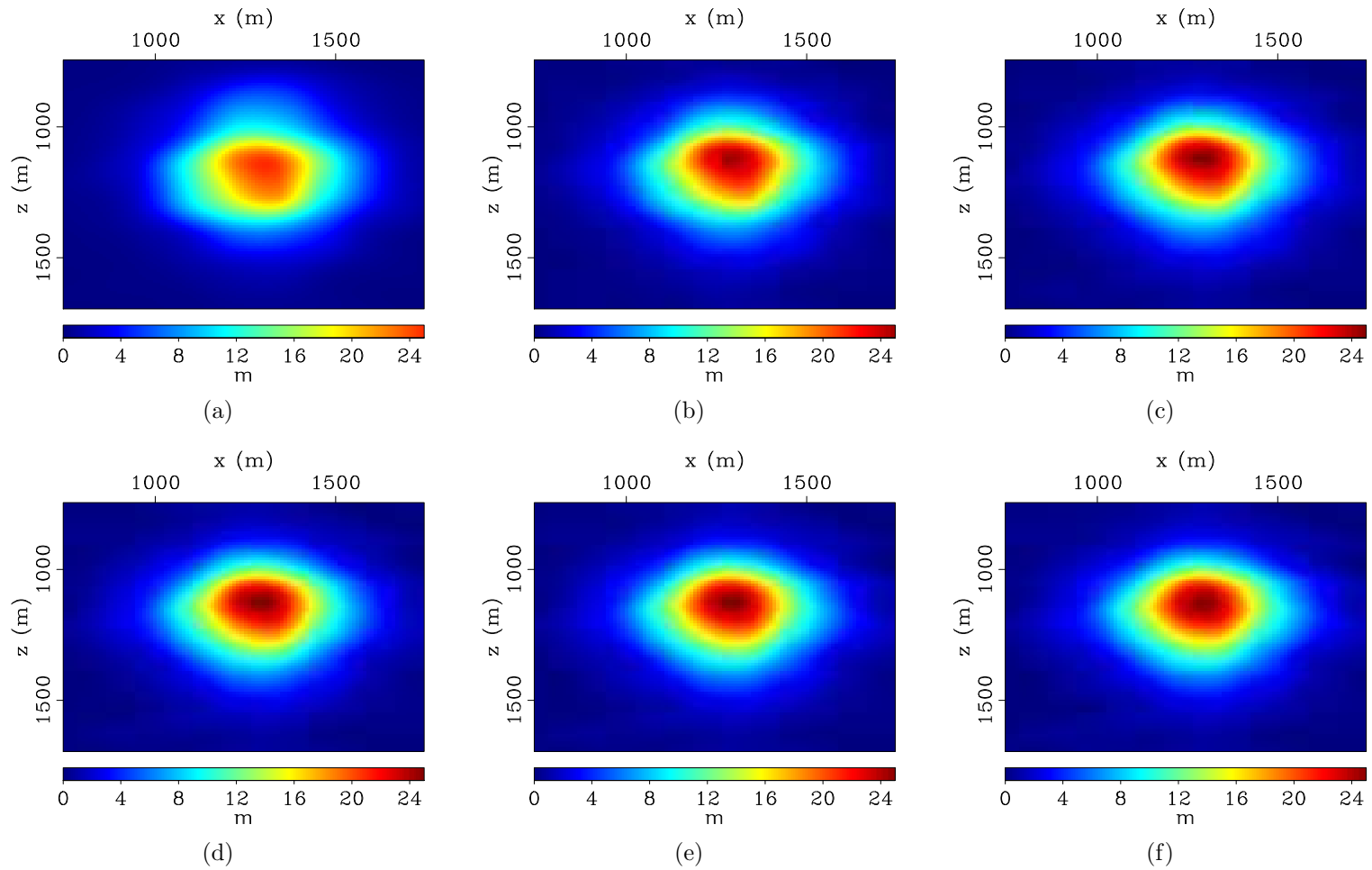


Figure 2.4: Evolution of the vertical displacement components between Figures 2.1(a) and 2.1(b) obtained via sequential 1D warping. These panels show the estimated displacements after one, two, four, six, eight and ten iterations, respectively. As a function of iterations, these displacements converge towards the actual values in Figure 2.1(d). [CR]. chap2/. s-warp-z1,s-warp-z2,s-warp-z3,s-warp-z4,s-warp-z5,s-warp-z6

## MATCHED FILTERING BY EVOLUTIONARY PROGRAMMING

To ensure that only production-related amplitude changes within the reservoir are interpreted, it is usually desired that amplitude and phase differences in non-reservoir regions be minimal. In time-lapse cross-equalization, this requirement is usually achieved by matched filtering. In general, it is assumed that non-production-related amplitude and phase differences that contaminate non-reservoir regions in the image volume are similar to the ones that contaminate the reservoir region. Therefore, by applying a matched filter that minimizes amplitude and phase differences in a non-reservoir region to a reservoir region, non-production-related artifacts within the reservoir can be attenuated. The filtering strategy can be global (a single filter for all trace locations), local (different filters for different trace locations), or a combination of the two. In this section, I consider only local one-dimensional matched filters.

Given baseline and monitor data  $\mathbf{b}$  and  $\mathbf{m}$ , the filter  $\mathbf{f}$  that matches the two sets of data in a least-squares sense is one that minimizes the quadratic cost function  $r$  given by

$$r(\mathbf{f}) = \|\mathbf{M}\mathbf{f} - \mathbf{b}\|_2, \quad (2.5)$$

where  $\mathbf{M}$  is a convolution matrix constructed from coefficients of the monitor data.

The matched filter obtained by minimizing the cost-function in equation 2.5 satisfies the expression

$$\mathbf{f} = (\mathbf{M}^T\mathbf{M})^{-1}\mathbf{M}^T\mathbf{b}, \quad (2.6)$$

where the superscript  $T$  denotes the matrix transpose.

In the frequency domain, equation 2.6 becomes

$$\mathbf{F}(w) = \frac{\overline{\mathbf{M}(w)}\mathbf{B}(w)}{\overline{\mathbf{M}(w)}\mathbf{M}(w)}, \quad (2.7)$$

where  $\mathbf{F}(w)$  is the matched filter,  $\mathbf{B}(w)$  is the baseline data, and  $\mathbf{M}(w)$  is the monitor data at frequency  $w$ . The overline denotes complex conjugation.

To avoid division by zero, a damping factor  $\epsilon$  is included in the denominator of equation 2.7 so that it becomes

$$\mathbf{F}(w) = \frac{\overline{\mathbf{M}}(\omega)\mathbf{B}(\omega)}{\overline{\mathbf{M}}(\omega)\mathbf{M}(\omega) + \epsilon^2}. \quad (2.8)$$

As mentioned earlier, at each trace location, the matched filter is derived within a window outside the reservoir, where no change is expected, and then it is applied to the full trace data. However, the matched filter derived at each trace location is a function of the estimation parameters. In this implementation, these parameters include the filter length, the top and bottom boundaries of the estimation window, and the damping factor. Conventionally, a single set of parameters derived by a manual trial-and-error approach is used at all trace locations. However, because the set of parameters that produces satisfactory filters in some parts of the image volume may produce very poor filters in other parts, obtaining an optimal set of parameters can be a tedious or impossible challenge.

In this dissertation, I apply an evolutionary programming (EP) method to estimate the optimal filter parameters for all trace locations. Evolutionary programming belongs to a class of global optimization methods called evolutionary algorithms (Bäck, 1996; Baeck et al., 1997; Yao et al., 1999; Eiben and Smith, 2003). These algorithms solve optimization problems using Darwinian evolutionary principles of natural selection (see Algorithm 2). In this application, I use the EP method because of its flexibility and robustness. Further discussions application of this method to selecting matched filtering parameters are presented in Ayeni and Nasser (2009) and Ayeni (2011).

The most important implementation considerations for the EP algorithm include the population size and initialization, the mutation operator, and the selection/rejection criterion. For the examples presented in the next section, I find that a population size of 20 produces satisfactory results. The initial population is derived as random parameters within  $\pm 10\%$  bounds of the best set of predetermined parameters. During each iteration, the *fittest* individuals in the population are perturbed to generate the

offspring (i.e., new sets of parameters) for the next iteration, whereas the worst half are rejected. The fittest individuals (half the population size) are defined as those with the lowest predefined error/fitness function.

Selecting an appropriate fitness function is critical, because this determines which of the solutions are kept and which are rejected at each iteration. In this dissertation, the fitness function is defined as the normalized root-mean-squared (NRMS) difference within a non-reservoir *validation* window which is different from that used to estimate the filter. The NRMS difference  $N_{bm}$  within the validation window is defined as

$$N_{bm} = 2 \times \frac{\sqrt{\sum_{i=1}^n b(i) - m(i)}}{\sqrt{\sum_{i=1}^n b(i) + \sum_{i=1}^n m(i)}}, \quad (2.9)$$

where  $n$  is the number of samples within the validation window.

By selection matched filter parameters such that NRMS difference within a different non-reservoir window is minimized, I ensure that no new artifacts are introduced into the matched data. As I shown in the field data example, one disadvantage of matched filtering as a cross-equalization tool is that if the parameters are poorly choosing, production-related amplitude differences can be contaminated by spurious matched filtering artifacts. Selecting filtering parameters that satisfy predefined criteria—such as minimum energy within a validation window—reduce such filtering spurious artifacts.

To ensure continuity from trace to trace, a smoothness constraint is applied and the estimation procedure repeated with an initial population based on the smoothed parameters. Furthermore, an additional smoothness constraint ensures that filter coefficients vary slowly from trace to trace. In the case where several partial stacks are to be matched, to preserve time-lapse Amplitude Variation with Angle (AVA) information, a further constraint can be introduced to ensure that the matched filters vary slowly between partial stacks.

---

**Algorithm 2** Optimal matched filtering by evolutionary programming
 

---

```

for  $irepeat = 1:nrepeat$  do
  for  $itrace = 1:ntrace$  do
    (Re)Initialize: estimation window, filter length, etc.
    Evaluate: fitness (nrms)
    while  $nrms_{iter} \geq nrms_{stop}; iter = 1 : niter$  do
      Select: fittest individuals
      Mutate: generate new offsprings
      Evaluate: fitness (nrms)
    end while
  end for
  Apply constraints
end for

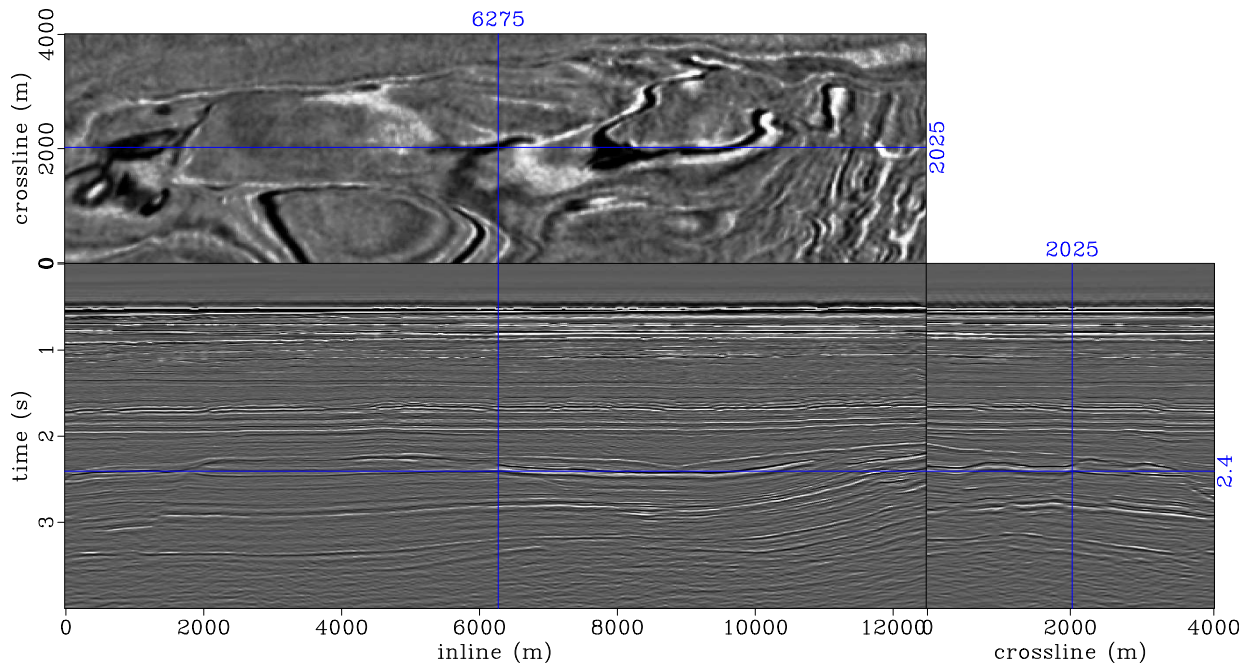
```

---

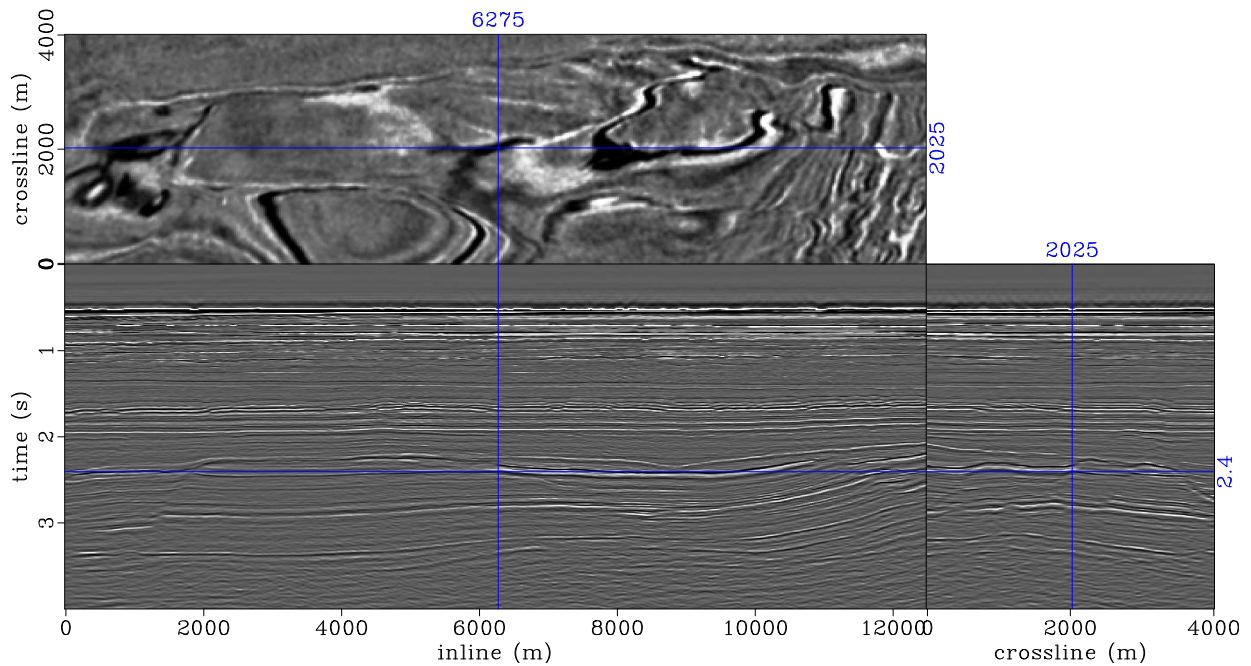
## FIELD DATA APPLICATION

In this section, I apply the warping and matched filtering methods described in the previous sections to four data sets from the Norne field, which is located in the Norwegian North Sea. The main field is a 9 km x 3 km horst block composed of high-porosity, high-permeability, high net-to-gross lower and middle Jurassic sandstones (Osdal et al., 2006). The field was discovered in 1991 and production started in 1997.

The baseline data were acquired in 2001, and the three monitor data sets were acquired in 2003, 2004 and 2006. These data sets have been preprocessed using conventional methods and imaged with Kirchhoff prestack time migration. Figure 2.5 shows full-stack images from the baseline and 2006 monitor data. Osdal et al. (2006) and Aarre (2008) provide detailed descriptions of the field geology, its production history, seismic data acquisition and processing, and some interpretation of the observed time-lapse seismic amplitudes.



(a)



(b)

Figure 2.5: Migrated images of the Norne field obtained from the 2001 baseline (a), and 2006 Monitor (b) data sets. The data processing steps are discussed by Osdal et al. (2006). [CR]. `chap2/. mig-full-2001,mig-full-2006`

First, using the sequential warping method described in a previous section, I estimate the apparent displacements between the baseline and the monitor images. For each sample point, at the first iteration, I use correlation windows of 0.4 s two-way travel-time, and 500 m half widths along the inline and crossline axes. These are systematically reduced to half the starting values at the third and final iteration. As discussed above, an acceptance criterion is defined such that points with relatively large displacements and low peak cross-correlation values are discarded. Specifically, in this example, image points with correlation coefficients lower than the 5th percentile and apparent displacements greater than the 95th percentile are discarded and interpolated from neighboring traces.

Figure 2.6 shows the vertical components of the apparent displacements (i.e., time-shifts) between the baseline and the 2006 monitor images after different iterations. Note that as mentioned earlier, the resolution of the displacements increases with the number of iterations. In Figure 2.6 (and in similar displays throughout this dissertation), the three panels are slices through a 3D volume at the positions indicated by the orthogonal lines. These time-shifts clearly show parts of the Norne horst block that have been produced between 2001 and 2006.

The lateral—inline and crossline—components of the apparent displacements between the baseline image and the 2006 monitor image are presented in Figures 2.7(a) and 2.7(b). Neglecting these lateral displacement components will create errors in the measured time-shifts (Figure 2.7(c)). In the examples presented in this chapter, I define errors in time-lapse attributes (time-shifts, velocity change, amplitudes, etc.) as the difference between values derived from considering only vertical displacement components and those derived from considering vertical and lateral displacement components. The time-shifts and lateral displacements extracted along the top of the reservoir are presented in Figure 2.8. In this figure, note that apparent displacements provide qualitative information about changes in properties around the reservoir. Quantitative interpretation of these displacement components is outside the scope of the current study.

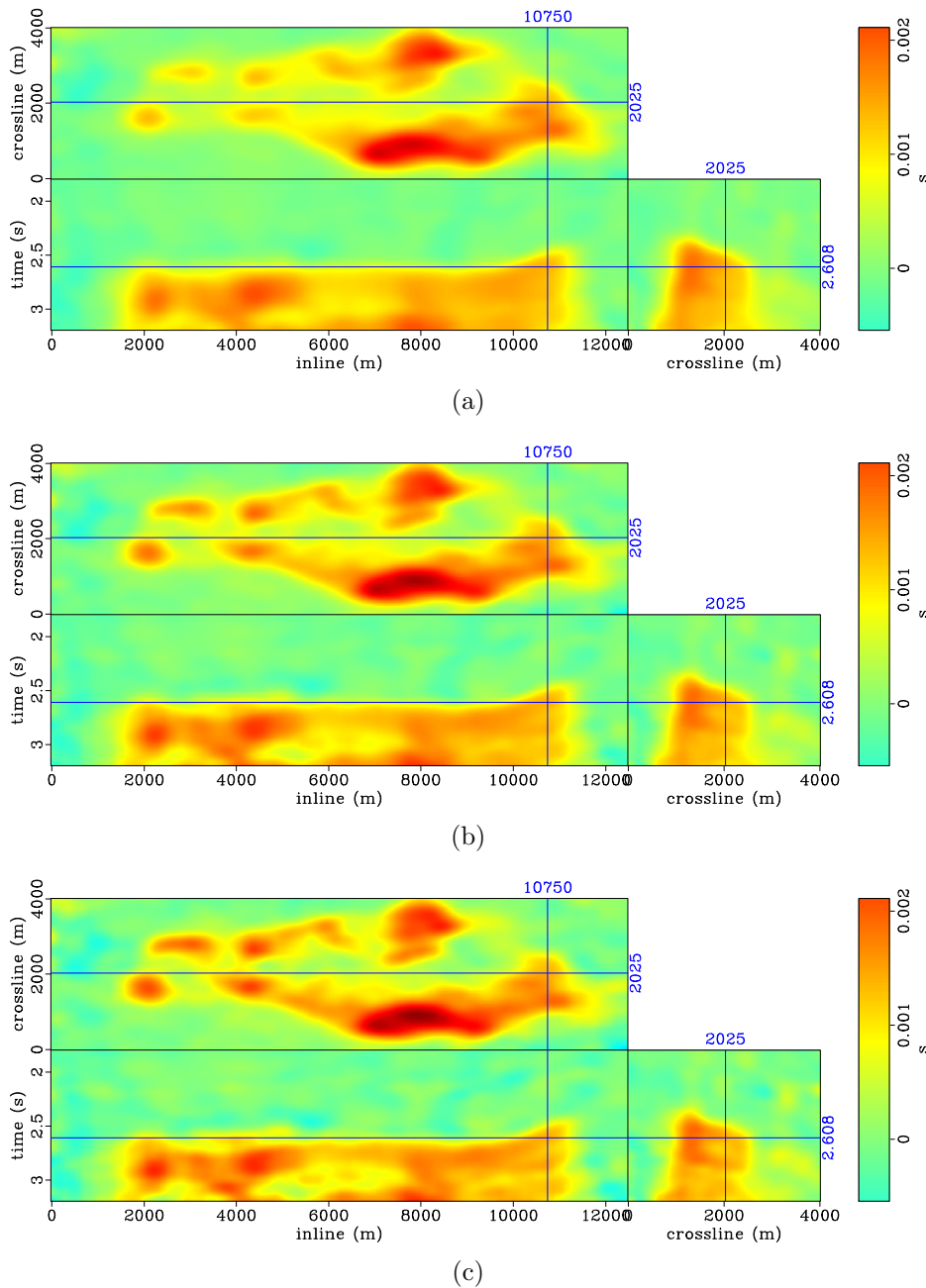


Figure 2.6: Vertical displacement components (time-shifts) between the 2006 monitor image and the baseline after one (a), two (b) and three (c) iterations. Note that the first iteration captures main features of the displacement field, whereas later iterations capture the higher-frequency details, thereby improving the resolution. The top of the producing segments between 2.5 s and 2.6 s can be mapped easily using these displacement components. [CR]. `chap2/. ts-20061,ts-20062,ts-20063`

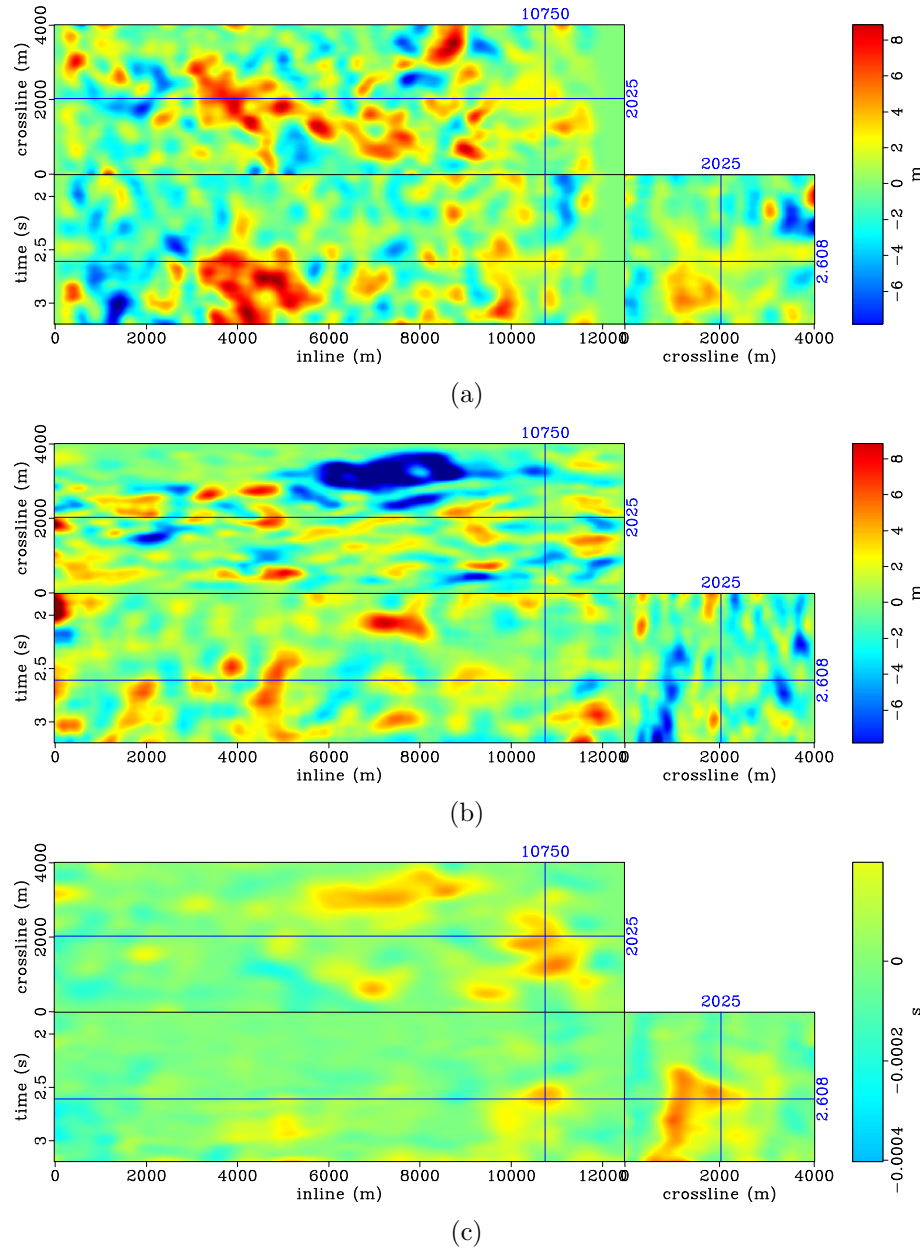


Figure 2.7: Horizontal displacement components between the 2006 monitor and the baseline in the inline (a), and crossline (b) directions; Time-shift errors (c) that are caused by neglecting horizontal displacements. [CR].

chap2/. x-20063,y-20063,ts-d-3

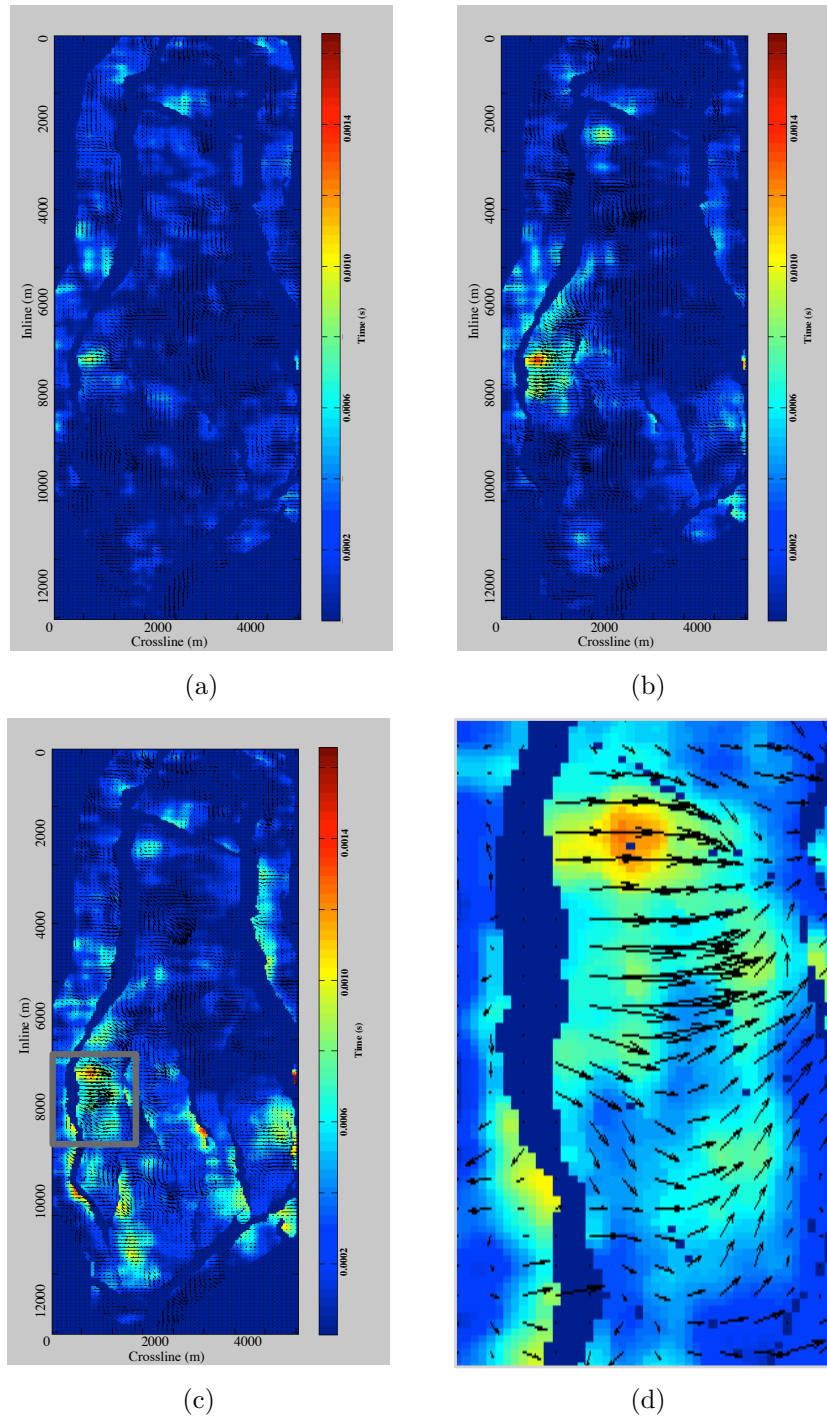


Figure 2.8: Absolute vertical and lateral displacements at the top of the reservoir between the baseline and the 2003 (a), 2004 (b), and 2006 (c) monitor images. In (c), the box indicates the location of the zoomed panel (d). The arrows indicate the displacement direction. [CR]. `chap2/. shift-top1,shift-top2,shift-top3,shift-top4`

Velocity changes between the baseline and the three monitor surveys, computed from equation 2.3, are presented in Figure 2.9. Figure 2.10 shows errors in the estimated velocity change that result from neglecting lateral displacements. Note that as production-induced changes increase, the errors introduced by considering only vertical displacements increase. Figure 2.11 shows the velocity changes between the baseline and the three monitor surveys extracted along the top of the reservoir (Figure 2.9). Velocity errors along the top of the reservoir caused by considering only vertical displacements are shown in Figure 2.12.

Before computing the final amplitude differences between the baseline image and the warped monitor images, I attenuate residual artifacts by the optimized matched filtering method described in a previous section. The starting parameters—derived by trial and error—and the optimization bounds are presented in Table 2.1. Selected optimized parameters derived from matching the baseline image to the 2006 monitor image are shown in Figure 2.13. The filters are estimated within a window that is 1.0 s long above the reservoir and a 0.6 s long below it. Note that the smoothness constraint on the filtering parameters ensures that the parameters (and hence the filters) do not change significantly from trace to trace.

Table 2.1: Matched filter parameters

	Lower bound	Starting guess	Upper bound
Filter length	0.50 s	0.65 s	0.80 s
Upper boundary perturbation	-0.08 s	0.00 s	0.08 s
Lower boundary perturbation	-0.08 s	0.00 s	0.08 s
Damping parameter	$1 \times 10^{-4}$	$1 \times 10^{-3}$	$1 \times 10^{-2}$

Figures 2.14 shows the time-lapse images between the baseline and the 2006 monitor obtained after different processing steps. Note how undesired artifacts in the time-lapse image are attenuated by warping and matched filtering. Note that the large amplitude differences caused by imaging the monitor data with the baseline velocity have been attenuated by warping (Figures 2.14(b)). In addition, note that residual amplitude differences generated by non-repeatability artifacts in the two seismic images have been attenuated by matched filtering (Figures 2.14(c)).

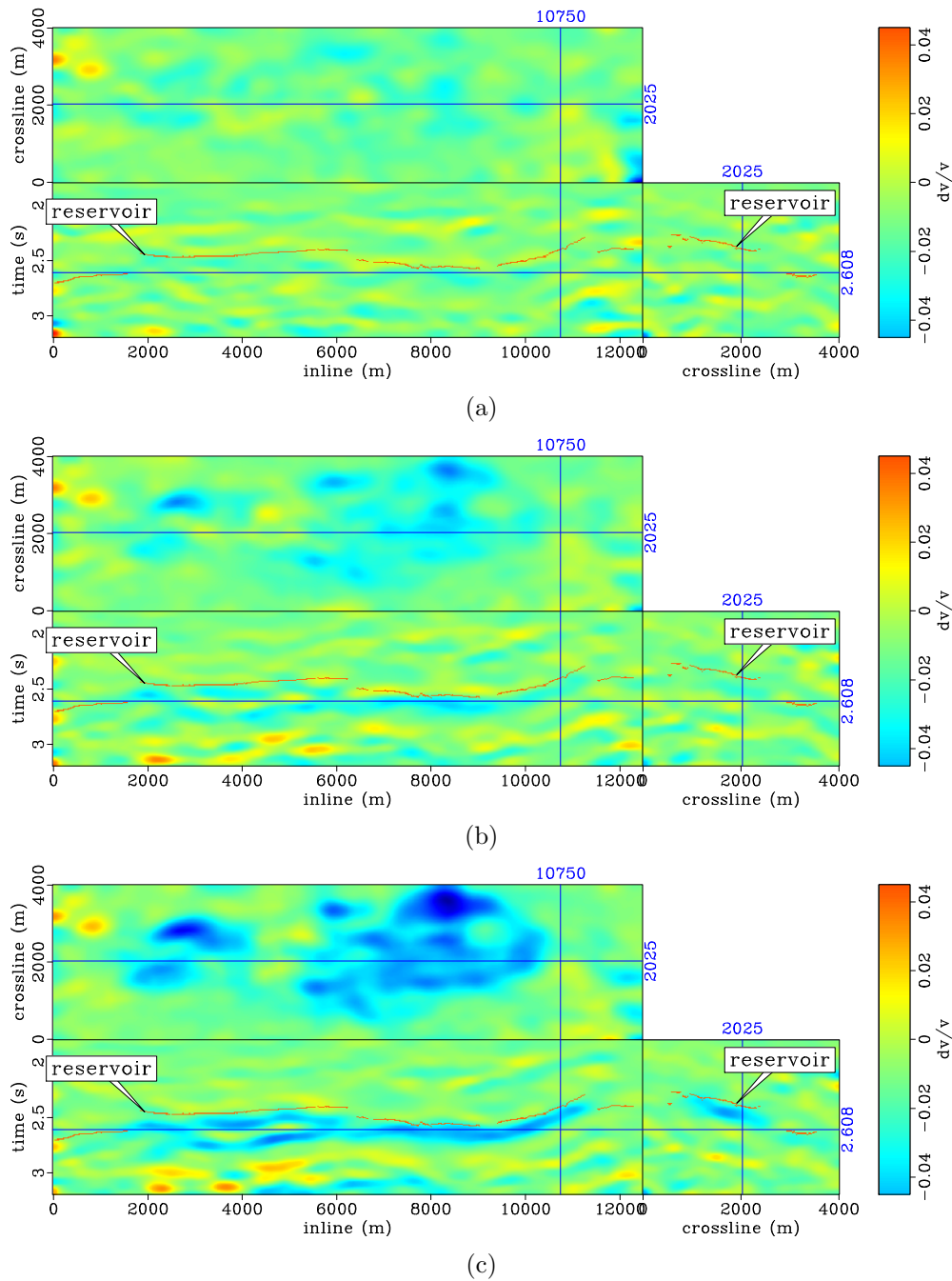


Figure 2.9: Fractional velocity change between the baseline and the 2003 (a), 2004 (b) and 2006 (c) monitor images. Note that in general, due to depletion, velocity within the reservoir decreases with time. The velocity change along the horizon (top of the reservoir) for these three cases are shown in Figure 2.11. [CR].  
 chap2/. vv-full-2003-f,vv-full-2004-f,vv-full-2006-f

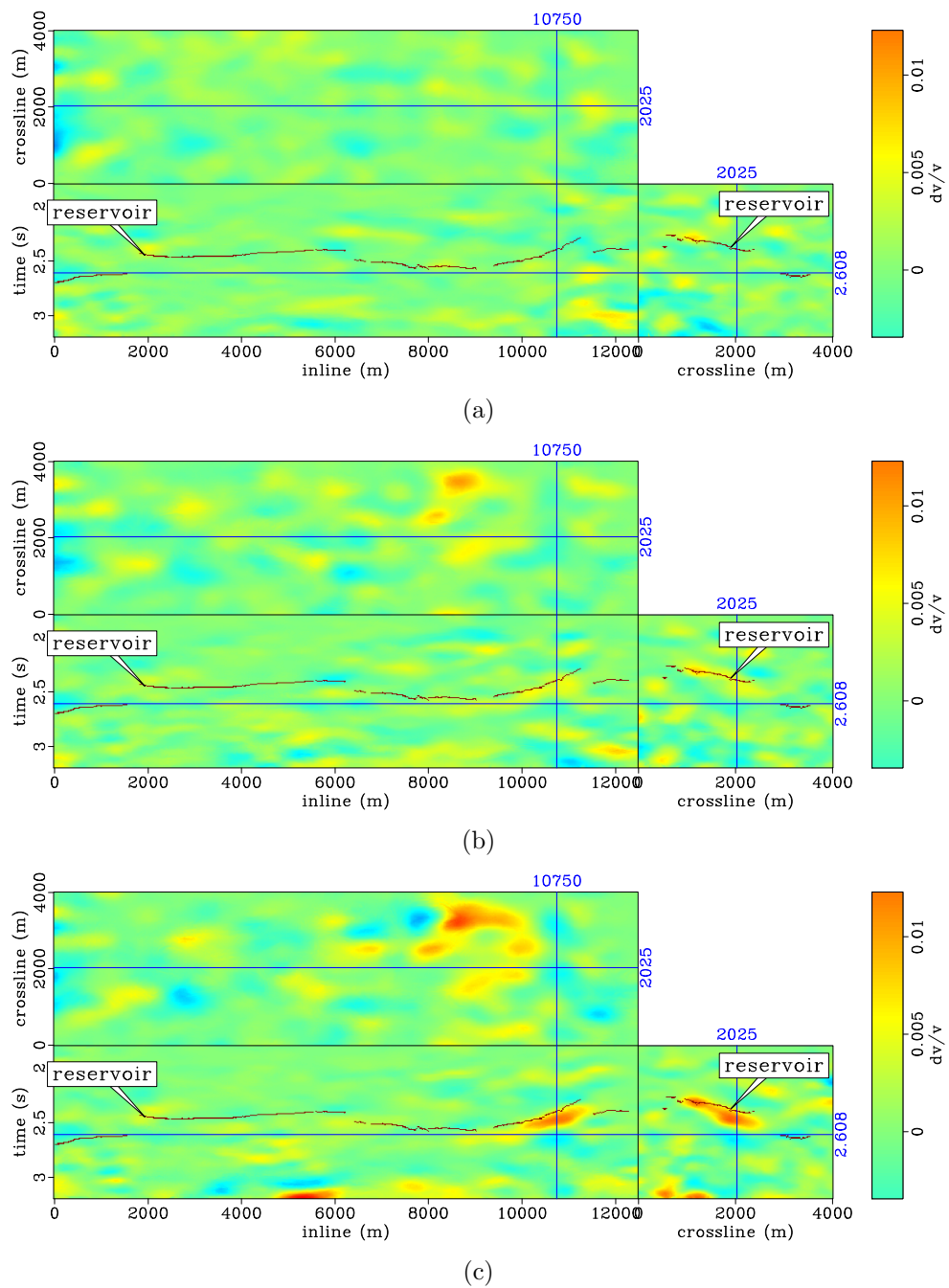


Figure 2.10: Velocity errors caused by neglecting horizontal displacements between the baseline and the 2003 (a), 2004 (b) and 2006 (c) monitor images. Note that the error in velocity increases with time. The errors in velocity change along the horizon (top of the reservoir) are shown in Figure 2.12. [CR].  
 chap2/. vv-d-full-2003,vv-d-full-2004,vv-d-full-2006

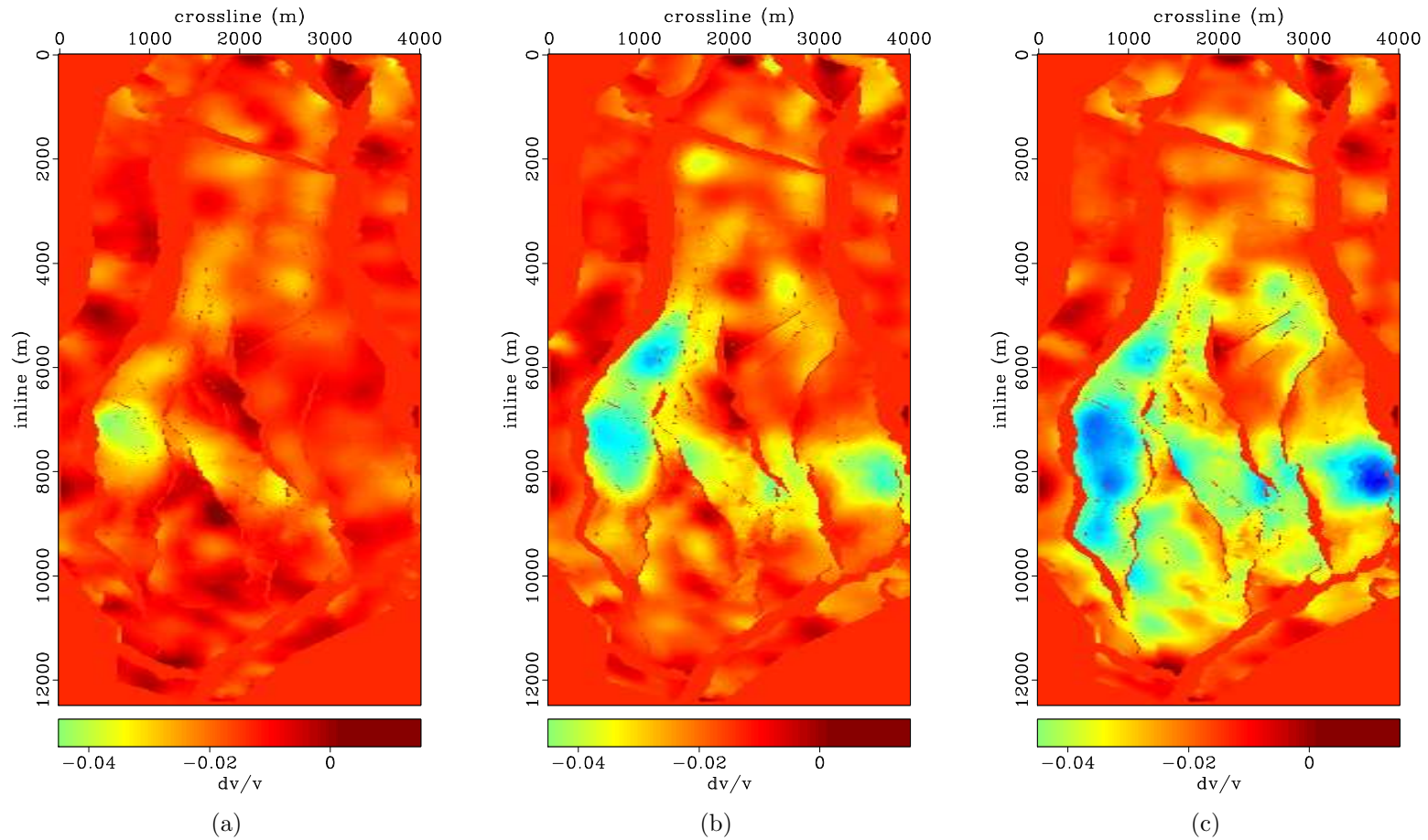


Figure 2.11: Maps of fractional velocity change at the top of the reservoir (Figure 2.9) between the baseline and the 2003 (a), 2004 (b) and 2006 (c) monitor images. Note that in general, due to depletion, velocity within the reservoir decreases with time. [CR]. `chap2/. vv-map-2003,vv-map-2004,vv-map-2006`

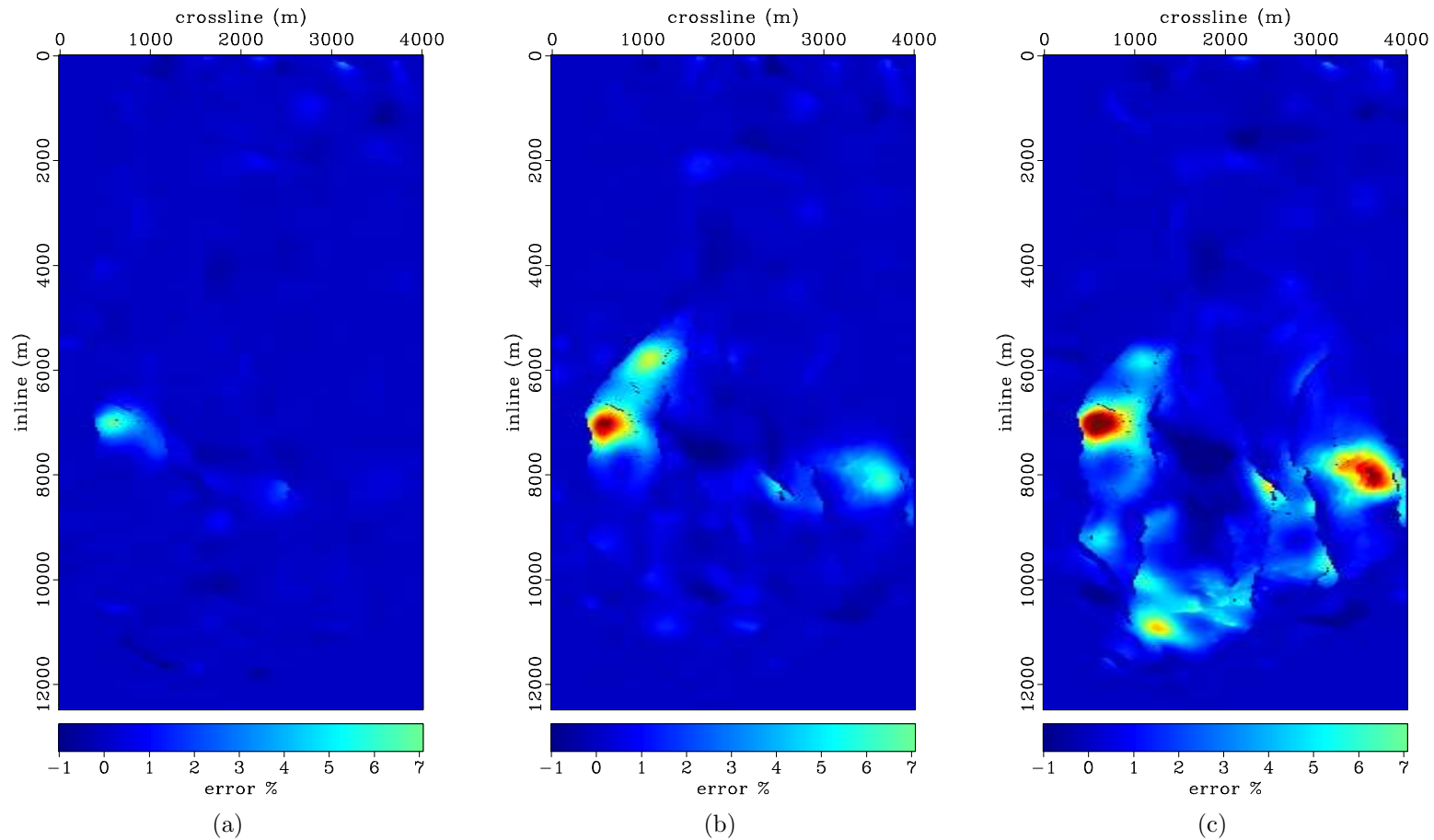


Figure 2.12: Maps of errors in fractional velocity change at the top of the reservoir (Figure 2.10) between the baseline and the 2003 (a), 2004 (b) and 2006 (c) monitor images. Note that the errors are greatest in parts of the field with the largest change (Figure 2.11). Furthermore, note how the errors increase with time. [CR].

chap2/. vv-d-map-2003,vv-d-map-2004,vv-d-map-2006

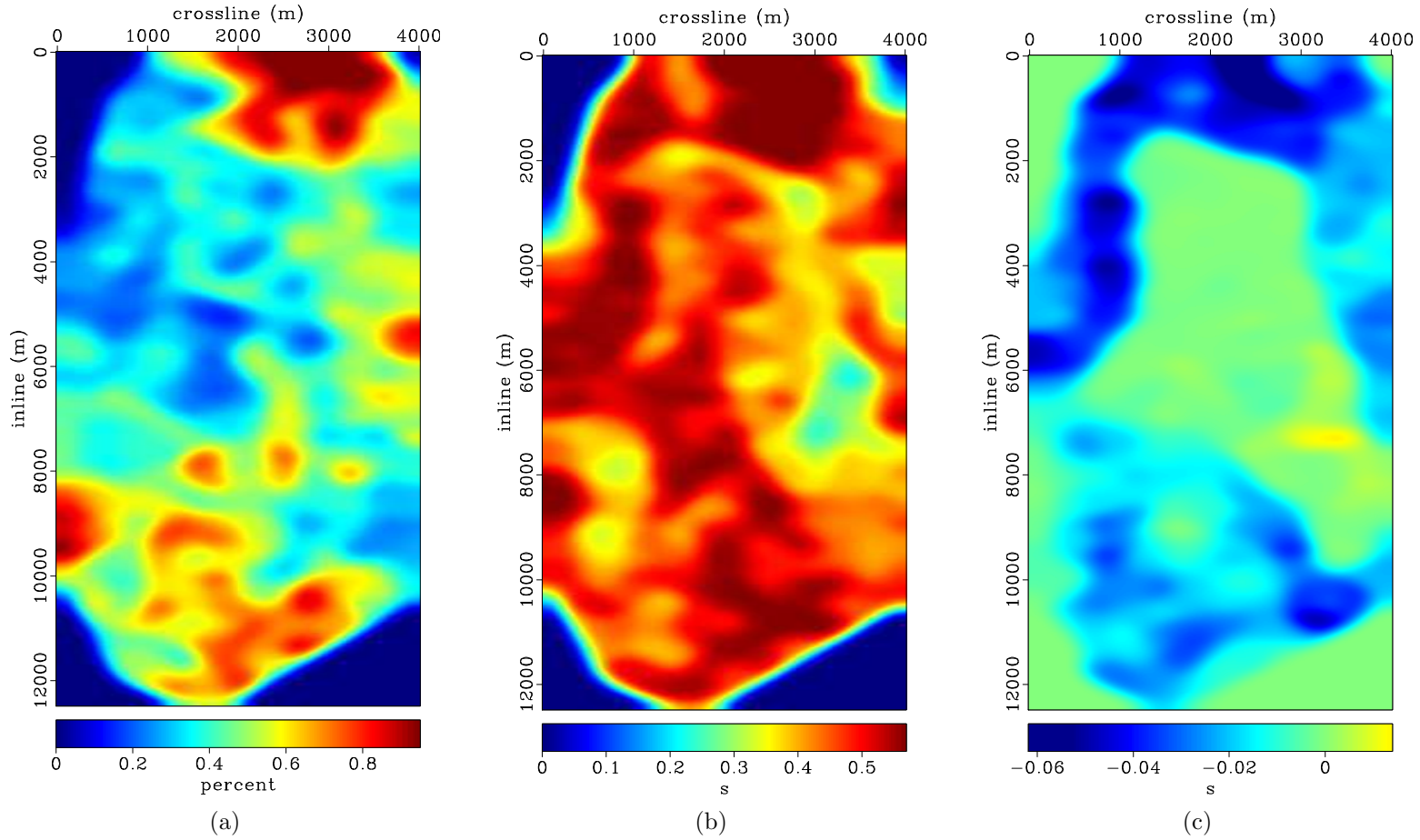


Figure 2.13: Maps of selected optimized matched filtering parameters. The panels show the damping parameter  $\epsilon$  (a), the filter length, and perturbations to the upper boundary of the estimation window. [CR].

chap2/. map-eps,map-filt,map-nup

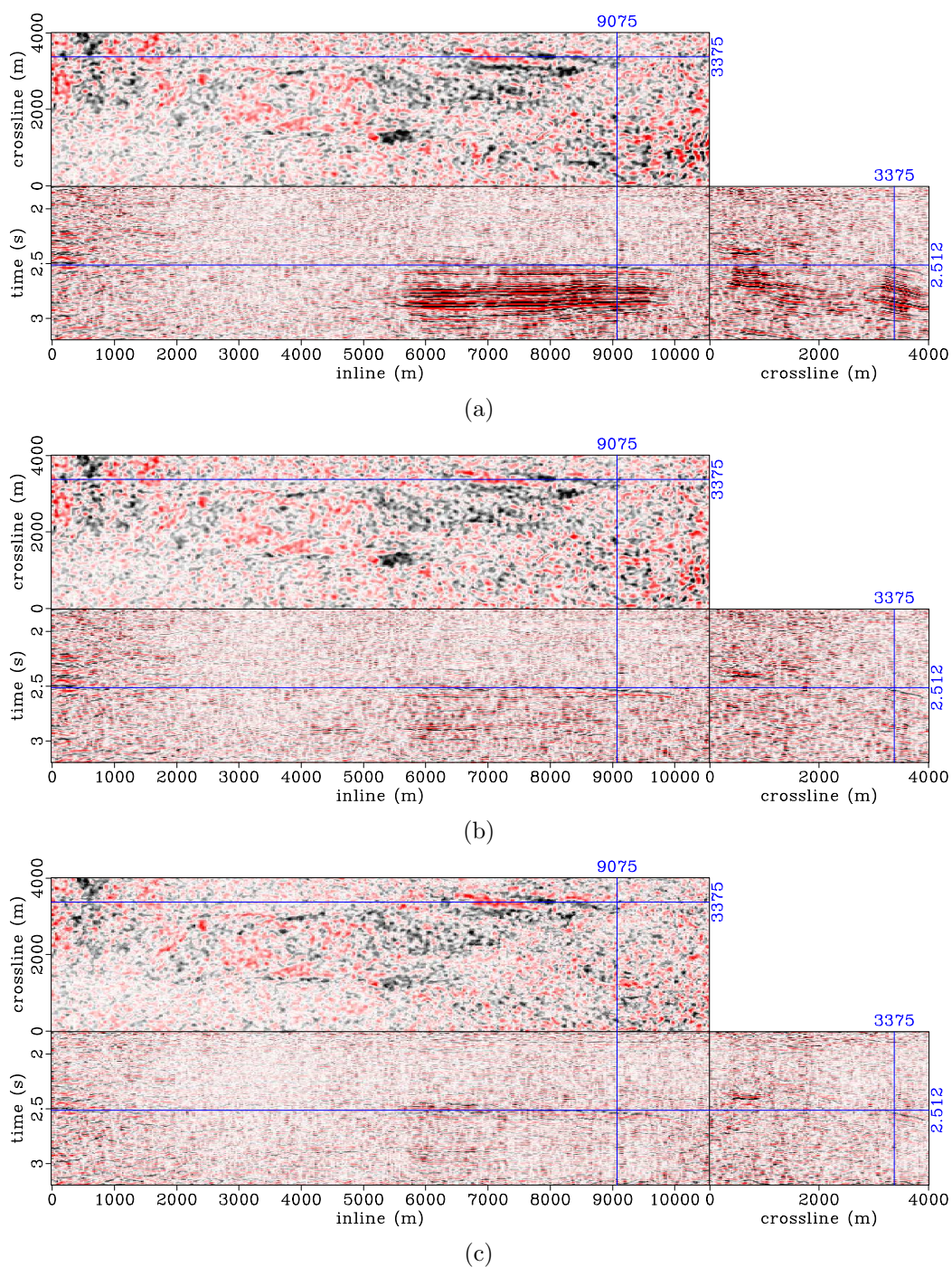


Figure 2.14: Time-lapse images between the 2006 monitor and the baseline after different processing steps. The panels show the time-lapse image before warping (a), after warping (b), and after optimized matched filtering. The time-lapse amplitudes of interest are located around the time-slice position. Note the improvements in quality of the time-lapse image after different processing steps. [CR].  
 chap2/. 4d-or0-2006,4d-org-2006,4d-opt-2006

Even when filter parameters have been selected carefully, using a single set of parameters will not provide optimal filters at all locations. For example, Figure 2.15 shows comparisons among enlarged sections of the time-lapse images after warping, after matched filtering with a single set of parameters, and after matched filtering with optimized parameters. In Figure 2.15(b), the reservoir time-lapse amplitudes are contaminated by vertical streak of filtering artifacts. Artifacts, such as these, are one reason why some practitioners argue avoid matched filtering in seismic cross-equalization (Lumley et al., 2003). In the time-lapse image obtained by optimized filtering, these artifacts are negligible in amplitude (Figure 2.15(c)).

To better understand the impact of matched filtering on reservoir time-lapse amplitudes, let us consider the average time-lapse amplitudes above, below, and within the reservoir. Figure 2.16 shows time-lapse amplitudes in a 0.6 s window around the reservoir. To obtain these (and similar) maps of average time-lapse amplitudes, I compute the difference between the sums of the absolute amplitudes in baseline and monitor images—within the specified window. The time-lapse amplitude maps in Figure 2.16 contain production-related changes overlain by varying levels of contaminating non-repeatability artifacts. In this figure, the most significant production-related amplitude changes are expected within ovals A and C, and in the segment labeled D. Amplitudes within oval B are predominantly non-repeatability artifacts.

Figure 2.16 clearly show one limitation of matched filters in seismic cross-equalization. Because it assumes that artifacts within the estimation window are stationary in time, where this assumption breaks down, matched filtering generates artifacts that further contaminate production-related differences. Comparing Figures 2.16(b) to 2.16(a), within the oval labeled A, note that matched-filtering leads to a improbable large increase in the time-lapse amplitudes. As would be shown later, this increase in time-lapse amplitudes is caused mainly by artifacts resulting from application of matched filters derived from a single set of parameters. Although the time-lapse amplitude map derived from the optimally filtered image contain some artifacts (e.g., within oval B in Figure 2.16(c)), these are fewer and are at relatively lower amplitudes compared to the single-parameter-filtering result (Figure 2.16(b)).

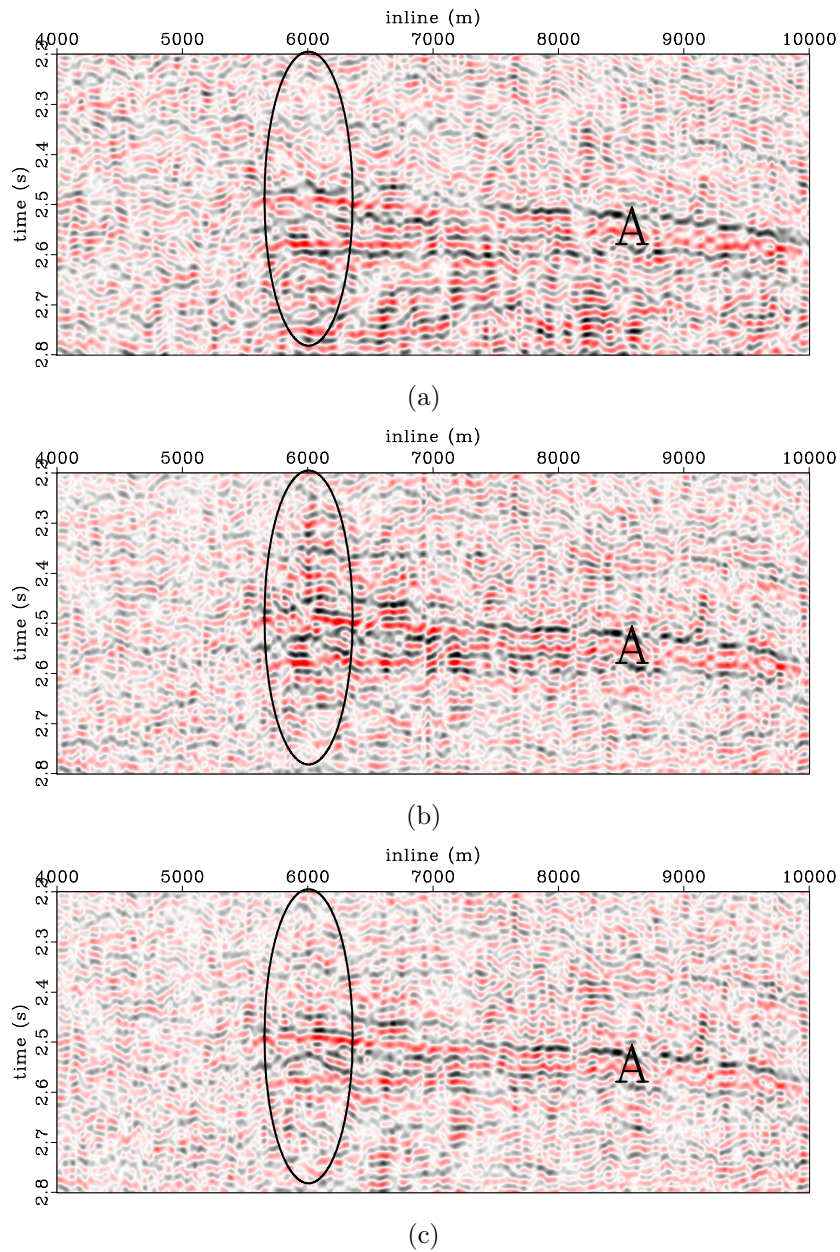


Figure 2.15: Comparison between time-lapse images after different processing steps. The panels show inline sections through the time-lapse image after warping (a), after matched filtering with a single set of parameters (b), and after matched filtering with optimized parameters (c). The time-lapse amplitudes of interest are indicated by label A. In the oval, note that whereas the time-lapse image from filtering with a single set of parameters (b) contains artifacts that are not present in the original time-lapse image (a), these artifacts are attenuated by filtering with optimized parameters (c).

[CR]. chap2/. 4d-org-2006-zm1,4d-smp-2006-zm1,4d-opt-2006-zm1

Figure 2.17 shows the average time-lapse amplitudes within a 0.5 s window above the reservoir. Because no production-related amplitude differences are expected in this non-reservoir region, all amplitudes in the images are undesirable artifacts. Note that the high amplitude artifacts within the oval labeled B in Figure 2.17(a) have been attenuated by matched filtering with a single set of parameters (Figure 2.17(b)). Furthermore, note that the optimally filtered results contain fewer artifacts in this part of the image (Figure 2.17(c)).

Although, in general, matched filtering with a single set of parameters attenuates contaminating artifacts in the non-reservoir region, it also introduces new artifacts in other parts. For example, within the oval labeled A in Figure 2.17(b), which is located directly above a producing segment in the field, note that some amplitudes that are not present in unfiltered image (Figure 2.17(a)) have been introduced. Such artifacts will also contaminate the measure time-lapse amplitudes within the reservoir. Note that within the same region in optimally filtered results (Figure 2.17(c)), these artifacts are negligible. In addition, note that in other areas identified in Figure 2.17, optimized matched filtering provides better results than matched filtering with single set of parameters.

Figure 2.18 shows time-lapse amplitudes within a 0.5 s window below the reservoir. As in Figure 2.17, the large amplitude differences within the oval labeled B, and in other parts of Figure 2.18(a) are undesired artifacts. Note that matched filtering with a single set of parameters attenuate these artifacts (Figure 2.18(b)). However, note that in parts of the field labeled A to D, the amplitude map obtained by optimized matched filtering contain fewer artifacts (Figure 2.18(b)).

As described above, if only vertical displacements are considered, time-lapse images will not be properly aligned. Figure 2.19 shows the errors in time-lapse amplitudes that will result if only vertical displacements are considered. Note that, as observed in estimates of velocity change (Figure 2.10), these errors increase as the production-induced differences between surveys increase.

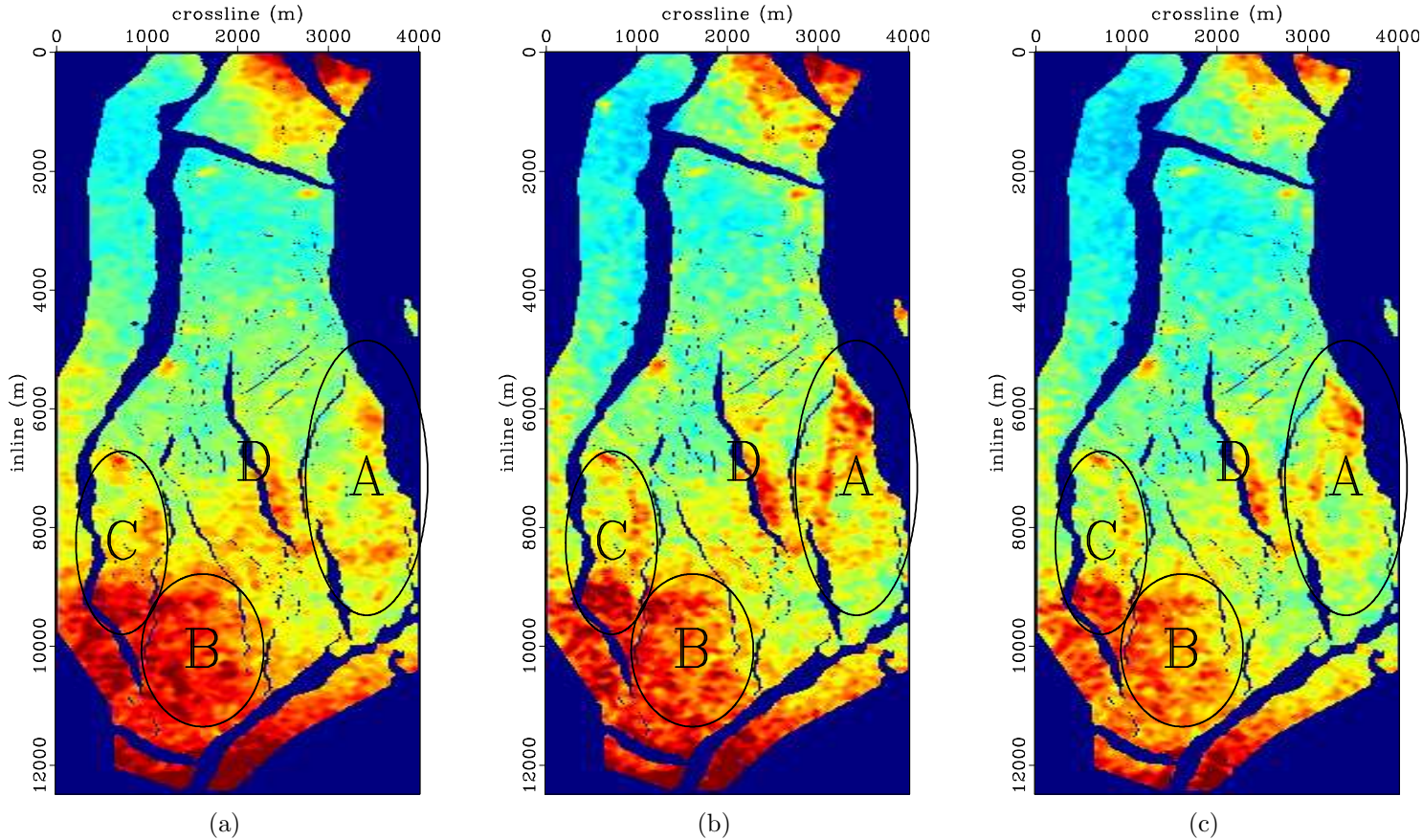


Figure 2.16: Maps of average time-lapse amplitudes between the baseline image and the 2006 monitor image within a 0.6 s window around the reservoir. The panels show amplitude difference after warping (a), after matched filtering with a single set of parameters (b), and after optimized matched filtering (c). As shown in Figures 2.17 and 2.18, amplitudes within oval B are artifacts. The most significant production-related changes are expected only within ovals A and C. These artifacts are better attenuated by optimized filtering (c). Note that the time-lapse amplitudes within oval A in (b) are corrupted by filtering artifacts. [CR]. chap2/. map-dif-org,map-dif-smp,map-dif-opt

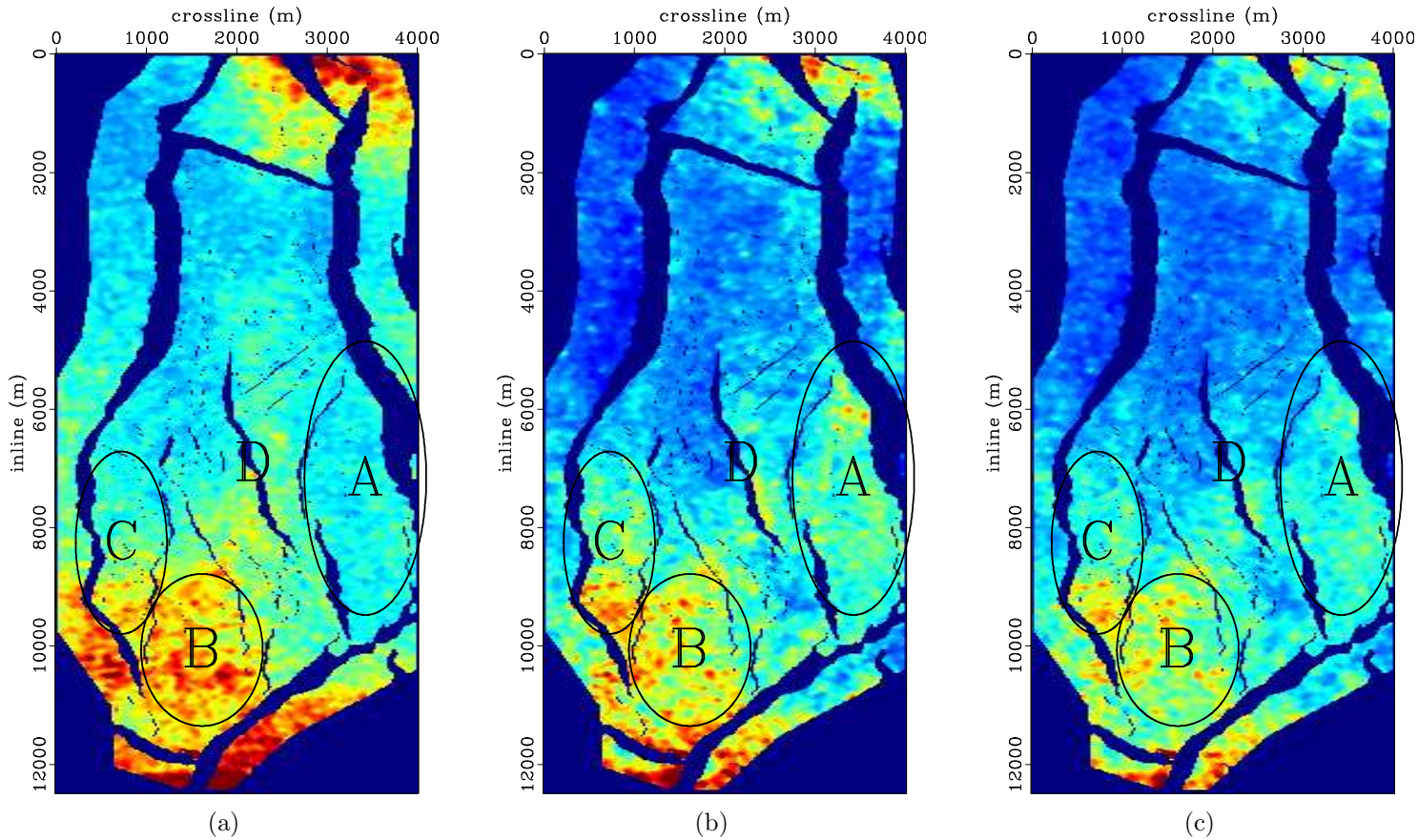


Figure 2.17: Maps of average time-lapse amplitudes between the baseline image and the 2006 monitor image within a 0.5 s window located above the reservoir, where no production-related amplitude change is expected. The panels show amplitude differences after warping (a), after matched filtering with a single set of parameters (b), and after optimized matched filtering (c). In (b), note that matched filtering with a single set of parameters attenuate many of the non-repeatability artifacts (e.g., oval B) but also introduces undesirable artifacts (e.g., oval A). Note in (c) that optimized matched filtering provides satisfactory attenuation of the artifacts without introducing new undesirable artifacts. [CR]. `chap2/. map-dif-org-up,map-dif-smp-up,map-dif-opt-up`

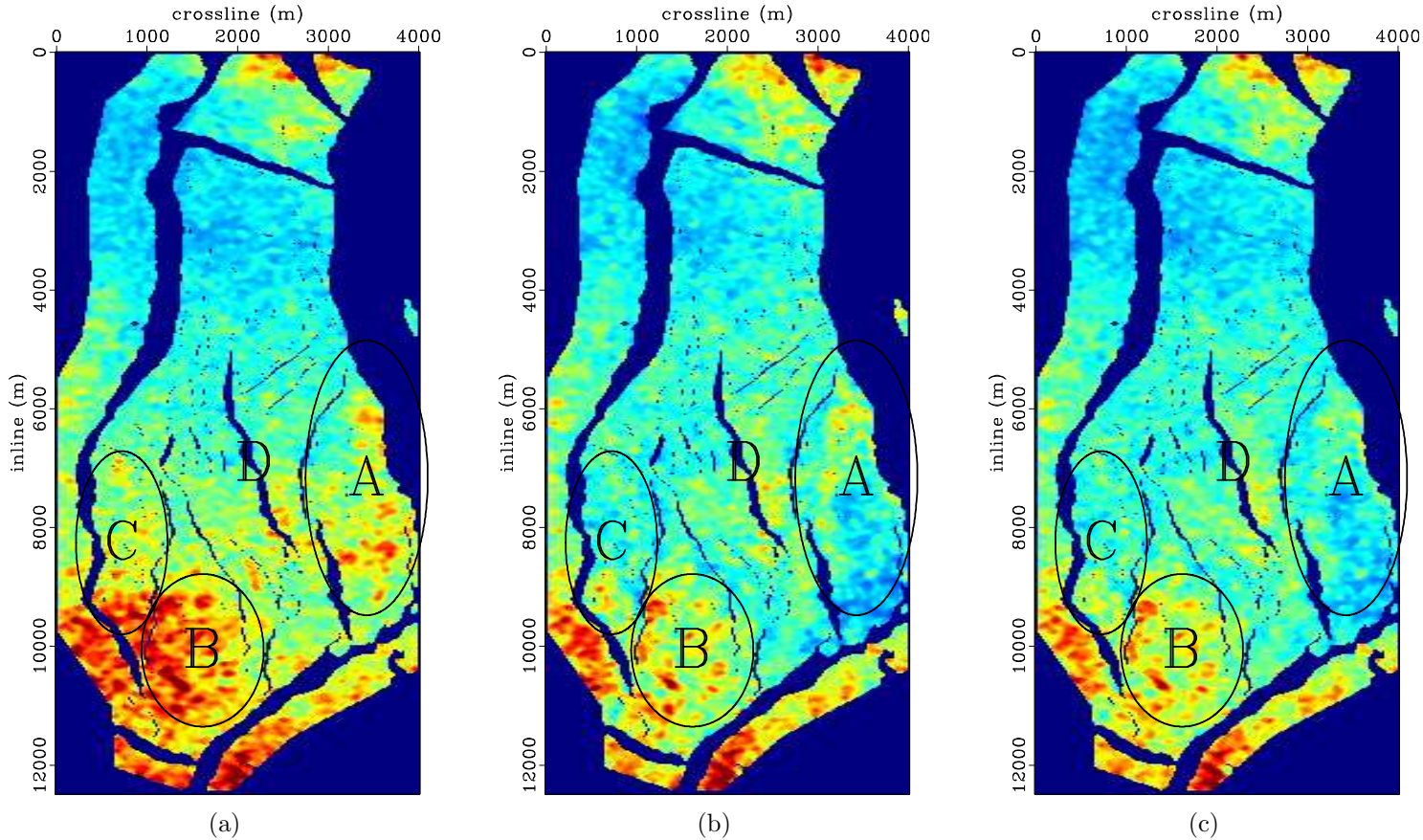


Figure 2.18: Maps of average time-lapse amplitudes between the baseline image and the 2006 monitor image within a 0.5 s window located below the reservoir, where no production-related amplitude change is expected. The panels show amplitude differences after warping (a), after matched filtering with a single set of parameters (b), and after optimized matched filtering (c). Note that matched filtering with provides satisfactory attenuation of the high amplitude artifacts in the (e.g., oval B). Furthermore, note that at several locations (e.g., oval A) the result from optimized filtering contain fewer artifacts. [CR]. chap2/. map-dif-org-dn,map-dif-smp-dn,map-dif-opt-dn

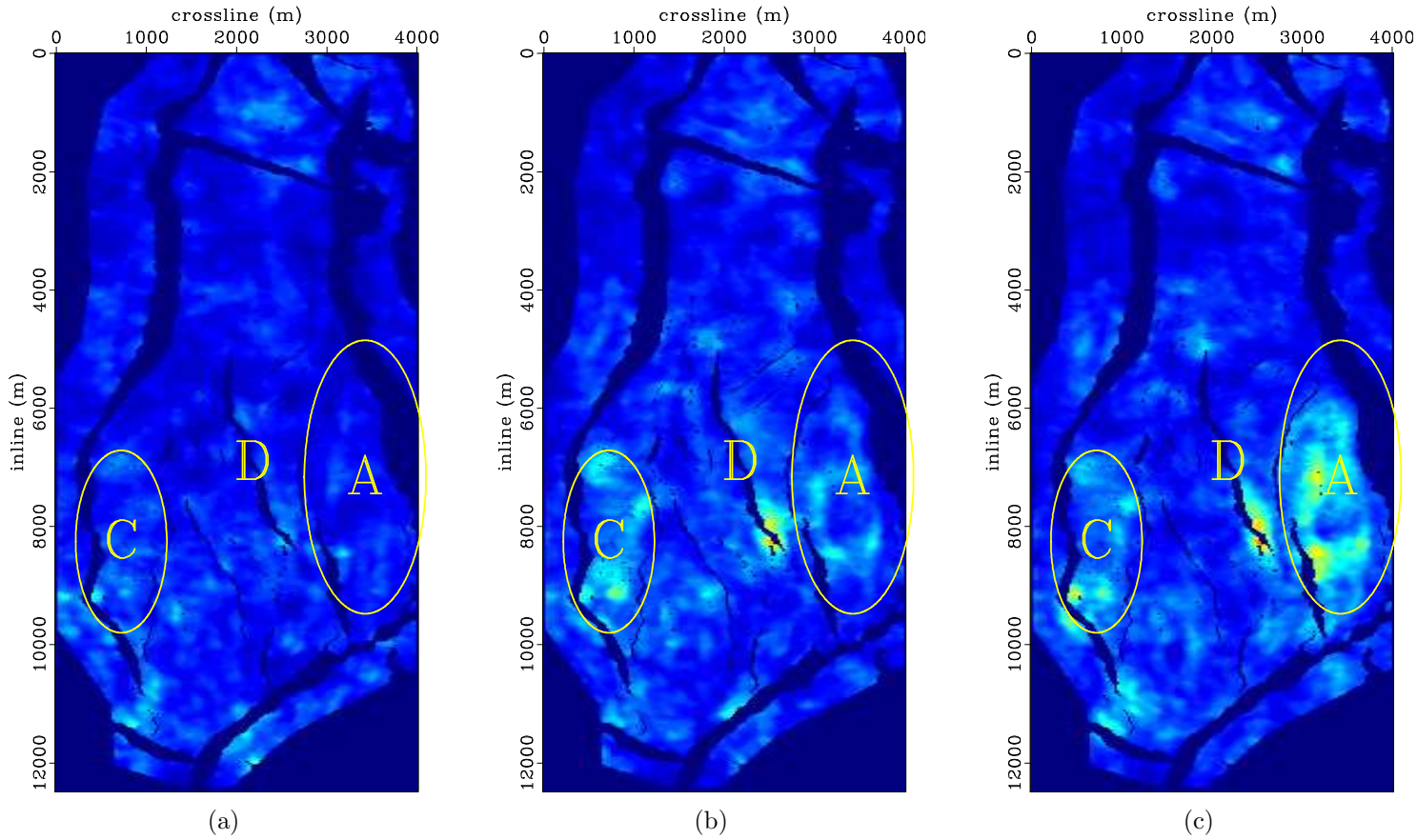


Figure 2.19: Maps showing errors in time-lapse amplitudes within the reservoir caused by considering only vertical displacements versus considering multidimensional displacements. The panels show amplitude differences between the baseline and the 2003 (a), 2004 (b), and 2006 (c) monitor surveys. These amplitude differences represent errors in time-lapse amplitudes caused by approximating multidimensional warping by vertical warping. [CR].

chap2/. map-dif-err1,map-dif-err2,map-dif-err3

## DISCUSSION

The sequential one-dimensional warping method described in this chapter provides a robust and efficient alternative to a full, computationally expensive 3D method. By iteratively estimating components of the displacement vectors in a sequential manner using variable correlation gates and lags, it is possible to obtain high-resolution estimates of apparent displacements between time-lapse seismic images (Figures 2.1 to 2.4; Figure 2.6). These apparent displacements contain information about changes within and around the reservoir, which may be interpreted qualitatively (Figures 2.8 and 2.9) or used to build robust geomechanical models (Hatchell and Bourne, 2005a).

Approximating multidimensional apparent displacements between time-lapse seismic images using only vertical time-shifts lead to errors in time-lapse images and their derivatives. In field data example, between 2001 and 2006, lateral displacements of up to 9 m are recorded (Figure 2.7). As shown in Figure 2.7(c), for the field data example, neglecting lateral displacements leads to time-shift overestimation below the reservoir, and time-shift underestimation above the reservoir. Analyses of the estimated displacements show that between 2001 and 2006, velocity within the reservoir has decreased by up to 5% (Figures 2.9 and 2.11). Errors in time-shift, which are more pronounced around dipping reflectors (e.g., Figure 2.7(c)), cause errors of up to 10% in estimates of velocity change (Figures 2.10 and 2.12). Such errors will also propagate to any other reservoir properties (e.g., geomechanical changes) derived from such time-shifts and to time-lapse amplitudes derived by subtracting the warped images (Figure 2.19).

Matched filtering attenuates residual differences that contaminate production-related amplitudes in time-lapse images (Figure 2.14). Although matched filtering with a single parameter set provides a good satisfactory results in parts of the time-lapse image, it also introduces artifacts in other parts (Figure 2.15(b)). However, optimized parameters derived from the proposed method enable computation of the optimal matched filters at each trace location, thereby improving the reliability

of time-lapse amplitudes within the reservoir (Figure 2.15(b)). As shown in Figures 2.17 and 2.18, optimally filtered time-lapse images contain fewer artifacts above and below the reservoir. Therefore, optimized matched filtering provides improved confidence in the time-lapse amplitudes within the reservoir (Figure 2.16).

## CONCLUSIONS

In this chapter, I discussed two common cross-equalization methods and how they can be improved. Using the Norne field time-lapse data sets, I showed how these improved methods can provide reliable information about changes within the reservoir.

The sequential one-dimensional warping method, adapted from Hale (2009), allows efficient multidimensional warping of time-lapse seismic images while overcoming cost limitations of full multidimensional warping and avoiding errors associated with vertical warping. Where the estimated apparent displacements are used to derive changes in reservoir properties, and where the reservoir and overburden formations are not horizontal, considering only vertical displacements may cause serious estimation errors. Importantly, this warping method will be used as a preprocessing step for the inversion methods developed in later chapters.

After warping, residual artifacts in time-lapse seismic images caused by non-repeatability between surveys are attenuated by matched filtering with optimized parameters. In this chapter, I showed how optimal filtering parameters can be obtained using an evolutionary programming algorithm. These filters provide more reliable time-lapse images than conventional matched filtering with single parameters. Together, sequential one-dimensional warping and optimized matched filtering form an efficient and robust cross-equalization scheme.

Although the methods described in this chapter perform satisfactorily in conventional time-lapse imaging, such as in the one discussed in this chapter, they are insufficient in many cases. In the next chapter, I discuss joint least-squares inversion methods that overcome some of the limitations of these conventional time-lapse cross-equalization methods.

## ACKNOWLEDGEMENTS

I thank Statoil and partners for releasing the Norne data through the NTNU/IO CENTRE. Bard Osdal and Trine Alsos (Statoil), Mohsen Dadashpour (NTNU) and David Echeverria (formerly of Stanford Smart Fields, now IBM) provided assistance throughout this study. Mosab Nasser (formerly of Shell, currently of Maersk Oil), my supervisor during an internship at Shell, suggested that I explore ways to improve local match-filtering of time-lapse data sets.



# Chapter 3

## Joint least-squares migration/inversion: theory

This chapter presents inversion methods that overcome some short-comings of conventional time-lapse imaging methods. In the previous chapter, I discussed how two common post-imaging time-lapse cross-equalization methods—warping and matched filtering—can improve the quality of time-lapse images. Today, these methods, together with a wide range of specialized pre-stack and post-stack processing steps form the state-of-the-art in time-lapse seismic imaging. Although these methods are well developed, and are adequate in many field and geological scenarios, they are inadequate in many others.

Two practical scenarios where conventional time-lapse imaging methods become inadequate are in reservoirs under complex overburden and where large geometry differences exist between surveys. For example, because complex overburden causes complicated and irregular subsurface illumination, conventional data regularization methods are inadequate. Conventional methods are also typically inadequate to reconcile large differences in acquisition geometries between surveys. Such geometry differences can be caused by changes in acquisition systems, new production facilities, or natural environmental changes. In many cases, artifacts in time-lapse seismic

images that are caused by complex overburden or geometry differences may strongly contaminate production-related image differences. Unless non-production-related artifacts in time-lapse seismic images are attenuated, it is impossible to accurately relate image differences to changes in reservoir properties. Because conventional methods are inadequate in these scenarios, new time-lapse imaging methods are required.

In this chapter, I discuss extension of linear least-squares imaging methods to joint inversion of time-lapse seismic data sets. Because inversion accounts for illumination mismatches—caused by differences in acquisition geometries—and for band-limited wave-propagation effects through reservoir overburden, it provides better estimates of production-related changes in reservoir acoustic properties than conventional time-lapse imaging methods. By joint inversion, I mean that data sets from multiple surveys are inverted together by minimizing a single (joint) objective function. One important advantage of time-lapse imaging by joint (versus separate) inversion is that it enables incorporation of a priori information in the form of temporal as well as spatial constraints. Because seismic inversion is inherently ill-posed, these constraints are required to ensure that the inversion is stable and that results are geologically plausible.

Regularized joint inversion of time-lapse data sets can be solved in either the data and image domains. In this chapter, I show how these spatio-temporal constraints can be incorporated into a regularized joint least-squares inversion framework in the data and image domains. One advantage of image-domain joint inversion is that it enables the problem to be solved in a target-oriented way. Because of the target-oriented nature of time-lapse imaging, in many practical applications, image-domain inversion is preferable. Furthermore, because joint image-domain inversion is relatively computationally inexpensive, it can be repeated several times with different temporal and spatial constraints. In chapters 4, 5 and 6, I show different applications of these methods to synthetic and field data examples.

First, I review data-domain and image-domain least-squares inversion methods. Next, I develop the theory of joint least-squares inversion of time-lapse data sets. Finally, I discuss the spatial and temporal constraints used in the inversion.

## SEISMIC IMAGING BY LEAST-SQUARES INVERSION

Linear least-squares inversion has been shown to improve structural and amplitude information in seismic images. For example, Nemeth et al. (1999) show that it improves imaging of incomplete seismic and ground penetrating radar data; Köhl and Sacchi (2003) show that it improves amplitude variation with angle (AVA) information in pre-stack gathers; and, Clapp (2005), Valenciano (2008), and Tang (2011) show that it improves images of reservoirs located under complex overburden. In these examples, the authors show that imaging by least-squares inversion provides more reliable results than conventional imaging by migration. In general, least-squares imaging of seismic data sets can be implemented in either the data domain or in the image domain.

**Data-domain least-squares inversion:** In this dissertation, I refer to methods that directly minimize the misfit between the recorded and modeled data as data-domain methods. One drawback of data-domain inversion methods is that they require migration and modeling (demigration) at every iteration (Nemeth et al., 1999; Köhl and Sacchi, 2003; Clapp, 2005). Because several iterations are required to reach convergence, in many practical applications, data-domain methods are too expensive. However, as I discuss later in chapter 4, by using phase-encoding methods, data-domain inversion of seismic data becomes practical. Such encoding can be either field-based (e.g., data acquisition with arbitrary number of simultaneous-sources (van Mastrigt et al., 2002; Hampson et al., 2008; Beasley, 2008; Berkhout et al., 2008; Howe et al., 2009)) or computer-based (i.e., phase-encoded imaging of conventional data sets (Krebs et al., 2009; Tang and Biondi, 2009; Verschuur and Berkhout, 2009; Schuster et al., 2011)). In chapter 4, I show an application of data-domain inversion to field-encoded time-lapse seismic data sets, with non-repeated geometries and relative shot times.

**Image-domain least-squares inversion:** Instead of the data-domain approach, the Hessian of the least-squares objective function can be approximated and the

problem solved in the image domain (Lambaré et al., 2003; Valenciano, 2008; Tang, 2011). In this approach, the input is the recorded data transformed (via migration) to the image domain—hence, both the input (migrated) and output (inverted) images have similar dimensions. Image-domain inversion has several desirable properties. First, as noted earlier, because the proposed formulations utilize pre-computed approximate (target-oriented) Hessian operators, no new migration and modeling are required during the inversion. Although, for many practical applications, the computational cost of the approximate Hessian is not trivial (Valenciano, 2008; Tang, 2011), once the Hessian is obtained, image-domain inversion can be done several orders of magnitude more cheaply than data-domain inversion. In addition, because the inversion problem is solved in the image domain, the computational domain can be reduced to only a target region around the reservoir, thereby reducing computational cost. This is particularly useful for time-lapse imaging, because the reservoir location and extent are usually well defined before seismic monitoring is performed. Furthermore, the imaging interest is usually limited to the regions within and around the reservoir. Finally, because it is computationally efficient, the image-domain inversion can be repeated quickly with different a priori constraints.

One way of obtaining inverted time-lapse images is by applying the least-squares inversion methods described above to individual data sets and then computing differences between inverted images. In this dissertation, this approach, which requires that the objective function for each survey be independently minimized, is called separate inversion. Because separate inversion allows only spatial constraints in the time-lapse inversion, it provides only limited improvements to the quality of time-lapse images. Nonetheless, because each problem is solved independently, artifacts in any one survey do not affect the results in other surveys.

Instead of inverting the data sets separately, by defining a single objective function for all data sets, time-lapse imaging can be posed as a joint inversion problem. For this joint inversion problem, data-domain operators are combinations of the modeling/migration operators of different surveys, whereas image-domain operators

are combinations of target-oriented approximations to the Hessians of different surveys. Importantly, joint inversion enables the incorporation of prior knowledge of the subsurface earth structure (e.g., reservoir location, extent and geometry), temporal constraints, and information from other sources (e.g., geological and petrophysical models) into the time-lapse imaging problem. Introduction of spatial and temporal constraints improve the quality and reliability of inverted time-lapse images.

Previous authors have discussed joint inversion applications to seismic data, such as impedance inversion (Sarkar et al., 2003) and crosswell ray-tomography (Ajo-Franklin et al., 2005). Other relevant time-lapse inversion methods include differential wave-equation velocity analysis (Albertin et al., 2006), sequential inversion with model-based regularization (Oldenborger et al., 2007; Miller et al., 2008; Routh and Anno, 2008), and differential travel-time tomography (Ajo-Franklin et al., 2007). Joint-inversion strategies are also common in medical imaging problems, including dynamic electrical impedance tomography (Schmitt and Louis, 2002; Schmitt et al., 2002) and electrocardiographic imaging (Messnarz et al., 2004; Guofa et al., 2006). Although my inversion goals differ from many of those listed, many of these formulations are directly extendable to inversion for time-lapse reflectivity amplitudes.

I consider two related formulations for regularized joint least-squares inversion of time-lapse seismic data sets. In the first formulation, called regularized joint inversion of multiple images (RJMI), I invert for seismic images for each input survey. In the second formulation, called regularized joint inversion for image differences (RJID), I invert for a static baseline image and for image differences between surveys. Both formulations allow for spatial and temporal constraints in the inversion. Without temporal constraints, both formulations yield results that are comparable to those from spatially regularized separate inversion. Both the RJID and RJMI formulations can be implemented in either the data domain or in the image domain.

In all the examples discussed in this dissertation, where applicable, the spatial regularization operator is a system of non-stationary dip-filters, whereas the temporal regularization operator is a gradient between surveys. First, I compute dips from the baseline image using the plane-wave destruction method (Fomel, 2002). I then

compute non-stationary dip-filters based on factorized directional Laplacians (Hale, 2007). In a later section, I discuss the spatial and temporal regularization operators in more detail.

In the next section, I discuss linear least-squares inversion of time-lapse data sets in the data and image domains.

## THEORY OF SEISMIC IMAGING BY LEAST-SQUARES INVERSION

From the Born approximation of the linearized acoustic wave equation, for a known velocity model, the synthetic seismic data  $d^s$  recorded by a receiver at  $\mathbf{x}_r$  due to a shot at  $\mathbf{x}_s$  is given by

$$d^s(\mathbf{x}_s, \mathbf{x}_r, \omega) = \omega^2 \sum_{\mathbf{x}} f_s(\omega) G(\mathbf{x}_s, \mathbf{x}, \omega) G(\mathbf{x}, \mathbf{x}_r, \omega) m(\mathbf{x}), \quad (3.1)$$

where  $\omega$  is frequency,  $m(\mathbf{x})$  is *reflectivity* at image points  $\mathbf{x}$ ,  $f_s(\omega)$  is the source waveform, and  $G(\mathbf{x}_s, \mathbf{x}, \omega)$  and  $G(\mathbf{x}, \mathbf{x}_r, \omega)$  are Green's functions from  $\mathbf{x}_s$  to  $\mathbf{x}$  and from  $\mathbf{x}$  to  $\mathbf{x}_r$ , respectively.

Taking the true recorded data at  $\mathbf{x}_r$  to be  $d^{obs}$ , I define a quadratic cost function given by

$$S(\mathbf{m}) = \|d^s(\mathbf{x}_s, \mathbf{x}_r, \omega) - d^{obs}(\mathbf{x}_s, \mathbf{x}_r, \omega)\|_2. \quad (3.2)$$

As shown by previous authors (Plessix and Mulder, 2004; Valenciano, 2008), the gradient  $g(x)$  of this cost function (summed over all frequencies, sources and receivers) with respect to the reflectivity is given by the real part of

$$g(\mathbf{x}) = \sum_w \omega^2 \sum_{\mathbf{x}_s} \sum_{\mathbf{x}_r} f_s(\omega) G(\mathbf{x}_s, \mathbf{x}, \omega) G(\mathbf{x}, \mathbf{x}_r, \omega) \left( \bar{d}^s(\mathbf{x}_s, \mathbf{x}_r, \omega) - \bar{d}^{obs}(\mathbf{x}_s, \mathbf{x}_r, \omega) \right), \quad (3.3)$$

and the Hessian (matrix of second derivatives) is the real part of

$$H(\mathbf{x}, \mathbf{x}') = \sum_w \omega^4 \sum_{\mathbf{x}_s} |f(s)|^2 G(\mathbf{x}_s, \mathbf{x}, \omega) \bar{G}(\mathbf{x}_s, \mathbf{x}', \omega) \sum_{\mathbf{x}_r} G(\mathbf{x}, \mathbf{x}_r, \omega) \bar{G}(\mathbf{x}', \mathbf{x}_r, \omega), \quad (3.4)$$

where  $\mathbf{x}'$  denotes all image points and  $\bar{G}$  is the complex conjugate of  $G$ . Plessix and Mulder (2004) and Valenciano (2008) discuss this derivation in detail.

Using matrix and vector notations, equation 3.1 can be written as

$$\mathbf{d} = \mathbf{L}\mathbf{m}, \quad (3.5)$$

and the objective function in equation 3.2 becomes

$$S(\hat{\mathbf{m}}) = \|\mathbf{d} - \mathbf{d}^{obs}\|_2 = \|\mathbf{L}\mathbf{m} - \mathbf{d}^{obs}\|_2 \quad (3.6)$$

where  $\mathbf{L}$  denotes the linear Born modeling operator,  $\mathbf{m}$  denotes the reflectivity model, and vectors  $\mathbf{d}$  and  $\mathbf{d}^{obs}$  denote the modeled and recorded data from all sources, respectively. The least-squares inverted model  $\hat{\mathbf{m}}$  satisfies the equation

$$\hat{\mathbf{m}} = (\mathbf{L}^T \mathbf{L})^\dagger \mathbf{L}^T \mathbf{d} = \mathbf{H}^\dagger \tilde{\mathbf{m}}, \quad (3.7)$$

where  $\mathbf{H} = \mathbf{L}^T \mathbf{L}$  is the Hessian of the cost function (equation 3.6),  $\tilde{\mathbf{m}}$  is the migrated image, and superscripts  $T$  and  $\dagger$  denote conjugate transpose and pseudo-inverse, respectively.

As discussed in the previous section, there are two ways of obtaining the inverted image  $\hat{\mathbf{m}}$ :

1. Minimizing the cost function in equation 3.6 such that the modeled and recorded data are similar:

$$S(\hat{\mathbf{m}}) = \|\mathbf{L}\mathbf{m} - \mathbf{d}^{obs}\|_2 \approx 0. \quad (3.8)$$

This represents the data-domain approach to least-squares inversion.

2. Computing an approximation of the Hessian and then minimizing the difference

between the migrated image and the Hessian times the inverted reflectivity:

$$\mathbf{H}\hat{\mathbf{m}} \approx \tilde{\mathbf{m}}. \quad (3.9)$$

This represents the image-domain approach to least-squares inversion.

## Data-domain versus image-domain inversion

Although results of data-domain and image-domain inversion are theoretically equivalent, the optimal implementation domain depends on the imaging goals, the acquisition geometry and the problem size. Below, I compare the two:

1. Data-domain inversion does not require pre-computation of an approximate Hessian matrix, whereas image-domain inversion does. However, as discussed below, there are practical methods of reducing the computational cost of the Hessian.
2. In data-domain inversion, each iteration requires at least one migration and one modeling, whereas in image-domain inversion, each iteration requires relatively cheap matrix-vector multiplication.
3. In general, data-domain inversion is slow for conventional acquisition geometries, whereas, once the approximate Hessian is computed, image-domain inversion is fast.
4. It is difficult to pose data-domain inversion as a target-oriented problem, whereas image-domain inversion is easily solved as a target-oriented problem.
5. Data-domain inversion of encoded/simultaneous-source data is relatively cheap, whereas image-domain inversion of such data is expensive in both computation and storage requirements because the Hessian is far from being diagonally dominant.

## Approximating the Hessian

For any practical application, because of the large computational cost, it is infeasible (and unnecessary) to compute the full Hessian matrix defined in equation 3.4. Previous authors have discussed approximations that reduce the computational cost or that remove the need for explicit estimation of the full Hessian (Santosa and Symes, 1988; Rickett, 2003; Guittou, 2004; Plessix and Mulder, 2004; Yu et al., 2006; Symes, 2008; Valenciano, 2008; Tang, 2011).

In this dissertation, I follow the target-oriented approximation of Valenciano (2008) and Tang (2011). Because for conventional geometries, the Hessian is diagonally-dominant, it can be approximated by computing limited number of off-diagonal elements. Furthermore, because reservoirs are limited in extent, the region of interest is usually smaller than the full image space; therefore, the Hessian can be explicitly computed for that region. The Hessian for each image point within this target region  $\mathbf{x}_T$  is then given by (Valenciano, 2008)

$$H(\mathbf{x}_T, \mathbf{x}_{T+a_x}) = \sum_w \omega^4 \sum_{\mathbf{x}_s} |f(s)|^2 G(\mathbf{x}_s, \mathbf{x}_T, \omega) \bar{G}(\mathbf{x}_s, \mathbf{x}_{T+a_x}, \omega) \sum_{\mathbf{x}_r} G(\mathbf{x}_T, \mathbf{x}_r, \omega) \bar{G}(\mathbf{x}_{T+a_x}, \mathbf{x}_r, \omega), \quad (3.10)$$

where  $\mathbf{x}_{T+a_x}$  represent neighboring image points. For any image point,  $\mathbf{H}(\mathbf{x}_T, \mathbf{x}_{T+a_x})$  represents a row of a sparse Hessian matrix  $\mathbf{H}$  whose non-zero components are defined by  $\mathbf{a}_x$ . The term  $\mathbf{a}_x$ , which includes all significant off-diagonal elements relative to the Hessian diagonal, represents the offset of points within a point spread function (PSF) around each image point. By approximating the Hessian in equation 3.4 with equation 3.10, the cost savings is given by

$$\left( \frac{N_{\mathbf{x}_T} \times N_{\mathbf{a}_x}}{N_{\mathbf{x}} \times N_{\mathbf{x}}} \right) = \left( \frac{n_{x_T} n_{y_T} n_{z_T}}{n_x n_y n_z} \right) \times \left( \frac{n_{a_x} n_{a_y} n_{a_z}}{n_x n_y n_z} \right), \quad (3.11)$$

where,  $N_{\mathbf{x}_T} = n_{x_T} n_{y_T} n_{z_T}$  is the number of samples in the target-area,  $N_{\mathbf{a}_x} = n_{a_x} n_{a_y} n_{a_z}$  is the number of off-diagonal elements, and  $N_{\mathbf{x}} = n_x n_y n_z$  is the number of elements in

the full model space. Valenciano (2008) discusses in detail the target-oriented Hessian and computational savings for different acquisition geometries.

Although the target-oriented Hessian (equation 3.10) is several orders of magnitudes cheaper than the full Hessian (equation 3.4), for a typical field seismic data set, explicit computation can be expensive and impractical. Tang (2011) show that by using phase-encoding methods, the target-oriented Hessian can be computed efficiently at orders of magnitude more cheaply than explicit implementation of equation 3.4. Where applicable, I randomly encode the receiver-side Green's functions, for which the target-oriented Hessian is given by

$$\begin{aligned} \tilde{H}(\mathbf{x}_T, \mathbf{x}_{T+a_x}) &= \sum_{\mathbf{z}_r} \sum_w \omega^4 \sum_{\mathbf{x}_s} |f(s)|^2 G(\mathbf{x}_s, \mathbf{x}_T, \omega) \bar{G}(\mathbf{x}_s, \mathbf{x}_{T+a_x}, \omega) \\ &\quad \times R(\mathbf{x}_T, \mathbf{x}_s, \mathbf{z}_r, \omega) \bar{R}(\mathbf{x}_{T+a_x}, \mathbf{x}_s, \mathbf{z}_r, \omega), \end{aligned} \quad (3.12)$$

where  $R(\mathbf{x}_T, \mathbf{x}_s, \mathbf{z}_r, \omega)$  denotes a random realization  $\mathbf{z}_r$  of the receiver wavefield for shot  $\mathbf{x}_s$ . When summed over several random realizations, equation 3.12 is approximately equivalent to equation 3.10. Each random realization of the receiver wavefield is defined as (Tang, 2011)

$$R(\mathbf{x}_T, \mathbf{x}_s, \mathbf{z}_r, \omega) = \sum_{\mathbf{x}_r} W(\mathbf{x}_r, \mathbf{x}_s) G(\mathbf{x}_r, \mathbf{x}, \omega) \alpha(\mathbf{x}_r, \mathbf{z}_r, \omega), \quad (3.13)$$

where  $W(\mathbf{x}_r, \mathbf{x}_s)$  is a geometry mask, and  $\alpha(\mathbf{x}_r, \mathbf{z}_r, \omega)$  is a random phase-encoding function. Tang (2011) provides detailed derivation of equation 3.12 and discussions on the associated cost savings.

## TIME-LAPSE SEISMIC IMAGING BY LEAST-SQUARES INVERSION

In time-lapse seismic imaging, several data sets acquired at different times over an evolving reservoir must be imaged such that only those image differences that reflect acoustic property changes due to production (or injection) are preserved.

Conventionally, a time-lapse image is computed as the difference between a baseline image  $\tilde{\mathbf{m}}_0$  and a monitor image  $\tilde{\mathbf{m}}_i$  obtained via migration:

$$\Delta\tilde{\mathbf{m}}_{0i} = \mathbf{L}_i^T \mathbf{d}_i - \mathbf{L}_0^T \mathbf{d}_0 = \tilde{\mathbf{m}}_i - \tilde{\mathbf{m}}_0, \quad (3.14)$$

where  $\Delta\tilde{\mathbf{m}}_{0i}$  is the migrated time-lapse image between baseline (survey 0) and monitor (survey  $i$ ). A time-lapse image computed this way has several undesirable artifacts that contaminate the time-lapse amplitudes of interest. As I discussed in chapter 2, in many cases, such artifacts can be attenuated by cross-equalization methods.

Instead of computing the time-lapse image as a difference between migrated images  $\tilde{\mathbf{m}}_i$ , we can compute it as a difference between inverted images  $\hat{\mathbf{m}}_i$ . In the data domain, the cost function defined for each individual experiment  $i$  can be minimized as follows:

$$S(\hat{\mathbf{m}}_i) = \|\mathbf{L}_i \mathbf{m}_i - \mathbf{d}_i^{obs}\|_2 \approx 0, \quad (3.15)$$

which in the image domain is equivalent to solving the system of equations given by

$$\mathbf{H}_i \hat{\mathbf{m}}_i \approx \tilde{\mathbf{m}}_i. \quad (3.16)$$

The inverted time-lapse image  $\Delta\hat{\mathbf{m}}_{0i}$  is then given by

$$\Delta\hat{\mathbf{m}}_{0i} = \hat{\mathbf{m}}_i - \hat{\mathbf{m}}_0. \quad (3.17)$$

As noted earlier, computing the time-lapse image  $\Delta\hat{\mathbf{m}}_{0i}$  from images obtained by solving equation 3.15 or equation 3.16 is called separate inversion. Separate inversion only allows us to introduce spatial constraints in the inversion.

For each survey, the spatially-regularized data domain inversion involves minimizing the cost function:

$$S(\hat{\mathbf{m}}_i) = \|\mathbf{L}_i \mathbf{m}_i - \mathbf{d}_i^{obs}\|_2 + \|\epsilon_i \mathbf{A}_i \mathbf{m}_i\|_2 \approx 0, \quad (3.18)$$

where  $\mathbf{A}_i$  is a spatial regularization operator and  $\epsilon_i$  is the spatial regularization parameter, which determines the relative weighting between image-fitting and spatial constraints. The equivalent regularized image-domain inversion requires a solution to the following system of equations:

$$\left[ \mathbf{H}_i + \epsilon_i^2 \mathbf{A}_i^T \mathbf{A}_i \right] \hat{\mathbf{m}}_i \approx \tilde{\mathbf{m}}_i, \quad (3.19)$$

or simply

$$\left[ \mathbf{H}_i + \mathring{\mathbf{A}}_i \right] \hat{\mathbf{m}}_i \approx \tilde{\mathbf{m}}_i, \quad (3.20)$$

where  $\mathring{\mathbf{A}}_i = \epsilon_i^2 \mathbf{A}_i^T \mathbf{A}_i$ . Because the operators defined on the right-hand-side of equation 3.20 may not be positive-definite, to solve the image-domain problem with a conjugate-gradients algorithm, we can solve a new least-squares fitting problem

$$\|\mathbf{H}_i \hat{\mathbf{m}}_i - \tilde{\mathbf{m}}_i\|_2 + \|\epsilon \mathbf{A}_i \hat{\mathbf{m}}_i\|_2 \approx 0. \quad (3.21)$$

Although solving equation 3.21 instead of equation 3.20 squares the condition number of the image-fitting problem, it ensures stable convergence.

As I show in chapter 4, although spatial regularization in linearized inversion improves the structural imaging of seismic data sets, it provides only limited improvements to time-lapse images. In the next section, I discuss the formulation of time-lapse seismic imaging as joint least-squares problems, which allow introduction of both spatial and temporal constraints into the inversion.

## Joint least-squares inversion

For simplicity, in this section, I assume that there are two data sets (baseline  $\mathbf{d}_0$  and monitor  $\mathbf{d}_1$ ) acquired at different times. Below, I describe two methods of computing time-lapse images by joint inversion, namely: joint inversion for image differences, and joint inversion of multiple images.

### Joint inversion for image differences (JID)

I formulate the joint modeling of the two data sets as follows:

$$\begin{bmatrix} \mathbf{L}_0 & \mathbf{0} \\ \mathbf{L}_1 & \mathbf{L}_1 \end{bmatrix} \begin{bmatrix} \mathbf{m}_0 \\ \Delta \mathbf{m} \end{bmatrix} = \begin{bmatrix} \mathbf{d}_0 \\ \mathbf{d}_1 \end{bmatrix}, \quad (3.22)$$

which can be divided into the following two parts:

$$\mathbf{L}_0 \mathbf{m}_0 = \mathbf{d}_0, \quad (3.23)$$

$$\mathbf{L}_1 \mathbf{m}_0 + \mathbf{L}_1 \Delta \mathbf{m} = \mathbf{d}_1, \quad (3.24)$$

which are the modeling equations for the baseline survey (equation 3.23) and for the monitoring survey (equation 3.24). The time-lapse reflectivity image  $\Delta \mathbf{m}$  is given by

$$\Delta \mathbf{m} = \mathbf{m}_1 - \mathbf{m}_0. \quad (3.25)$$

### Kinematic corrections for geomechanical changes

An inherent assumption in equation 3.22 is that both  $\mathbf{m}_0$  and  $\mathbf{m}_1$  are collocated. This suggests that there are no physical movements of the reflector between the baseline and the monitor surveys. In addition, equation 3.22 assumes that there are no overburden velocity changes. In reality, stress changes associated with production (or injection) can cause physical movement of a subsurface point from baseline position  $\mathbf{x}_0(x_0, y_0, z_0)$  in  $\mathbf{m}_0$  to monitor position  $\mathbf{x}_1(x_1, y_1, z_1)$  in  $\mathbf{m}_1$ .

First, let us assume that the correct migration velocities for the baseline and monitor data sets are available. If there are stress-induced physical movements of subsurface points, equation 3.24 can be updated such that during modeling, a point at position  $\mathbf{x}_0$  in  $\mathbf{m}_0$  is repositioned/warped to position  $\mathbf{x}_1$ . An important assumption here—and in time-lapse imaging in general—is that residual errors introduced by this kinematic image correction are of smaller magnitudes than the reflectivity change of

interest. The updated monitor data modeling (equation 3.24) then becomes

$$\mathbf{L}_1 \mathbf{S}^{m^-} \mathbf{m}_0 + \mathbf{L}_1 (\mathbf{m}_1 - \mathbf{S}^{m^-} \mathbf{m}_0) = \mathbf{L}_1 \mathbf{S}^{m^-} \mathbf{m}_0 + \mathbf{L}_1 \Delta \mathbf{m}^m = \mathbf{d}_1, \quad (3.26)$$

where  $\mathbf{S}^{m^-}$  is an orthogonal warping operator that aligns  $\mathbf{m}_0$  to  $\mathbf{m}_1$ , and

$$\Delta \mathbf{m}^m = \mathbf{m}_1 - \mathbf{S}^{m^-} \mathbf{m}_0 \quad (3.27)$$

is the time-lapse image estimated at the monitor position  $\mathbf{x}_1$ . Therefore, I re-write the baseline and monitor data modeling defined in equation 3.22 as follows:

$$\begin{bmatrix} \mathbf{L}_0 & \mathbf{0} \\ \mathbf{L}_1 \mathbf{S}^{m^-} & \mathbf{L}_1 \end{bmatrix} \begin{bmatrix} \mathbf{m}_0 \\ \Delta \mathbf{m}^m \end{bmatrix} \approx \begin{bmatrix} \mathbf{d}_0 \\ \mathbf{d}_1 \end{bmatrix}. \quad (3.28)$$

Note in equation 3.28 that to define the warping operator  $\mathbf{S}^{m^-}$ , the true monitor reflector position must be known. This information can be obtained from a geomechanical model, or since I have so far assumed that the monitor data are imaged with the true monitor velocity, from misalignments between migrated baseline and monitor images. Where there are neither velocity change nor stress-induced compaction between surveys,  $\mathbf{S}^{m^-}$  becomes an identity operator. Furthermore, note that equation 3.28, requires that any regularization on the time-lapse image must be applied at the monitor position, or by first repositioning the time-lapse image to the baseline position as follows:

$$\Delta \mathbf{m} = \Delta \mathbf{m}^b = \mathbf{S}^{m^+} \Delta \mathbf{m}^m, \quad (3.29)$$

where  $\Delta \mathbf{m}^b$  is the time-lapse image at the baseline position, and  $\mathbf{S}^{m^+} \approx (\mathbf{S}^{m^-})^{-1}$  is an operator that repositions events from the monitor position to the baseline position.

In the data domain, the inverted baseline image  $\mathbf{m}_0$  and time-lapse image  $\Delta \mathbf{m}$  can be obtained by minimizing the cost function  $r_d$ :

$$\left\| \begin{bmatrix} \mathbf{L}_0 & \mathbf{0} \\ \mathbf{L}_1 \mathbf{S}^{m^-} & \mathbf{L}_1 \end{bmatrix} \begin{bmatrix} \mathbf{m}_0 \\ \Delta \mathbf{m}^m \end{bmatrix} - \begin{bmatrix} \mathbf{d}_0 \\ \mathbf{d}_1 \end{bmatrix} \right\|^2 = r_d \approx 0. \quad (3.30)$$

In the image domain,  $\hat{\mathbf{m}}_0$  and  $\Delta\hat{\mathbf{m}}^m$  can be obtained by solving the system

$$\begin{bmatrix} \mathbf{L}_0^T \mathbf{L}_0 + \mathbf{S}^{m+} \mathbf{L}_1^T \mathbf{L}_1 \mathbf{S}^{m-} & \mathbf{S}^{m+} \mathbf{L}_1^T \mathbf{L}_1 \\ \mathbf{L}_1^T \mathbf{L}_1 \mathbf{S}^{m-} & \mathbf{L}_1^T \mathbf{L}_1 \end{bmatrix} \begin{bmatrix} \hat{\mathbf{m}}_0 \\ \Delta\hat{\mathbf{m}}^m \end{bmatrix} \approx \begin{bmatrix} \mathbf{L}_0^T & \mathbf{S}^{m+} \mathbf{L}_1^T \\ \mathbf{0} & \mathbf{L}_1^T \end{bmatrix} \begin{bmatrix} \mathbf{d}_0 \\ \mathbf{d}_1 \end{bmatrix}, \quad (3.31)$$

or simply

$$\begin{bmatrix} \mathbf{H}_0 + \mathbf{S}^{m+} \mathbf{H}_1 \mathbf{S}^{m-} & \mathbf{S}^{m+} \mathbf{H}_1 \\ \mathbf{H}_1 \mathbf{S}^{m-} & \mathbf{H}_1 \end{bmatrix} \begin{bmatrix} \hat{\mathbf{m}}_0 \\ \Delta\hat{\mathbf{m}}^m \end{bmatrix} \approx \begin{bmatrix} \tilde{\mathbf{m}}_0 + \mathbf{S}^{m+} \tilde{\mathbf{m}}_1 \\ \tilde{\mathbf{m}}_1 \end{bmatrix}. \quad (3.32)$$

Again, note in equation 3.32 that the time-lapse image obtained is  $\Delta\hat{\mathbf{m}}^m$  at the monitor position and not  $\Delta\hat{\mathbf{m}} = \Delta\hat{\mathbf{m}}^b$  at the baseline position. As shown later in this section, this formulation can be re-written in terms of  $\Delta\hat{\mathbf{m}}^b$ .

Now, let us consider the case where the monitor data are imaged with the baseline velocity. In this scenario, equation 3.31 then becomes

$$\begin{bmatrix} \mathbf{L}_0^T \mathbf{L}_0 + \mathbf{S}^{\alpha+} \check{\mathbf{L}}_1^T \mathbf{L}_1 \mathbf{S}^{m-} & \mathbf{S}^{\alpha+} \check{\mathbf{L}}_1^T \mathbf{L}_1 \\ \check{\mathbf{L}}_1^T \mathbf{L}_1 \mathbf{S}^{m-} & \check{\mathbf{L}}_1^T \mathbf{L}_1 \end{bmatrix} \begin{bmatrix} \hat{\mathbf{m}}_0 \\ \Delta\hat{\mathbf{m}}^m \end{bmatrix} \approx \begin{bmatrix} \mathbf{L}_0^T & \mathbf{S}^{\alpha+} \check{\mathbf{L}}_1^T \\ \mathbf{0} & \check{\mathbf{L}}_1^T \end{bmatrix} \begin{bmatrix} \mathbf{d}_0 \\ \mathbf{d}_1 \end{bmatrix}, \quad (3.33)$$

where  $\check{\mathbf{L}}_1^T$ , the migration operator with the monitor geometry but with baseline velocity, images the monitor data to apparent position  $\mathbf{x}'_1(x'_1, y'_1, z'_1)$ . The operator  $\mathbf{S}^{\alpha+}$  repositions the migrated image from  $\mathbf{x}'_1$  to  $\mathbf{x}_0$ .

Because the operator  $\mathbf{L}_1$  is a function of the true monitor velocity, if the true monitor velocity is known, we should solve equation 3.32 instead of equation 3.33. Where the monitor migration velocity is the correct one, equation 3.32 and equation 3.33 are equivalent. In most cases, the baseline velocity is a good approximation to the monitor velocity, resulting in only small kinematic errors in the monitor image. Where the change in velocity between surveys is large, kinematic corrections with a warping operator may be insufficient. In such scenario, it may be necessary to take into account such changes in computation of the monitor Hessian. One way to do this is by using the apparent displacements between the baseline and monitor images to update the Green's functions in the monitor Hessian. However, for the examples

considered in this thesis, I assume that kinematic errors introduced by imaging the monitor data with the baseline velocity are small enough that kinematic corrections with a warping operator are sufficient.

### Inverting for the time-lapse image at the baseline position

If the monitor data are imaged with the correct velocity, to directly invert for  $\Delta\hat{\mathbf{m}}^b = \Delta\hat{\mathbf{m}}$  at the baseline position, I make the substitution

$$\Delta\mathbf{m}^m = \mathbf{S}^{m-} \Delta\mathbf{m} \quad (3.34)$$

into equation 3.30 to obtain

$$\begin{bmatrix} \mathbf{L}_0 & \mathbf{0} \\ \mathbf{L}_1\mathbf{S}^{m-} & \mathbf{L}_1\mathbf{S}^{m-} \end{bmatrix} \begin{bmatrix} \mathbf{m}_0 \\ \Delta\mathbf{m} \end{bmatrix} \approx \begin{bmatrix} \mathbf{d}_0 \\ \mathbf{d}_1 \end{bmatrix}. \quad (3.35)$$

Therefore, in the data domain,  $\hat{\mathbf{m}}_0$  and  $\Delta\hat{\mathbf{m}}$  can be obtained by minimizing the objective function:

$$\left\| \begin{bmatrix} \mathbf{L}_0 & \mathbf{0} \\ \mathbf{L}_1\mathbf{S}^{m-} & \mathbf{L}_1\mathbf{S}^{m-} \end{bmatrix} \begin{bmatrix} \hat{\mathbf{m}}_0 \\ \Delta\hat{\mathbf{m}} \end{bmatrix} - \begin{bmatrix} \mathbf{d}_0 \\ \mathbf{d}_1 \end{bmatrix} \right\|^2 = r_d \approx 0, \quad (3.36)$$

which leads to the image-domain formulation

$$\begin{bmatrix} \mathbf{H}_0 + \mathbf{S}^{m+}\mathbf{H}_1\mathbf{S}^{m-} & \mathbf{S}^{m+}\mathbf{H}_1\mathbf{S}^{m-} \\ \mathbf{S}^{m+}\mathbf{H}_1\mathbf{S}^{m-} & \mathbf{S}^{m+}\mathbf{H}_1\mathbf{S}^{m-} \end{bmatrix} \begin{bmatrix} \hat{\mathbf{m}}_0 \\ \Delta\hat{\mathbf{m}} \end{bmatrix} \approx \begin{bmatrix} \tilde{\mathbf{m}}_0 + \mathbf{S}^{m+}\tilde{\mathbf{m}}_1 \\ \mathbf{S}^{m+}\tilde{\mathbf{m}}_1 \end{bmatrix} = \begin{bmatrix} \tilde{\mathbf{m}}_0 + \tilde{\mathbf{m}}_1^b \\ \tilde{\mathbf{m}}_1^b \end{bmatrix}, \quad (3.37)$$

where  $\tilde{\mathbf{m}}_1^b$ , the migrated monitor image repositioned to the baseline position  $\mathbf{x}_0$ , is defined as

$$\tilde{\mathbf{m}}_1^b = \mathbf{S}^{m+}\tilde{\mathbf{m}}_1. \quad (3.38)$$

If the monitor data are imaged with the baseline velocity, provided velocity and stress-induced geomechanical changes are small, equation 3.37 can be approximated

as follows:

$$\begin{bmatrix} \mathbf{H}_0 + \mathbf{S}^{\alpha+} \check{\mathbf{H}}_1 \mathbf{S}^{\alpha-} & \mathbf{S}^{\alpha+} \check{\mathbf{H}}_1 \mathbf{S}^{\alpha-} \\ \mathbf{S}^{\alpha+} \check{\mathbf{H}}_1 \mathbf{S}^{\alpha-} & \mathbf{S}^{\alpha+} \check{\mathbf{H}}_1 \mathbf{S}^{\alpha-} \end{bmatrix} \begin{bmatrix} \hat{\mathbf{m}}_0 \\ \Delta \hat{\mathbf{m}} \end{bmatrix} \approx \begin{bmatrix} \tilde{\mathbf{m}}_0 + \mathbf{S}^{\alpha+} \tilde{\mathbf{m}}_1^a \\ \mathbf{S}^{\alpha+} \tilde{\mathbf{m}}_1^a \end{bmatrix} = \begin{bmatrix} \tilde{\mathbf{m}}_0 + \tilde{\mathbf{m}}_1^b \\ \tilde{\mathbf{m}}_1^b \end{bmatrix}, \quad (3.39)$$

where,

$$\mathbf{S}^{\alpha+} \tilde{\mathbf{m}}_1^a \approx \tilde{\mathbf{m}}_1^b = \mathbf{S}^{m+} \tilde{\mathbf{m}}_1, \quad (3.40)$$

and  $\tilde{\mathbf{m}}_1^a$  is the monitor image at position  $\mathbf{x}'$  obtained by migrating the monitor data by the baseline velocity.

As previously stated, to arrive at equation 3.40, I assume that the amplitude errors that are caused by imaging the monitor data with the baseline velocity are negligible compared to the amplitude differences that are caused by production-induced changes in acoustic properties of the reservoir. Furthermore, as shown in Appendix A, provided our assumption of small kinematic errors holds, the migrated monitor image can be approximated as follows:

$$(\mathbf{L}_1^b)^T \mathbf{L}_1^b \mathbf{m}_1^b \approx \mathbf{S}^{m+} \mathbf{L}_1^T \mathbf{L}_1 \mathbf{S}^{m-} \mathbf{m}_1^b \approx \mathbf{S}^{m+} \mathbf{L}_1^T \mathbf{d}_1 \approx \mathbf{S}^{\alpha+} \tilde{\mathbf{m}}_1^a \approx \tilde{\mathbf{m}}_1^b, \quad (3.41)$$

where,  $(\mathbf{L}_1^b)^T \mathbf{L}_1^b = \mathbf{H}_1^b$  is the Hessian computed using the baseline velocity but with the monitor geometry. Substituting these into equation 3.37, I arrive at the the JID formulation:

$$\begin{bmatrix} \mathbf{H}_0 + \mathbf{H}_1^b & \mathbf{H}_1^b \\ \mathbf{H}_1^b & \mathbf{H}_1^b \end{bmatrix} \begin{bmatrix} \hat{\mathbf{m}}_0 \\ \Delta \hat{\mathbf{m}} \end{bmatrix} \approx \begin{bmatrix} \tilde{\mathbf{m}}_0 + \tilde{\mathbf{m}}_1^b \\ \tilde{\mathbf{m}}_1^b \end{bmatrix}. \quad (3.42)$$

Because the formulation in equation 3.42 enables corrections for kinematic errors in the migrated images, it does not require application of a warping operator at every iteration. In addition, an important feature of this formulation is that it allows for direct regularization of the time-lapse image. However, it may be desirable to invert directly for the individual seismic images. In the next section, I show how this can be accomplished.

### Joint inversion of multiple images (JMI)

Instead of formulating the baseline and monitor data modeling in terms of a static baseline image and a time-lapse image (equation 3.22), I formulate it here in terms of the individual reflectivity images:

$$\begin{bmatrix} \mathbf{L}_0 & \mathbf{0} \\ \mathbf{0} & \mathbf{L}_1 \end{bmatrix} \begin{bmatrix} \mathbf{m}_0 \\ \mathbf{m}_1 \end{bmatrix} = \begin{bmatrix} \mathbf{d}_0 \\ \mathbf{d}_1 \end{bmatrix}. \quad (3.43)$$

Using the same procedure as in the previous section, if the monitor data are imaged with the correct velocity, we can invert jointly for the individual images in data domain by minimizing the following objective function:

$$\left\| \begin{bmatrix} \mathbf{L}_0 & \mathbf{0} \\ \mathbf{0} & \mathbf{L}_1 \end{bmatrix} \begin{bmatrix} \mathbf{m}_0 \\ \mathbf{m}_1 \end{bmatrix} - \begin{bmatrix} \mathbf{d}_0 \\ \mathbf{d}_1 \end{bmatrix} \right\|^2 = r_d \approx 0, \quad (3.44)$$

and in the image domain by solving the system:

$$\begin{bmatrix} \mathbf{H}_0 & \mathbf{0} \\ \mathbf{0} & \mathbf{H}_1 \end{bmatrix} \begin{bmatrix} \hat{\mathbf{m}}_0 \\ \hat{\mathbf{m}}_1 \end{bmatrix} \approx \begin{bmatrix} \tilde{\mathbf{m}}_0 \\ \tilde{\mathbf{m}}_1 \end{bmatrix}. \quad (3.45)$$

As in the previous section, to invert for all images collocated at the baseline position, equations 3.44 and 3.45 become

$$\left\| \begin{bmatrix} \mathbf{L}_0 & \mathbf{0} \\ \mathbf{0} & \mathbf{L}_1 \mathbf{S}^{m-} \end{bmatrix} \begin{bmatrix} \mathbf{m}_0 \\ \hat{\mathbf{m}}_1^b \end{bmatrix} - \begin{bmatrix} \mathbf{d}_0 \\ \mathbf{d}_1 \end{bmatrix} \right\|^2 = r_d \approx 0, \quad (3.46)$$

and

$$\begin{bmatrix} \mathbf{H}_0 & \mathbf{0} \\ \mathbf{0} & \mathbf{S}^{m+} \mathbf{H}_1 \mathbf{S}^{m-} \end{bmatrix} \begin{bmatrix} \hat{\mathbf{m}}_0 \\ \hat{\mathbf{m}}_1^b \end{bmatrix} \approx \begin{bmatrix} \tilde{\mathbf{m}}_0 \\ \tilde{\mathbf{m}}_1^b \end{bmatrix}, \quad (3.47)$$

respectively. As previously stated, where there are no stress-induced compaction or velocity changes,  $\mathbf{S}^{m+}$  is an identity matrix. These JMI formulations are equivalent to the JID formulations presented in equations 3.36 and 3.37, respectively.

If the monitor data are imaged with the baseline velocity, using the same assumptions and procedure as in the previous section, equation 3.47 becomes

$$\begin{bmatrix} \mathbf{H}_0 & \mathbf{0} \\ \mathbf{0} & \mathbf{H}_1^b \end{bmatrix} \begin{bmatrix} \hat{\mathbf{m}}_0 \\ \hat{\mathbf{m}}_1^b \end{bmatrix} \approx \begin{bmatrix} \tilde{\mathbf{m}}_0 \\ \tilde{\mathbf{m}}_1^b \end{bmatrix}. \quad (3.48)$$

## Inverting multiple data sets

As shown in Appendix B, both the JID and JMI formulations are directly extendable to any number of data sets. In the data domain, the JID formulation for  $n$  surveys requires minimization of the cost function

$$S(\hat{\mathbf{m}}_0, \Delta\hat{\mathbf{m}}_1, \dots, \Delta\hat{\mathbf{m}}_n) = \|\mathbf{L}_0\mathbf{m}_0 - \mathbf{d}_0\|^2 + \sum_{i=1}^n \left\| \left( \mathbf{L}_j\mathbf{m}_0^m + \sum_{j=1}^i \mathbf{L}_j\Delta\mathbf{m}_j^m \right) - \mathbf{d}_i \right\|^2, \quad (3.49)$$

where,  $\Delta\mathbf{m}_j^m = \mathbf{m}_j^m - \mathbf{m}_{j-1}^m$  is the time-lapse image between survey  $j$  and survey  $j - 1$ , and,  $\mathbf{m}_j^m$  is defined at the monitor  $j$  position. The JMI formulation requires a minimization of the objective function

$$S(\hat{\mathbf{m}}_0, \dots, \hat{\mathbf{m}}_n) = \sum_{i=0}^n \|\mathbf{L}_i\mathbf{m}_i - \mathbf{d}_i\|^2. \quad (3.50)$$

In Appendix B, I develop the equivalent image domain formulations for equations 3.49 and 3.50.

## REGULARIZED JOINT INVERSION

The JID and JMI formulations described in the previous section allows us to regularize the time-lapse imaging problem in different ways. Neglecting numerical errors, without regularization, results from both methods are similar. As previously stated, an important advantage of joint (versus separate) inversion is that it allows incorporation of both spatial and temporal regularization in the inversion.

For the generalized JID case (equation 3.49), assuming all data are imaged with the correct velocity, spatio-temporally regularized inversion involves minimization of the objective function

$$\begin{aligned}
S(\hat{\mathbf{m}}_0, \Delta\hat{\mathbf{m}}_1, \dots, \Delta\hat{\mathbf{m}}_n) = & \|\mathbf{L}_0\mathbf{m}_0 - \mathbf{d}_0\|^2 + \sum_{i=1}^n \left\| \left( \mathbf{L}_j\mathbf{m}_0^m + \sum_{j=1}^i \mathbf{L}_j\Delta\mathbf{m}_j^m \right) - \mathbf{d}_i \right\|^2 \\
& + \|\epsilon_0\mathbf{A}_0\mathbf{m}_0\|^2 + \sum_{j=1}^n \|\epsilon_j\mathbf{A}_j\Delta\mathbf{m}_j^m\|^2 \\
& \sum_{j=1}^n \left\| -\zeta_{j-1}\mathbf{\Lambda}_{j-1}\Delta\mathbf{m}_{j-1}^m + \zeta_j\mathbf{\Lambda}_j\Delta\mathbf{m}_j^m \right\|^2,
\end{aligned} \tag{3.51}$$

where  $\mathbf{\Lambda}_j$  is the temporal coupling operator, and  $\zeta_j$  is the temporal regularization parameter. The other terms are as previously defined.

For the generalized JMI case (equation 3.49), spatio-temporally regularized inversion involves minimization of the objective function

$$S(\mathbf{m}_0, \dots, \mathbf{m}_n) = \sum_{i=0}^n \|\mathbf{L}_i\mathbf{m}_i - \mathbf{d}_i\|^2 + \sum_{i=0}^n \|\epsilon_i\mathbf{A}_i\mathbf{m}_i\|^2 + \sum_{i=1}^n \|\zeta_i\mathbf{\Lambda}_i(\mathbf{m}_{i-1}, \mathbf{m}_i)\|^2, \tag{3.52}$$

where the parameters  $\epsilon_i$  and  $\zeta_i$  determine the strengths of the spatial and temporal regularization operators,  $\mathbf{A}$  and  $\mathbf{\Lambda}$  respectively. Equation 3.52 is similar to the method applied by Ajo-Franklin et al. (2005) to a spatio-temporally regularized ray-tomography problem. Throughout the rest of this dissertation, I refer to solving equation 3.51 as regularized joint inversion for image differences (RJID), and solving equation 3.52 as regularized joint inversion of multiple images (RJMI).

Although both formulations provide reliable results, the RJMI formulation is preferable. Importantly, solving the joint inversion problem using the RJMI formulation is cheaper. For example, in the data domain, the JMI formulation requires fewer modeling and migration calls per iteration, and, in the image domain, it requires fewer matrix-vector multiplications. In the next section, I discuss different ways of incorporating spatial and temporal constraints in the the RJMI formulation.

## Regularized joint inversion of multiple images (RJMI)

For simplicity, I consider two data sets. In the RJMI formulation, because models are completely decoupled, different spatial regularizations (second term in equation 3.52) can be defined for the two images as follows:

$$\left\| \left[ \begin{array}{cc} \epsilon_0 \mathbf{A}_0 & \mathbf{0} \\ \mathbf{0} & \epsilon_1 \mathbf{A}_1 \end{array} \right] \left[ \begin{array}{c} \hat{\mathbf{m}}_0 \\ \hat{\mathbf{m}}_1 \end{array} \right] \right\|^2 \approx 0 . \quad (3.53)$$

and the temporal coupling (third term in equation 3.52) is given by

$$\left\| \left[ \begin{array}{cc} -\zeta_0 \mathbf{\Lambda}_0 & \zeta_1 \mathbf{\Lambda}_1 \end{array} \right] \left[ \begin{array}{c} \hat{\mathbf{m}}_0 \\ \hat{\mathbf{m}}_1 \end{array} \right] \right\|^2 \approx 0 . \quad (3.54)$$

Therefore, in the data domain, the full spatio-temporally regularized inversion requires a minimization of the norm:

$$\left\| \left[ \begin{array}{cc} \mathbf{L}_0 & \mathbf{0} \\ \mathbf{0} & \mathbf{L}_1 \\ \hline \epsilon_0 \mathbf{A}_0 & \mathbf{0} \\ \mathbf{0} & \epsilon_1 \mathbf{A}_1 \\ \hline -\zeta_0 \mathbf{\Lambda}_0 & \zeta_1 \mathbf{\Lambda}_1 \end{array} \right] \left[ \begin{array}{c} \hat{\mathbf{m}}_0 \\ \hat{\mathbf{m}}_1 \end{array} \right] - \left[ \begin{array}{c} \mathbf{d}_0 \\ \mathbf{d}_1 \\ \mathbf{0} \\ \mathbf{0} \\ \mathbf{0} \end{array} \right] \right\|^2 \approx 0 , \quad (3.55)$$

which is equivalent to solving the image domain problem

$$\left( \left[ \begin{array}{cc} \mathbf{H}_0 & \mathbf{0} \\ \mathbf{0} & \mathbf{H}_1 \end{array} \right] + \left[ \begin{array}{cc} \mathbf{A}_{00} & \mathbf{0} \\ \mathbf{0} & \mathbf{A}_{11} \end{array} \right] + \left[ \begin{array}{cc} \mathbf{\Lambda}_{00} & -\mathbf{\Lambda}_{01} \\ -\mathbf{\Lambda}_{10} & \mathbf{\Lambda}_{11} \end{array} \right] \right) \left[ \begin{array}{c} \hat{\mathbf{m}}_0 \\ \hat{\mathbf{m}}_1 \end{array} \right] \approx \left[ \begin{array}{c} \tilde{\mathbf{m}}_0 \\ \tilde{\mathbf{m}}_1 \end{array} \right], \quad (3.56)$$

where  $\mathbf{A}_{ii} = \epsilon_i^2 \mathbf{A}_i^T \mathbf{A}_i$  and  $\mathbf{\Lambda}_{ij} = \zeta_i \mathbf{\Lambda}_i^T \zeta_j \mathbf{\Lambda}_j$  are the spatial and temporal constraints, respectively.

In this dissertation, to construct the spatial regularization operator  $\mathbf{A}_i$ , I first estimate dips on the baseline image. For this, I use the plane-wave destruction method

of Fomel (2002). Using the estimated dips, I then compute stable non-stationary dip-filters based on factorized directional Laplacians (Fomel et al., 2003; Hale, 2007). Figure 3.1 shows the impulse responses of the three-dimensional dip-filters derived from cascaded two-dimensional filters (Clapp, 2000, 2005; Tang, 2011) and by full 3D factorization. To construct the factorized three-dimensional directional Laplacians, I follow the approach of Fomel (2000). Figure 3.2 shows the filters derived from two different dip combinations and different ranges.

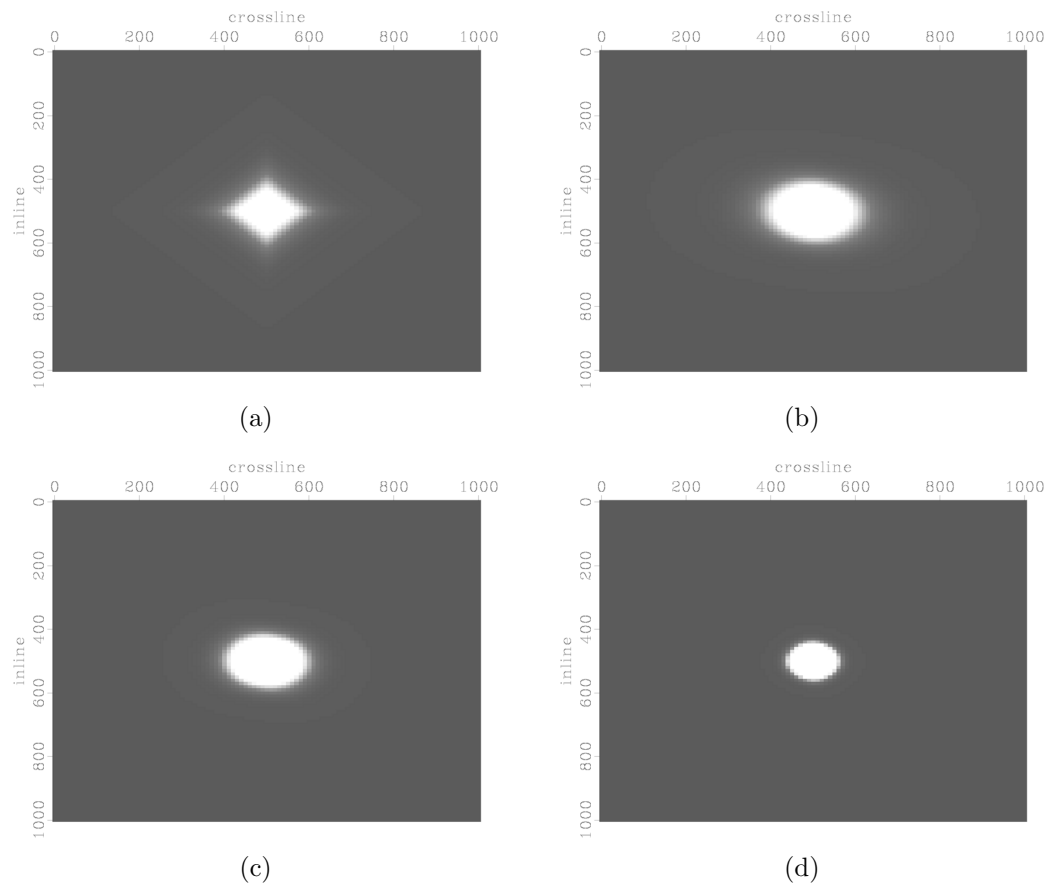
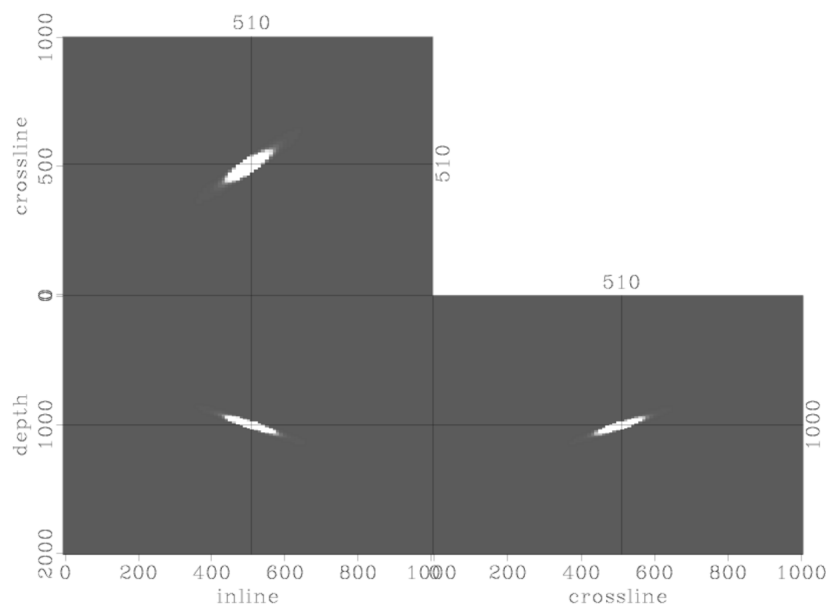
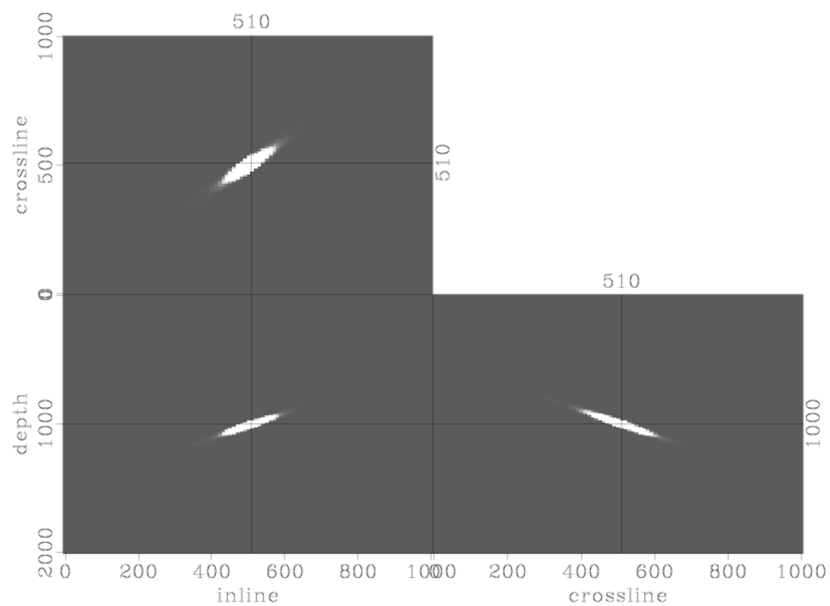


Figure 3.1: Two-dimensional slices through 3D impulse responses derived by cascaded two-dimensional filtering (a) and full 3D factorization (b)-(d). Note that the impulse responses derived from full factorization are more isotropic than the one derived from cascaded two-dimensional filtering. Furthermore, note that the filters in (b), (c), and (d) have large, medium and small ranges. [ER].

chap3/. imp-cascade,imp-0005,imp-005,imp-01



(a)



(b)

Figure 3.2: Impulse response for two different dip combinations derived from full factorization. The filter in (a) has a positive inline dip and negative crossline dip, whereas the filter in (b) has a negative inline dip and positive crossline dip. Furthermore, note that the filter in (a) has a smaller range than the filter in (b). [ER].

chap3/. imp-a,imp-b

In the RJMI formulation, these filters serve two important functions. First, they ensure smoothness along local dips that define the subsurface structure. In addition, by using variable filter ranges at different locations within and outside the reservoir, I limit the amount of temporal coupling and smoothness applied within and outside the reservoir region. This is important because it ensures that important time-lapse amplitude information within the reservoir is not destroyed by the regularization.

As I demonstrate in the next chapter, the choice of temporal regularization is also important. For example, if the images are collocated, it is straightforward to define a temporal constraint between the images. If the temporal regularization is a difference operator, equation 3.54 becomes

$$\left\| \zeta \begin{bmatrix} -\mathbf{I} & \mathbf{I} \end{bmatrix} \begin{bmatrix} \hat{\mathbf{m}}_0 \\ \hat{\mathbf{m}}_1 \end{bmatrix} \right\|^2 \approx 0 , \quad (3.57)$$

However, if the images are not collocated, in order to add any temporal regularization, the monitor image must first be warped to the baseline. For example, in the case where the temporal regularization is a difference operator, equation 3.54 becomes

$$\left\| \zeta \begin{bmatrix} -\mathbf{I} & \mathbf{S}^{m+} \end{bmatrix} \begin{bmatrix} \hat{\mathbf{m}}_0 \\ \hat{\mathbf{m}}_1 \end{bmatrix} \right\|^2 \approx 0 , \quad (3.58)$$

where, as previously defined, operator  $\mathbf{S}^{m+}$  warps the monitor image to the baseline. Where the temporal operator includes some weighting (e.g. according to the illumination, or reservoir position), then equation 3.58 becomes

$$\left\| \zeta \mathbf{Q} \begin{bmatrix} -\mathbf{I} & \mathbf{S}^{m+} \end{bmatrix} \begin{bmatrix} \hat{\mathbf{m}}_0 \\ \hat{\mathbf{m}}_1 \end{bmatrix} \right\|^2 \approx 0 , \quad (3.59)$$

where  $\mathbf{Q}$  defines the coupling characteristics according to predefined criteria. For example, regions with the poorest illumination may be assigned more larger weights than regions with high illumination. In addition, to preserve the time-lapse amplitude characteristics, regions outside the reservoir may be assigned a different coupling.

If the time-lapse image is to be computed at the baseline position, using the same procedure and assumptions as in the previous section, the regularized image-domain inversion problem is given by

$$\left( \begin{bmatrix} \mathbf{H}_0 & \mathbf{0} \\ \mathbf{0} & \mathbf{H}_1^b \end{bmatrix} + \begin{bmatrix} \mathbf{A}_{00} & \mathbf{0} \\ \mathbf{0} & \mathbf{A}_{11}^b \end{bmatrix} + \begin{bmatrix} \mathbf{\Lambda}_{00} & -\mathbf{\Lambda}_{01}^b \\ -\mathbf{\Lambda}_{10}^b & \mathbf{\Lambda}_{11}^b \end{bmatrix} \right) \begin{bmatrix} \hat{\mathbf{m}}_0 \\ \hat{\mathbf{m}}_1 \end{bmatrix} \approx \begin{bmatrix} \tilde{\mathbf{m}}_0 \\ \tilde{\mathbf{m}}_1 \end{bmatrix}, \quad (3.60)$$

where all operators and images are referenced to the baseline position. In Appendix B, I extend this formulation to an arbitrary number of surveys. In addition, I show how the formulation in equation 3.60 can be transformed into a preconditioned problem.

## CONCLUSIONS

Time-lapse imaging can be posed as a joint linear least-squares problem. In this chapter, I have developed different formulations for regularized inversion of time-lapse seismic data sets in both the data domain and in the image domain. These inversion methods are suitable under different scenarios.

In chapter 4, using two- and three-dimensional synthetic data sets, I show how data-domain and image-domain inversion can be applied to different time-lapse imaging problems. In chapter 5, using two-dimensional field data sets, I show how time-lapse data sets can be conditioned to satisfy the assumptions made in this chapter. In addition, I show how time-lapse amplitudes in images derived from complete and incomplete data can be improved. In chapter 6, I show applications of image-domain inversion to complete and incomplete full-azimuth ocean-bottom-cable data sets.

As noted in this chapter, an important advantage of image-domain inversion is that, because it can be solved in a target-oriented manner, it is computationally inexpensive. Therefore it can be repeated quickly using different regularization parameters. I show in later chapters that by choosing different regularization parameters, regularized image-domain inversion can be used to obtain different plausible time-lapse images.

Because of its flexibility and easy parameterization, in all regularized image-domain examples, I use the RJMI formulation.

## ACKNOWLEDGMENTS

In developing the methods in this chapter, I benefitted from previous work and collaborations with Alejandro Valenciano and Yaxun Tang.

# Chapter 4

## Synthetic examples

In chapter 3, I developed formulations for regularized data-domain and image-domain joint inversion of time-lapse data sets. In this chapter, I present applications of these methods to synthetic data sets. These carefully designed synthetic examples represent various time-lapse imaging problems where it is difficult to apply the conventional methods described in chapter 2.

This chapter is divided into two broad sections:

1. Data-domain inversion: Using a two-dimensional model derived from the Marmousi model (Bourgeois et al., 1991), I show that regularized joint data-domain inversion can be used for direct imaging of simultaneous-source time-lapse data sets. Because the migration operator does not account for cross-talk between different sources, and for geometry and timing differences between simultaneous-source data sets, it generates artifacts that contaminate the time-lapse amplitudes of interest. This example shows that regularized joint data-domain inversion can attenuate these artifacts, producing images that are similar in quality to those derived from conventional data sets. In this example, image-domain inversion is not applicable because the Hessian matrix of its least-squares objective function is far from being diagonal, and cannot be sufficiently approximated by its truncated form.

2. Image-domain inversion: Although image-domain inversion is not readily applicable to the example described above, it can be applied to several practical time-lapse imaging problems. As discussed in chapter 3, one advantage of image-domain inversion is that it can be easily solved in a target-oriented manner. In this section, I demonstrate that target-oriented regularized joint image-domain inversion can be used to correct for distortions and artifacts in time-lapse images caused by:

- *Poor and Irregular illumination due to complex overburden.* Using a two-dimensional sub-salt model modified from the SEAM model (Fehler and Larner, 2008), I show that, even for perfectly repeated geometries, the time-lapse image in reservoirs under complex overburden can be strongly distorted. I demonstrate that regularized joint inversion can correct for such distortions, thereby providing a more reliable time-lapse image.
- *Non-repeated geometries due to obstructions in monitor acquisition.* I present two examples that show how regularized joint inversion can be used to correct for acquisition differences between seismic surveys.
  - Using a two-dimensional model modified from the SEAM model (Fehler and Larner, 2008), I show how joint inversion can be used to correct for artifacts in time-lapse images caused by obstructions in the geometry of the monitoring survey.
  - Using a three-dimensional synthetic model derived by convolving Hessian matrices from three ocean-bottom-cable (OBC) field-data geometries (discussed in chapter 5) with carefully designed time-lapse reflectivity models. Furthermore, I demonstrate how different regularization parameters in the inversion affect the quality of time-lapse images. Because image-domain is relatively computationally inexpensive, it is possible to test different plausible regularization parameters in near real-time.

These synthetic examples show that regularized joint inversion provides better quality time-lapse images than conventional imaging by migration.

## DATA-DOMAIN INVERSION

In this section, I describe an application of data-domain inversion to synthesized *field-encoded* simultaneous-source data sets. First, I discuss the concept of acquiring seismic data with simultaneous sources and how this can be advantageous to time-lapse seismic imaging. I also discuss how acquiring data this way may lead to discrepancies that will contaminate production-related time-lapse amplitude signals. I then apply the data-domain inversion method developed in chapter 3 to synthesized simultaneous-source time-lapse data with non-repeated source geometries and non-repeated relative shot times.

### *Example I: Inversion of simultaneous-source time-lapse data*

Conventional seismic data acquisition involves a single seismic source and a recording array of receivers. Although it is not a new idea (Womack et al., 1990), recent advances in acquisition technology enable seismic acquisition with multiple sources (Hampson et al., 2008; Beasley, 2008). This acquisition approach, also called simultaneous shooting (or multi-shooting, or blended acquisition), can be used to achieve longer offsets, better shot-sampling, and improved time and cost efficiency (van Mastriigt et al., 2002; Berkhout et al., 2008; Howe et al., 2009). The recorded data can be separated into independent shot records and then imaged with conventional methods (Hampson et al., 2008; Spitz et al., 2008; Ikelle, 2009; Ayeni et al., 2011), or they can be imaged directly without separation (Berkhout et al., 2008; Tang and Biondi, 2009; Ayeni et al., 2009).

Although time-lapse seismic imaging is an established technology for monitoring hydrocarbon reservoirs, it still has several limitations. First, because of the high cost of conventional (single-source) acquisition, it is impractical to have short time intervals between surveys. Therefore, typical time-intervals between monitoring surveys may be too large to measure production-related, short-period variations in reservoir properties. Because of the large time intervals between conventional time-lapse seismic surveys, it may be difficult to match time-lapse seismic signatures to changes

in reservoir properties derived from temporally continuously-sampled sources (e.g., production data).

Secondly, in many time-lapse seismic applications, inaccuracies in the replication of acquisition geometries for different surveys (*geometry non-repeatability*) is a recurring problem. Although modern acquisition techniques can improve repeatability of shot-receiver geometries, field conditions usually prevent perfect repetition. As discussed in previous chapters, in order to correctly interpret differences in time-lapse seismic images that are caused by changes in reservoir properties, non-repeatability effects must be removed.

Thirdly, because of operational, climatic, and other limitations, the acquisition time-window may be too small for conventional seismic data acquisition. In such cases, it would be difficult to acquire conventional seismic data sets at desirable intervals.

Some limitations in current and conceptual time-lapse seismic applications can be overcome by simultaneous-source acquisition. First, acquiring time-lapse data sets with multiple seismic sources can reduce acquisition time and cost, making it possible to acquire more data sets at shorter time intervals. Sufficiently small survey intervals will enable *quasi-continuous* monitoring of changes in reservoir properties. Other methods for quasi-continuous monitoring have been suggested (Arogunmati and Harris, 2009). Secondly, the ability to account for differences in survey geometries during imaging makes repetition of survey geometries unnecessary. Furthermore, because of its high efficiency, simultaneous-source acquisition can be used for seasonal time-lapse seismic data acquisition in areas with short acquisition time-windows (Berkhout, 2008). Depending on operational limitations, an arbitrary number of seismic sources can be used for each survey.

There are two sources of discrepancies in time-lapse seismic data sets recorded with multiple sources, namely, geometry and shot-timing non-repeatabilities (Ayeni et al., 2009). As mentioned above, geometry non-repeatability is a result of differences in acquisition geometries for different surveys. Shot-timing non-repeatability between

different surveys is a result of mismatches in their relative shooting times. Neglecting survey geometry and shot-timing repeatability during acquisition ensures time and cost efficiency. However, if not accounted for, these two discrepancies will degrade the resulting time-lapse seismic images. Because conventional imaging and time-lapse processing methods are inadequate to account for such discrepancies, I apply the data-domain inversion method developed in the previous chapter (equation 3.52). Data-domain phase-encoded inversion removes discrepancies between different surveys and provides reliable estimates of the time-lapse amplitude changes. In addition, this method avoids the cost of separating the acquired data into individual records.

For this problem, the image-domain formulation is not applicable. This is because, as shown by Tang (2008), the Hessian matrix of the objective function of simultaneous-source data-fitting problem is far from being diagonal. Therefore, in this example, the truncated target-oriented Hessian (defined in equation 3.10) is a poor approximation of the full Hessian matrix. Because it is impractical to compute the full Hessian for any realistic imaging problem, a data-domain formulation is more appropriate in this example.

In the next section, I discuss linear phase-encoded modeling of simultaneous-source data sets.

## Linear phase-encoded modeling and simultaneous-shooting

From the linearized Born modeling equation in equation 3.1, the recorded data due to shots starting from  $s = q$  to  $s = p$  is given by

$$d(\mathbf{x}_{spq}, \mathbf{x}_r, \omega) = \sum_{s=p}^q a(\gamma_s) \omega^2 \sum_{\mathbf{x}} f_s(\omega) G(\mathbf{x}_s \mathbf{x}, \omega) G(\mathbf{x}, \mathbf{x}_r, \omega) m(\mathbf{x}), \quad (4.1)$$

where  $a(\gamma_s)$  is

$$a(\gamma_s) = e^{i\gamma_s} = e^{i\omega t_s}, \quad (4.2)$$

and  $\gamma_s$ , the time-delay function, depends on the delay time  $t_s$  at shot  $s$ .

For acquisition efficiency, it is unnecessary to repeat either the acquisition geometry or the relative shot timings for different surveys. By eliminating the cost associated with ensuring repeatability between surveys, the total acquisition cost can be reduced significantly. Because acquisition cost is usually several times higher than the processing cost, a reduction in acquisition cost will significantly reduce the total seismic monitoring cost. In addition, further cost reduction is achieved by imaging all the data sets directly.

Figure 4.1 shows examples of wavefields from two configurations of simultaneous-shooting. In both figures, the third dimension represents the survey time, while the orthogonal lines indicate positions of the displayed slices within the image cube.

## Regularized phase-encoded joint inversion

To perform regularized phase-encoded inversion, the data-domain RJMI formulation in equation 3.52 is modified as follows:

$$S(\mathbf{m}_0, \dots, \mathbf{m}_n) = \sum_{i=0}^n \left\| \tilde{\mathbf{L}}_i \mathbf{m}_i - \tilde{\mathbf{d}}_i \right\|^2 + \sum_{i=0}^n \|\epsilon_i \mathbf{A}_i \mathbf{m}_i\|^2 + \sum_{i=1}^n \|\zeta_i \mathbf{\Lambda}_i(\mathbf{m}_{i-1}, \mathbf{m}_i)\|^2, \quad (4.3)$$

where  $\tilde{\mathbf{d}}_i = \mathbf{B}_i \mathbf{L}_i \mathbf{m}_i$  is the recorded simultaneous-source data,  $\mathbf{B}$  is the encoding operator,  $\mathbf{m}$  is the earth reflectivity,  $\tilde{\mathbf{L}} = \mathbf{B}\mathbf{L}$  is the phase-encoded modeling operator in equation 4.2, and other terms are as defined in chapter 3.

The migrated image, computed by applying the adjoint operator  $\tilde{\mathbf{L}}^T$  to  $\tilde{\mathbf{d}}$ , will contain crosstalk artifacts generated by cross-correlation between incongruous source and receiver wavefields (Romero et al., 2000; Tang and Biondi, 2009). In addition, because of the associated geometry and relative shot-time non-repeatability, different surveys have unique crosstalk artifacts. As shown below, regularized phase-encoded joint inversion can attenuate these artifacts.

Because several shots are encoded and directly imaged, the computational cost of this approach is considerably reduced compared to the cost of inverting non-encoded

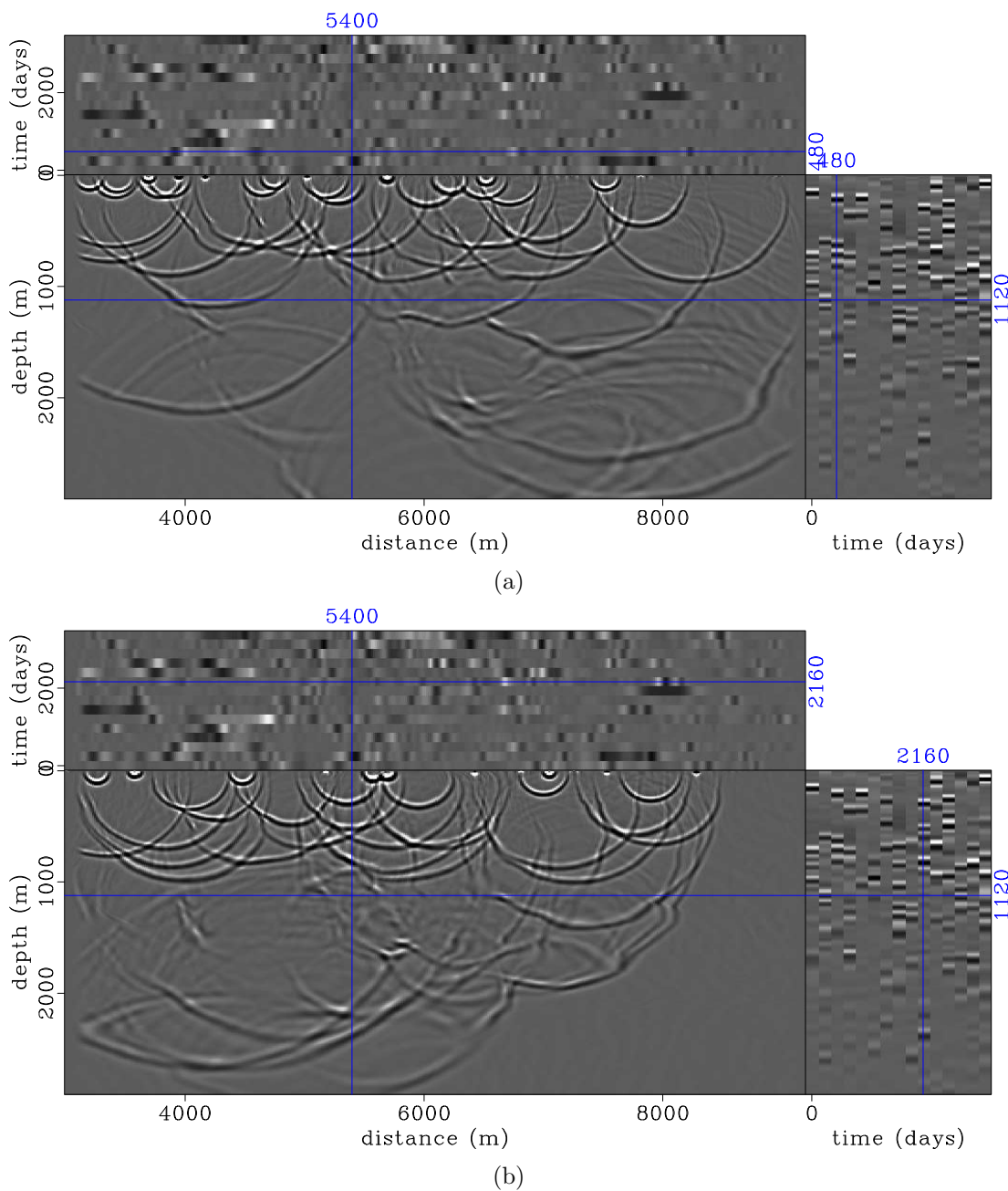


Figure 4.1: Wavefields from multiple randomized simultaneous sources (a), and from two continuously shooting seismic sources (b). In each figure, the blue line indicates intersecting positions of the the three slices that are displayed. In Panel (a), the geometry and relative shot-timing are different for all surveys, whereas in Panel (b), only the acquisition geometry differs between surveys. The third dimension denotes survey/recording time. [CR]. `chap4/. wave-dat0,wave-dat1`

data sets. Furthermore, because the data are already encoded in the field, and they are not separated prior to imaging, it is impossible to change the encoding function during iterative inversion. However, because the data sets are encoded differently, artifacts are incoherent between images.

## Example

Figure 4.2 shows a modified section of the Marmousi velocity model (Versteeg, 1994). I represent the production-related changes between surveys as changes in reflectivity within the reservoir (Figure 4.2). For simplicity, I assume that there are no geometrical changes in the overburden between the surveys. In addition, I assume that there are no changes in the background velocity.

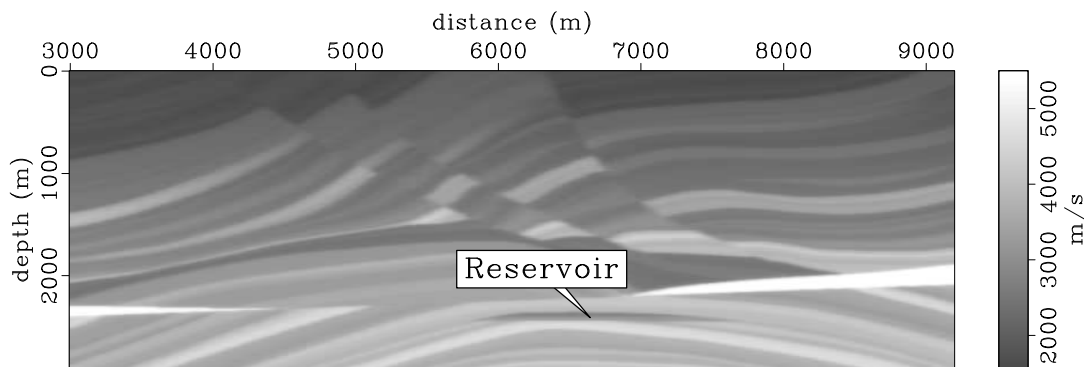


Figure 4.2: Baseline velocity model of the modified Marmousi model. The only changes between surveys are reflectivity changes within the reservoir. [CR].

chap4/. vel-0

Using these modified models, I simulate 15 simultaneous-source data sets, which represent different production stages (Figure 4.3). Each data set comprises 56 randomly encoded shot records with unique shot positions and unique relative shot-timings (Figure 4.4). The receiver spread, which covers the length of the model, is fixed for all data sets. I simulate these data using a phase-encoding one-way wave-equation operator.

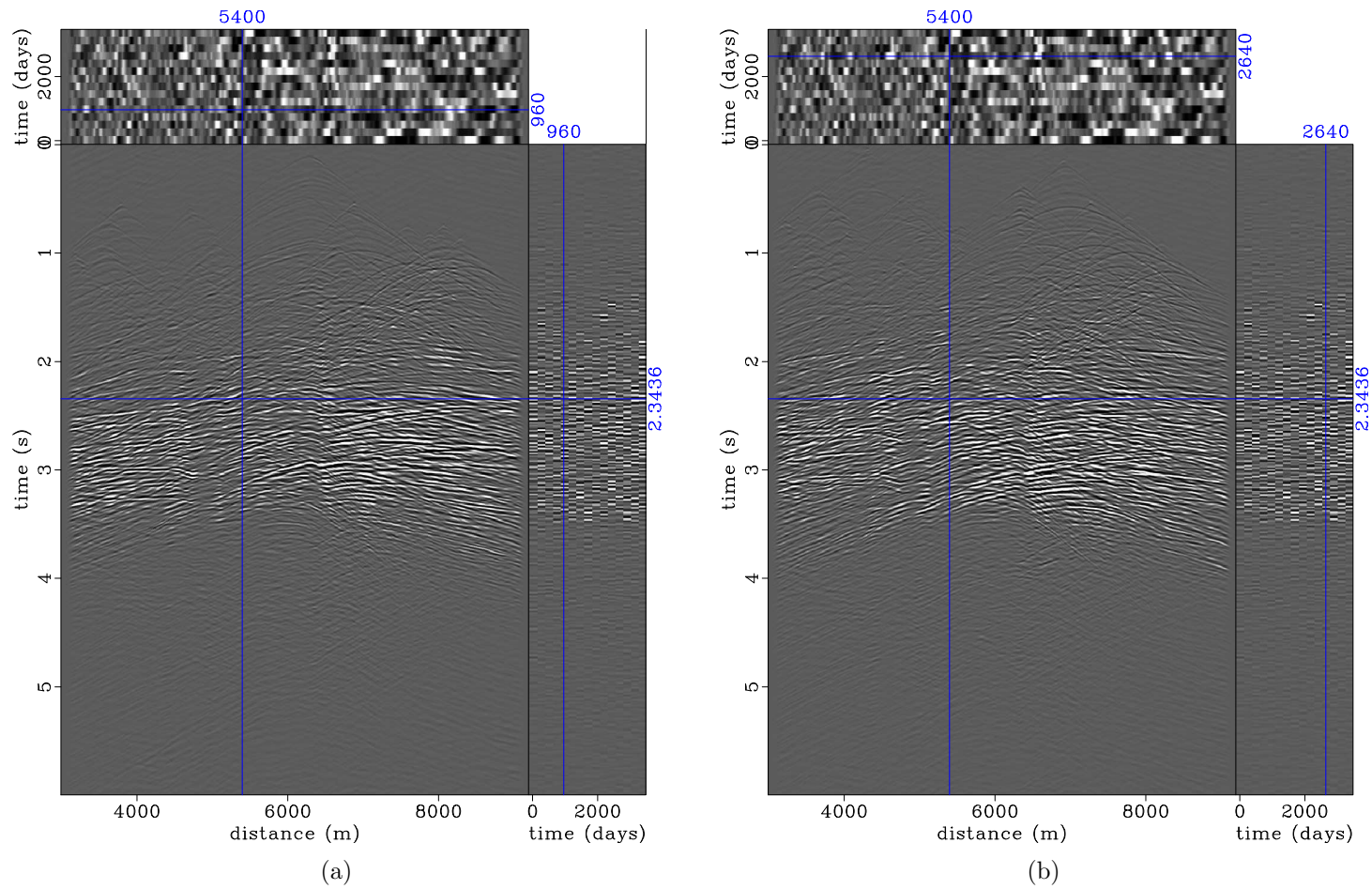


Figure 4.3: Synthetic data from multiple asynchronous sources. In (a) and (b), the front panels show the encoded data for two different surveys. In addition to varying the relative shot time, the source positions are also different for each survey (Figure 4.4). Note that, whereas the first dimension denote two-way travel time, the third dimension denotes survey/recording time. [CR]. `chap4/. tdat-10,tdat-11`

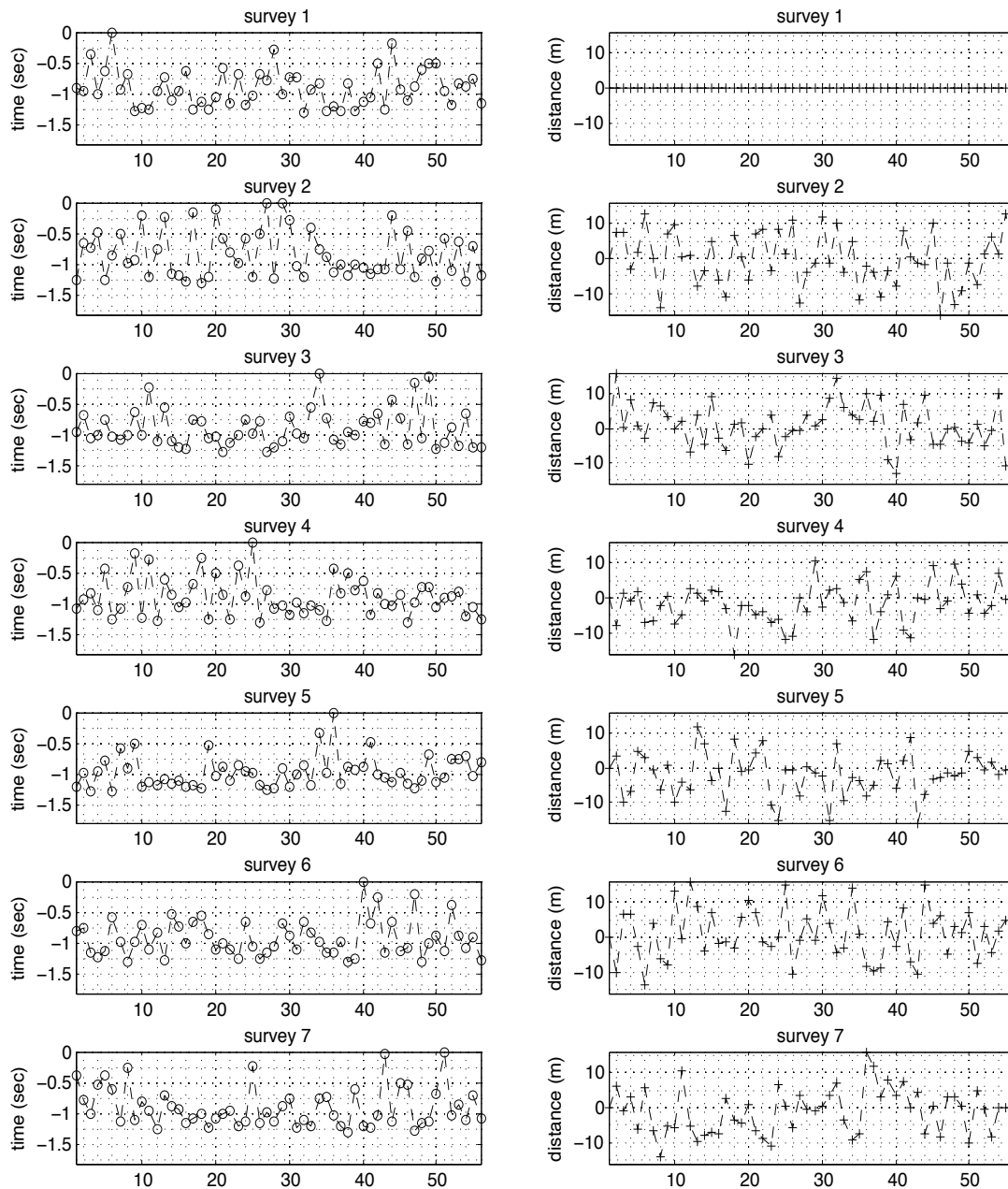


Figure 4.4: Plots of relative time-delays (left) and shot-displacements for seven out of the fifteen numerical models that were used to generate the data in Figure 4.3. In all plots, the horizontal axis indicates shot position. The relative shooting times are referenced to the earliest shot in each survey, whereas shot-displacements are referenced to the baseline shot positions. [CR]. `chap4/. source-time`

For comparison, using the same models, the same number of shots and receivers and assuming perfect repeatability, I also simulate 15 conventional single-source data sets. I image these data with the same algorithm as in the simultaneous-source case (described below), but without phase-encoding. Figure 4.5 shows the migrated images, and the corresponding time-lapse images, derived from these data.

Figure 4.6(a) shows the migrated images derived from the simultaneous-source data sets. The corresponding time-lapse images are presented in Figure 4.6(b). These results are obtained by direct imaging of the encoded data with a phase-encoded migration operator. As shown in Figure 4.6(a), compared to the reference images (Figure 4.5(a)), these migrated images—and as a consequence, the time-lapse images—are contaminated by strong non-repeatability and crosstalk artifacts. These contaminating artifacts make it difficult to relate the amplitudes in the time-lapse images (Figure 4.6(b)) to actual changes in properties within the reservoir.

Next, using the plane-wave destruction method (Fomel, 2002), I estimate the dip-field from the migrated baseline image (Figures 4.7). I assume that prior to the start of monitoring with simultaneous-source data, a reference baseline image derived from conventional (single-source) data is available. These dips are used to construct the spatial regularization operator that is used in the inversion.

In Figure 4.7, to preserve faults in image, I manually picked the faults in the migrated images and then estimate the dips along them. Furthermore, based on the locations of these faults, I define dip-contrast parameters, which depend on the distance of an image point from a fault location (Figure 4.8). To obtain these parameters, I smooth the manually picked faults with a triangular filter such that the largest values are close to the fault locations. Then, by changing the filter range at each image point according to these values, the faults are preserved during inversion. I change the filter range by modifying the spectral factorization weights (Fomel et al., 2003). In general, the filter strength reduces as its range increases, and vice versa.

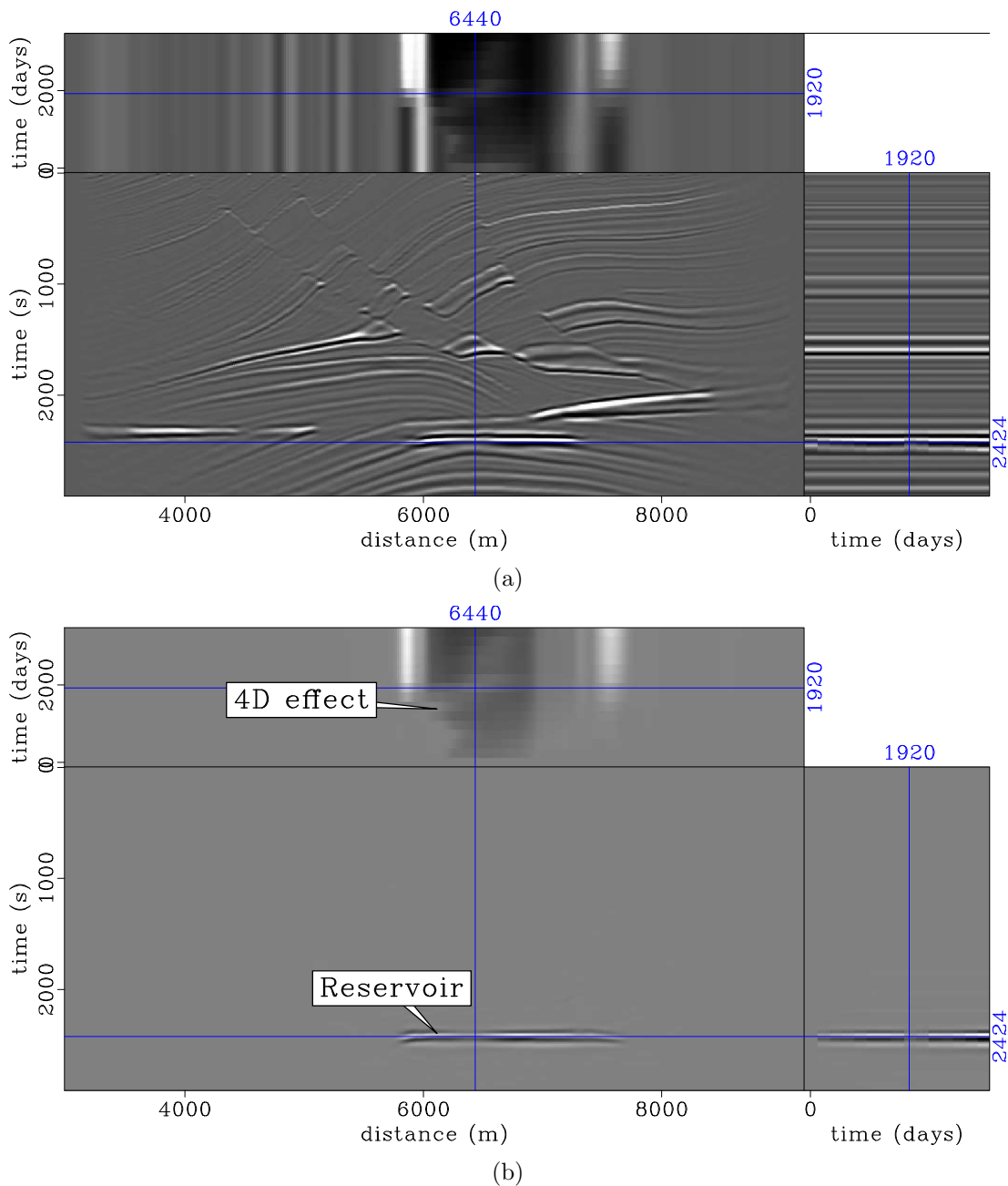


Figure 4.5: Migrated images (a) and corresponding time-lapse estimates (b) obtained from perfectly repeated conventional (single-source) data sets. In these (and in similar Figures), the side panel (third axis) shows the seismic properties (a) and time-lapse changes (b) at a fixed spatial position, whereas the top panel shows the spatial-temporal distribution seismic properties. [CR]. `chap4/. pnomig-0,pnomig4d-1`

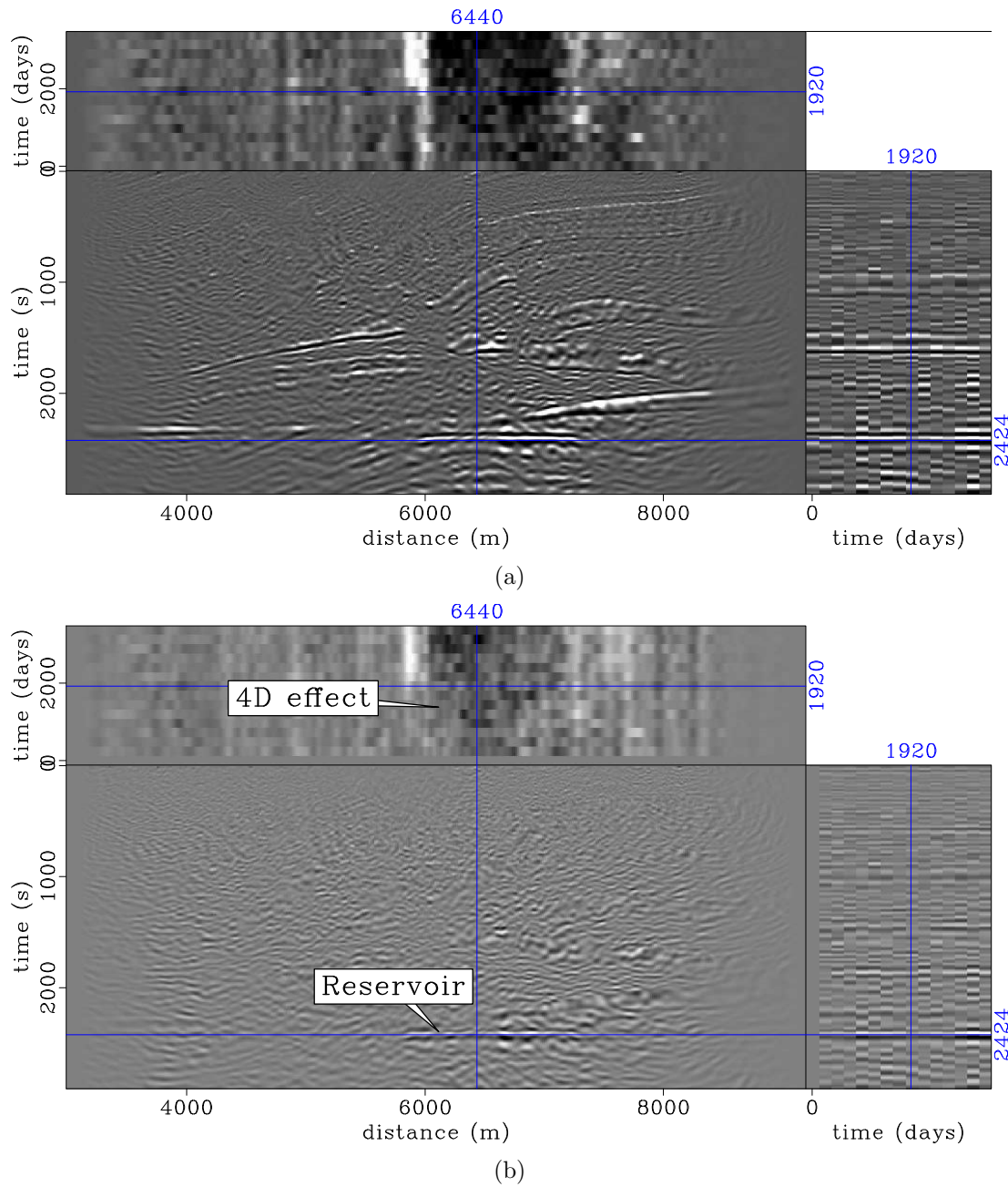


Figure 4.6: Images (a) and corresponding time-lapse estimates (b) obtained from migrating the data sets in Figure 4.3. In both Figures, note the numerous artifacts caused by geometry and shot-timing non-repeatability and crosstalk artifacts. Without attenuating these artifacts, it would be difficult to accurately interpret the time-lapse information. [CR]. chap4/. pmig-0,pmig4d-1

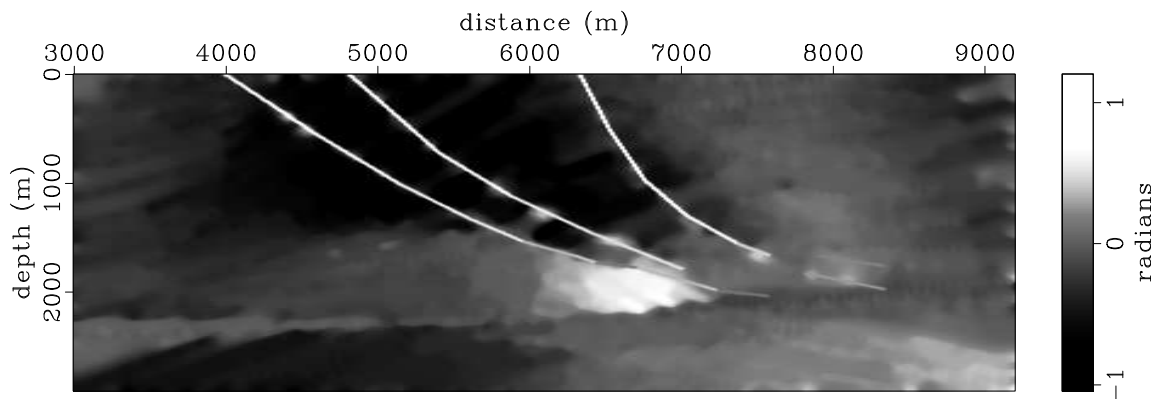


Figure 4.7: Dips derived from the migrated baseline image. These dips are used to construct the spatial regularization operator for the inversion. Note that the faults in the dip field are picked manually from the baseline image. [CR]. `chap4/. dip-0`

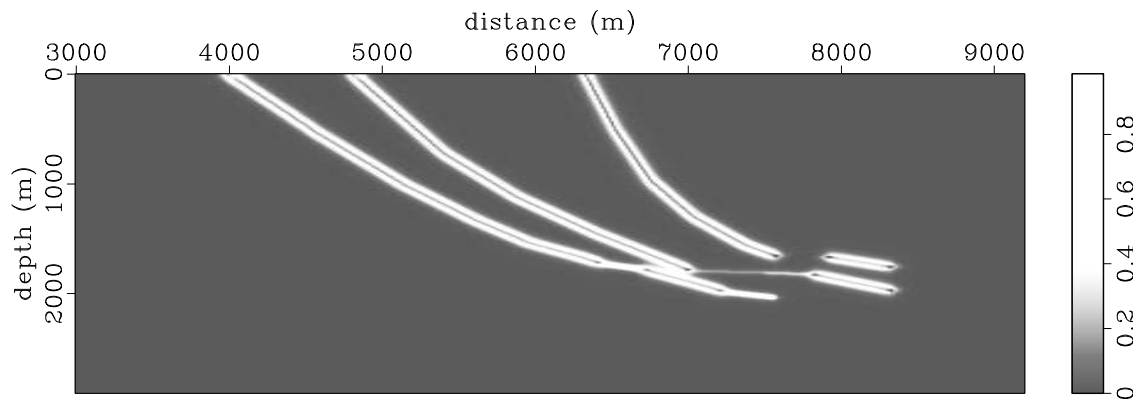


Figure 4.8: Dip-contrast computed based on how rapidly the dips change in the model. To obtain this image, the picked faults are smoothed to obtain variances based on the distance from the faults. By changing the filter range according to these variances, the faults are preserved during regularized inversion. [CR]. `chap4/. var-0`

I introduce temporal constraints into the inversion as a difference operator between the images. These constraints ensure coupling between the images during inversion, and helps with the attenuation of the incoherent crosstalk and non-repeatability artifacts between the images. In addition, temporal constraints ensure that the reflectivity changes smoothly between surveys.

Figure 4.9(a) shows the images derived from the simultaneous-source data sets by minimizing the global objective function defined in equation 4.3. These images are obtained after fifty-six conjugate gradients iterations. The corresponding time-lapse images are presented in Figure 4.9(b). A comparison of these time-lapse images with those derived from migration (Figure 4.6(b)) show that inversion has attenuated the contaminating crosstalk and non-repeatability artifacts. These time-lapse images are comparable in quality to those derived from migration of conventional data (Figure 4.5(b)). Finally, note that the inverted images in Figure 4.9 show significantly improved resolution over the migrated images derived from conventional data (Figure 4.5).

The time-lapse images derived after different numbers of iterations are presented in Figures 4.10 and 4.11. These images show how the contaminating cross-talk and non-repeatability artifacts in the time-lapse image are reduced as the number of iteration increases. For example, many of the artifacts that are present at early iterations (e.g., Figure 4.10(a)) have been attenuated after fifty iterations (e.g., Figure 4.11(b)). In this example, the cost of inverting the simultaneous data is the similar to the cost of migrating the conventional single-source data.

## **Discussion**

If the temporal spacing between seismic surveys is small, a near-continuous image of reservoir property change can be obtained (Figure 4.5). By using simultaneous sources, the acquisition cost of such seismic surveys can be reduced. Instead of being separated, the recorded data can be imaged directly with a phase-encoding operator. However, direct imaging causes crosstalk artifacts that degrade the quality of time-lapse images (Figure 4.6). Furthermore, artifacts caused by non-repeated acquisition geometries and relative shot-timings will degrade the quality of the time-lapse images (Figure 4.6(b)).

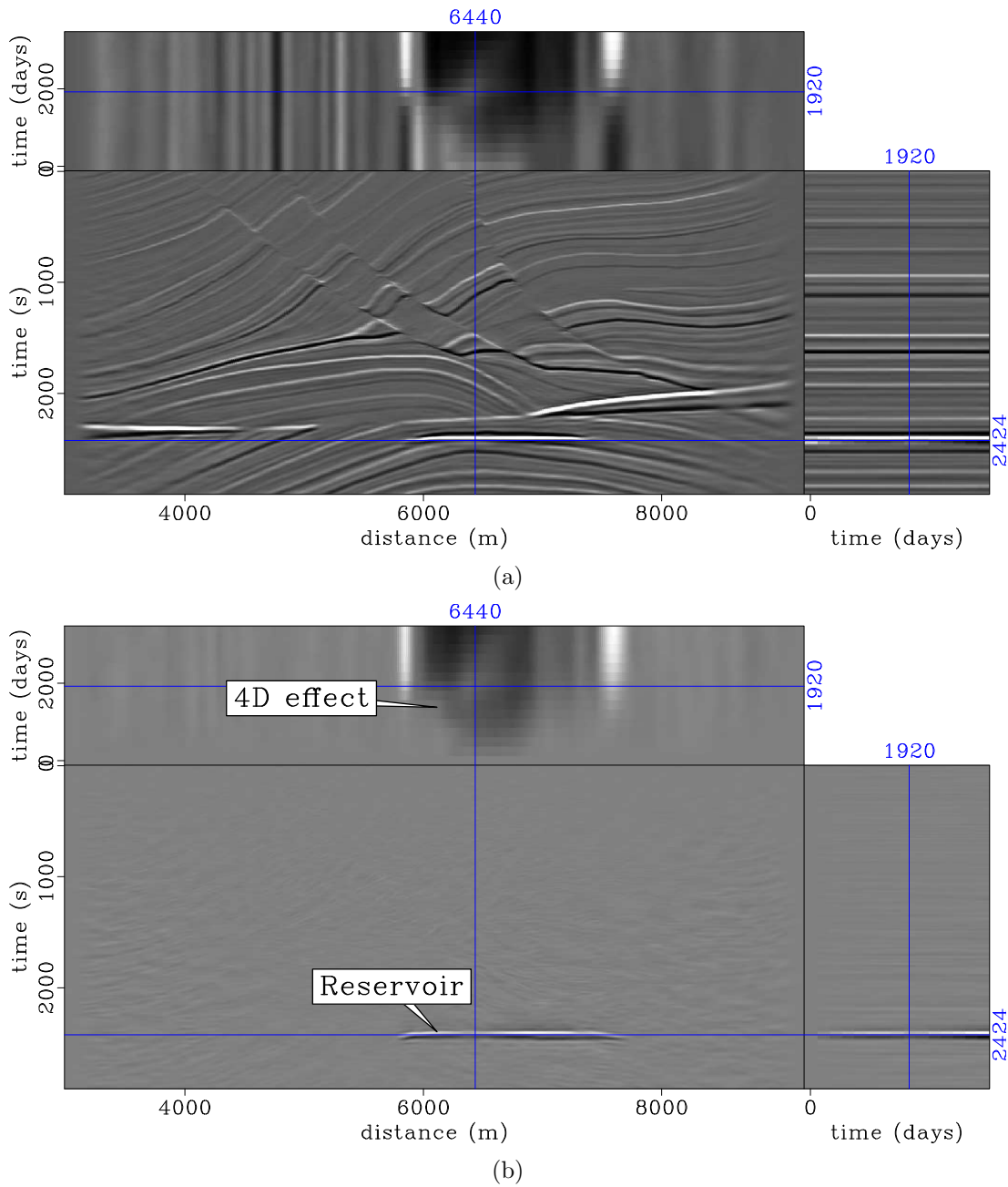


Figure 4.9: Images (a) and corresponding time-lapse estimates (b) obtained from inversion of the simultaneous-source data sets in Figure 4.3. These results are obtained after fifty-six conjugate gradients iterations. Note that the non-repeatability and crosstalk artifacts in the migrated images (Figure 4.6) have been attenuated by inversion. Also, note the improved resolution of the inverted images compared to the migrated single-source data (Figure 4.5). [CR]. `chap4/. pinv-0,pinv4d-1`

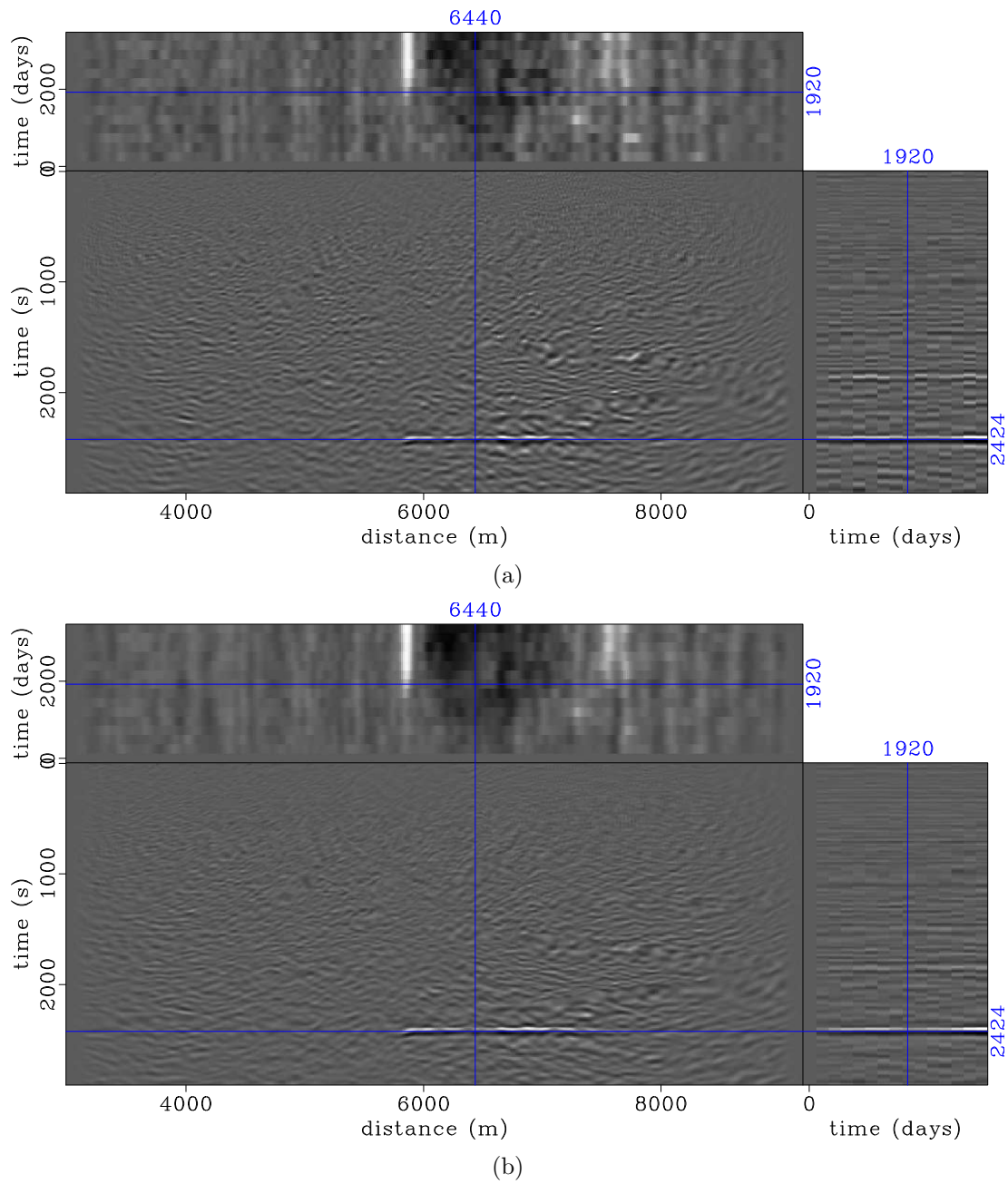


Figure 4.10: Time-lapse seismic images obtained after two and five conjugate gradient iterations (a) and (b), respectively. Note the gradual reduction in the artifacts compared to the time-lapse images from migration (Figure 4.6(b)). Furthermore, note that the artifacts have decreased in (b) compared to (a). [CR].

chap4/. pmmov4d-1,pmmov4d-2

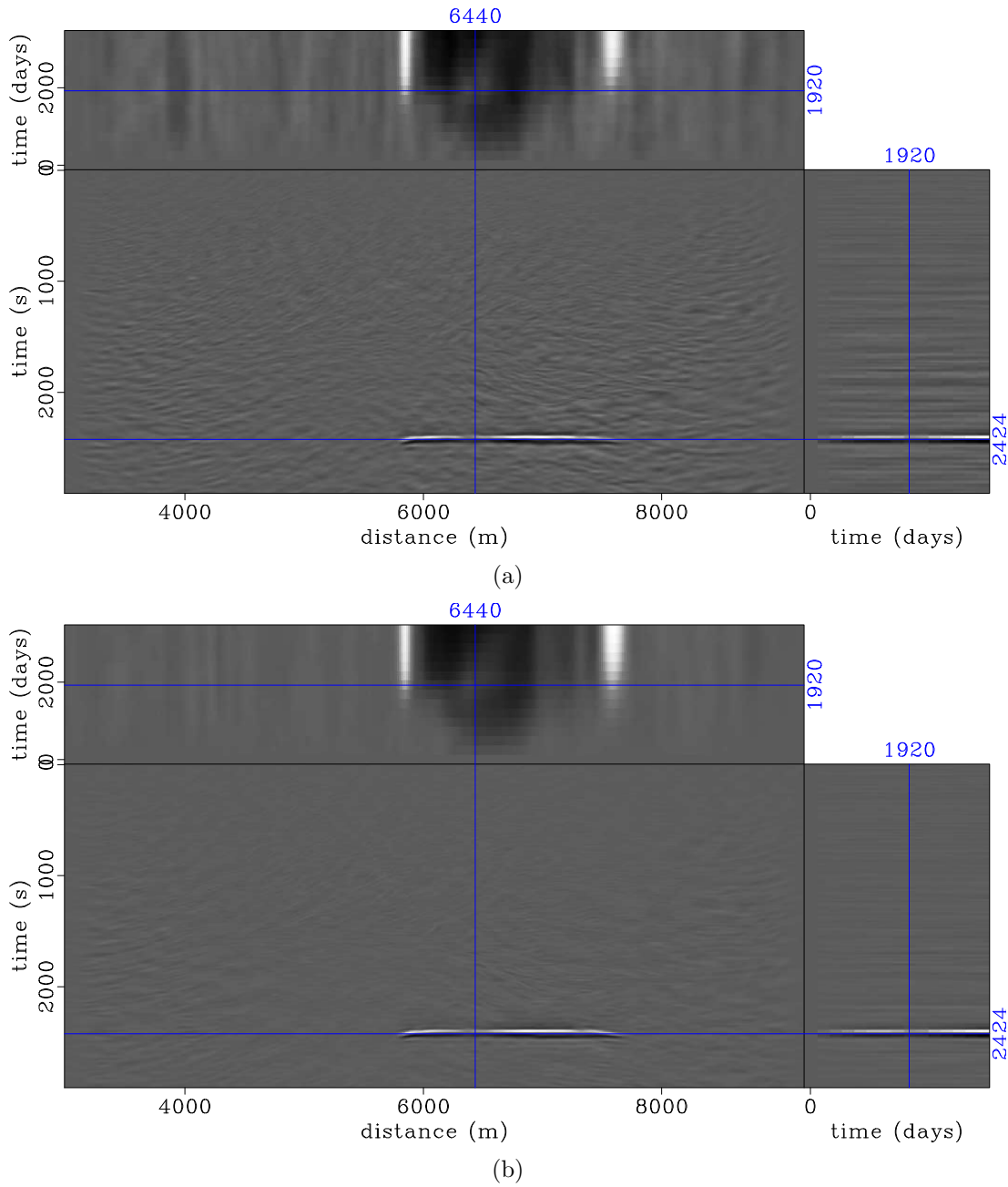


Figure 4.11: Time-lapse seismic images obtained after fifteen and fifty conjugate gradient iterations (a) and (b), respectively. Note the reduction in the artifacts compared to the time-lapse images from migration (Figure 4.6(b)). Furthermore, note that the artifacts have further decreased in (b) compared to (a) and compare to Figures 4.10(a) and 4.10(b). [CR]. `chap4/. pmmov4d-3,pmmov4d-4`

Time-lapse data sets acquired with simultaneous sources can be adequately imaged by regularized data-domain joint inversion without need for separation. Minimizing a single global objective function enables incorporation of both spatial and temporal constraints into the inversion. As shown in this example, this method attenuates both crosstalk and non-repeatability artifacts in *field-encoded* time-lapse data sets (Figure 4.9(a)). Therefore, it provides time-lapse images (Figure 4.9(b)), which are of comparable quality to those derived from perfectly repeated conventional *single-source* data sets (Figure 4.5(b)). Furthermore, images obtained from inversion of simultaneous-source data sets have higher resolution than those derived by migration of conventional single-source data sets (Figure 4.9 versus Figure 4.5). By carefully selecting both the spatial and temporal constraints, the contaminating artifacts in the time-lapse images are reduced as a function of iterations (Figures 4.10 and 4.11).

Although image-domain inversion is not easily applicable to this problem, it is more applicable than data-domain inversion to other time-lapse imaging problems. I present some of these applications in the next section.

## IMAGE-DOMAIN INVERSION

In this section, I present applications of regularized image-domain joint inversion to three synthetic examples—numbered *II* to *IV*. In example *II*, I invert for the time-lapse image below a complex salt body, correcting distortions due to complex (and irregular) illumination. Examples *III* and *IV* represent situations where surface facilities prevent data acquisition in parts of a field, thereby causing discrepancies in survey geometries. Example *III* is a two-dimensional application, while example *IV* is a three-dimensional application. Both examples show how obstruction artifacts can be attenuated by regularized joint inversion. In addition, example *IV* shows how different regularization parameters affect the quality of inverted time-lapse images. Because image-domain inversion is computationally inexpensive, an interpreter can repeat it in near real-time with various realistic constraints.

### *Example II: Inversion of sub-salt time-lapse data*

Using a single-scattering Born modeling operator, I generate two data sets over a two-dimensional sub-salt model (Figure 4.12). This model is sampled at 25 m along the horizontal axis and 10 m along the vertical axis. Each data set consists of 141 shots spaced at 50 m and 321 receivers spaced at 25 m. The maximum offset is 3000 m and the receiver spread is *rolled-along* for each shot. Apart from a change in seismic amplitudes within the reservoir, I use the same modeling parameters for both the baseline and the monitor data sets.

For reference, I also model two data sets recorded using the same geometry and the same change in reflectivity but with no salt in the overburden (Figure 4.13). In both this reference and the sub-salt models, I migrate the data sets with a shot-profile one-way wave-equation algorithm using 160 frequencies between 0.25 and 40 Hz.

The target area for inversion is indicated in both Figures 4.12 and 4.13. I compute the Hessian for the target area using 27 equally spaced frequencies within the frequency band of the data. Figure 4.14 shows the migrated monitor image, the time-lapse image, and the Hessian diagonal (subsurface illumination) for the reference, simple-overburden case (Figure 4.13). The corresponding images for the sub-salt model are presented in Figure 4.15. Note that, for the same geometry, compared to the subsurface illumination in the reference model (Figure 4.14(c)), the illumination under the complex salt body is highly irregular (Figure 4.15(c)).

The highly irregular illumination under the salt leads to inconsistent and distorted reflectivity estimates along the reservoir (Figure 4.15(a)). In addition, recall that in chapter 1, I show that because of the complex overburden, PSFs at the three closely spaced points ( $X$ ,  $Y$ , and  $Z$ ) along the reservoir in Figure 4.15(c) vary significantly in their spreading—and hence in the range of illuminated wavenumbers (Figure 1.9). Compared to the migrated time-lapse image in the simple overburden model (Figure 4.14(b)), note that the migrated time-lapse image obtained in the sub-salt model is strongly distorted (Figure 4.15(b)).

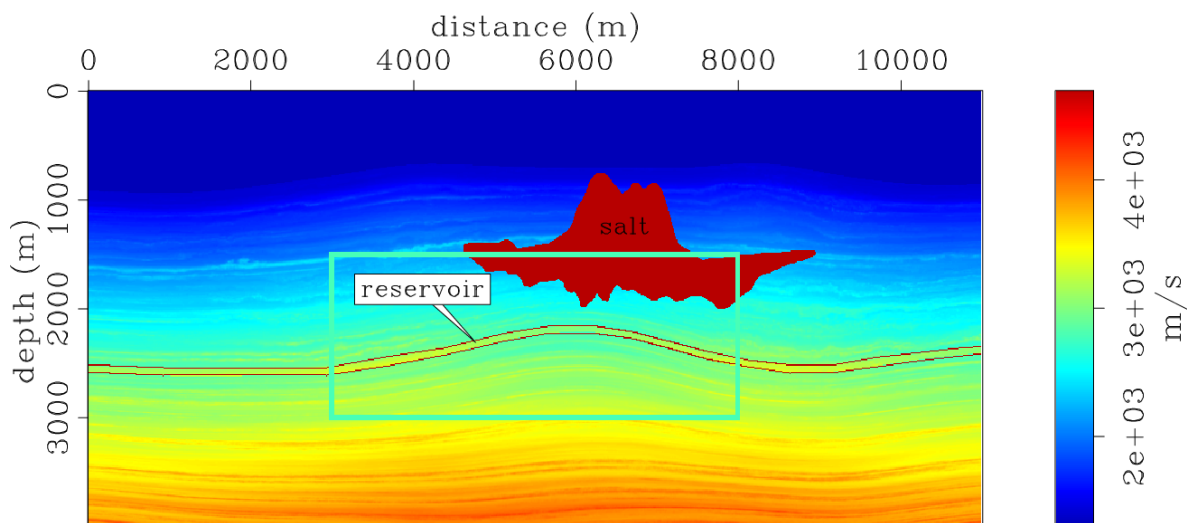


Figure 4.12: Numerical two-dimensional velocity model used in Example *II*. The box indicates the location of the target-area around the crest of the folded reservoir (top-and base indicated by the red horizon). [CR] chap4/. sm-vel-salt-3

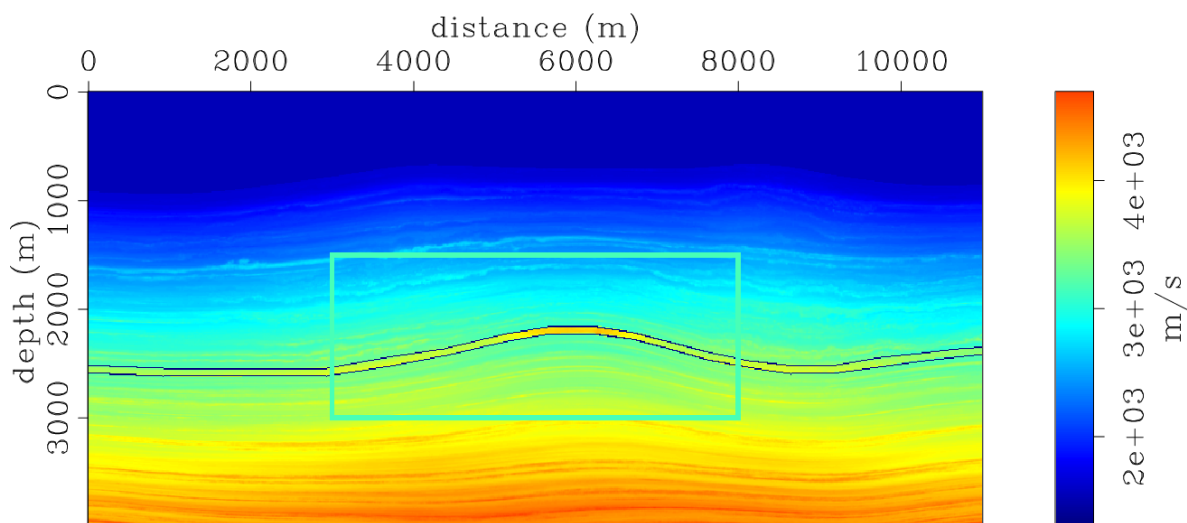


Figure 4.13: Numerical two-dimensional velocity model used to generate the reference images in Figure 4.14 and in Example *III*. The box indicates the location of the target-area around the crest of the folded reservoir (top-and base indicated by the red horizon). [CR] chap4/. sm-vel2

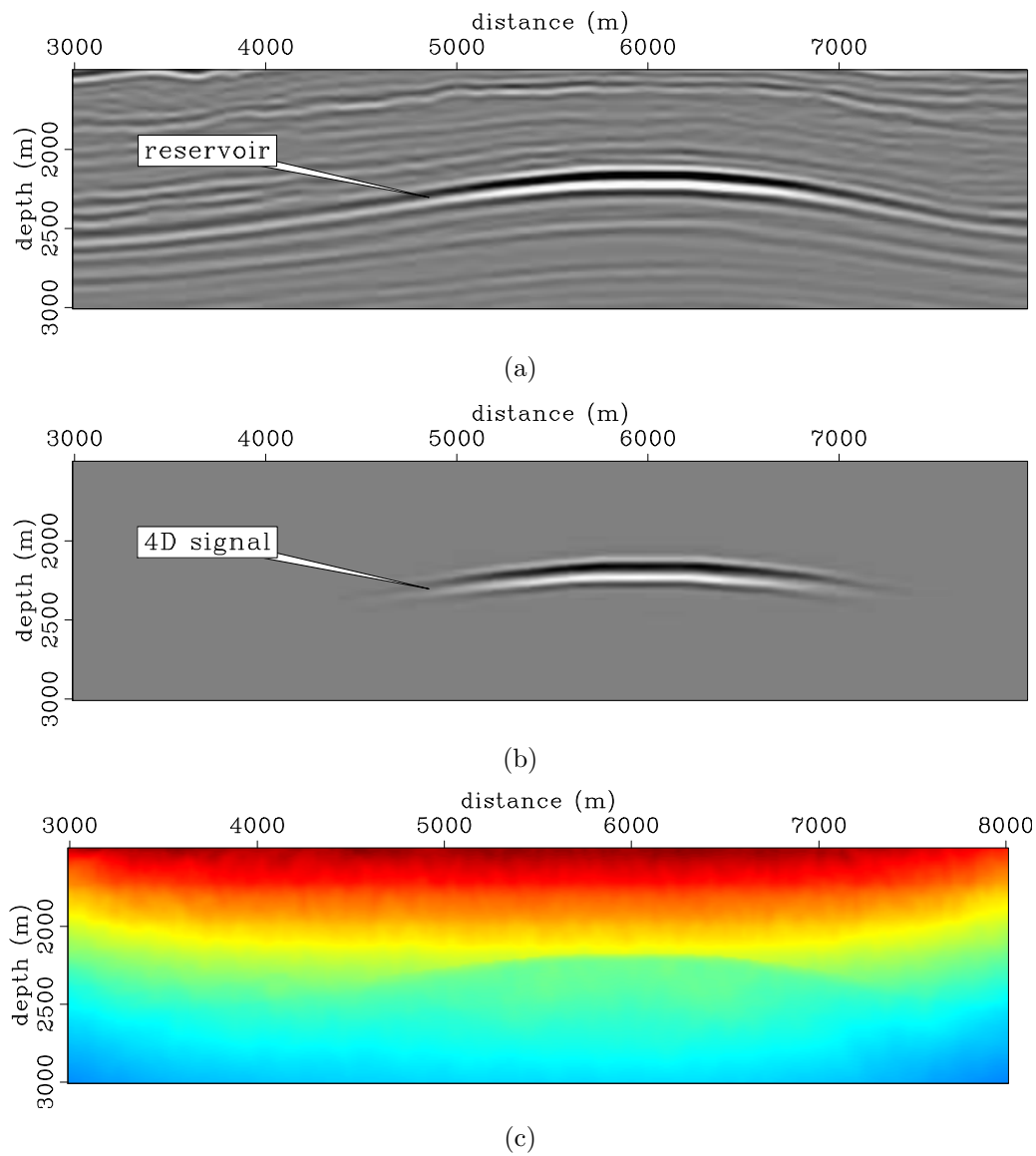


Figure 4.14: Migrated monitor (a) and time-lapse (b) images, and subsurface illumination (c) for the target area shown in Figure 4.13. In (c), red indicates high illumination, whereas blue indicates low illumination. Compare these images to those in Figures 4.15 and 4.18. [CR] chap4/. s-mig-2l,s-mig-dl,s-dhes

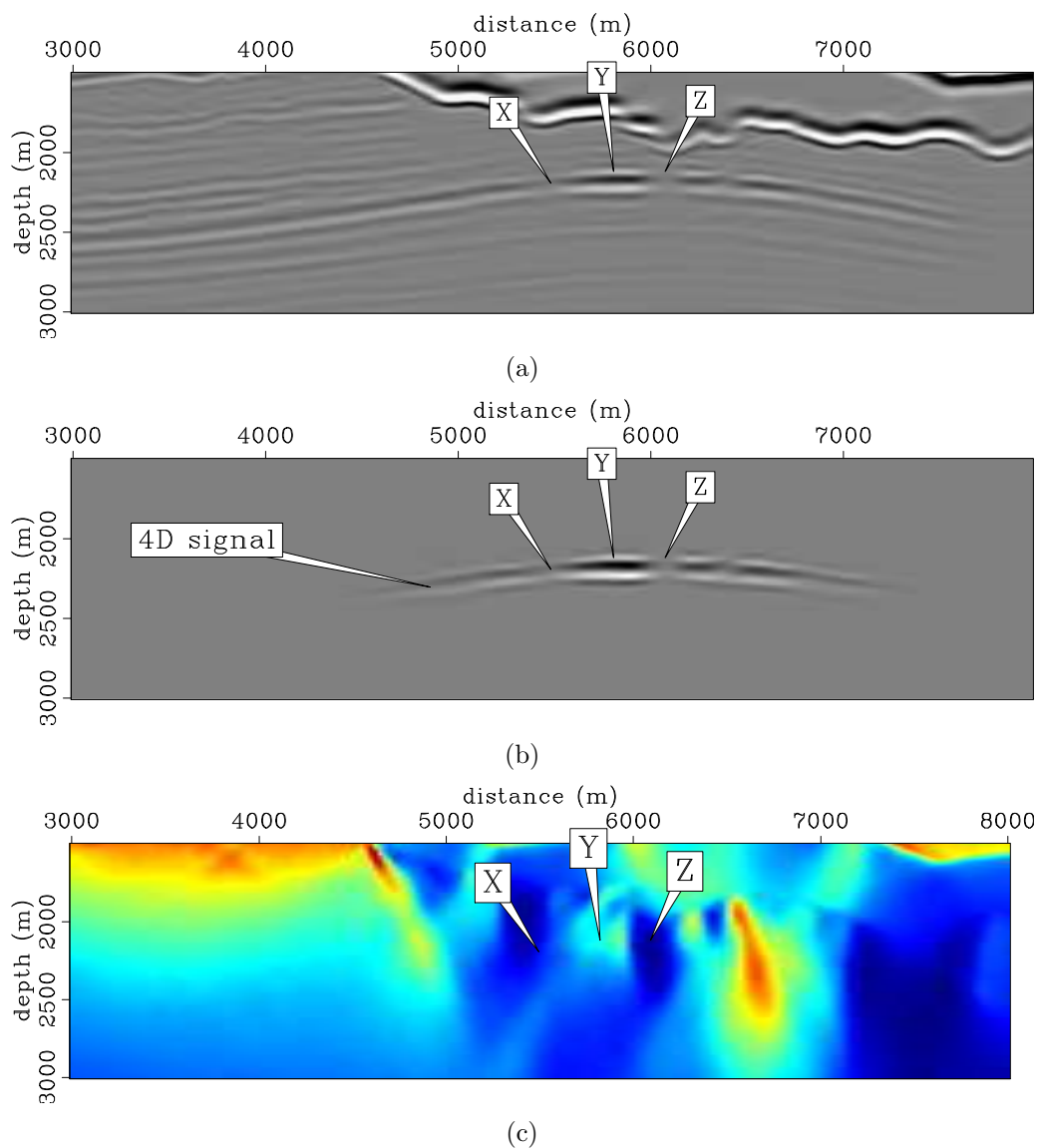


Figure 4.15: Migrated monitor (a) and time-lapse (b) images, and subsurface illumination (c) for the target area shown in Figure 4.12. At points  $X$ ,  $Y$ , and  $Z$  along the reservoir, note that the illumination is highly irregular, the migrated image is distorted, and compared to Figure 4.15(b), the time-lapse image is distorted. Recall that point-spread-functions at points  $X$ ,  $Y$ , and  $Z$  are shown in Figure 1.9. [CR] chap4/. s-mig-salt-2l,s-mig-salt-dl,s-dhes-saltl

Prior to inversion, to simulate incoherent noise between the surveys, I add 5% uniformly distributed random noise to each data set. The monitor and time-lapse images derived from regularized joint inversion of the reference data are presented in Figure 4.16. The corresponding inverted images derived from the sub-salt data are presented in Figure 4.17.

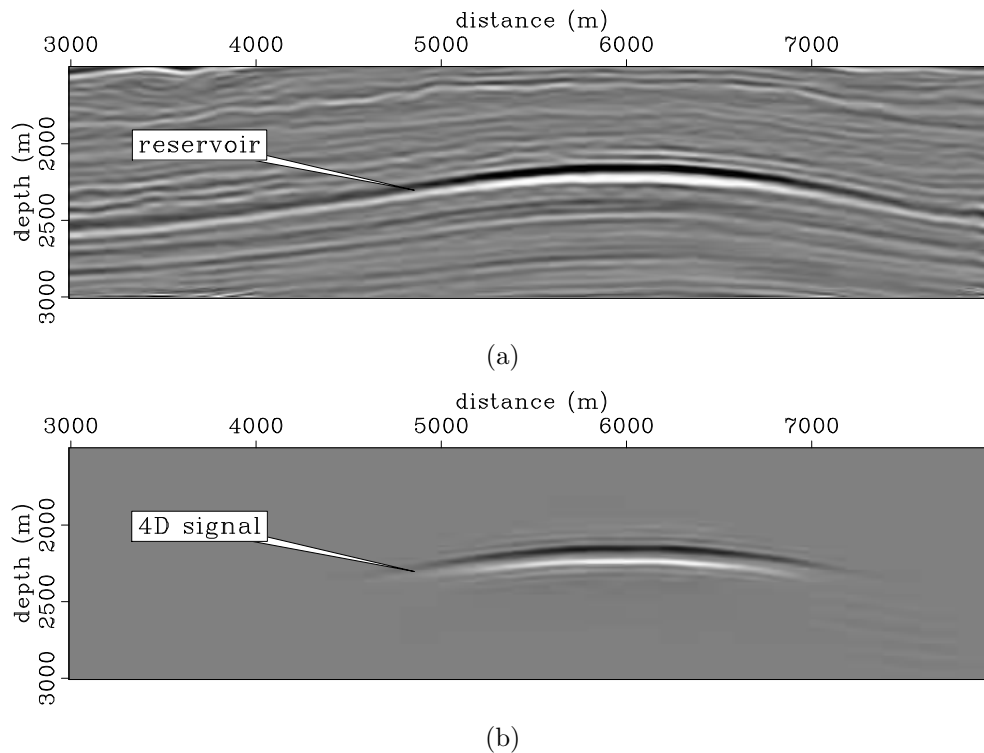


Figure 4.16: Inverted monitor (a) and time-lapse (b) images for the target area shown in Figure 4.13. Note that these images show improved resolution over the migrated images (Figure 4.14). Compare these to the inverted images in Figures 4.17 and 4.19. [CR] chap4/. s-inv-2l,s-inv-dl

Compared to the migrated reference images (Figure 4.14), the inverted reference images show improved resolution. Importantly, the distortions present in the migrated time-lapse image (Figure 4.15(b)) have been corrected in the inverted time-lapse image (Figure 4.17(b)). The subs-salt time-lapse image derived from regularized inversion is of comparable quality to that derived from the reference model (Figure 4.16(b)).

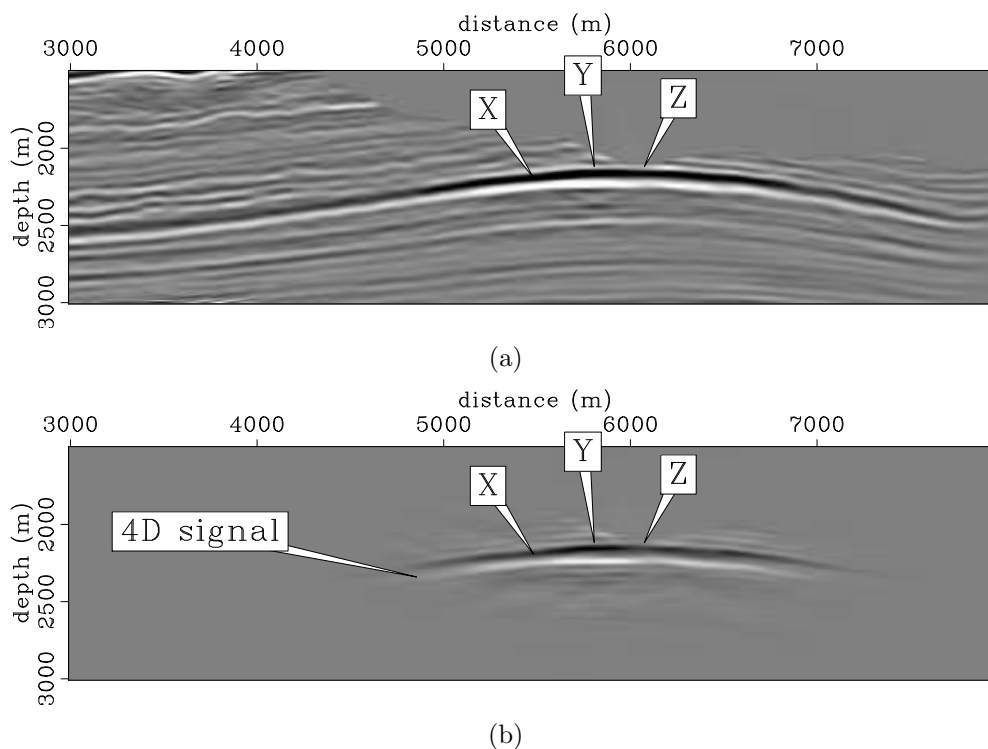


Figure 4.17: Inverted monitor (a) and time-lapse (b) images for the target area shown in Figure 4.12. Note that these images are comparable to those in Figure 4.16. Importantly, at points  $X$ ,  $Y$ , and  $Z$ , note that distortions in the migrated time-lapse image (Figure 4.15(b)) have been corrected by inversion. The salt body in these images has been cropped for clarity. [CR] `chap4/. s-inv-salt-2l,s-inv-salt-dl`

## Discussion

Conventional imaging with a migration operator is sufficient to image targets when the overburden is simple and where survey geometries are repeated for the baseline and monitor surveys (Figure 4.14). This is because, in such a case, the reservoir is sufficiently illuminated (Figure 4.14(c)) and migration is a good approximation to the inverse. However, where the reservoir overburden is complex, the subsurface illumination becomes highly irregular and the migrated image—and as a consequence the time-lapse image—is strongly distorted (Figure 4.15). This distortion results from

the high variability in the sets of angles at which points along the reservoir are illuminated (Figure 1.9). In this case, migration is a poor approximation to the inverse of the linearized seismic modeling operator.

Regularized image-domain inversion provides a way to remove the band-limited wave-propagation effects through the complex reservoir overburden. As shown in this example, even for the simple overburden example, image-domain inversion provides time-lapse images with better resolution compared to migration (Figure 4.16(b)). In the complex overburden example, inversion corrects for the distortions in the migrated image (Figure 4.17(a)), and consequently in the time-lapse image (Figure 4.17(b)). Importantly, whereas the time-lapse reflectivity images obtained from migration are different for the simple and complex overburden examples (Figure 4.14(b) versus Figure 4.15(b)), those from inversion are similar (Figure 4.16(b) versus Figure 4.17(b)). Therefore, with image-domain inversion, the time-lapse reflectivity image becomes less sensitive to the overburden complexity.

### *Example III: Inversion of incomplete data - 2D example*

In this example, using the same modeling parameters as in example *II*, I generate two data sets along the reference model in Figure 4.13. However, to simulate an obstruction in the monitor data, I create a 400 m and a 1200 m hole along the shot and receiver axes, respectively.

Figure 4.18 shows the migrated monitor image, the time-lapse image and the subsurface illumination for the target area. In Figure 4.18(b), note that compared to the reference time-lapse image (Figure 4.14(b)), the time-lapse amplitudes are contaminated by the obstruction artifacts. Recall that in chapter 1, I show that because of the differences in acquisition geometries, PSFs at the image point on reservoir marked in Figure 4.18 vary significantly in their spreading and range of illuminated wavenumbers (Figure 1.8).

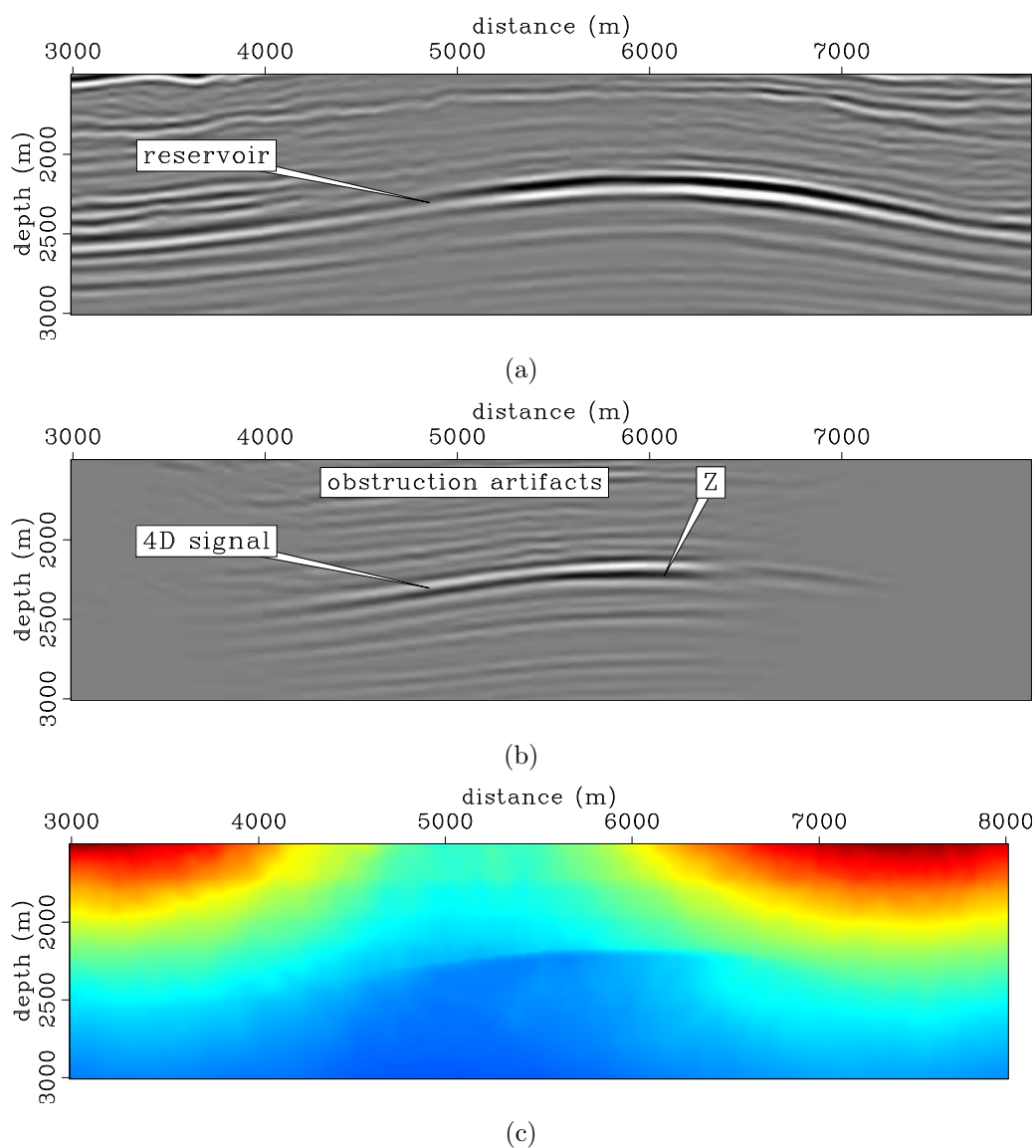


Figure 4.18: Migrated monitor image (a), time-lapse image (b), and subsurface illumination (c) for the target area shown in Figure 4.13, where an a simulated obstruction causes a gap in the monitor data. Note that, compared to the reference time-lapse image (Figure 4.14(b)), the time-lapse image (b) is contaminated by obstruction artifacts. The difference in the point-spread-functions for the baseline and monitor geometries at point  $Z$  is shown in Figure 1.8. [CR] chap4/. s-mig-gap-2l,s-mig-gap-dl,s-dhes-gap

The monitor and time-lapse images derived from regularized joint inversion are presented in Figure 4.19. Note that the obstruction artifacts in the migrated time-lapse image (Figure 4.18(b)) have been attenuated by inversion (Figure 4.19(b)), thereby providing a time-lapse image of comparable quality to the reference model (Figure 4.16(b)).

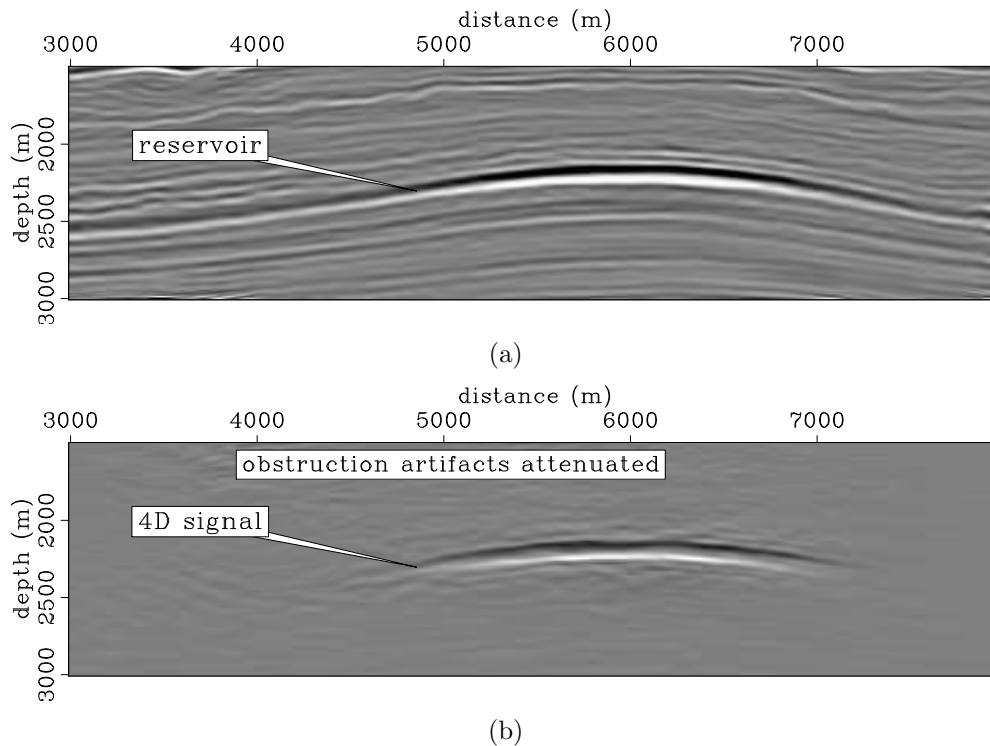


Figure 4.19: Inverted monitor (a) and time-lapse (b) images for the target area shown in Figure 4.13 with a simulated obstruction in the monitor data. Note that these images are comparable to those in Figure 4.16. [CR] chap4/. s-inv-gap-2l,s-inv-gap-dl

## Discussion

Differences in the acquisition geometries of time-lapse seismic surveys result in artifacts that can mask reflectivity change of interest (Figure 4.18). Such artifacts result because the migration operator cannot fully account for differences in the acquisition geometries. As in Example II, in this example, migration is a poor approximation

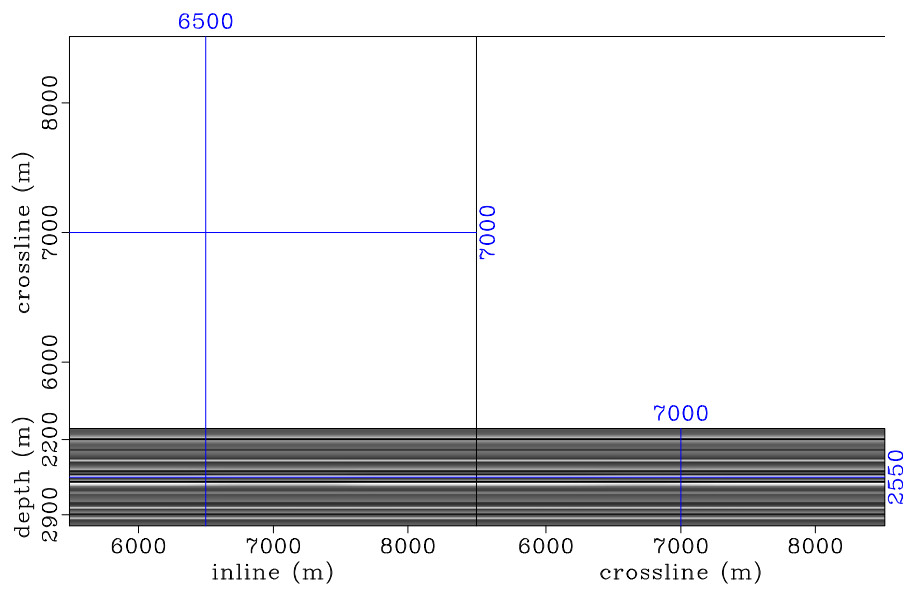
to the inverse of the linearized seismic modeling operator.

Regularized image-domain inversion provides a way to account for differences in acquisition geometries between time-lapse surveys. As shown in Figure 4.19(b), the inverted time-lapse image is comparable in quality to that obtained from for the perfectly repeated geometries (Figure 4.16(b)). Furthermore, the time-lapse image in this example (Figure 4.19(b)) is comparable to the one derived in the sub-salt example (Figure 4.17(b)). Therefore, regularized image-domain inversion makes the time-lapse image less sensitive to the overburden complexity—as shown in example *II*—and to the differences in acquisition geometries—as shown in this example.

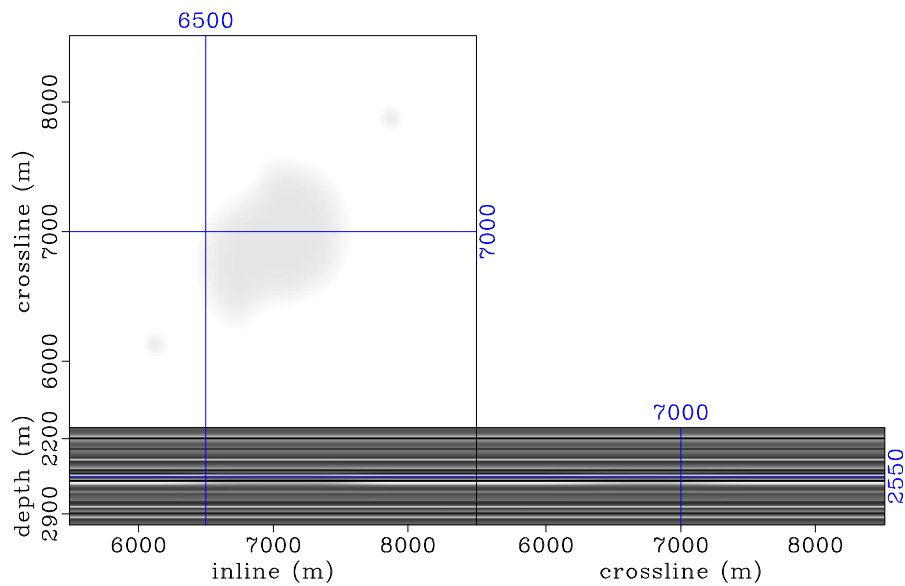
#### *Example IV: Inversion of incomplete data - 3D example*

In this example, I simulate three migrated images by convolving the Hessian matrices of three OBC field-data geometries (discussed in detail in chapter 6) with carefully designed time-lapse reflectivity models. The reflectivity models consist of horizontally-layered events with both positive and negative time-lapse amplitude changes. I assume expanding regions of change in the seismic amplitudes of opposite polarities along the top and bottom of the reservoir. In addition, I assume that the reservoir is faulted, causing strike-slip displacement of the central time-lapse amplitudes.

The baseline reflectivity (not shown) is constant along each reflectors. Figure 4.20 shows band-limited versions of the two monitor reflectivity models. Figure 4.21 shows the time-lapse amplitudes obtained by subtracting the reference baseline image from the two reference monitor images (Figure 4.20). As discussed in chapter 6, whereas the baseline is modeled with a complete geometry, the two monitor geometries contain different sizes of overlapping gaps. The simulated migrated time-lapse images are shown in Figure 4.22. Note that, because of the differences in the acquisition geometries, compared to the *true* reflectivity images (Figure 4.21), these time-lapse images are strongly contaminated.

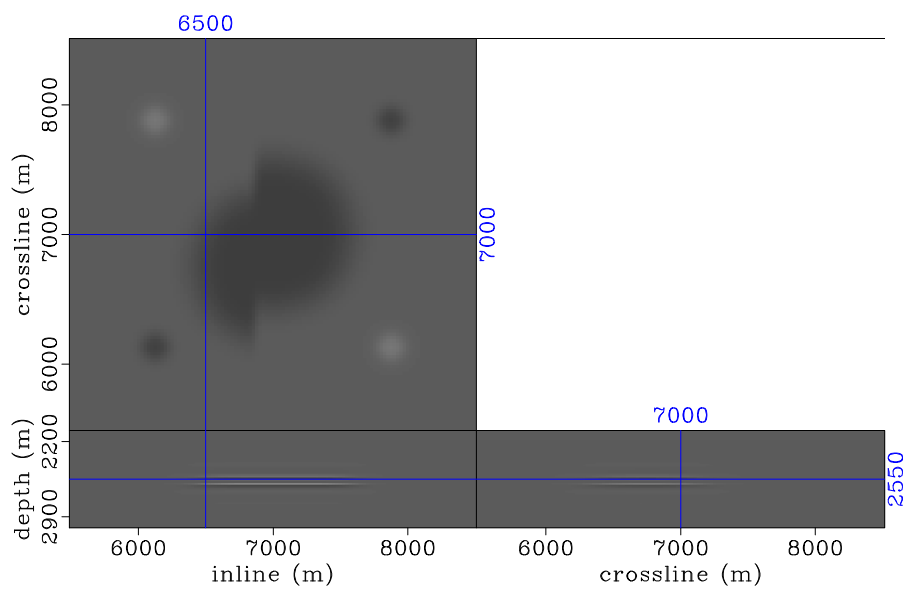


(a)

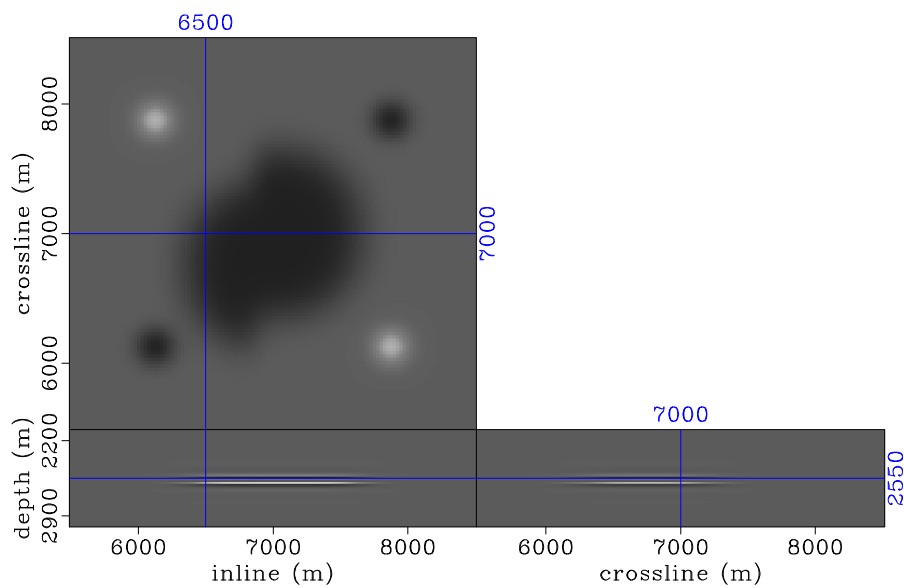


(b)

Figure 4.20: Band-limited reference reflectivity models for the first (a), and second (b) monitors. The baseline model is similar to these but with constant reflectivity along each horizontal reflector. The reference time-lapse models computed as the differences between (a) and (b), and the baseline reflectivity model are shown in Figure 4.21. [CR]. chap4/. ref-2,ref-3

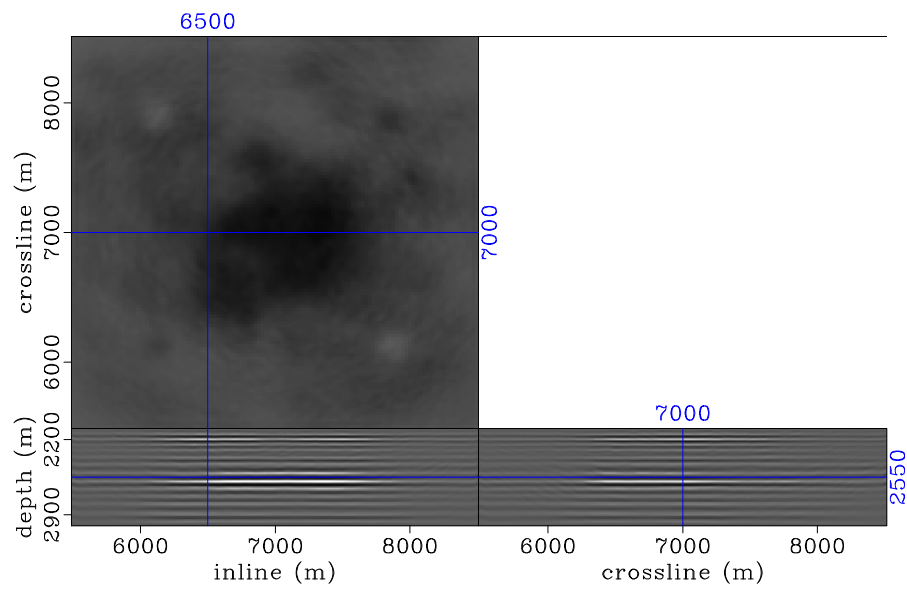


(a)

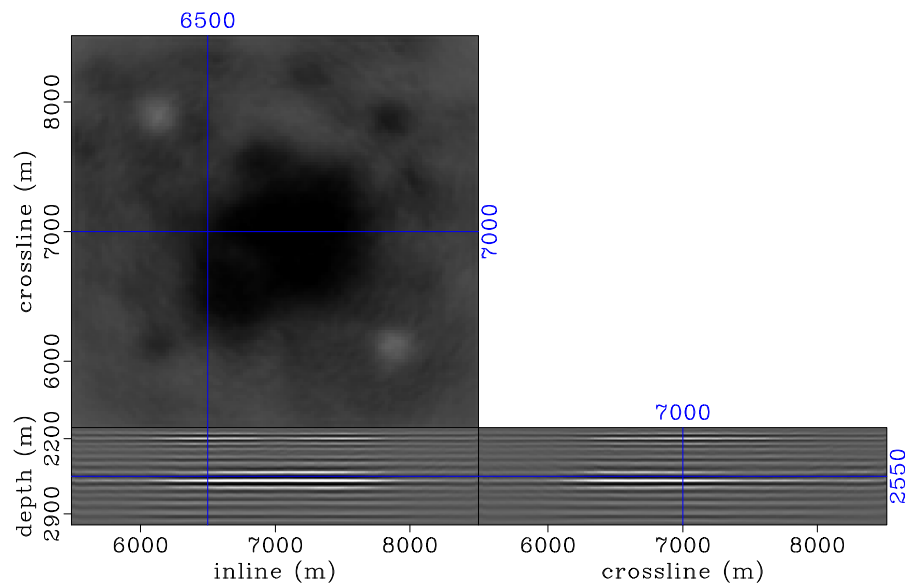


(b)

Figure 4.21: Reference time-lapse images between the first (a), and second (b) monitor models (Figure 4.20) and the baseline model (not shown). Note that reflectivity changes increase in amplitude and size with time. [CR]. chap4/. ref-d1,ref-d2



(a)



(b)

Figure 4.22: Migrated time-lapse images between the first (a), and second (b) synthesized monitor images and the baseline. Note that, compared to the reference time-lapse images (Figure 4.21), the time-lapse amplitudes are contaminated by obstruction artifacts. [CR]. `chap4/. smig-d1,smig-d2`

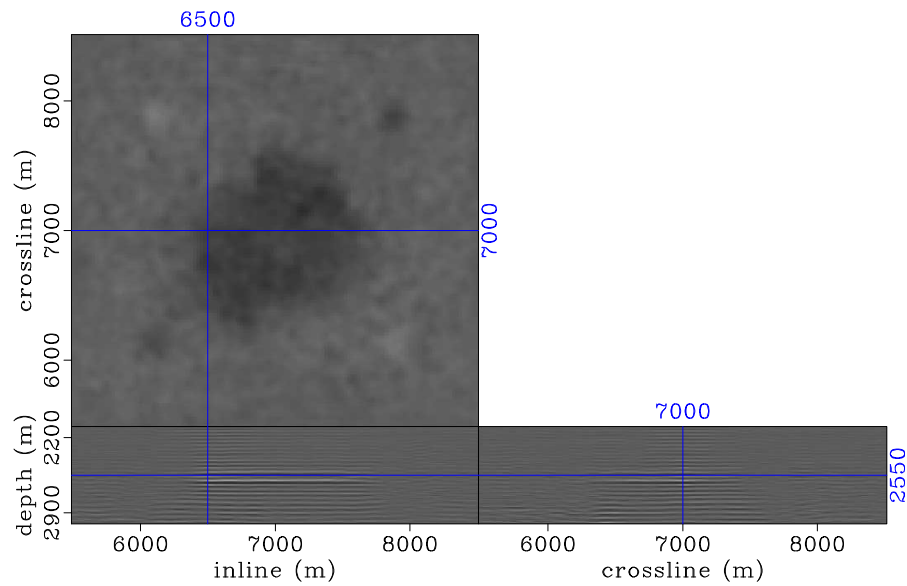
The time-lapse images obtained by inversion with weak coupling between the images are shown in Figure 4.23. This is equivalent to inverting the images separately. Note that, although the time-lapse images are improved, they still contain several artifacts absent in the reference model (Figure 4.21). The inverted time-lapse images derived using the same spatial regularization parameters as in Figure 4.23, but temporal coupling that is too strong are shown in Figure 4.24. Note that although artifacts have been reduced in the images, the time-lapse amplitudes have also been destroyed.

Figure 4.25 shows the inverted time-lapse images derived using the same spatial regularization parameters as in Figures 4.23 and 4.24, but intermediate temporal coupling between the image. Note that the time-lapse images obtained in this case are comparable in quality to the reference time-lapse models (Figure 4.21).

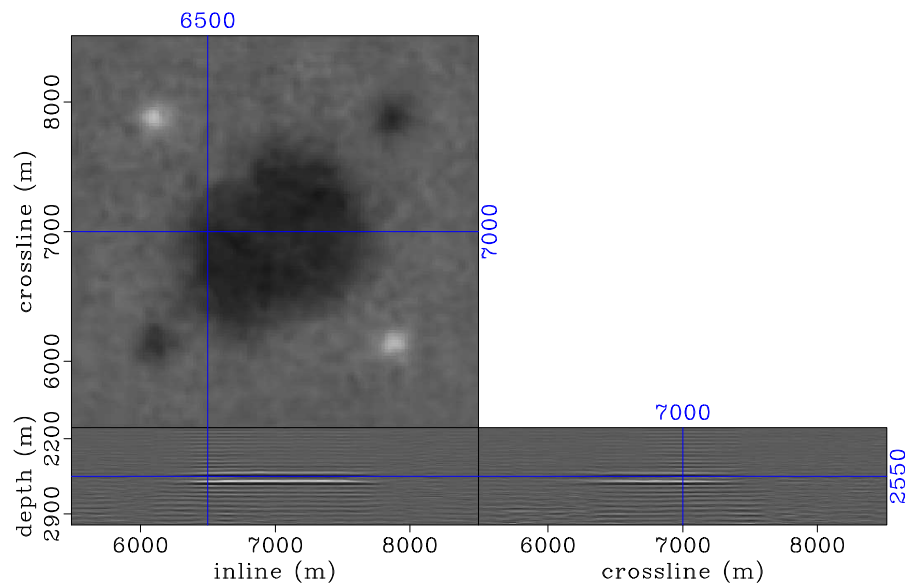
## Discussion

As discussed earlier, because linearized inversion of time-lapse seismic data sets is an ill-posed problem, it is often necessary to regularize it. Therefore, the choice of regularization operators and parameters is an important component of solving this problem. As demonstrated in this and previous examples, solving this inversion jointly enables incorporation of spatial and temporal regularization. In practice, because it is usually difficult to determine the optimum regularization parameters prior to inversion, it is usually necessary to test different parameters. An important advantage of image-domain inversion is that once the approximate Hessian is precomputed, it can be reused for different regularization parameters.

In this example, artifacts in the migrated time-lapse images (Figure 4.22), resulting from differences in acquisition geometries, can be attenuated by inversion weakly-coupled (Figure 4.23). However, because this is similar inverting the images separately, it is difficult to obtain temporally-consistent inverted images. Therefore, differences in residual artifacts between these *separately-inverted* images still contaminate the inverted time-lapse images.



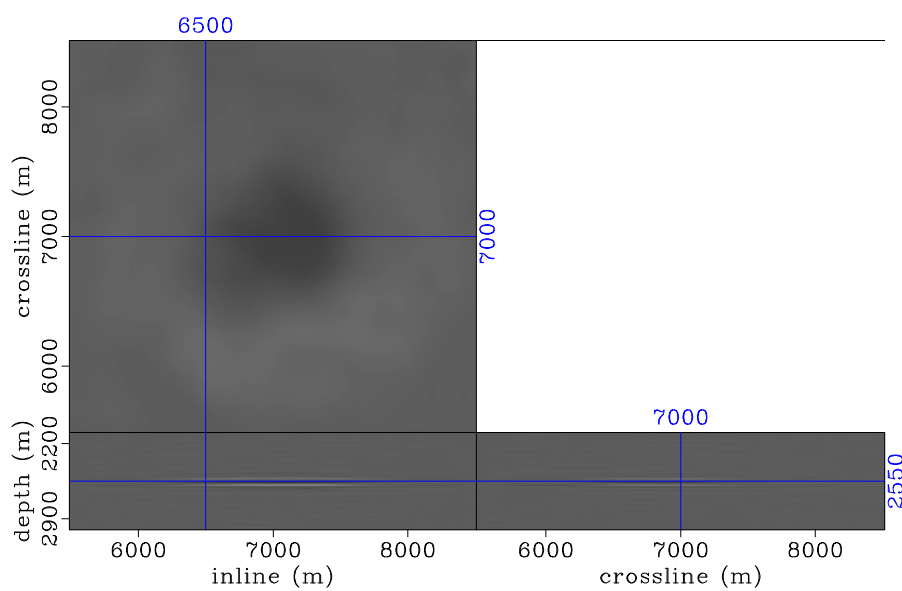
(a)



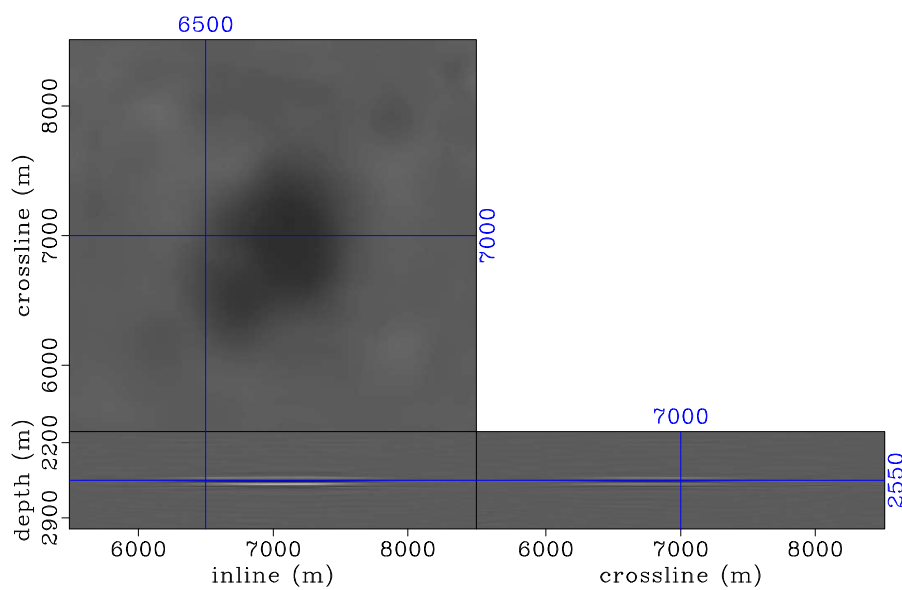
(b)

Figure 4.23: Inverted time-lapse images between the first (a), and second (b) monitor and the baseline, derived from weakly-coupled joint inversion between the baseline and monitor images. Note that, although most of the obstruction artifacts in Figure 4.22 have been attenuated, the time-lapse amplitudes are still contaminated by numerous artifacts not present in the reference time-lapse images (Figure 4.21).

chap4/. small-d1,small-d2

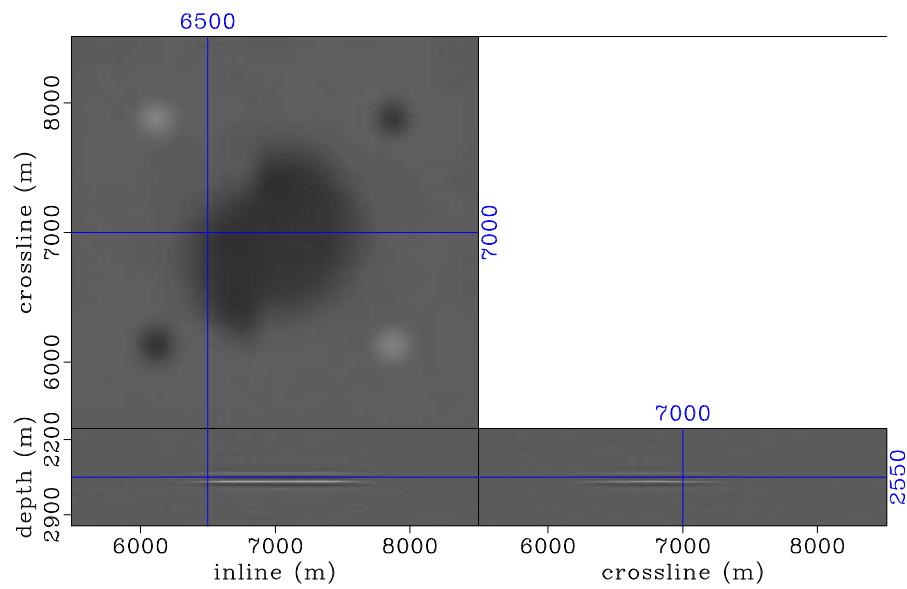


(a)

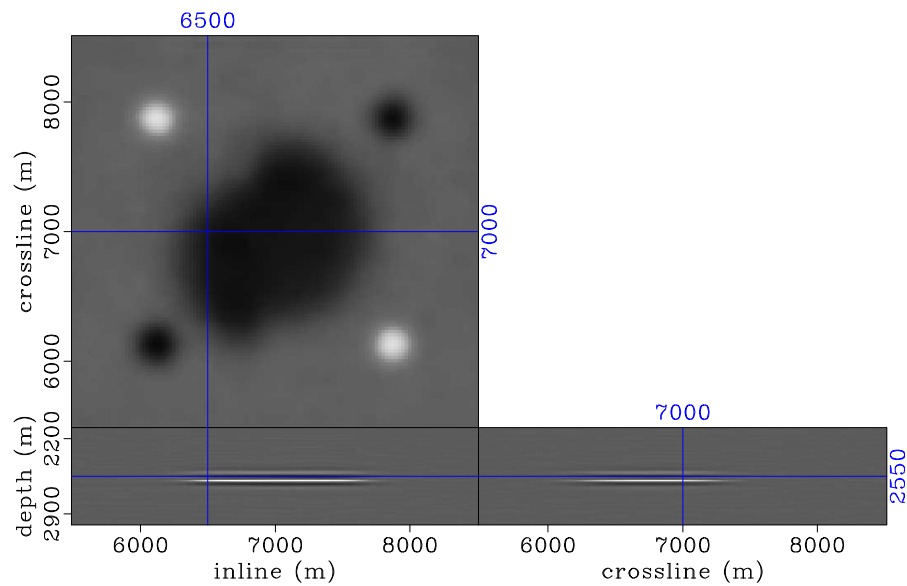


(b)

Figure 4.24: Inverted time-lapse images between the first (a), and second (b) monitor and the baseline derived from strongly-coupled joint inversion between the baseline and monitor images. Note that, although the artifacts in Figures 4.23 and 4.22 have been attenuated, compared to the reference time-lapse images (Figure 4.21), the time-lapse amplitudes have been destroyed. chap4/. high-d1,high-d2



(a)



(b)

Figure 4.25: Inverted time-lapse images between the first (a), and second (b) monitor and the baseline, derived from satisfactorily coupled joint inversion of the baseline and monitor images. Note that the obstruction artifacts are sufficiently attenuated, whereas the time-lapse amplitudes are preserved. These results are comparable in quality to the reference time-lapse images (Figure 4.21). chap4/. med-d1,med-d2

Using a temporal regularization parameter that is too large leads to too-strong coupling between the inverted images. As noted above, although strong temporal coupling attenuates differences in residual artifacts between images, it also destroys the time-lapse reflectivity of interest (Figure 4.24). By using a temporal regularization parameter that sufficiently couples the inverted images without destroying the time-lapse reflectivity, it is possible to obtain time-lapse images (Figure 4.25), which are comparable to the reference images (Figure 4.21).

## CONCLUSIONS

In this chapter, I have demonstrated applications of regularized joint inversion in the data domain and in the image domain. I showed that by inverting field-encoded data acquired with simultaneous sources, it is possible to attenuated artifacts caused by geometry and shot-time non-repeatabilities. This approach can speed up both seismic acquisition and imaging and may make possible near-continuous monitor of reservoirs. Another application of data-domain joint inversion is in the least-squares imaging of conventional time-lapse data, where computer-base encoding is applied to individual *single-source* data sets.

In addition, I showed how distortions in time-lapse images caused by complex overburden can be attenuated by regularized joint image-domain inversion. Furthermore, I showed regularized joint image-domain inversion can be used to attenuate artifacts in time-lapse images caused by obstructions in time-lapse seismic acquisition surveys. These examples demonstrate that it is possible to obtain reliable time-lapse images that are independent of overburden complexity and differences in seismic acquisition geometries.

Lastly, using a three-dimensional example, I showed how the choice of regularization parameters affect the inverted time-lapse image. Without coupling between the inverted images, because the inverse problem is ill-posed, it is difficult to obtain reliable time-lapse images. However, if the temporal coupling is too strong, the time-lapse amplitudes of interest may become destroyed. Image-domain inversion

requires pre-computation of an approximate *truncated* Hessian matrix of the least-squares objective function. Once this matrix is computed, image-domain inversion is relatively cheap. Therefore it is possible to try several regularization parameters until satisfactory results are obtained.

In chapters 5 and 6, I show applications of regularized joint image-domain inversion to two- and three-dimensional field data sets.

## ACKNOWLEDGEMENTS

The original Marmousi velocity model, which was modified and used to synthetic models in example *I*, was provided by Institut. Franais du Petrole (IFP). I thank SEG for providing the SEAM model, from which the two-dimensional models in examples *II* and *III* are extracted and modified. The Hessian matrices in example *IV* were generated using velocity models and data geometries modified from the Valhall Life-of-Field-Seismic data sets provided by BP.

# Chapter 5

## 2D field data applications

In chapter 4, using synthetic examples, I showed how the regularized joint data-domain and image-domain inversion methods developed in chapter 3 overcome different time-lapse imaging challenges. In this chapter, I apply joint image-domain inversion to subsets of a North Sea field time-lapse data set. These two-dimensional marine streamer data are extracted from three-dimensional seismic surveys acquired as part of Statoil's time-lapse seismic monitoring project at the Norne field. Recall that in chapter 2, I used the preprocessed, pre-stack time-migrated (PSTM) images obtained from four years (2001, 2003, 2004 and 2006) to demonstrate applications of conventional post-imaging time-lapse cross-equalization methods.

In this chapter, I utilize two raw data sets recorded in 2006 and 2008 to demonstrate how different preprocessing steps improve time-lapse amplitude information and condition the data for inversion. Data preprocessing is important to ensure that as nearly as possible, the data satisfy the assumptions made in chapter 3. If these assumptions are not satisfied, the inversion methods developed in this dissertation cannot give reliable results. First, to satisfy the primaries-only assumption, multiples and other uncorrelated noise must be removed. Then, bulk amplitude difference between the data sets (e.g., due to differences in acquisition instruments), must be taken into account. Finally, all image points between the baseline and monitor images must

be collocated. In addition, I show that that linearized inversion can improve time-lapse images in conventional acquisition geometries. Furthermore, I demonstrate that this method can be used to attenuate obstruction artifacts in time-lapse images.

As discussed in chapter 2, the Norne field is located in the Norwegian sector of the North Sea. A summary of the field geology and production history is presented in chapter 2. Osdal et al. (2006) and Aarre (2008) provide more detailed description of the Norne field geology, the production history, the monitoring objectives, the time-lapse seismic data acquisition and processing, and some interpretation of the time-lapse seismic responses observed in the field. For this study, the baseline data were acquired in 2006, whereas the monitor data were acquired in 2008. The shots and receivers are binned to 25 m spacings with a maximum offset of 3,200 m. Figure 5.1 shows a portion of the raw baseline data set.

This chapter is divided into two broad sections:

- First, using the complete baseline and monitor data sets, I show how different preprocessing steps and joint image-domain inversion improve time-lapse amplitude information. In this example, the baseline and monitor data sets have similar geometries.
- Second, I simulate an obstruction in the monitor data with a gap 400 m wide. In this example, except at the obstruction where no sources or receivers are present in the monitor, the baseline and monitor data sets have similar geometries.

Figure 5.2 shows the full migrated baseline and monitor stacked sections. To obtain these images, I migrate the data sets with a shot-profile one-way wave-equation algorithm using 290 frequencies up to 40 Hz. Note that the subsurface geology along this section of the field is relatively simple, with predominantly horizontal reflectors. The target area for inversion is between 1,500 m and 4,000 m along the vertical (depth) axis and between 0 m and 11,100 m along the horizontal (common-midpoint) axis. Henceforth, I show the results only for this target area. In this chapter, all inversion results are obtained using the RJMI formulation.

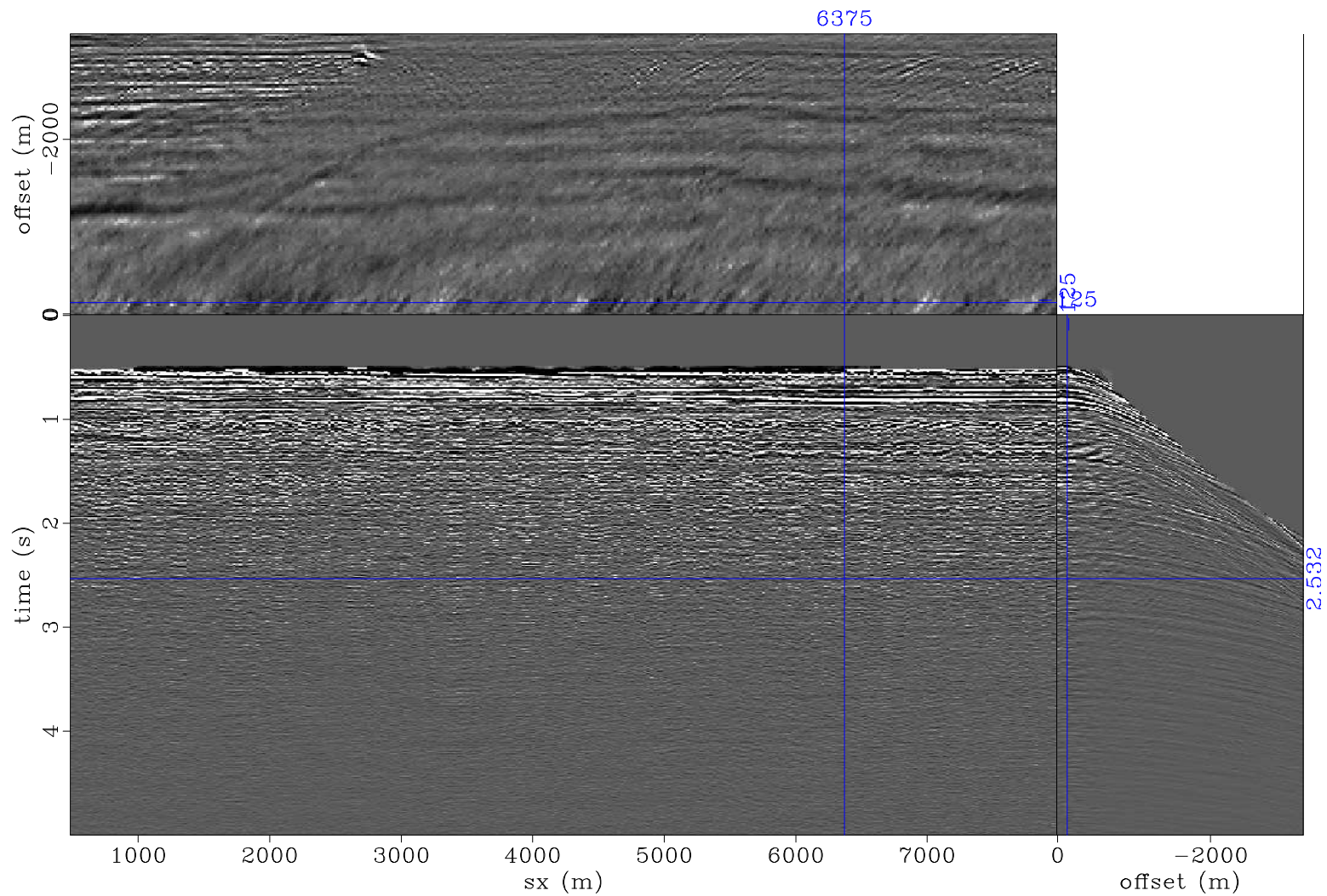


Figure 5.1: A portion of the raw two-dimensional streamer data from the Norne 2004 (baseline) data set. [CR] chap5/. dmhl-dat-2759-b4

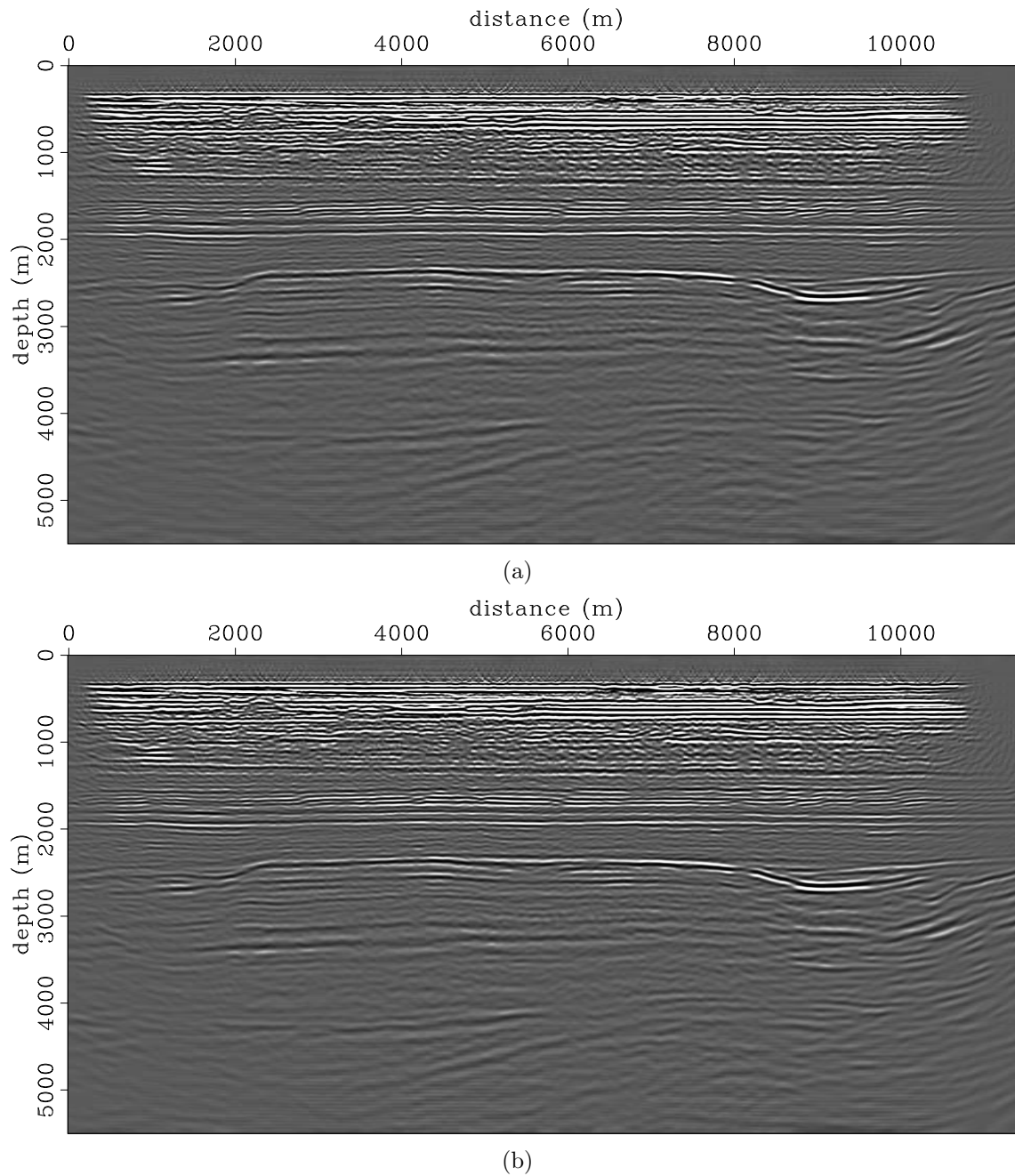


Figure 5.2: Raw baseline (a) and monitor (b) stacked images. Note that, along this section, the geology is relatively simple, with predominantly horizontal reflectors. The reservoir is located at approximately 2600 m depth. [CR]

chap5/. raw-2759-full-g-06,raw-2759-full-g-08

### *Example I: Inversion of complete data sets*

In this example, I present the processing and inversion of the complete baseline and monitor data sets. Figure 5.3 shows the migrated pre-stack images obtained from the raw baseline and monitor data sets.

In Figure 5.3, note that the events showing significant curvature in the pre-stack image are multiples, whereas the horizontal events are the correctly migrated horizontal primaries. Because of small differences in the characteristics of multiples between the baseline and monitor surveys, if they are not attenuated, the multiples will contaminate the time-lapse amplitude information of interest. Figure 5.4 shows the pre-stack baseline and monitor images after high-resolution multiple attenuation. I perform this multiple-attenuation procedure using a parabolic Radon operator (Trad et al., 2003) and a robust conjugate-directions solver (Claerbout and Fomel, 2011).

First, I derive an inverted Radon model that predicts all events in the CMP-sorted data sets. Then, I determine a range of curvature parameters that contains all primary events. Seismic events predicted by the Radon model outside this range of curvature parameters are then subtracted from the recorded data sets. In this preprocessing step, I use the same parameters for both the baseline and the monitor data sets.

Note that several artifacts that are present in the migrated images obtained from the raw data (Figure 5.3) have been attenuated in the migrated images obtained from the preprocessed data (Figure 5.4). As mentioned above, and as I will show later in this section, differences between multiples of different surveys contaminate the time-lapse image.

Using images obtained from the preprocessed data, I estimate and apply a bulk amplitude correction to the monitor data. Differences in energy between seismic images may be caused by differences in the acquisition instruments for the different surveys. Prior to inversion, bulk amplitude differences between the baseline and monitor images must be removed. This ensures that such amplitude differences do not mask production-related amplitude differences between the images.

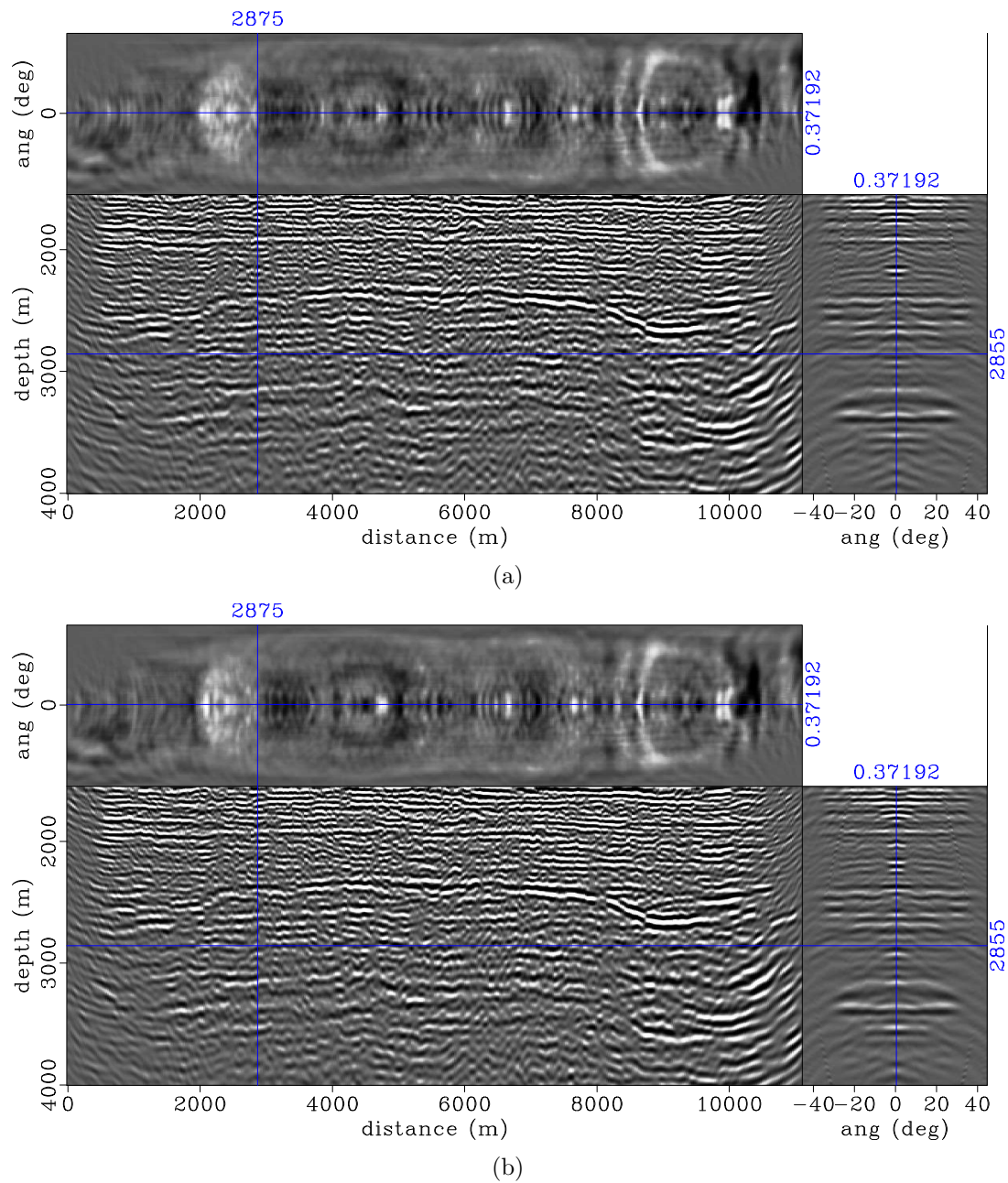
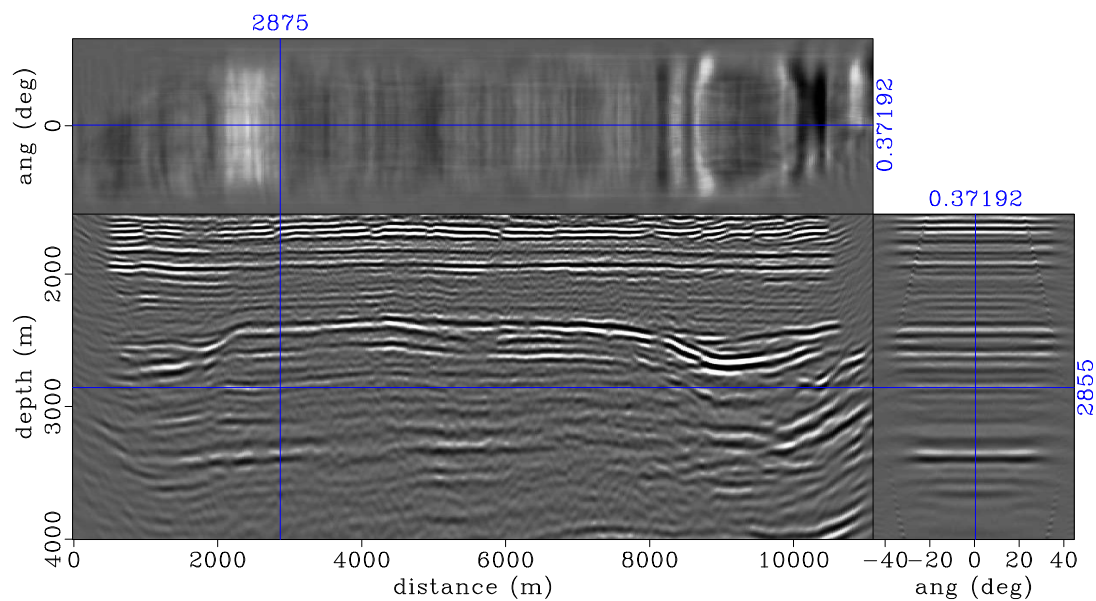
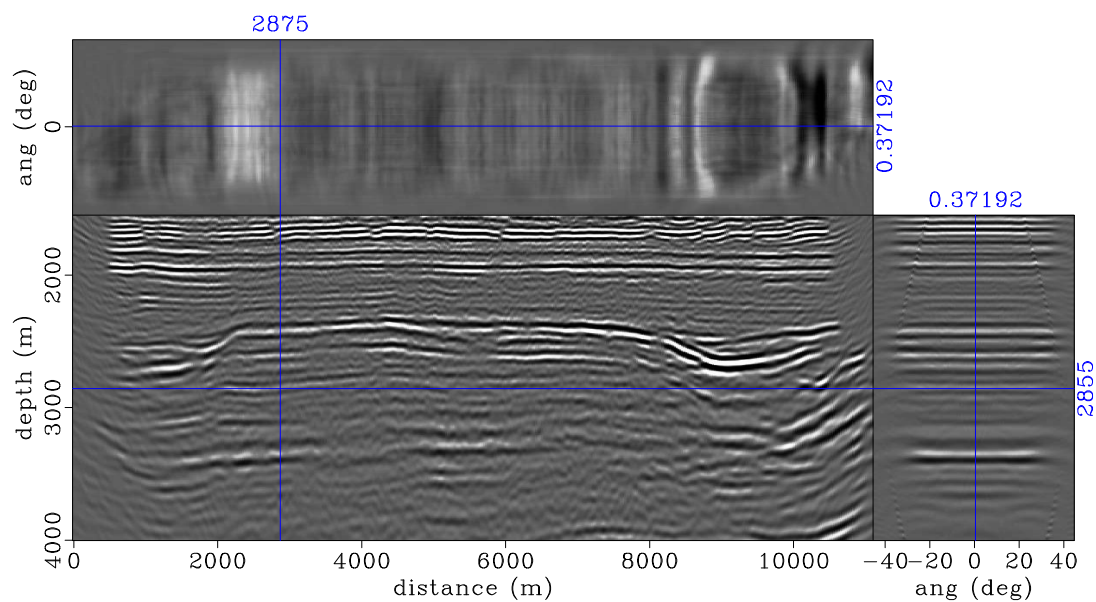


Figure 5.3: Raw pre-stack baseline (a) and monitor (b) images of the target area. In these images, the horizontal events are primaries, which have been adequately imaged. The dominant artifacts in both images are multiples, which show significant curvature across angles. If they are not adequately attenuated, these multiples will contaminate the time-lapse difference between these images. [CR]

chap5/. raw-2759-06,raw-2759-08



(a)



(b)

Figure 5.4: Pre-stack baseline image (a) and monitor image (b) of the target area obtained from the preprocessed data sets. Note that the artifacts in the raw image (Figure 5.3) have been attenuated. In addition, note that the monitor image has been warped (using apparent displacements in Figures 5.5) to the baseline image. [CR]

chap5/. flat-2759-06-s,warp-2759-08

I estimate the amplitude correction as the ratio of the root-mean-square (RMS) energy in the baseline image versus the monitor image:

$$A_m = \frac{E_b}{E_m}, \quad (5.1)$$

where  $A_m$  is the amplitude correction term that is applied to the monitor image,  $E_b$  is the RMS energy in the baseline image, and  $E_m$  is the RMS energy in the monitor image. In this example, I compute this correction term within a 500 m window above the reservoir. I determine that for these images,  $A_m = 1.102$  equalizes the energy between the images and attenuates artifacts caused by bulk amplitude differences between them.

Next, to correct for production-induced velocity changes and compaction between surveys, I warp the pre-stack monitor image to the baseline image. Prior to warping the images, to correct for small velocity errors, I first remove any residual moveout in the pre-stack baseline image by aligning all events to the zero-angle image. Then, I compute the apparent displacements between this RMO-corrected baseline image and the monitor image.

Figure 5.5 shows the vertical components of the apparent displacements between these images. These apparent displacements are obtained using the sequential cross-correlation method described in chapter 2. In Figure 5.5, the region with the largest apparent displacements corresponds to the reservoir location. In addition, I observe the presence of a static (almost constant) apparent displacement of approximately 1 m at all image points. This static apparent displacement between the images causes many of the differences between the unaligned images—discussed below. Such displacements may be caused by small changes in the source wavelet, inadequate tidal corrections, or changes in the water velocity.

In order to remove any residual apparent displacements between the stacked baseline and monitor images, using the same sequential warping procedure, I further align these images. However, in this example, the apparent displacements between the stacked images (not shown) are negligible.

Warping the monitor image to the baseline image ensures that all image points become collocated at the baseline position. Because the survey geometries are similar for these surveys, the Hessian matrices for the two aligned images can be approximated by the Hessian matrix obtained with the baseline velocity and geometry.

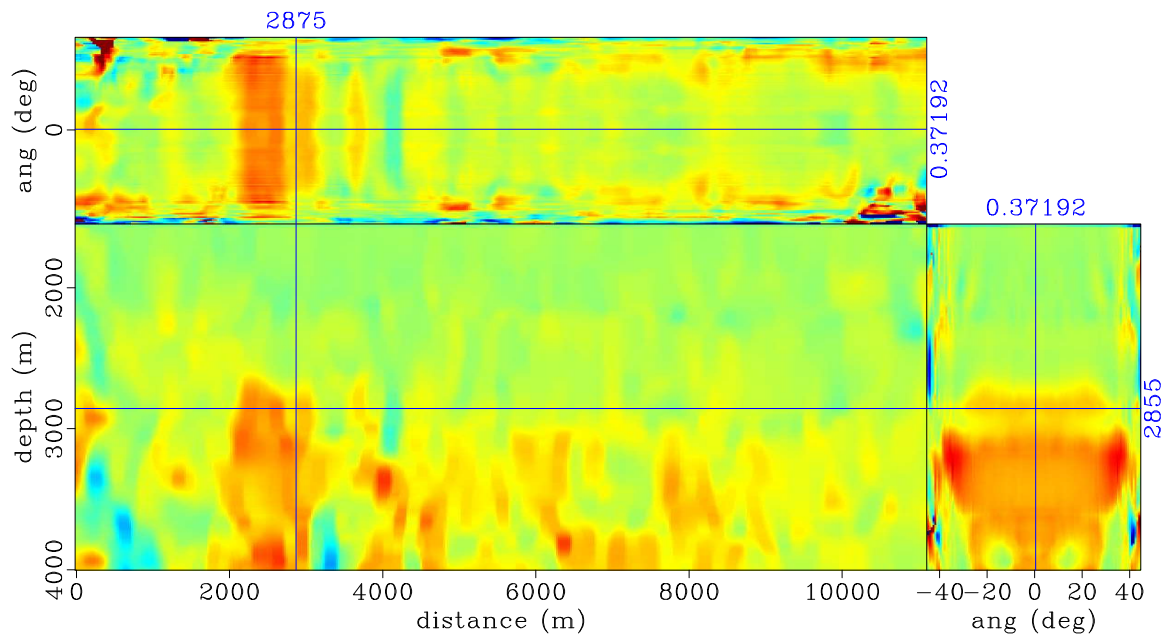


Figure 5.5: Pre-stack apparent vertical displacements between the baseline and monitor images (Figures 5.4(a) and 5.4(b)). Red, blue and green denote positive, negative and zero displacements, respectively. Note that the maximum apparent displacements correspond to the reservoir location in the horizontal range between 2000 m and 3000 m. Also, note that the apparent displacement varies with opening angle.

[CR] chap5/. warp-2759-08-rflat-ts

In this example, I compute the Hessian matrix for the target area using 27 equally spaced frequencies within the frequency band of the data. Because the study area is small, I compute the Green's functions for all surface positions explicitly, and then compute the target-oriented Hessian using the approximation defined in equation 3.10. I compute off-diagonal elements of the Hessian matrix in the range  $-150$  m to  $+150$  m along the vertical (depth), and horizontal (common-midpoint) axes. In general, for this example, the Hessian matrix is diagonally dominant.

Figure 5.6 shows the Hessian diagonal (subsurface illumination) for the target area. Note that for this complete geometry, because of the relatively simple overburden geology, the estimated subsurface illumination is well-behaved, with gradually decreasing illumination with depth. An example of the off-diagonal elements of this Hessian at a sample sub-surface location, represented as elements of the PSF at that location, is shown later in the chapter (Figure 5.13).

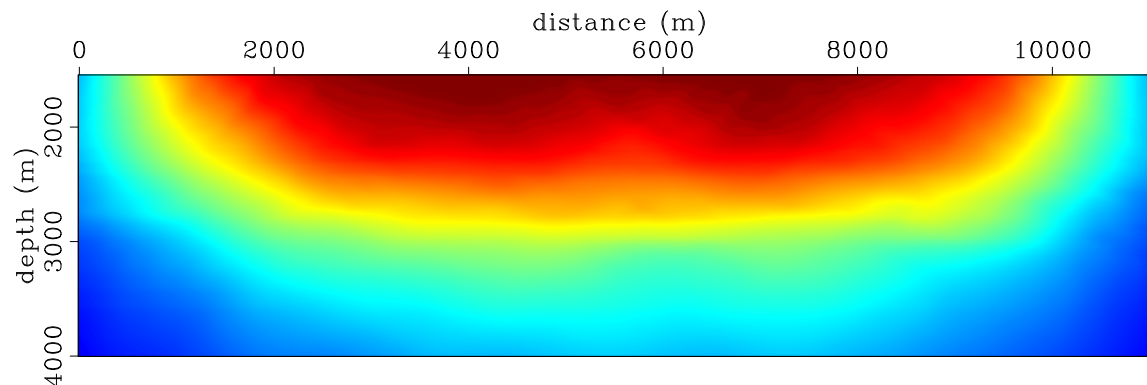


Figure 5.6: Hessian diagonal (subsurface illumination) for the target area. Red indicates regions with high illumination, whereas blue indicates regions with low illumination. [CR] chap5/. hs-06

The spatial regularization operator used in this example is constructed from non-stationary dip-filters derived from factorized directional Laplacians (Hale, 2007). Figure 5.7 shows the local dips obtained from the stacked preprocessed baseline image using the plane-wave destruction method (Fomel, 2002). Because both images have been aligned by prior to inversion, I use the same spatial regularization operator for both of them. As in chapter 4, the temporal regularization in the inversion is a difference operator applied to the images. This provides coupling between the inverted images and ensures that there are only limited differences between them.

Figure 5.8 shows the migrated time-lapse image from the raw data, after Radon demultiple, and after amplitude balancing. Figure 5.9 shows the same image after pre-stack warping, after residual post-stack warping, and after inversion. Note that the raw migrated time-lapse image contain several artifacts that are not associated

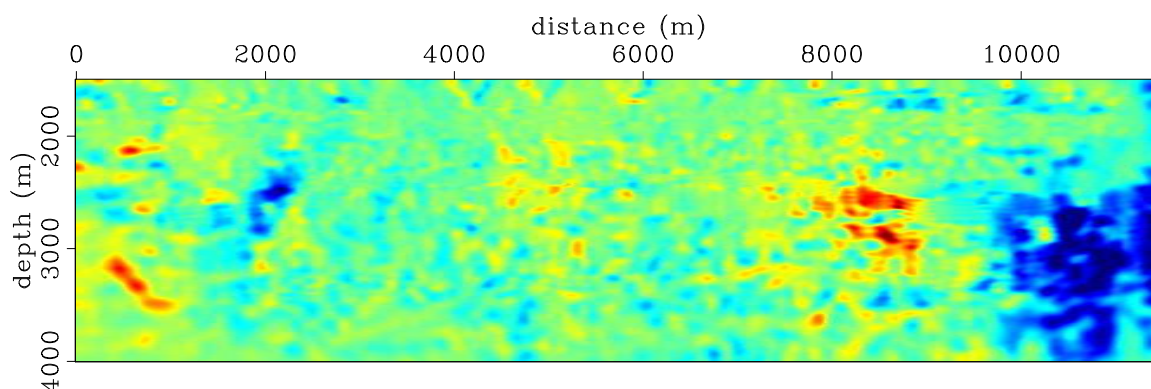


Figure 5.7: Dips derived from the stacked baseline image. Red indicates positive dips, whereas blue indicates negative dips. These dips are used to construct the spatial regularization operator used in the inversion. [CR] chap5/. dm-dip-2759

with production-induced changes in the reservoir properties (Figure 5.8(a)). Note the incremental improvements in the time-lapse image quality after different preprocessing steps and after inversion.

In Figure 5.8(b), note that the multiple attenuation step described above has reduced most of the incoherent artifacts in the time-lapse image. Furthermore, by balancing the RMS energy between the baseline and monitor images, differences between them are reduced further (Figure 5.8(c)). Importantly, a comparison of the time-lapse images in Figures 5.8(c) and 5.9(a) shows that the biggest improvements in the time-lapse image-quality are after removal of the static and dynamic displacements by warping the monitor image to the baseline image. For example, the strong artifact in the time-lapse image around 9,000 m, which is caused by differencing two misaligned large amplitude events in the baseline and monitor images, have been removed after warping. Furthermore, geologically consistent artifacts, which are caused by the static displacement between the images, have been attenuated. As described above, in this example, residual warping of the stacked images provides only limited improvements to the time-lapse image (Figure 5.9(b)).

Finally, because inversion attenuates most of the residual artifacts between the images, the quality of the time-lapse image is improved further (Figure 5.9(c)).

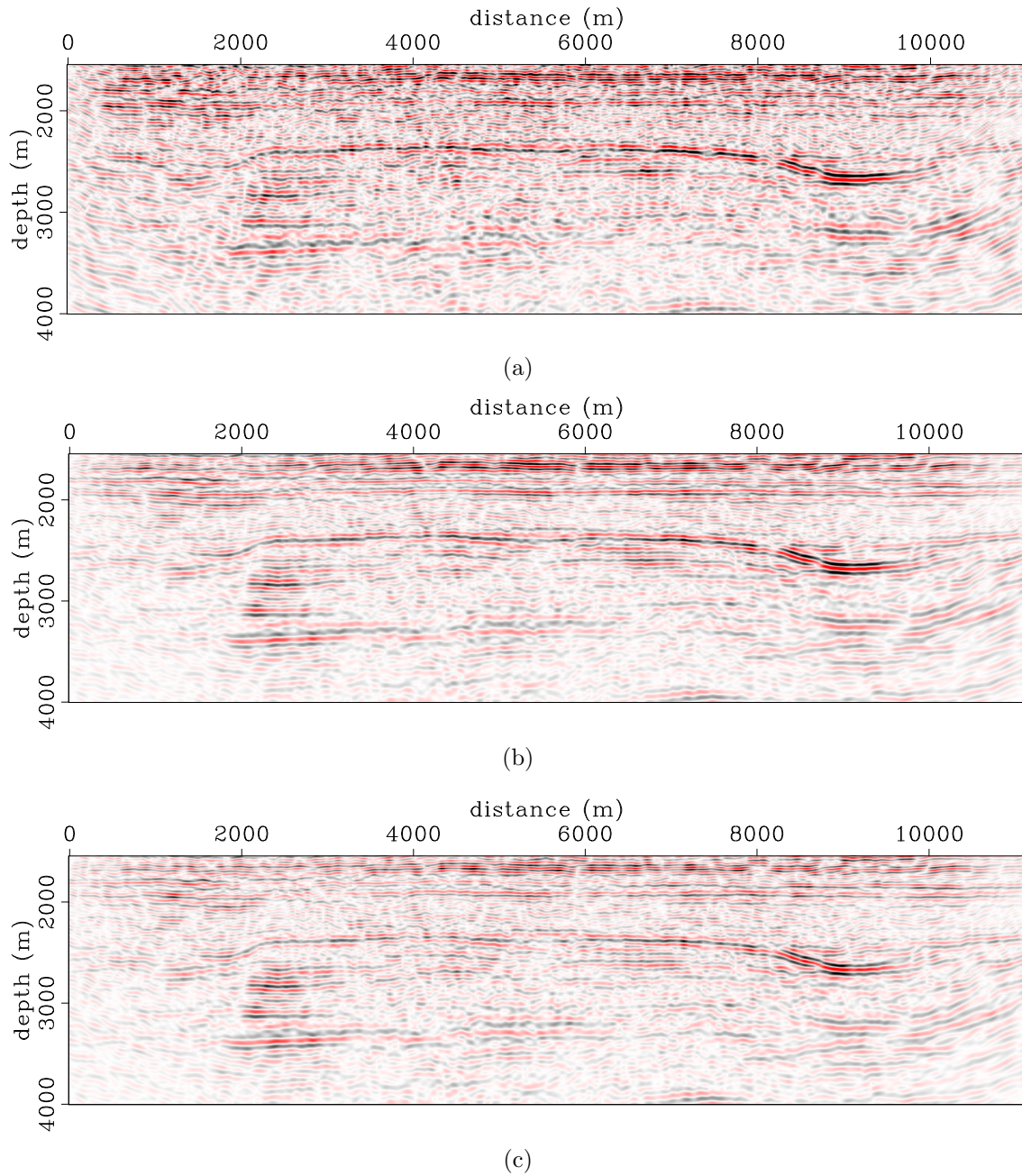


Figure 5.8: Time-lapse images obtained from the raw data (a), after multiple attenuation by parabolic Radon demultiple (b), and after amplitude correction (c). Note the incremental improvements in the time-lapse image from (a) to (c). [CR]

chap5/. raw-2759-4d,dmult-2759-4d,amp-2759-4d

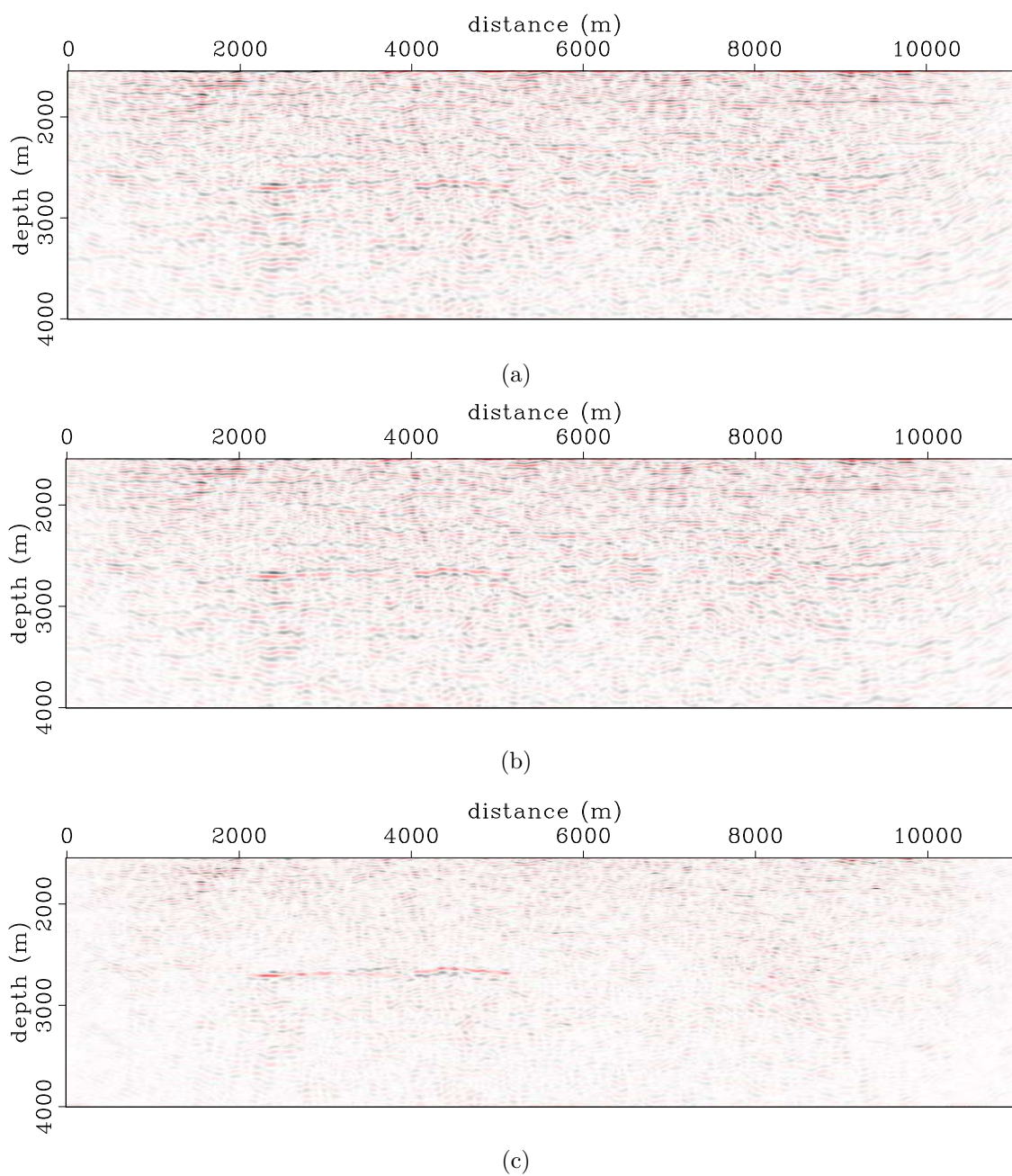


Figure 5.9: Time-lapse images obtained after pre-stack warping (a), after residual post-stack warping (b), and after image-domain inversion (c). Note the incremental improvements in the time-lapse image from (a) to (c). [CR]

chap5/. warp-2759-4d,rwarp-2759-4d,inv-2759-4d

### *Example II: Inversion of incomplete data sets*

In this example, I present the preprocessing and inversion of the complete baseline and incomplete monitor data sets. As previously stated, I simulate an obstruction in the monitor geometry such that neither sources nor receivers are present between 2500 and 2900 m. Apart from the presence of this gap in the monitor geometry, the baseline and monitor geometries in this example are the same as those used in example *I*.

Figure 5.10 shows a portion of the gapped monitor data. Note that the gap in this data set is located directly above the area of interest. In this example, the preprocessing steps and migration parameters are the same as those used in example *I*. However, there are some differences necessitated by the obstruction in the monitor geometry. First, the multiple attenuation requires a mask that accounts for the presence of the gap in the monitor data. This ensures that this gap does not affect the estimated Radon model. The masking operator is a diagonal operator with zeros in the gap area and ones at all other locations.

Second, to obtain the amplitude correction, as in example *I*, I utilize a window above the reservoir, but in parts of the image unaffected by the gap in the monitor geometry. This ensures that the measured difference in RMS amplitudes is not caused by the gap in the monitor geometry. As in the previous example, I obtain an amplitude correction  $A_m = 1.102$ .

Third, in order to align events in this incomplete monitor image to the complete baseline image, I first perform interpolation to fill in the hole in the monitor data. As in the multiple attenuation step, this interpolation operator is a parabolic Radon function. The interpolated monitor data (not shown) are then imaged and processed using the same parameters as in the complete monitor case. The resulting pre-stack image is then used to estimate the apparent displacement vectors that are used to warp the incomplete monitor image to the baseline. This approach ensures that the pre-stack baseline and monitor images have similar kinematics, and ensures more reliable estimates of the apparent displacements between the migrated images.

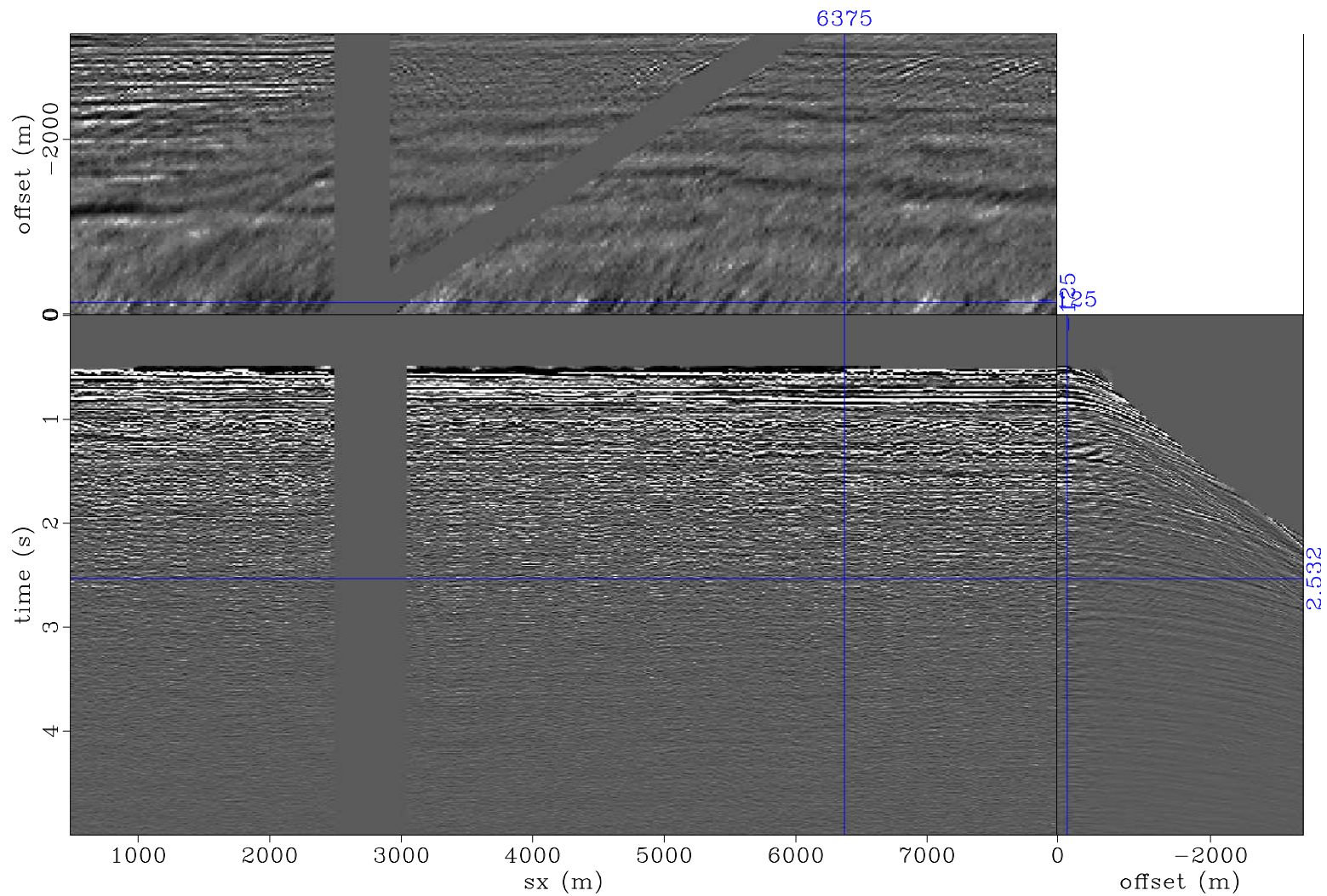


Figure 5.10: Gapped monitor data. Note that sources and receivers are missing within the simulated obstruction.  
 [CR] chap5/. dmhl-dat-2759-b4-hole

Figure 5.11 shows the vertical components of the apparent displacements between the baseline and monitor images. Note that these apparent displacements are comparable to those obtained in example *I* (Figure 5.5). As in example *I*, in this image, the region with the largest apparent displacements correspond to the reservoir location.

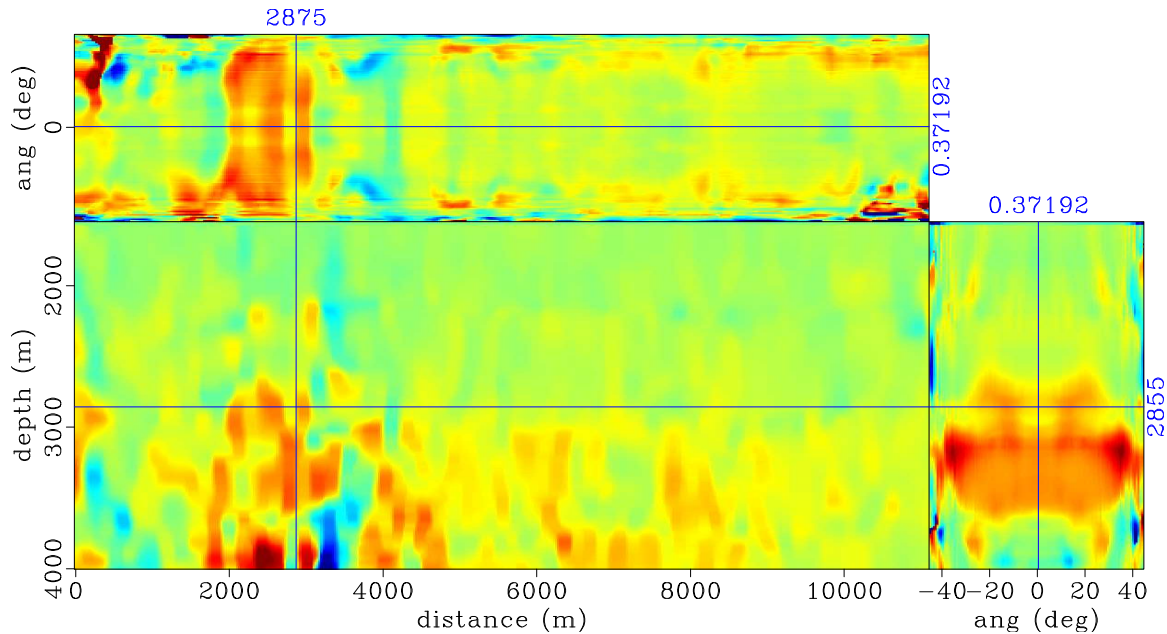


Figure 5.11: Pre-stack apparent vertical displacements between the complete baseline image and the image from interpolated monitor data sets. Comparing this to Figure 5.5, note that estimates of the apparent displacements are similar to those from the complete data case. [CR] chap5/. dmhl-warp-2759-08-rflat-ts

I compute the Hessian for the incomplete monitor geometry with the same parameters used for the complete baseline geometry in example *I*. The illumination ratio between the baseline and monitor geometries (monitor illumination divided by baseline illumination) is shown Figure 5.12. Note that, in general, regions of the subsurface that are imaged with the same survey geometries have similar illumination, and hence the illumination ratio equals unity. Regions of the subsurface that are imaged with different geometries have different illumination, and hence illumination ratios in these regions are less than unity. In this example, the region with low illumination ratios corresponds to parts of the subsurface that are affected by the

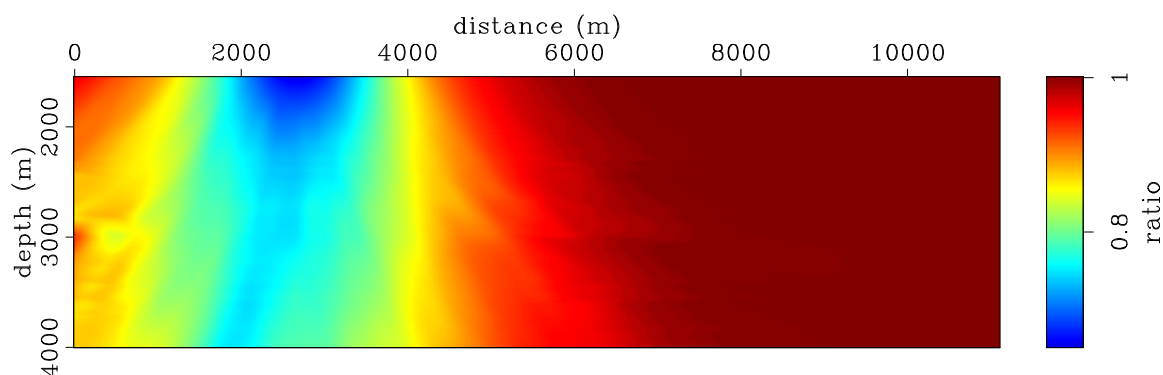


Figure 5.12: Illumination ratio between the baseline and monitor. Red indicates regions with equal illumination (i.e., ratio equals unity) whereas blue indicates unequal illumination (i.e., ratio less than unity). [CR] chap5/. hs-rat

simulated obstruction in the monitor geometry (Figure 5.12). Note that this region also corresponds to the reservoir location.

Figure 5.13 shows the spatial- and wavenumber-domain point-spread functions at point  $x = 2600$  m and  $z = 2600$  m. Because of the gap in the monitor geometry, as expected, a comparison of the two PSFs shows that this image point is illuminated with a lower seismic energy in the monitor survey than in the baseline. Figure 5.14 shows the differences in the PSFs in the spatial and wavenumber domains. The difference in geometry leads to significant differences off-diagonal elements (i.e., points away from the central point of the spatial PSF). These differences are equivalent to differences in the ranges of illuminated wavenumbers for the two geometries (Figure 5.14(b)).

Figure 5.15 shows the time-lapse images obtained after different processing steps. Note the incremental improvements in the time-lapse image quality after processing and after inversion. In Figure 5.15(a), in addition to artifacts present in the raw time-lapse image in example  $I$  (Figure 5.8(a)), high-amplitude artifacts are also present in parts of the image below the obstruction. Because of these artifacts, compared to the complete data example (Figure 5.9(b)), the time-lapse image from conventional processing (Figure 5.15(b)) is of poorer quality. These artifacts have been attenuated in the inverted time-lapse image (Figure 5.15(c)).

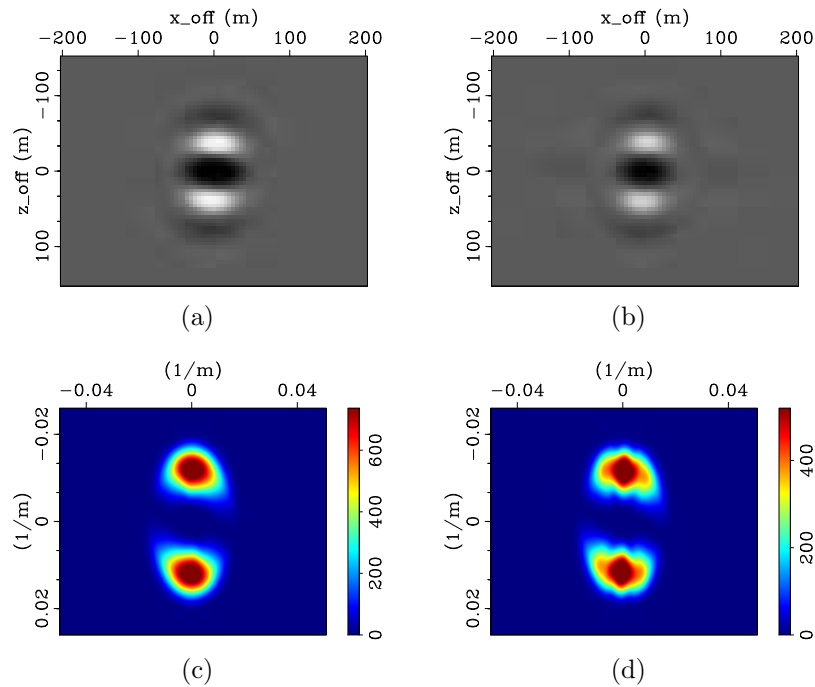


Figure 5.13: PSFs at point  $x = 2600$  m and  $z = 2600$  m for the baseline (a) and (c), and the monitor (b) and (d). The panels show the PSFs in the spatial domain (a) and (b), and in the wavenumber domain (c) and (d). The differences between these PSFs are shown in Figures 5.14. [CR] chap5/. hs-offd-06,hs-offd-08,hs-fft-06,hs-fft-08

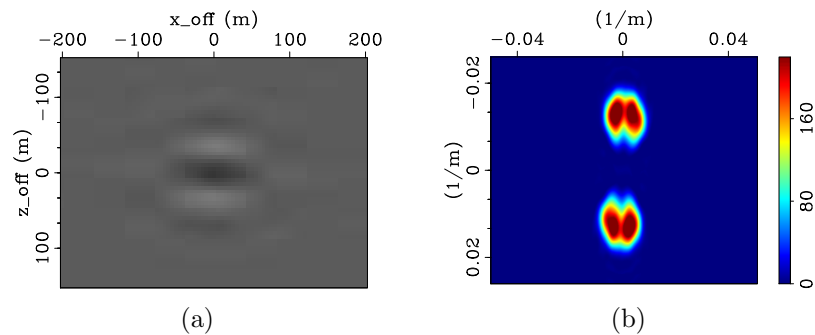


Figure 5.14: Differences between the baseline and monitor PSFs at  $x = 2600$  m and  $z = 2600$  m in the spatial domain (a) and wavenumber domain (b). In (a), note that there are significant differences between PSFs away from the central point (i.e., in the off-diagonal elements of the Hessian matrices). Likewise, in (b), there are significant differences in wavenumber illumination for the two geometries. [CR] chap5/. hs-offd-diff,hs-fft-diff

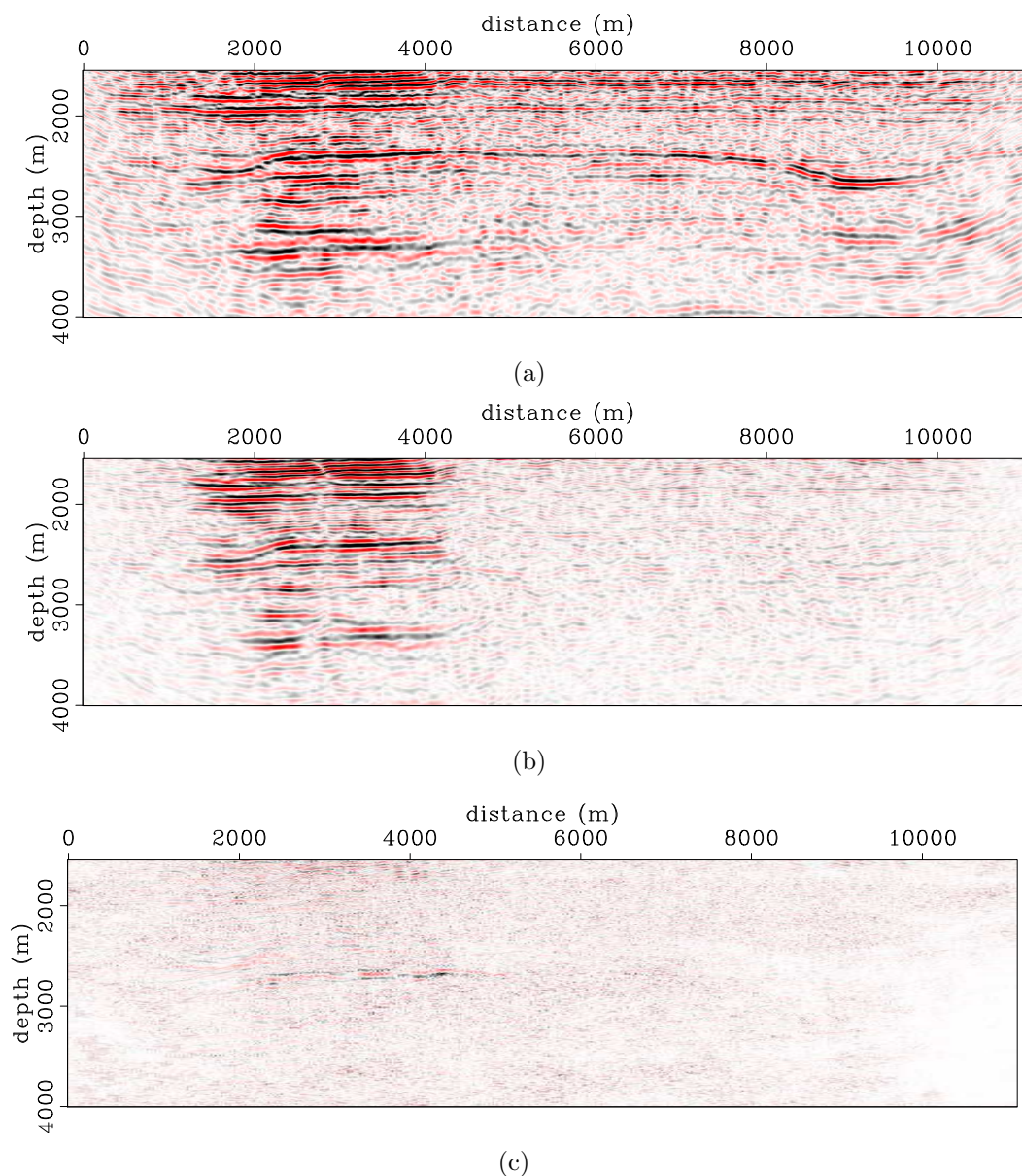


Figure 5.15: Time-lapse images obtained from the raw data (a), after conventional time-lapse processing (b), and after image-domain inversion (c). Because of artifacts introduced by the incomplete monitor data, conventional methods fail to provide results of comparable quality to the complete data example (Figure 5.9(b)). As shown in (c), regularized joint inversion provides satisfactory results. [CR]

chap5/. dmhl-raw-2759-4d,dmhl-rwarp-2759-4d,dmhl-inv-2759-4d

One common way to account for subsurface illumination variations in migrated images is through weights defined as the inverse of the diagonal of the Hessian (Plessix and Mulder, 2004; Etgen et al., 2009). Approximating the Hessian matrix by its diagonal assumes that at any subsurface point, all illuminated wavenumbers/angles should be weighted equally by the value of the Hessian diagonal. For the time-lapse problem, this approximation is sufficient if the acquisition geometries—and hence, differences in the properties of the Hessian matrices—for different surveys are similar. However, where the geometry differences are large, the diagonal of the Hessian is a poor approximation. For example, Figure 5.16 shows the time-lapse

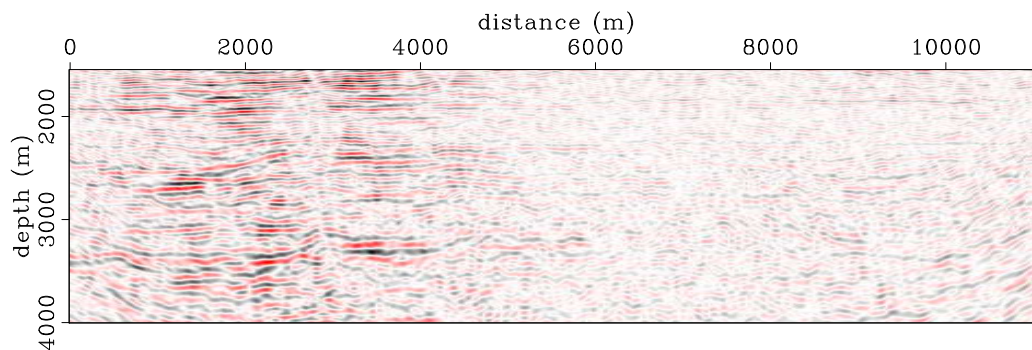


Figure 5.16: Time-lapse image obtained after weighting the baseline and monitor images by the diagonal of the Hessian matrices. Because the diagonal of the Hessian does not contain full information about subsurface illumination discrepancies, it only provides limited improvements compared to conventional methods (Figure 5.15(b)). As shown in Figure 5.15(c), regularized joint inversion provides a time-lapse image that is more comparable in quality to the complete data example (Figure 5.9(b)).

[CR] chap5/. dmhl-dinv-2759-4d

image derived as the difference between the weighted migrated images derived from the complete baseline and incomplete monitor data sets. Although, compared to the time-lapse image from the unweighted migrated images (Figure 5.15(b)), this image contains fewer artifacts, it is of poorer quality than the image derived from regularized inversion (Figure 5.15(c)).

## Discussion

Example *I* demonstrates that in order to obtain reliable estimates of the production-related changes in time-lapse seismic data sets, even where the data are acquired with state-of-the-art methods, careful data preprocessing is necessary. In addition to improving the quality of time-lapse amplitude information, these preprocessing steps are required to ensure that the data satisfy sufficiently the primaries-only assumption in the inversion formulations.

First, using a parabolic Radon operator, multiples and other artifacts in the raw data are attenuated. Compared to the pre-stack images obtained from the raw time-lapse data (Figures 5.3), the preprocessed pre-stack images contain significantly fewer artifacts (Figure 5.4). In addition, because of small differences in the acquisition instruments, there is a bulk amplitude difference between the baseline and monitor images. Amplitudes between the baseline and monitor images are sufficiently balanced by multiplying the monitor image by the ratio of the RMS energy between the migrated images outside the reservoir region.

In this example, by first warping the images prior to stacking, I ensure that image defocusing—due to production-induced velocity changes and compaction—is minimized. In addition, warping provides a way to remove the static apparent displacements of approximately 1 m between the baseline and monitor images. As previously discussed, in this example, these static displacements may have been caused by small changes in the source wavelet, inadequate tidal corrections, or changes in the water velocity. The sequential one-dimensional warping method described in chapter 2 provides an efficient way to align these pre-stack images. Because the overburden geology along the studied section is relatively simple, the baseline image (Figure 5.4(a)) and the monitor image (Figure 5.4(b)) are sufficiently aligned using only vertical components of the prestack apparent displacement vectors (Figure 5.5). The apparent displacements between the stacked baseline and monitor images are negligible.

As shown in the Figure 5.8(a), even with good repeatability between survey geometries, it is often impossible to interpret an unprocessed time-lapse image. However,

after careful processing, it is possible to make meaningful interpretations of amplitude information in the time-lapse image (Figure 5.9(b)). Although in many cases, results obtained from a conventional processing workflow may suffice, the quality of the time-lapse image can be improved by inversion (Figure 5.9(c)).

In example *II*, the simulated obstruction in the monitor geometry represents a practical problem in many field applications, where the construction of production facilities causes differences between the baseline and monitor geometries. As discussed earlier in this dissertation, if such differences are small, data-regularization methods (e.g., interpolation) may be sufficient to correct for them. However, although the time-lapse amplitude information derivable from the interpolated monitor data (not shown) is of poor quality, the kinematics of the monitor image are similar to those of the complete baseline image. Therefore, these provide adequate estimates of the warping parameters (Figure 5.11) that are comparable to those from the complete data case (Figure 5.5).

Because the monitor data is incomplete, the effective geometries differ for the two surveys, thereby leading to illumination mismatch (i.e., illumination ratios less than unity) in parts of the target area (Figure 5.12). However, the Hessian diagonal gives only a partial measure of the illumination mismatch between time-lapse surveys (Figure 5.12). Large geometry differences (e.g., an obstruction in the monitor acquisition) can cause large differences in the off-diagonal elements of the Hessian (Figures 5.13 and 5.14). As a consequence, as shown in Figures 5.13 and 5.14, such geometry differences lead to differences in the range of illuminated wavenumbers/angles between surveys. Therefore, a point-by-point amplitude compensation using only the Hessian diagonal is inadequate.

In this example, artifacts in Figure 5.15(a), caused by the large differences in acquisition geometries between the baseline and monitor surveys, cannot be adequately attenuated by conventional time-lapse processing methods (Figure 5.15(b)). In this case, regularized joint image-domain inversion provides a significant improvement to the time-lapse image (Figure 5.15(c)). Finally, as shown in figure 5.16, because it contains only limited information about subsurface illumination discrepancies, the

diagonal of the Hessian cannot fully account for the effects of geometry differences between time-lapse seismic data sets.

## CONCLUSIONS

Careful data preprocessing is an important part of time-lapse seismic imaging—even more when performing inversion, as processed in this dissertation. In this chapter, I showed how data preprocessing helps to remove uncorrelated artifacts and multiples in the recorded data. In addition, I showed that it helps to account for small differences in recording equipment and environmental conditions for different surveys. And, importantly, I showed that these preprocessing steps can be used to condition the recorded data for regularized joint inversion.

For data sets recorded with carefully repeated conventional acquisition geometries, the preprocessing methods described in this chapter can provide time-lapse images that are representative of the actual changes in reservoir properties. However, where there are significant differences between the acquisition geometries of different surveys, these preprocessing methods are insufficient. This is because differences in acquisition geometries cause differences in the range of illuminated wavenumbers/angles at subsurface image points. Because regularized joint image-domain inversion accounts for such illumination mismatches and for band-limited wave-propagation effects, it provides images with improved resolution and better definition of seismic amplitude changes.

In the next chapter, I demonstrate different applications of regularized joint inversion to three-dimensional ocean-bottom-cable (OBC) time-lapse data sets.

## ACKNOWLEDGMENTS

I thank Statoil and partners (ENI and Petoro) for donating the Norne data. I thank the Stanford Center for Computational Earth & Environmental Science (CEES) for providing the computer resources used in these studies.



# Chapter 6

## 3D field data applications

In this chapter, I present different applications of regularized joint image-domain inversion—developed in chapter 3—to three-dimensional time-lapse ocean-bottom-cable (OBC) data sets. Recall that in chapter 5, I described some important preprocessing steps required for regularized joint image-domain inversion and showed that the method improves time-lapse amplitude information in a two-dimensional marine streamer time-lapse data set. The data studied in this chapter are preprocessed subsets of full-azimuth OBC data sets acquired as part of BP’s Valhall Life of Field Seismic (LoFS) reservoir-monitoring project.

Valhall is a giant oil field located in the southern part of the Norwegian sector of the North Sea. The reservoir in this field is made up of high-porosity, low-permeability Cretaceous chalk at a depth of approximately 2,400 m—at the crest of the structure (Munns, 1985). The reservoir thickness varies between 10 and 60 m (Munns, 1985). This field is located at a water depth of about 60 m, and has been on production since 1982 (Barkved et al., 2003).

The Valhall LoFS project utilizes a permanent recording system of ocean bottom cables to provide continuous monitoring of changes in reservoir and overburden properties caused by hydrocarbon production and water injection in the field. Changes in fluid content, together with the associated changes in the pressure and stress regimes,

result in large changes in the acoustic properties of the rocks within and around the reservoir. In addition, because of the high porosity of the reservoir rocks, hydrocarbon production and water injection cause compaction and overburden subsidence in the field (van Gestel et al., 2008). Therefore, there are strong time-lapse seismic responses associated with hydrocarbon production and water injection in the field.

The Valhall field has been studied extensively. Today, there is a wide range of published work on different aspects of hydrocarbon exploration, on the field development and production history, and on various aspects of the LoFS reservoir monitoring project. For example, Munns (1985) discusses the geology and stratigraphy of the Valhall field in detail; Ali and Alcock (1994) and Barkved et al. (2003) discuss the production history and development plans for the field; Barkved (2004) discusses the permanent seismic acquisition array and the key objectives of the LoFS reservoir monitoring project; Kommedal et al. (2007) and van Gestel et al. (2008) discuss aspects of the seismic data acquisition, processing, and analysis; Hatchell et al. (2005) and van Gestel et al. (2011) discuss aspects of the seismic data interpretation and integration with other reservoir data; and Barkved et al. (2010) discuss the impact of robust velocity model building—by full waveform inversion—on static and dynamic imaging in the field.

For this study, I use available subsets of the original LoFS seismic data sets. These subsets cover the Southern flank of the Valhall structure, far away from the gas clouds located above the crest of the Valhall structure. Figure 6.1 shows the location of gas cloud within the baseline velocity model—obtained by full waveform inversion (Sirgue et al., 2010). Note the location of the target area for this study relative to the gas clouds (Figure 6.1). These gas clouds present some challenges to seismic imaging, and consequently to seismic monitoring. As noted in previous chapters, conventional imaging does not fully account for illumination distortions, which in this case are caused by the relatively low velocity of the gas clouds. Therefore, regularized joint inversion—which compensates for such distortions—will potentially have more positive impact in monitoring the reservoir under the gas clouds. However, the data required for such a study are currently not available at Stanford.

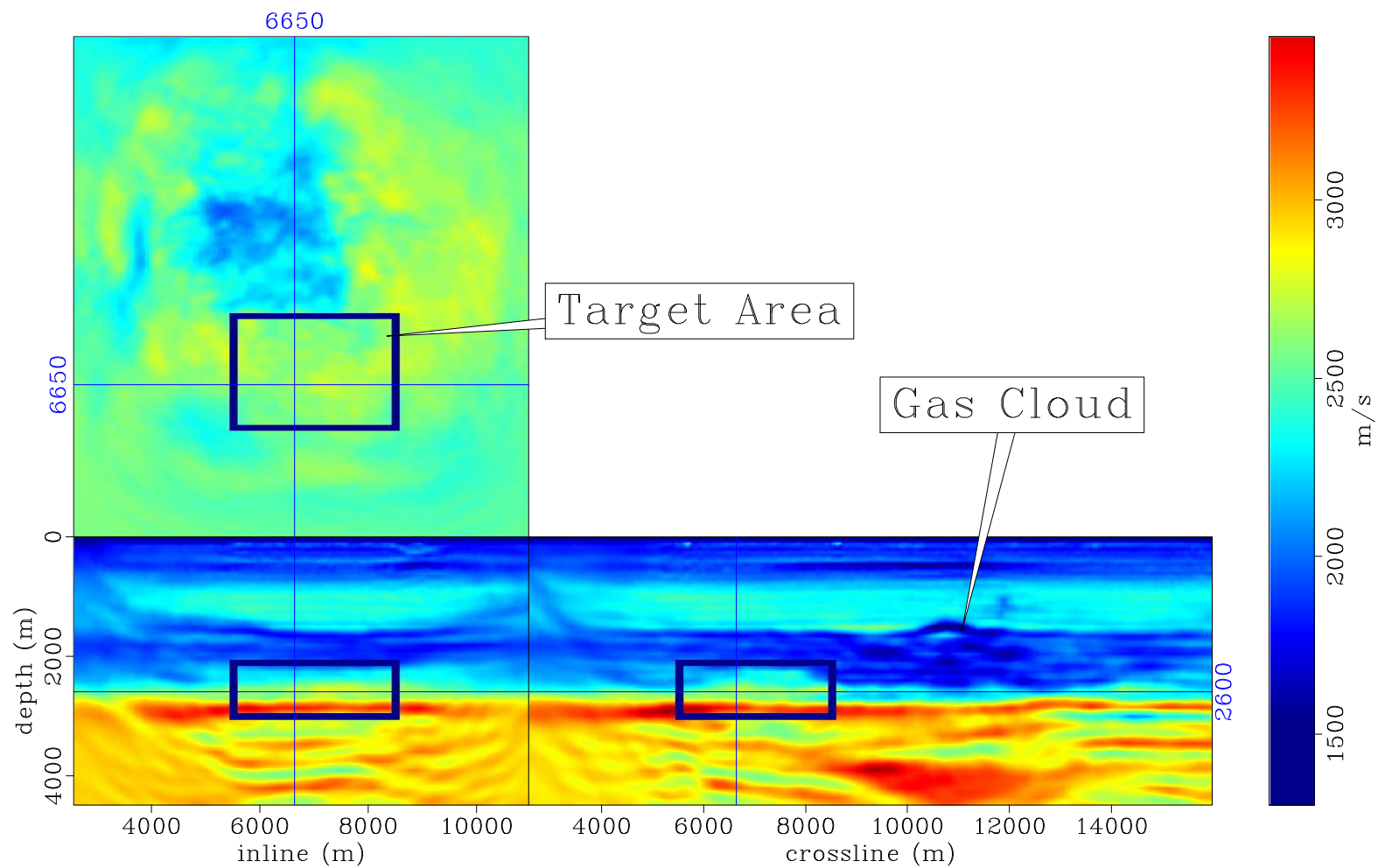


Figure 6.1: Baseline migration velocity obtained by full waveform inversion (see Sirgue et al. (2010)). This velocity model was used to image all data sets in this study. The target area—indicated by the box—is restricted to a small area of interest around the reservoir. The gas cloud, located outside the study area, does not cause significant imaging challenges in the target area. [NR] chap6/. vel-11

Figure 6.2 shows the full acquisition geometry of the Valhall LoFS project and the location of the study area considered in this chapter. Whereas the original (full) data consists of approximately 50,000 shots and 2,400 receivers, the available data subset consists of approximately 33,000 shots and 470 receivers. Figure 6.3 shows the geometry for the data subset, and the location of a gap within the study area that represents a simulated obstruction in the monitor geometry (described in detail later in Figure 6.6).

An enlarged view of the source-receiver geometry within the study area (Figure 6.3) is presented in Figure 6.4. The shots are spaced at 50 m in both the inline and crossline directions, while the receivers, located along 10 permanent cables, are spaced at 50 m in the inline and 300 m in the crossline directions (Figure 6.4). The receiver cables are buried at a depth from the water surface of approximately 70 m. For the data subset used in this chapter, the maximum absolute source-receiver offset is approximately 5 km.

The donor (BP) has adequately preprocessed these data sets, such that only the up-going primary compressional wave data are preserved. Therefore, unlike in the previous chapter, no additional preprocessing is applied to these data prior to migration. Examples of the preprocessed receiver gathers from the first survey (LoFS 1) and the ninth survey (LoFS 9) are presented in Figure 6.5. As shown in Figure 6.5, these receiver gathers, which are from the same location in the two surveys, contain data from the full range of azimuths.

The setup of the LoFS acquisition geometry allows for good repeatability of both source and receiver positions between surveys. For each survey, the source positions are repeated almost perfectly, with a standard deviation of approximately 5 m. Because the receiver cables are permanently installed, the receiver locations are repeated to a high degree of accuracy for all surveys. For this study, results from the original geometry provide a good reference to which results obtained from simulated problems in the recording geometry can be compared. Furthermore, the good source-receiver geometry repeatability allows testing of geophysical effects that are not associated with the data recording.

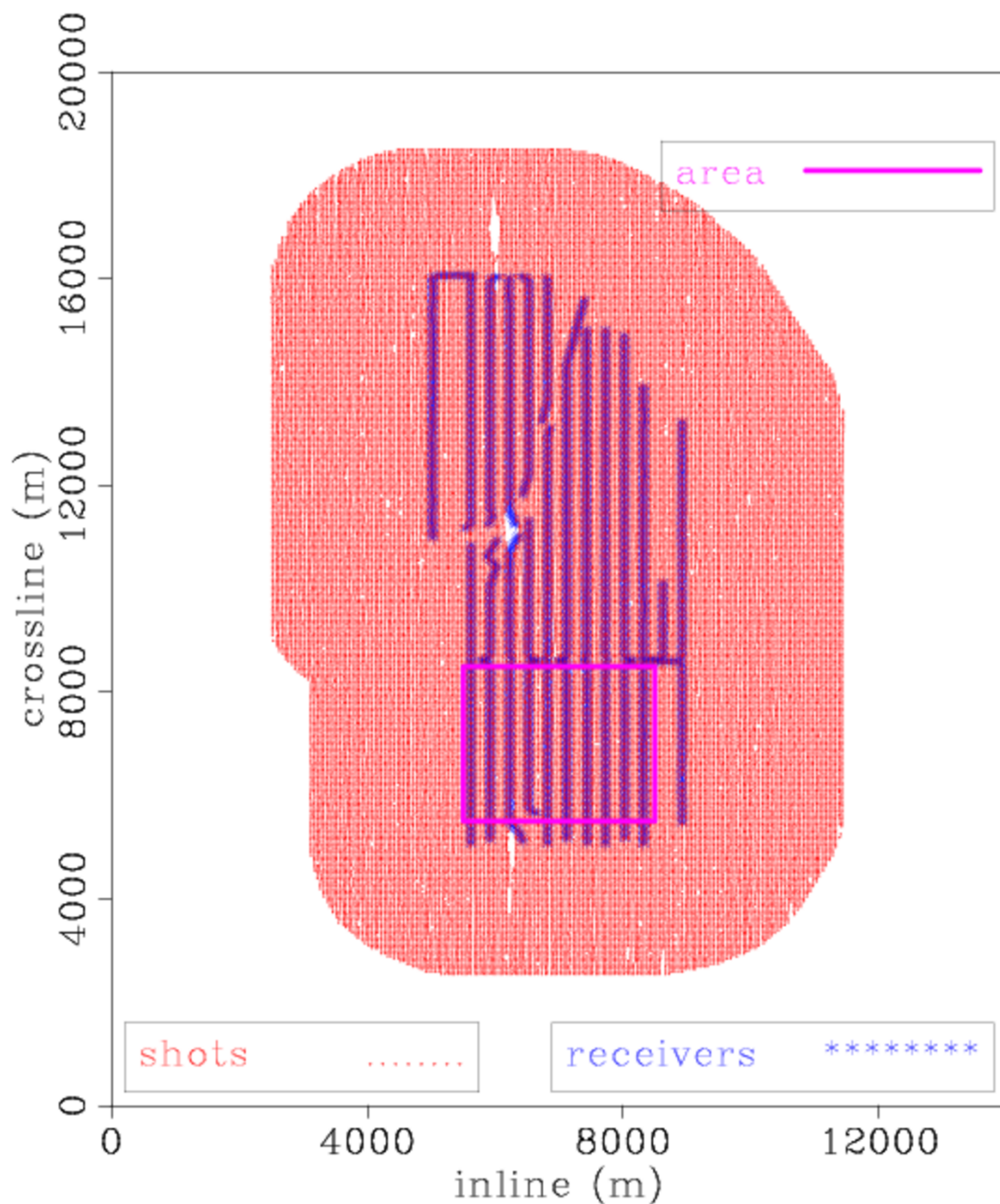


Figure 6.2: Full LoFS acquisition geometry showing locations of all shots and receivers. The purple box indicates the location of the study area, shown in detail in Figure 6.3. The coordinate axes in these figures (and in all figures) are distances in meters. [ER] chap6/. sgorig-1

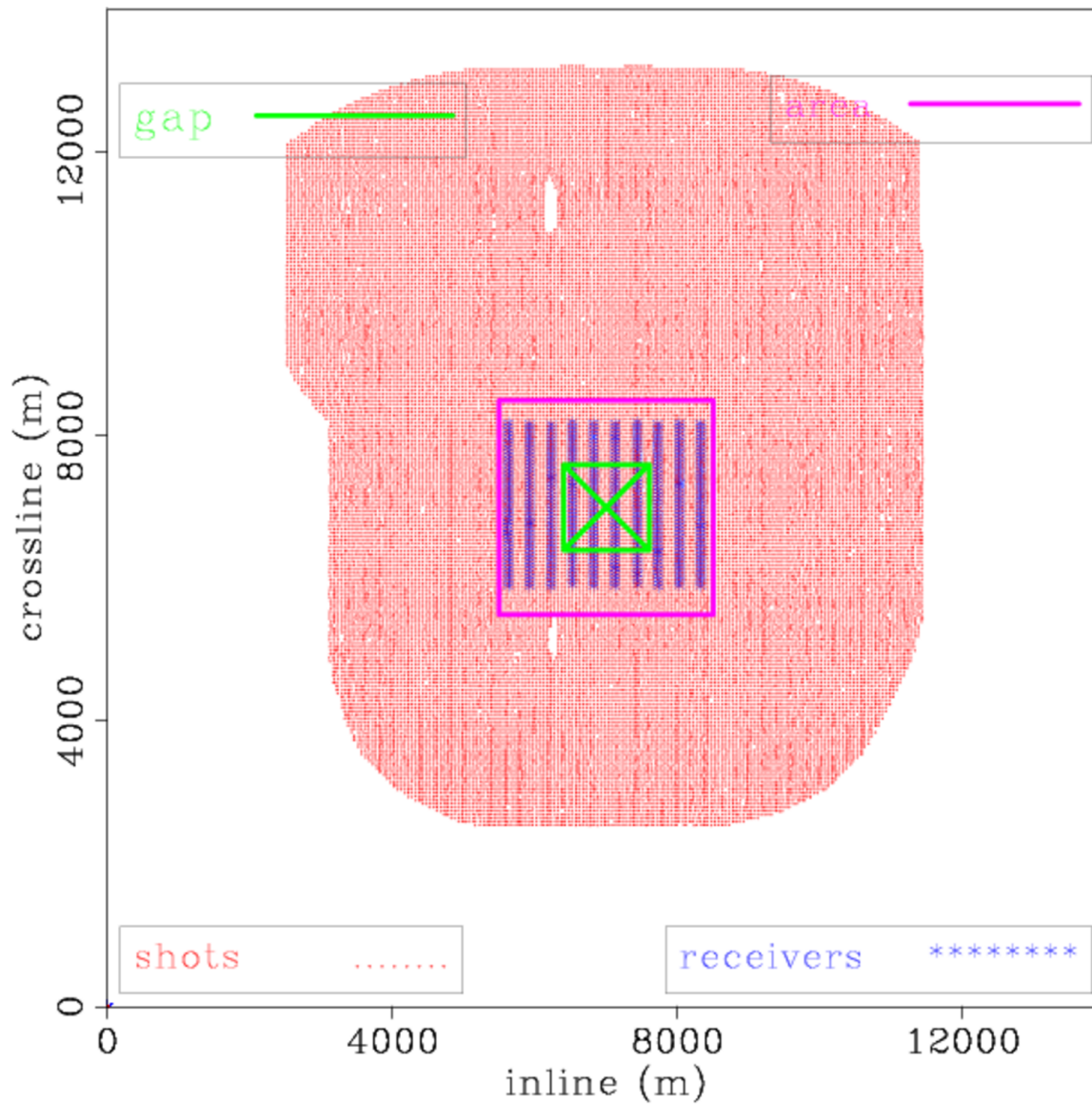


Figure 6.3: Acquisition geometry showing locations of all shots and receivers for the data subsets used in this study. Apart from the introduction of gaps in some examples, the source-receiver geometry is closely repeated for all data sets. The gap is located at the center of the study area (see Figure 6.6). An enlarged view of the study area is presented in Figure 6.4. [ER] `chap6/. sgfull-1-gap`

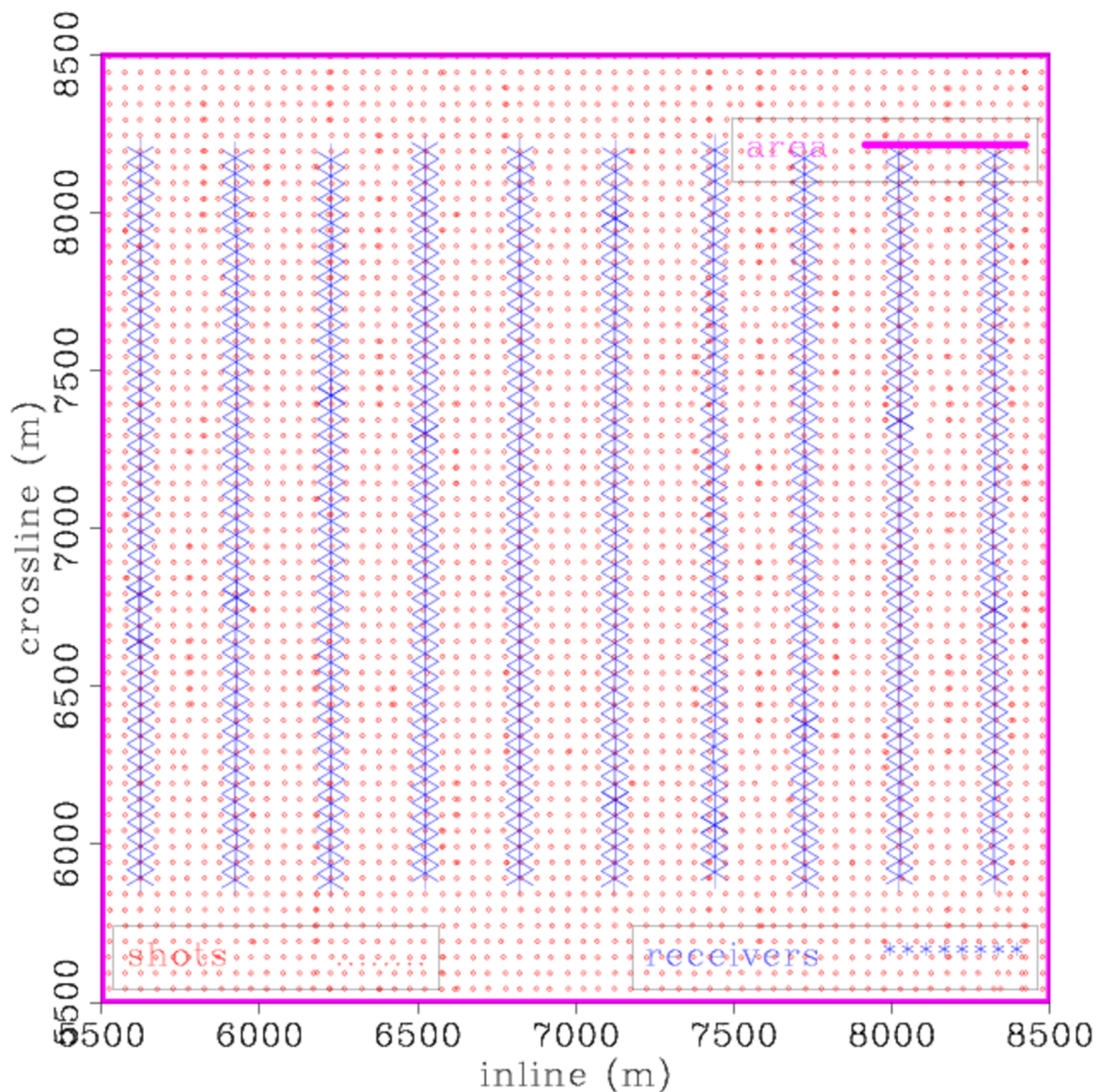


Figure 6.4: An enlarged view of the study area (Figure 6.3) showing the complete source-receiver geometry. The shot spacing is 50 m in both the inline and crossline directions, while the receiver spacing is 50 m in the inline direction and 300 m in the crossline direction. [ER] chap6/. sgwfull-1

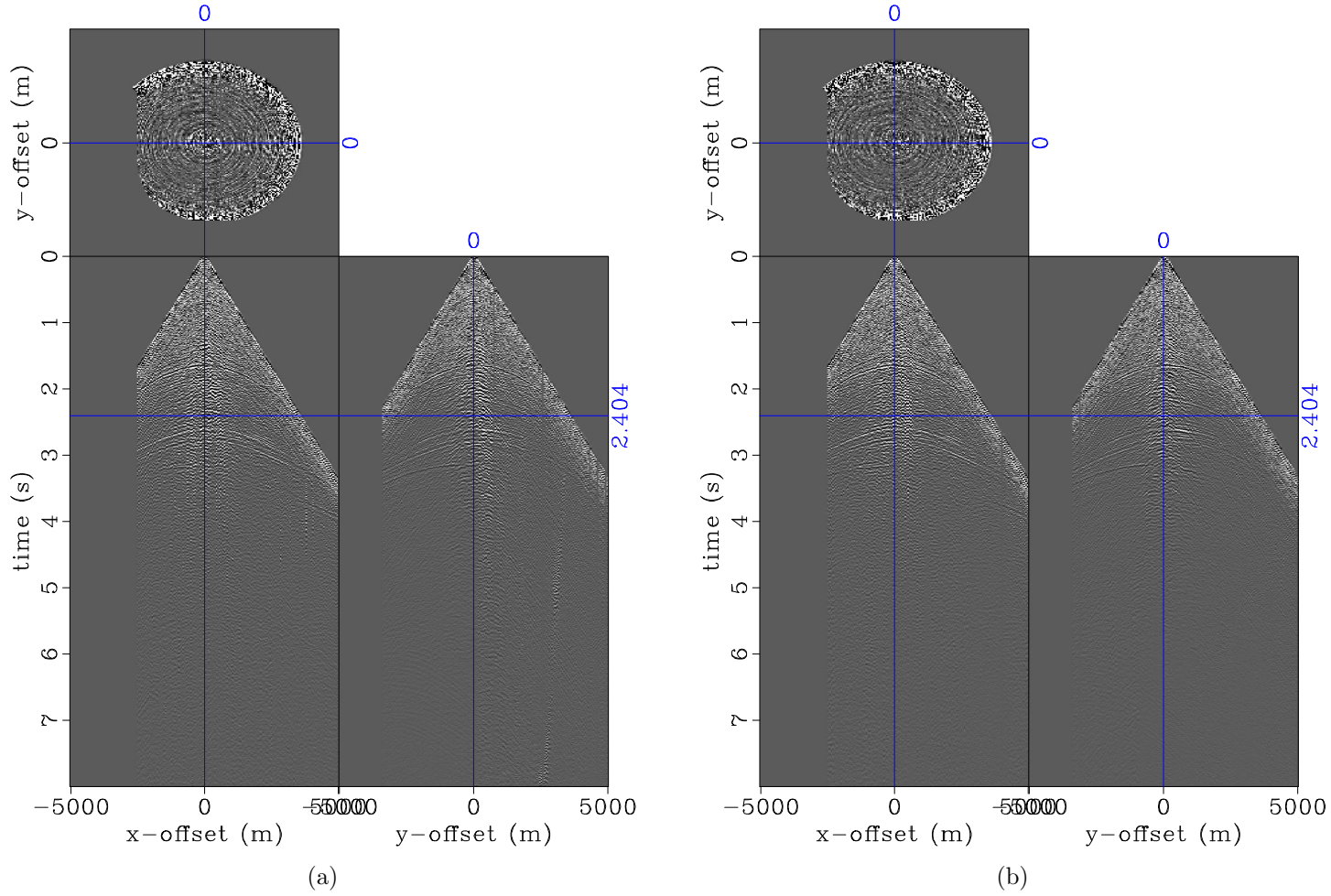


Figure 6.5: Sample receiver gathers acquired at the same location for the first (a), and ninth (b) LoFS surveys. Note in both gathers the full azimuth of the recording geometry. In both panels, the second and third dimensions are the inline and crossline offsets, respectively. [ER] chap6/. shot-11,shot-19

In the following sections, I present three examples that demonstrate applications of regularized joint image-domain inversion:

- First, using two data sets from the first and ninth LoFS surveys, as in the previous chapter, I show how regularized joint image-domain inversion can be used to attenuate artifacts that are caused by a simulated obstruction in the monitor geometry. This example shows that inversion of these incomplete data provides time-lapse amplitudes that are comparable to those obtained from the complete data.
- Second, using three data sets from the first, fifth, and ninth surveys, I show how regularized joint image-domain inversion can be applied to multiple data sets. In this example, as in the previous, I assume that these three surveys have different geometries caused by the presence of simulated obstructions in the monitor surveys. Recall that in chapter 4, I demonstrated an application of joint image-domain inversion to synthetic migrated images obtained by multiplying the Hessian matrices corresponding to these three surveys with synthetic reflectivity images.
- Third, using the complete data from the first and ninth surveys, I demonstrate that because of its high computational efficiency, regularized joint image-domain inversion method can be used to obtain multiple realistic time-lapse images by choosing multiple regularization parameters. This is advantageous because it allows the testing of different geological and petrophysical scenarios that might explain the changes observed in the acoustic properties of the reservoir and surrounding rocks. This can help in the quantification of uncertainties associated with interpretation of the time-lapse seismic data.

These examples demonstrate that regularized joint image-domain inversion is an effective tool for obtaining time-lapse seismic images that have better resolution, better quality, and higher reliability than those obtained from conventional imaging by migration.

### *Example I: Inversion of incomplete data*

In this section, I consider data from the first survey (LoFS 1) and the ninth survey (LoFS 9), acquired in November 2003 and December 2007, respectively. In this example (and in other examples presented in this chapter), LoFS 1 is the baseline.

To simulate an obstruction in the monitor geometry, I create a 1.44 km<sup>2</sup> gap at the center of the 9 km<sup>2</sup> study area (Figures 6.3). Figure 6.6 shows an enlarged view of the study area indicating the location of the simulated obstruction. As shown in Figure 6.6, in order to maximize the geometry difference between the baseline and monitor surveys, no shots and receivers are present within the obstruction area in the monitor geometry.

Figure 6.7 shows the common-midpoint (CMP) fold for the complete (baseline) and incomplete (monitor) geometries. The highest fold is approximately 1,900 in the baseline geometry (Figure 6.7(a)), whereas it is approximately 1,600 in the monitor geometry (Figure 6.7(b)). Because of the full azimuth coverage of the recording geometry, these CMP folds are higher than those in typical seismic surveys. As shown in Figure 6.7, the differences in fold between the two geometries are largest within the obstruction area. Although CMP folds provide a measure of the geometry difference, as I will show later, differences in subsurface illumination associated with such geometry difference are too complex to be represented by CMP fold differences.

### Subsurface illumination (Hessian diagonal) of study area

As described in previous chapters, one measure of the subsurface illumination is the diagonal of the Hessian. For both geometries, I compute the diagonal of the Hessian for the study area using 64 frequencies, which are spaced equally within the migration frequency band (described later in this section). In this and in other examples presented in the chapter, I use the random phase-encoded approximation of the Hessian defined in equation 3.12 and described in detail by Tang (2011). For each geometry, I use four random realizations of the receiver-side Green's functions.

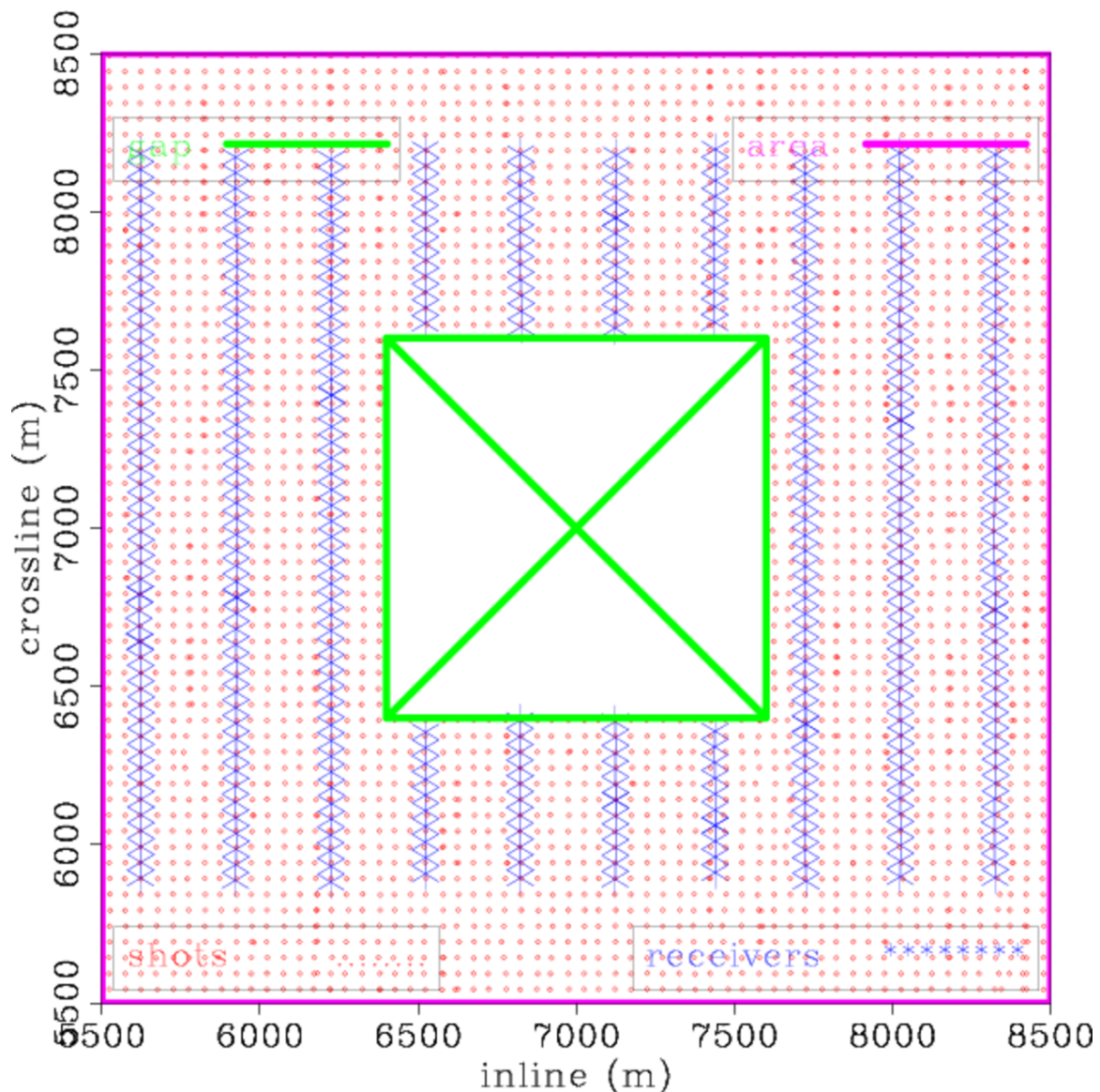


Figure 6.6: An enlarged view of the study area (Figure 6.3) showing the shot and receiver locations within the study area, and the location of the simulated obstruction in the monitor geometry. There are not sources and receivers within the gap. Compare this to Figure 6.4, which shows the complete geometry of the baseline survey. [ER] chap6/. Osgwfull-9-gap

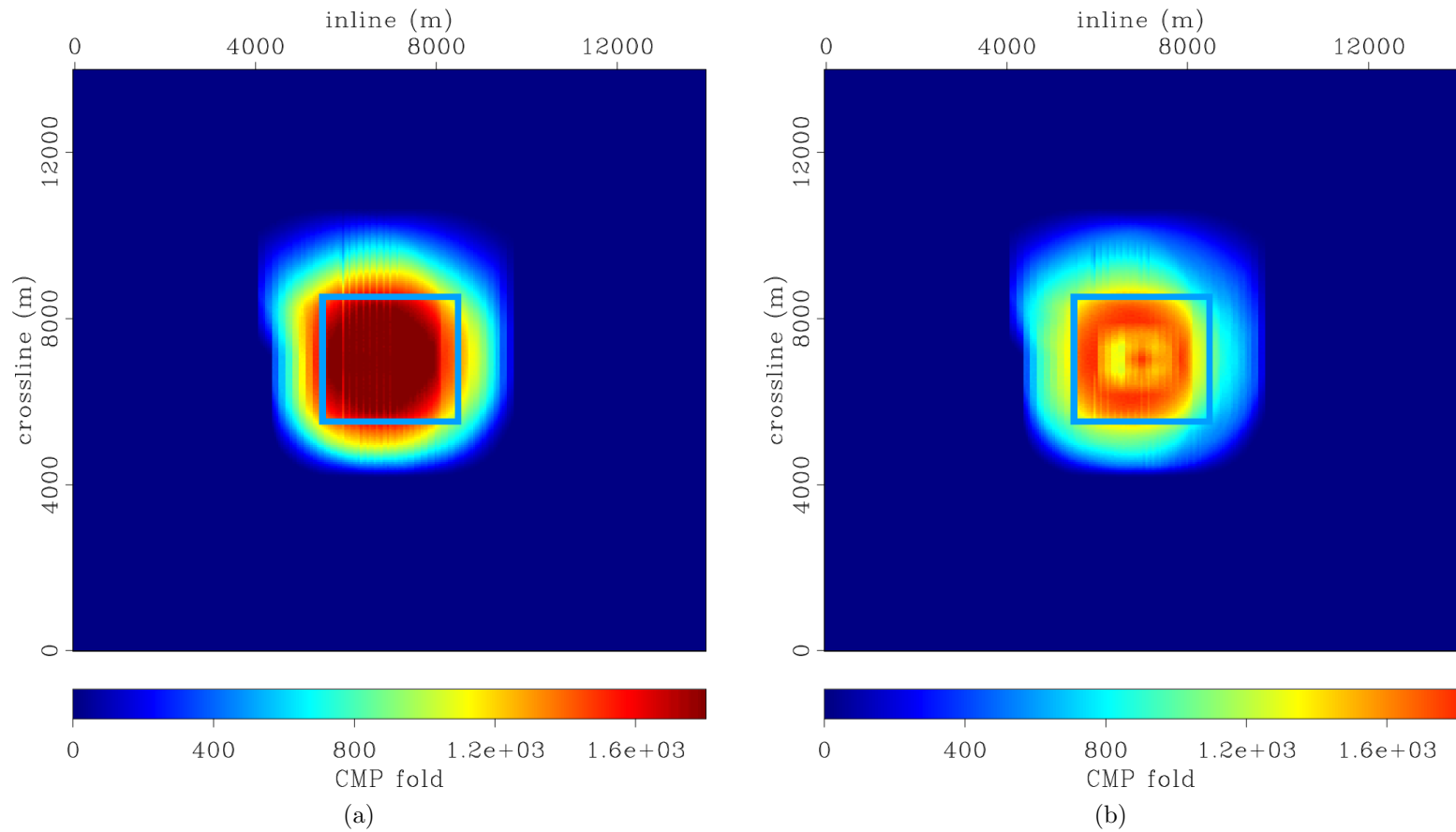


Figure 6.7: Surface (CMP) fold for the baseline (a) and monitor (b). Red indicates high fold, whereas blue indicates low fold. Note that whereas the baseline fold is mostly uniform within the study area, the gapped monitor geometry causes significant non-uniformity of fold. The box indicates the same study area shown in Figures 6.3. [ER]

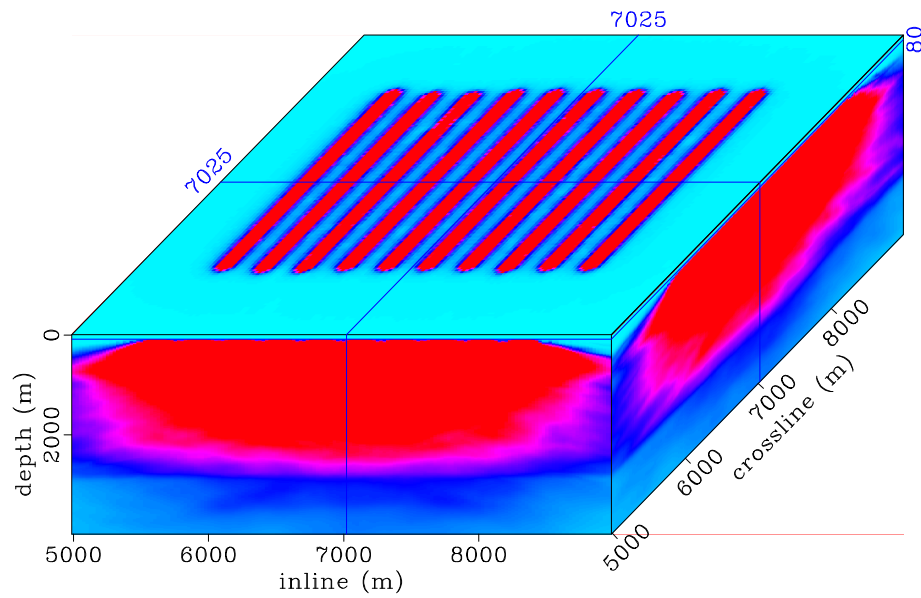
chap6/. cfold-1-full,cfold-9-gap

The subsurface illumination of the study area for the baseline and monitor geometries are presented in Figures 6.8 to 6.10. Figure 6.8 shows the subsurface illumination with a depth slice at the ocean bottom. The locations of the 10 receiver cables, and of the simulated obstruction can be seen clearly in Figure 6.8. Figure 6.9 shows the subsurface illumination with a depth slice at 1,750 m, above the reservoir and outside the target area for inversion. The subsurface illumination for the two geometries showing a depth slice through the reservoir at 2,600 m, is presented in Figure 6.10. In general, the subsurface illumination increases in complexity with depth. In both the baseline and monitor geometries, the subsurface illumination distribution is highly non-stationary throughout the study area.

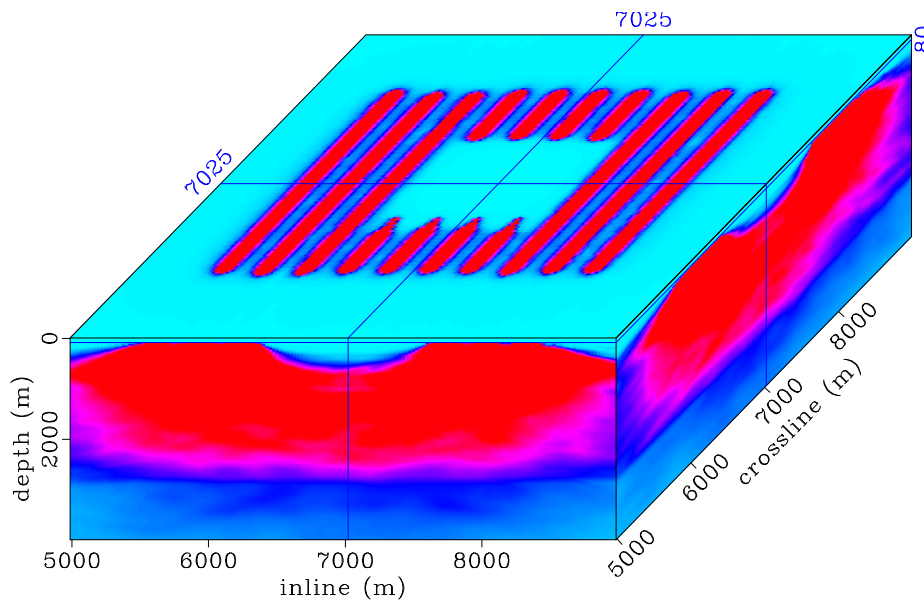
To measure the difference in subsurface illumination, I compute the ratio of the subsurface illumination between the baseline and monitor geometries. The illumination ratio is presented in Figure 6.11 with depth slices at the ocean bottom and at the reservoir depth. Although the illumination discrepancy is simple at the ocean bottom (Figure 6.11(a)), it becomes highly complex at the reservoir depth (Figure 6.11(b)). Comparing this subsurface illumination ratio with the difference in surface CMP folds (Figure 6.7), it is clear that it is impossible to fully account for the geometry difference using information derived from only CMP folds. However, as shown in chapter 4, one important limitation in the use of the Hessian diagonal as a weighting function to correct for illumination discrepancies in migrated images is that it applies equal weights to all illuminated wavenumbers/angles. To obtain more complete information about differences in the dip-dependent subsurface illumination between surveys, in the next section, I compute the off-diagonal elements of the Hessian matrices.

### Hessian matrix of the target area

The target area for inversion is a small (700 x 3000 x 3000 m) window around the reservoir, located within the study area (Figure 6.1). For this target area, I compute the approximate Hessian using 64 frequencies and six random realizations of the receiver-side Green's functions. At each subsurface location within the target area, the off-diagonal elements (PSFs) are 300 x 300 x 300 m in size.

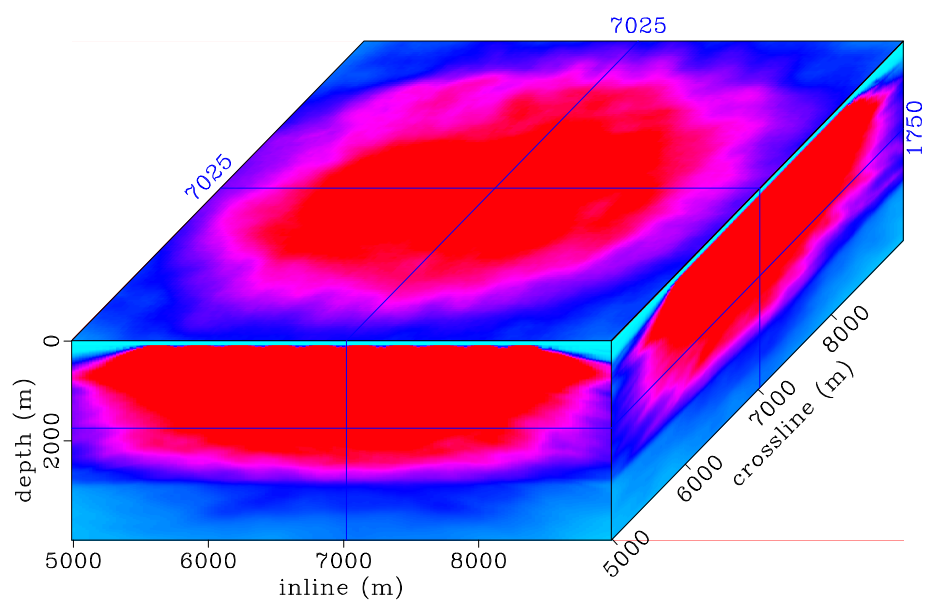


(a)

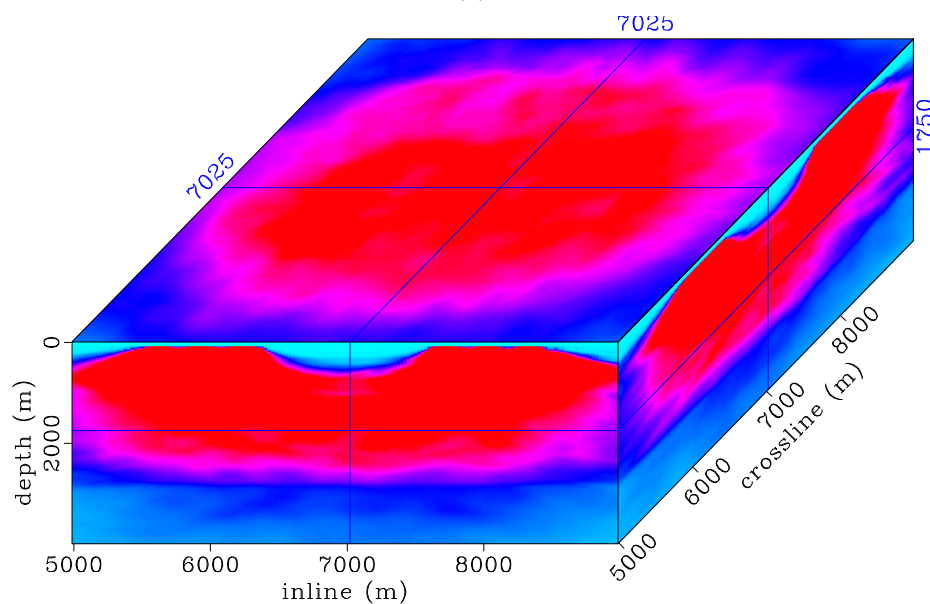


(b)

Figure 6.8: Hessian diagonal for the complete baseline (a) and incomplete monitor (b) geometries. In these (and similar) displays throughout this chapter, the top panel is a depth slice and the side panels are the inline and crossline slices. The crosshairs show the position of the slices in the image cube. The depth slices show the illumination at the ocean bottom (a) and (b). Red indicates high illumination, whereas cyan indicates low illumination. [CR] chap6/. ilum-1,ilumg2-1



(a)



(b)

Figure 6.9: Hessian diagonal for the complete baseline (a) and incomplete monitor (b). The depth slices show the illumination at a depth the above the reservoir. Red indicates high illumination, whereas cyan indicates low illumination. [CR] chap6/. ilum-3,ilung2-3

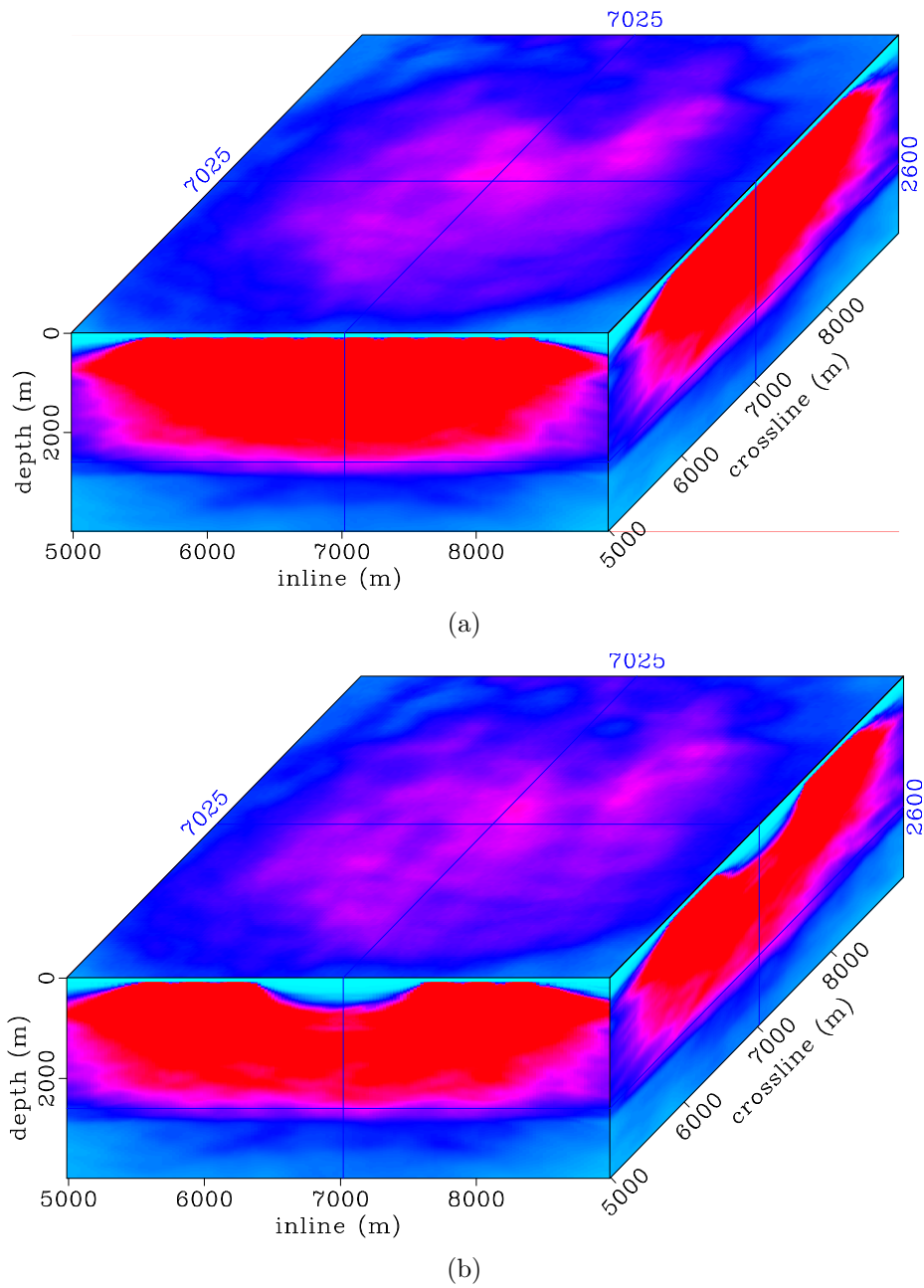
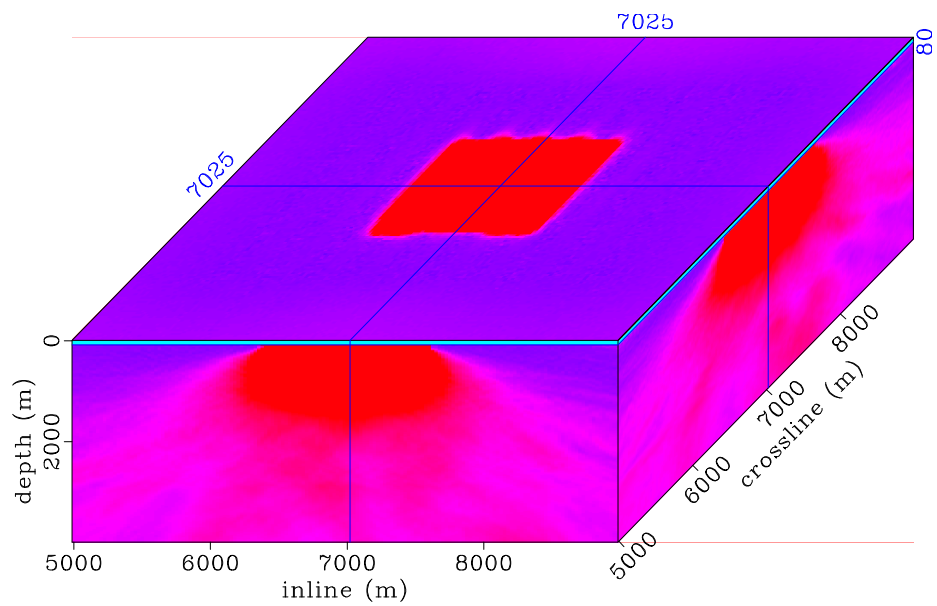
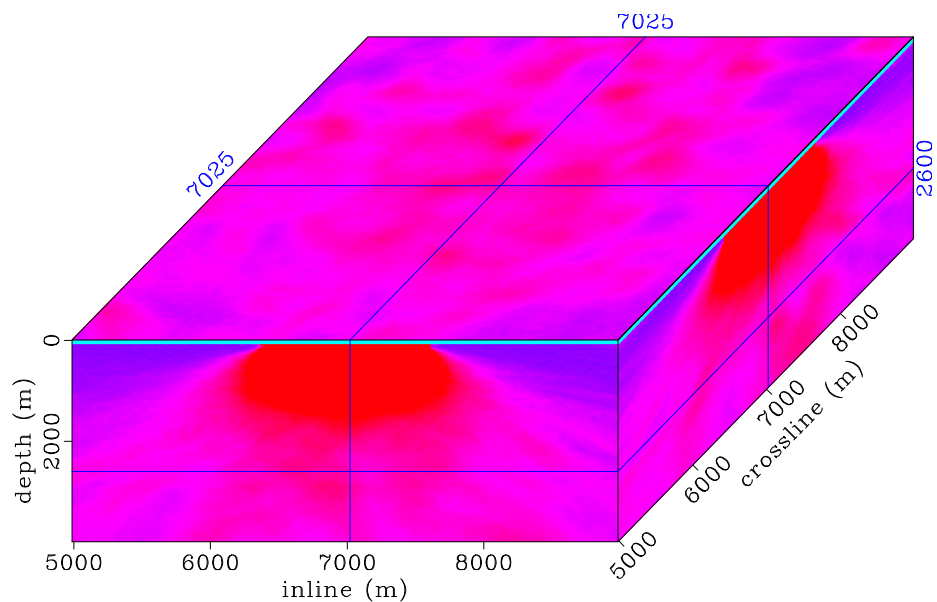


Figure 6.10: Hessian diagonal for the complete baseline (a) and incomplete monitor (b). The depth slices show the illumination within the reservoir. Red indicates high illumination, whereas cyan indicates low illumination. [CR] chap6/. ilum-4,ilumg2-4



(a)



(b)

Figure 6.11: Illumination ratio between the baseline and monitor at the ocean bottom (a) and at the reservoir depth (b). Note that the simple rectangular illumination disparity at the ocean bottom becomes more complex at the reservoir depth. [CR] chap6/. ilumr2-1,ilumr2-4

Figure 6.12 shows an example of the off-diagonal elements along the a row the Hessian matrix (PSF) derived from the baseline geometry in the spatial and wavenumber domains. As shown in Figure 6.12(b), at this subsurface position, the baseline ge-

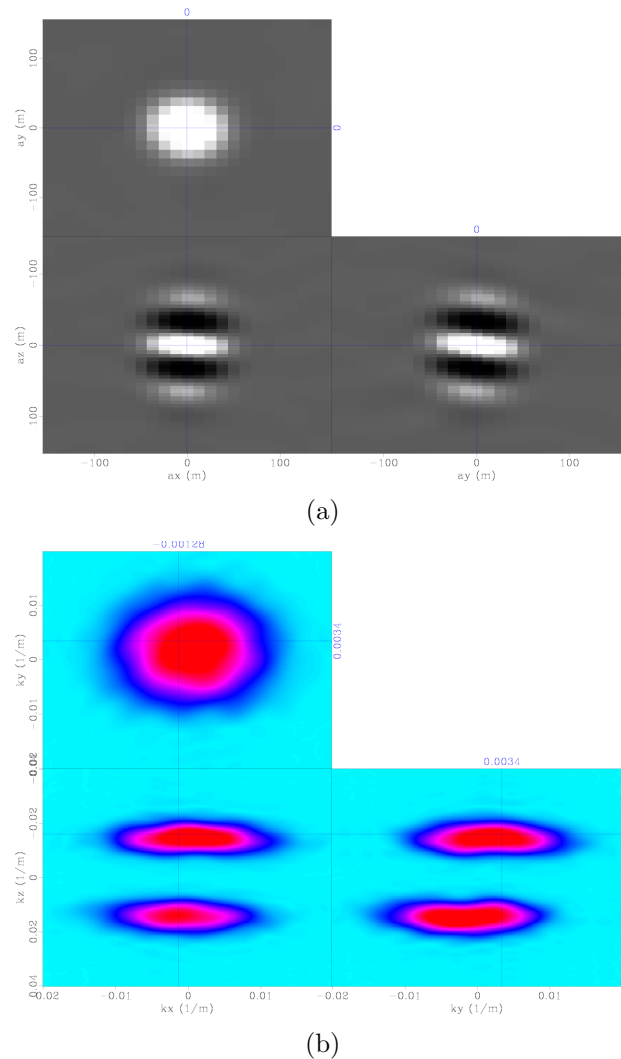


Figure 6.12: Point spread function (row of the baseline Hessian matrix) at subsurface point inline 6,600 m, crossline 6,475 m and depth 2,580 m in the spatial domain (a), and in the wavenumber domain (b) for the complete (baseline) geometry. [CR] chap6/. 3d3-psf-1,3d3-psf-fft-1

ometry provides sufficient coverage in all directions. Figure 6.13 shows the difference between the baseline and monitor PSFs in the spatial and wavenumber domains. As

shown in Figure 6.13(b), the gap in the monitor geometry (Figure 6.6) leads to incomplete illumination of various wavenumbers. Instead of equal weighting assumed by

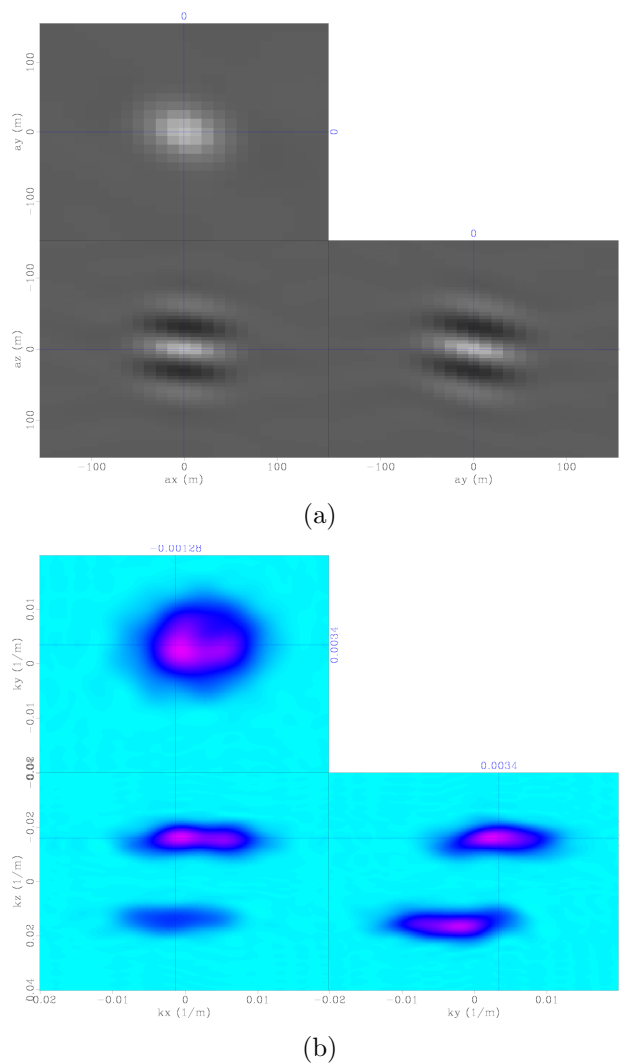


Figure 6.13: Difference between the baseline point spread function at subsurface point inline 6,600 m, crossline 6,475 m and depth 2,580 m (Figure 6.12) and the monitor point spread function at the same point in the spatial domain (a), and in the wavenumber domain (b). [CR] chap6/. 3d3-psf-19,3d3-psf-fft-19

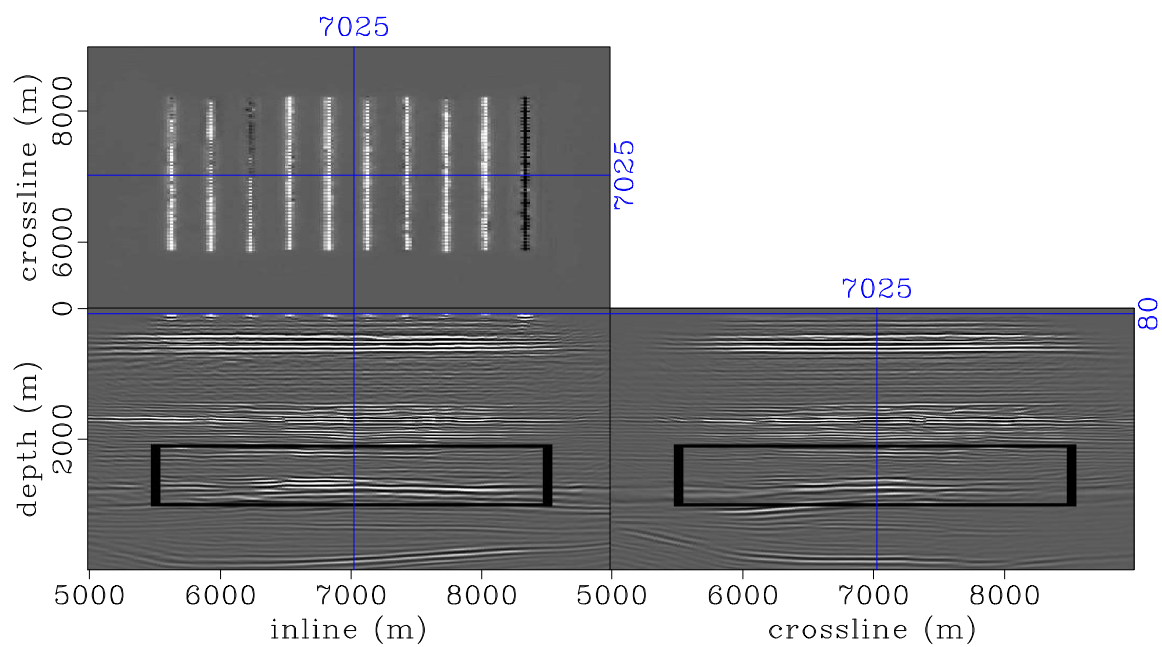
the use of only the diagonal of the Hessian, the off-diagonal elements allow accurate compensation of illumination discrepancies for different wavenumbers.

## Migration

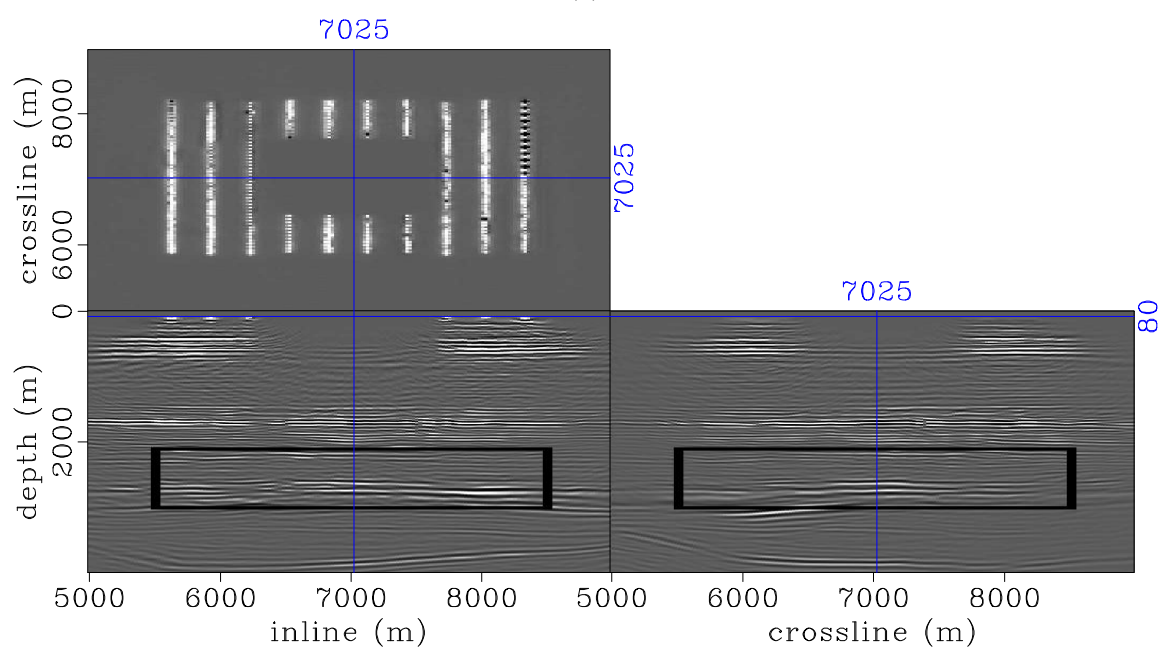
Using reciprocity, the shot and receiver locations are swapped, such that for imaging purposes, the receiver gathers are treated as shot records. Recall that examples of these full-azimuth receiver gathers were presented in the previous section (Figure 6.5). The data are migrated using 320 equally spaced frequencies up to 35 Hz with a split-step one-way wave-equation shot-profile migration algorithm. The same propagator was used to compute the Hessian described above. Both the baseline and monitor data sets are migrated with the baseline velocity model (Figure 6.1). This velocity model was obtained to a high degree of accuracy—a requirement for the regularized inversion method—thereby providing high-quality imaging of the study area. The migrated baseline and monitor images, showing different depth slices through key formations, are presented in Figures 6.14 to 6.17.

Figure 6.14 shows the migrated baseline and monitor images with depth slices at the ocean bottom. As in the images of the subsurface illumination (Figure 6.8), the positions of the receiver cables and the location of the rectangular gap in the monitor geometry—created by a simulated obstruction—can be seen clearly. Figure 6.15 shows the migrated baseline and monitor images with depth slices at 500 m, showing the locations of shallow faults in the area. Comparing Figure 6.15(b) to Figure 6.14(b), note that at this depth, the effect of the gap on the migrated monitor image has reduced. Figure 6.16 shows the migrated baseline and monitor images with depth slices at 1,750 m, showing clear images of a dominant faulted and channelized unconformity above the reservoir. At this depth, differences between the baseline and monitor images have been further reduced.

The migrated images showing a depth slice through the reservoir are presented in Figure 6.17. At the reservoir depth, differences between the baseline and monitor images are a combination of the effects of geometry difference, and of production- and injection-induced changes in reflectivity. In this example, the goal is to account for geometry difference between the surveys, while preserving production- and injection-induced changes in reflectivity between the baseline and monitor images.

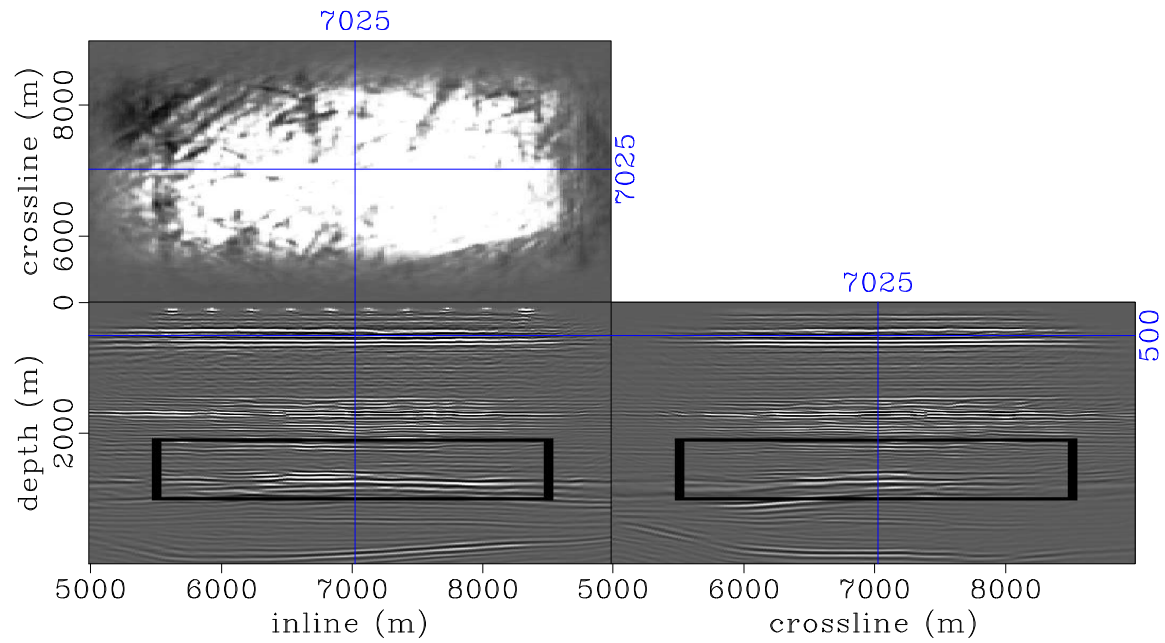


(a)

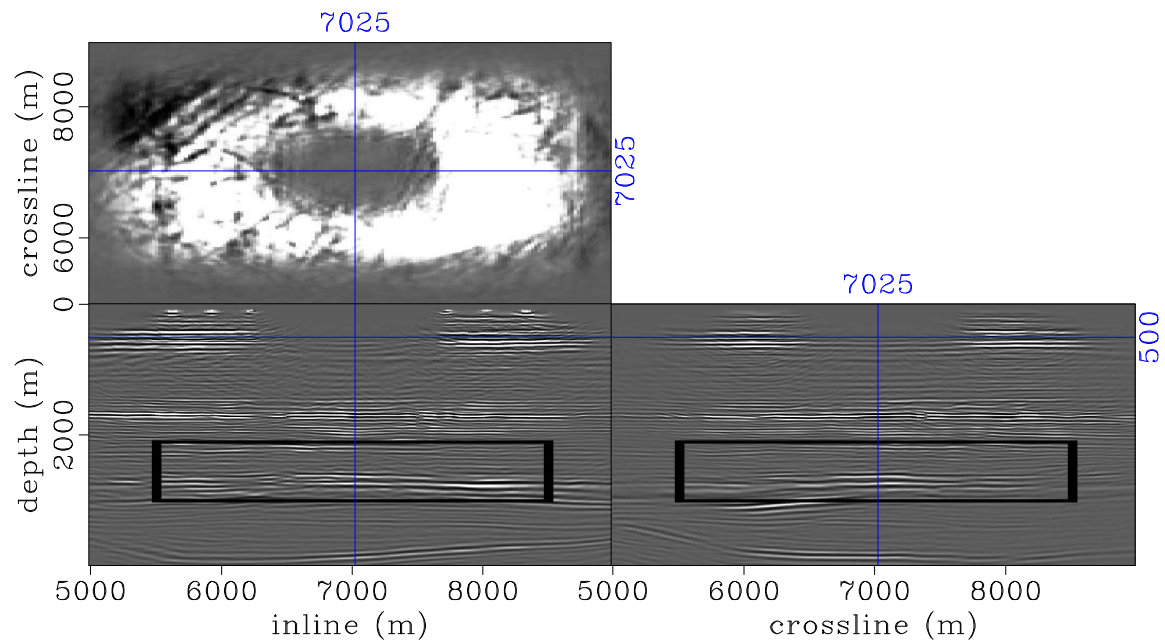


(b)

Figure 6.14: Migrated images showing depth slices at the ocean bottom. The box indicates the target area in the baseline image (a) and in the monitor image (b). Note the location of the gap in the monitor. [CR] chap6/. mig-1-box,migg-1-box

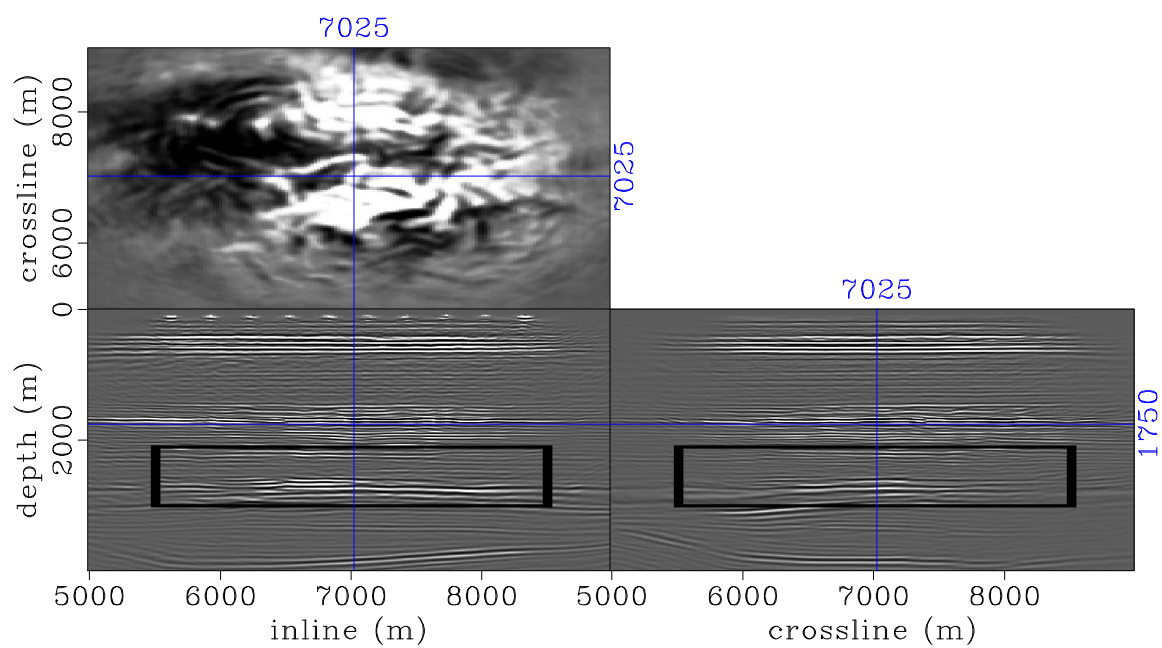


(a)

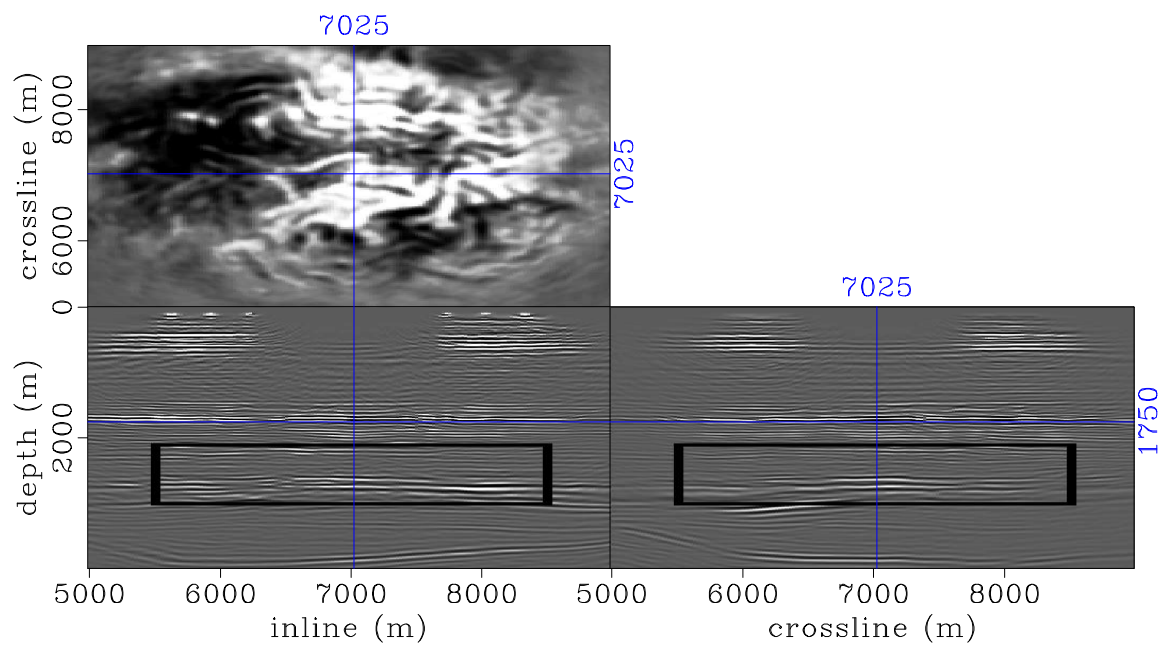


(b)

Figure 6.15: Migrated images showing depth slices at 50 m. The box indicates the target area in the baseline image (a) and in the monitor image (b). The shallow faults at this depth are clearly imaged. [CR] chap6/. mig-2-box,migg-2-box



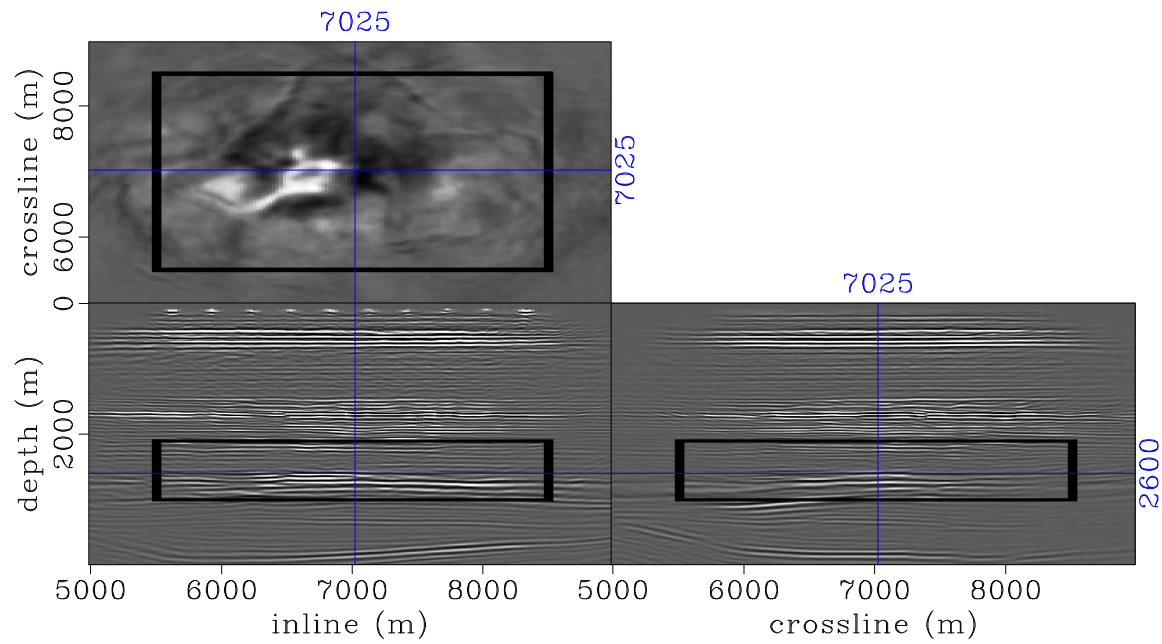
(a)



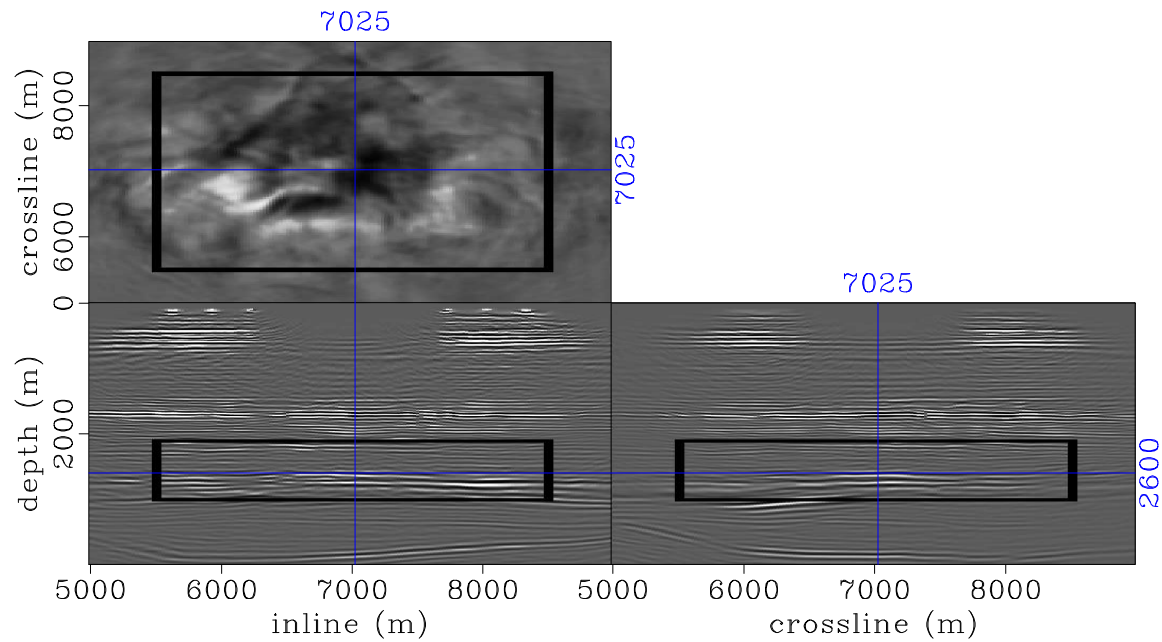
(b)

Figure 6.16: Migrated images showing depth slices above the reservoir at 1,750 m. The box indicates the target area in the baseline image (a) and in the monitor image (b). The well-imaged unconformity show evidence of faulting and channelization.

[CR] chap6/. mig-3-box,migg-3-box



(a)



(b)

Figure 6.17: Migrated images showing depth slices at the reservoir depth. The box indicates the target area in the baseline image (a) and in the monitor image (b). In (a) and (b), the flanks of the Valhall structure are imaged clearly. [CR]

chap6/. mig-4-box,migg-4-box

The boxes in the migrated images (Figures 6.14 to 6.17) indicate the location of the target area. This target area, was chosen to include the reservoir and surrounding rocks. Figure 6.18 shows the migrated baseline and monitor images of the target area, obtained from complete and incomplete geometries respectively. The time-lapse image obtained as the difference between these images is presented in Figure 6.19.

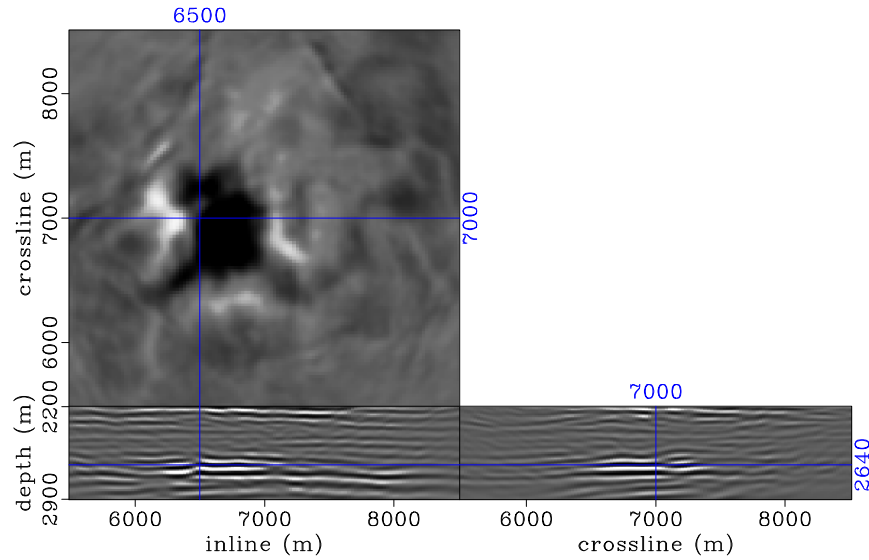
### **Multidimensional warping**

As discussed earlier, we expect that hydrocarbon production and water injection in the reservoir will cause fluid changes and pressure depletion. These will lead to velocity changes and compaction between surveys. Therefore, migrating the monitor data with the baseline velocity causes apparent displacements between the baseline and monitor images. As a result, the time-lapse image in Figure 6.19 contains amplitude differences that are caused not only by production and geometry effects, but also by misalignments between the images associated with velocity changes and compaction between surveys.

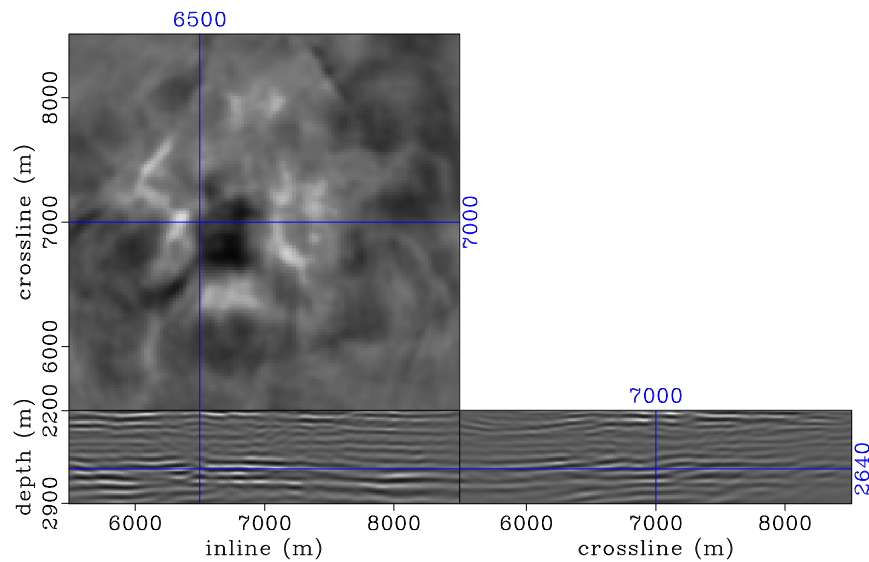
As in the previous chapter, before an interpretable difference image can be obtained between the baseline and monitor images, the apparent displacements must be removed. In addition, as described in chapter 3, removal of these apparent displacements from the migrated images ensures that all image points are collocated. Collocation of baseline and monitor image points is a prerequisite for the regularized joint image-domain inversion method developed in this dissertation.

I estimate the three-dimensional components of the apparent displacements between the baseline and monitor images using the sequential one-dimensional correlation method described in chapter 2. Figure 6.20 shows the vertical (depth) components of the apparent displacement vectors between the baseline image (Figure 6.18(a)) and the monitor image (Figure 6.18(b)). The corresponding inline and crossline components are presented in Figure 6.21.

Figure 6.22(a) shows the time-lapse image between the warped images. For comparison, Figure 6.22(b) shows the reference time-lapse image between the migrated



(a)



(b)

Figure 6.18: Migrated images of the target area obtained from the complete baseline data (a), and the incomplete monitor data (b). The time-lapse image between these images is shown in Figure 6.19. Compare these images to the inverted images in Figure 6.25. [CR] chap6/. gap-b4-mod1,gap-b4-mod2

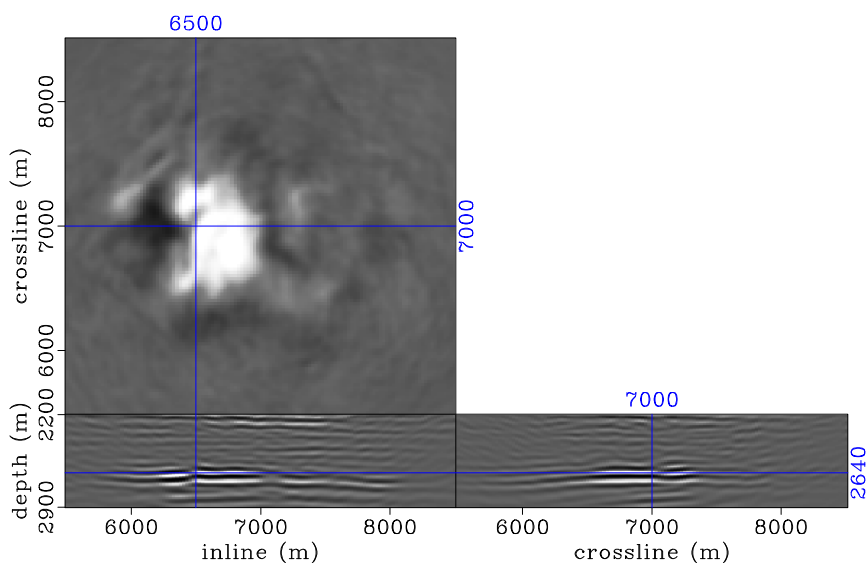


Figure 6.19: Time-lapse image obtained as the difference between the migrated baseline and monitor images (Figure 6.18) prior to warping. Compare this to the time-lapse image difference between the warped images (Figure 6.22(a)), and between the inverted images (Figure 6.24(a)). [CR] chap6/. gap-b4-d-mod

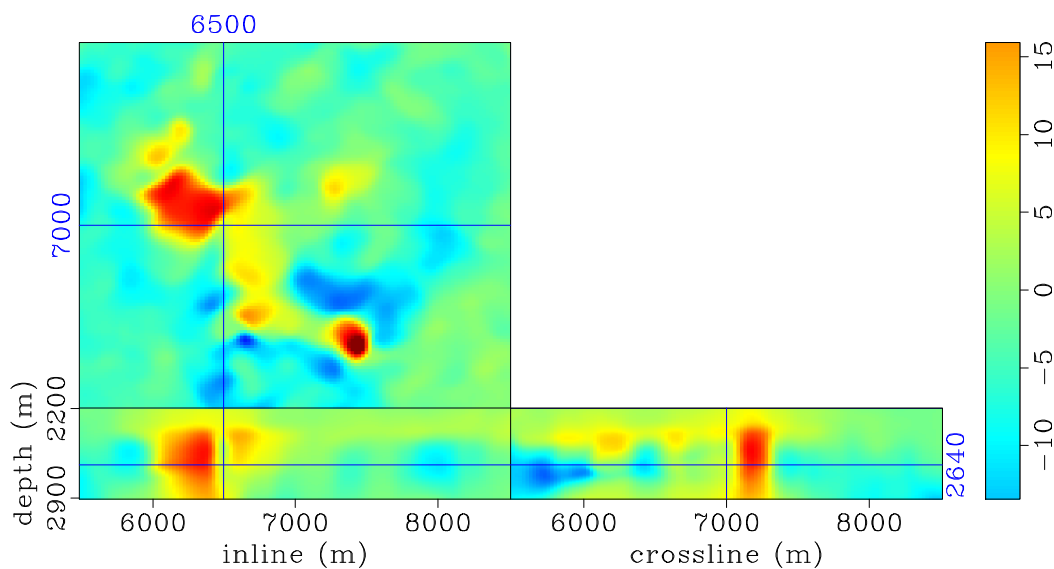
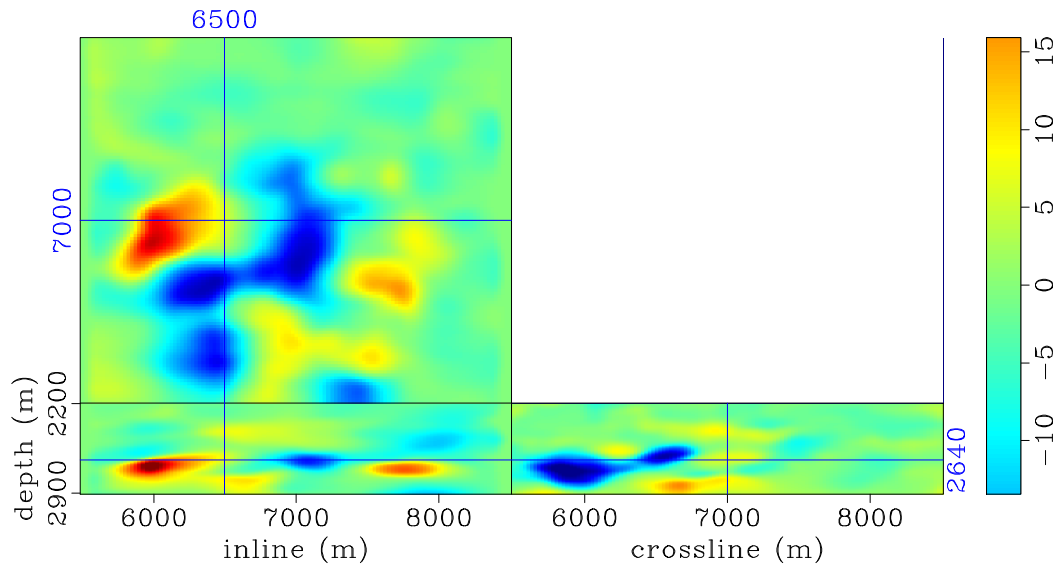
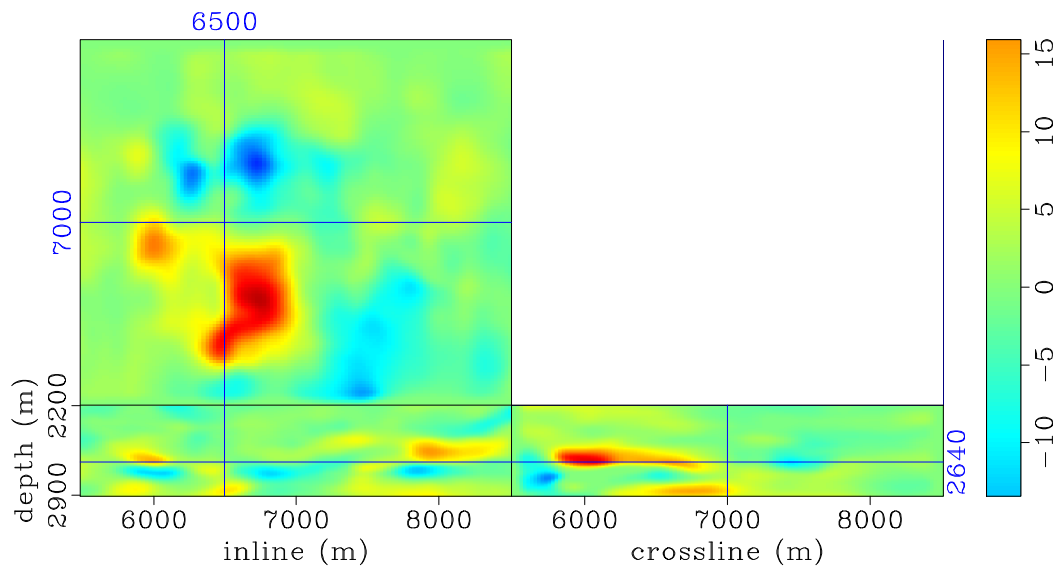


Figure 6.20: Vertical (a) components of apparent displacement vectors between the baseline and monitor images within the target area. Red indicates downward displacements, whereas blue indicates upward displacements. The inline and crossline components of these displacement vectors are presented in Figure 6.21. [CR] chap6/. ts-1



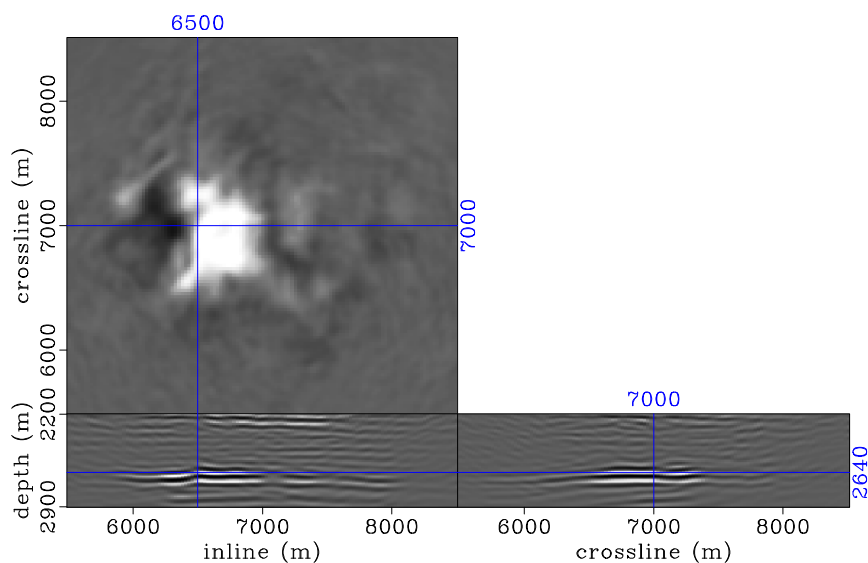
(a)



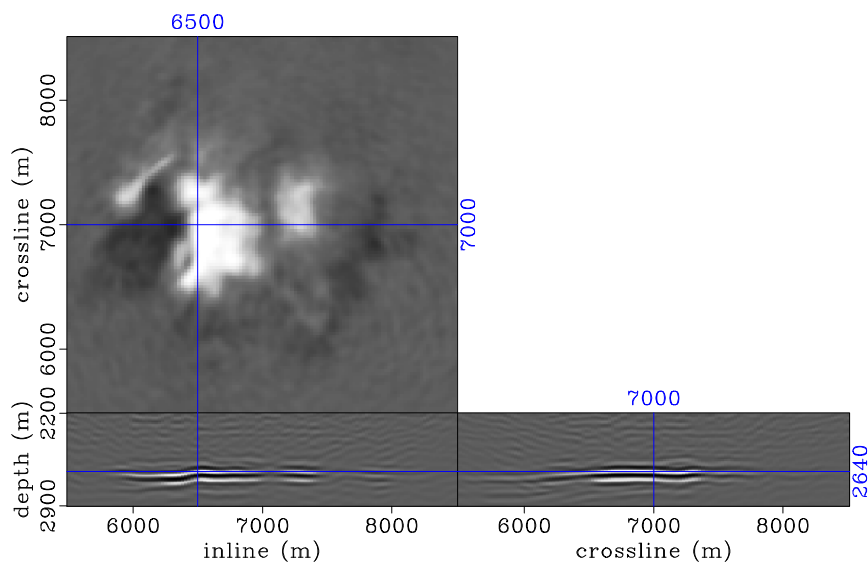
(b)

Figure 6.21: Inline (a) and crossline (b) components of apparent displacement vectors between the baseline and monitor images within the target area. In these figures, Red indicates rightward displacements, whereas blue indicates leftward displacements. The corresponding vertical (depth) components are shown in Figure 6.20. [CR]

chap6/. ts-2,ts-3



(a)



(b)

Figure 6.22: Migrated time-lapse images of the target area obtained after warping the monitor image to the baseline image. Panel (a) shows the time-lapse image derived from the complete baseline and incomplete monitor, whereas panel (b) shows the time-lapse image derived from complete baseline and complete monitor data sets. In (a), artifacts caused by misalignments due to velocity and compaction have been removed, leaving only differences due to production-induced reflectivity changes and difference in geometry between the baseline and monitor data. The differences between (a) and (b) are caused by the incomplete monitor geometry in (a). [CR]

chap6/. gap-d-mod,fine-d-mod

(and warped) baseline and monitor images derived from complete data sets. To obtain this reference time-lapse image, I migrate the complete baseline and monitor data using the same parameters applied to the incomplete data (described above). I then apply the same warping procedure as in Figure 6.22(a) to remove the apparent displacements between them.

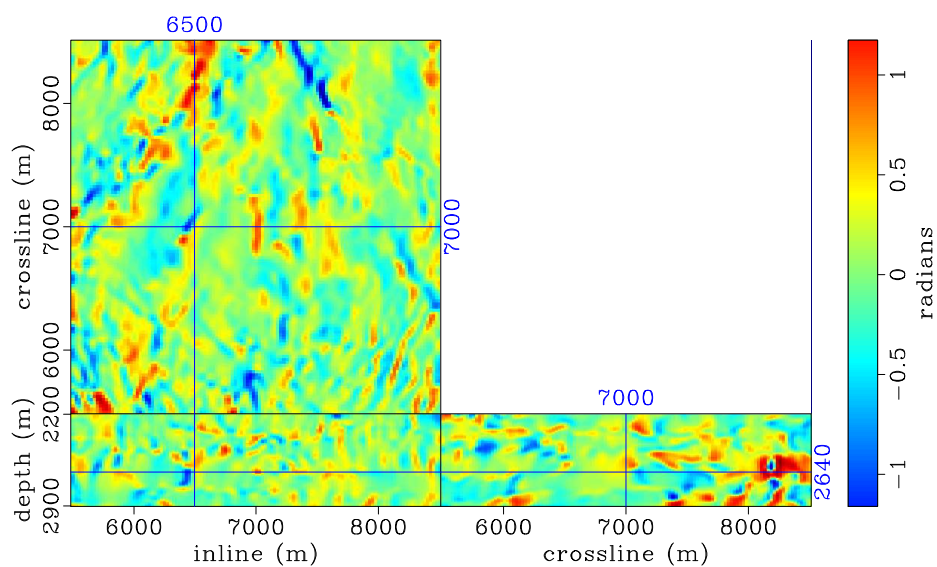
Because warping ensures that subsurface image points in the baseline and monitor images are collocated, artifacts in the initial time-lapse image (Figure 6.19) caused by misalignments due to velocity changes and compaction, have been removed in Figure 6.22(a). As discussed chapters 3, I assume that errors introduced by this kinematic correction are negligible compared to the changes in reflectivity of interest. Therefore, amplitude differences between the warped time-lapse image derived from the incomplete data sets (Figure 6.22(a)) and that from the complete data sets (Figure 6.22(b)) are due to the incomplete monitor geometry in Figure 6.22(a).

The aligned baseline and monitor images are the inputs into regularized joint image-domain inversion.

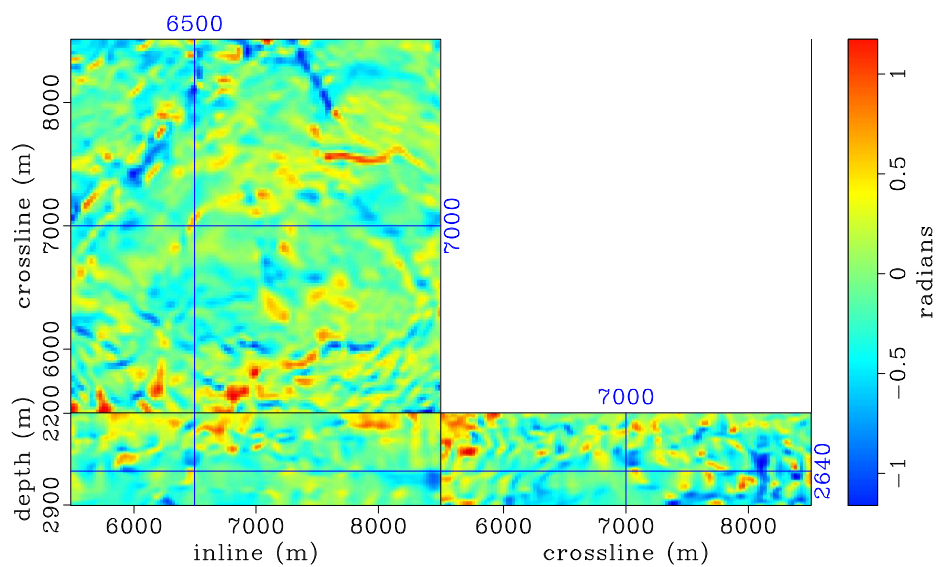
### **Inversion**

The structure of the target-oriented Hessian matrices for the complete (baseline) and incomplete (monitor) geometries has been previously described in this section. Using these matrices, I perform regularized joint image-domain inversion for the target area. To obtain the inverted images, I perform 200 conjugate-direction iterations (Claerbout and Fomel, 2011).

As in previous chapters, I regularize the inversion spatially using factorized directional Laplacians based on dips estimated from the baseline image. Because the monitor image is aligned to the baseline image, I use the same dips to build the spatial regularization operators for both images. Figure 6.23 shows the inline and crossline dips obtained by plane-wave destruction (Fomel, 2002). In this example (and in other inversion results in this chapter), I use the full factorized three-dimensional dip filters, which are constructed as described in chapter 3. As in previous examples, the tem-



(a)



(b)

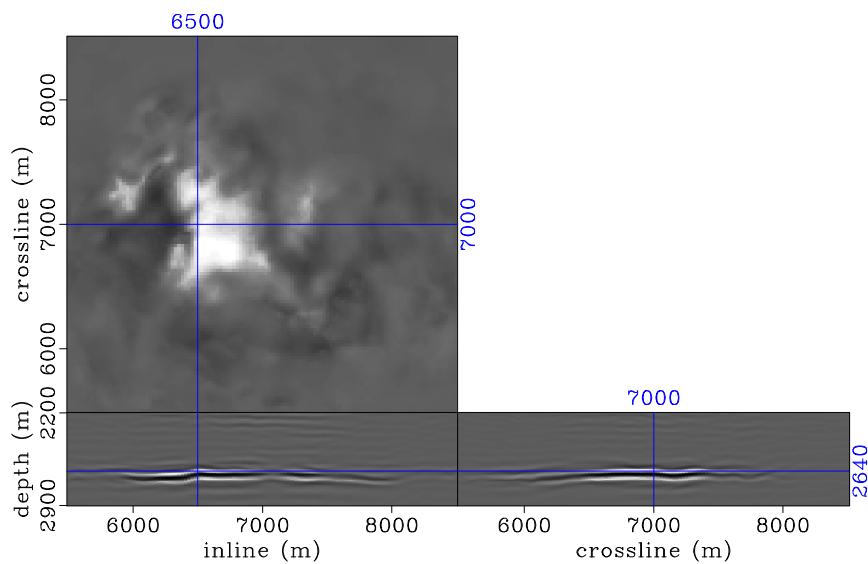
Figure 6.23: Inline (a) and crossline (b) dips estimated from the baseline image (Figure 6.18(a)) using the plane-wave destruction method (see Fomel (2002)). These dips are used to construct the spatial regularization operator for the inversion. [CR] chap6/. dip-x,dip-y

poral regularization is a difference operator between the baseline and monitor images. This temporal regularization operator provides coupling between the inverted baseline and monitor images and ensures that there are only limited differences between them.

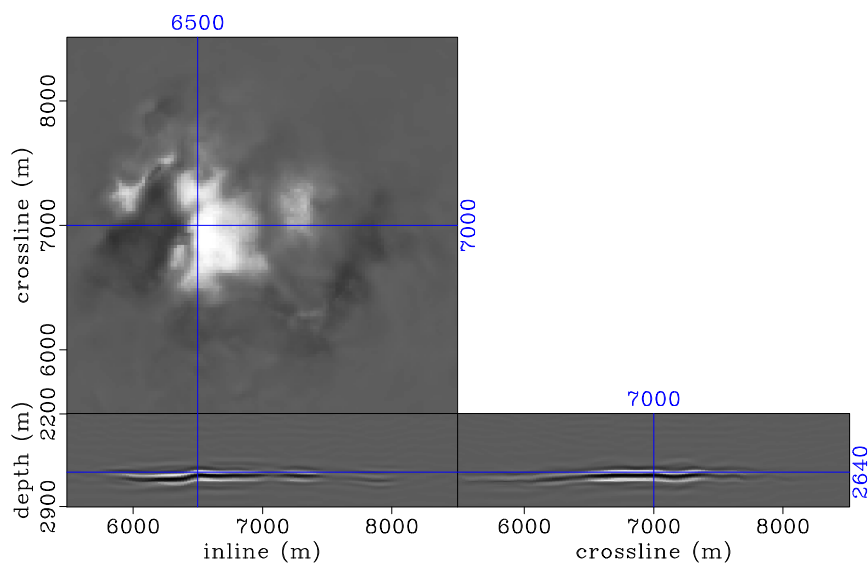
The time-lapse image of the target area obtained by regularized joint image-domain inversion of the complete baseline and incomplete monitor data sets is presented in Figure 6.24(a). For comparison, the time-lapse image obtained from inversion of the complete baseline and complete monitor data sets is presented in Figure 6.24(b). As shown in Figure 6.24, the inverted time-lapse images obtained in both cases are relatively similar, compared to those obtained from migration (Figure 6.22). Importantly, note that the inverted time-lapse image derived from the complete baseline and incomplete monitor data (Figure 6.24(a)) contain fewer obstruction artifacts, compared to those in the migrated time-lapse image derived from the same data (Figure 6.22(a)). In addition, the inverted time-lapse images (Figure 6.24) have better resolution than the migrated time-lapse images (Figure 6.22).

The inverted baseline and monitor images, from which the time-lapse image in Figure 6.24(a) is computed, are presented in Figure 6.25. A comparison of these inverted images with the migrated baseline and monitor images (Figures 6.18) shows that inversion provides reflectivity images with better resolution and more balanced amplitudes than migration.

To study the improvements provided by regularized joint image-domain inversion, I compute the average time-lapse amplitudes within a 60 m window around the reservoir. I obtain these amplitudes by computing difference between the average absolute amplitudes in the baseline and monitor images. The time-lapse amplitudes obtained by migration and by inversion are presented in Figure 6.26. Figures 6.26(a) and 6.26(b) are the migrated time-lapse amplitude maps from the incomplete and complete data sets, respectively. The corresponding time-lapse amplitude maps, from the incomplete and complete data are presented in Figures 6.26(c) and 6.26(d), respectively. A comparison of these amplitude maps shows that, whereas the results from the migrated images differ significantly, those obtained from inversion are similar.

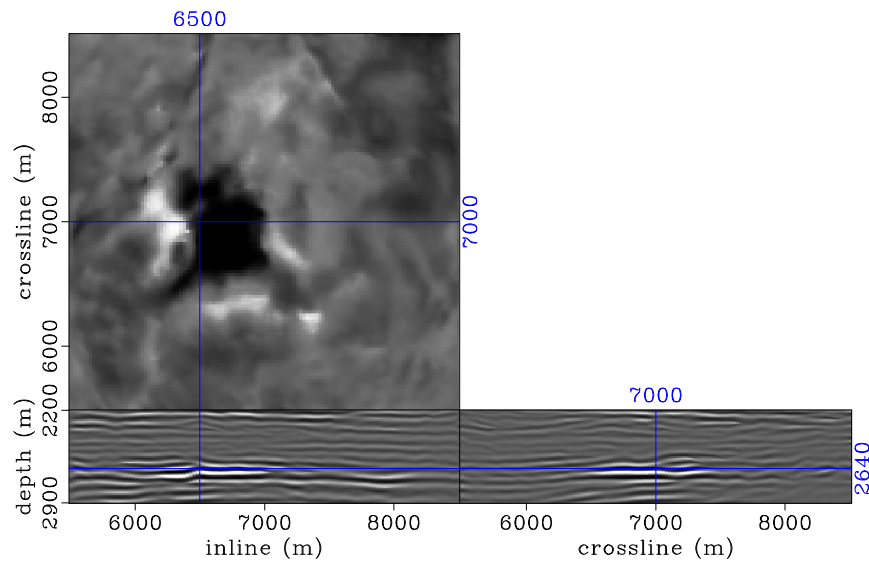


(a)

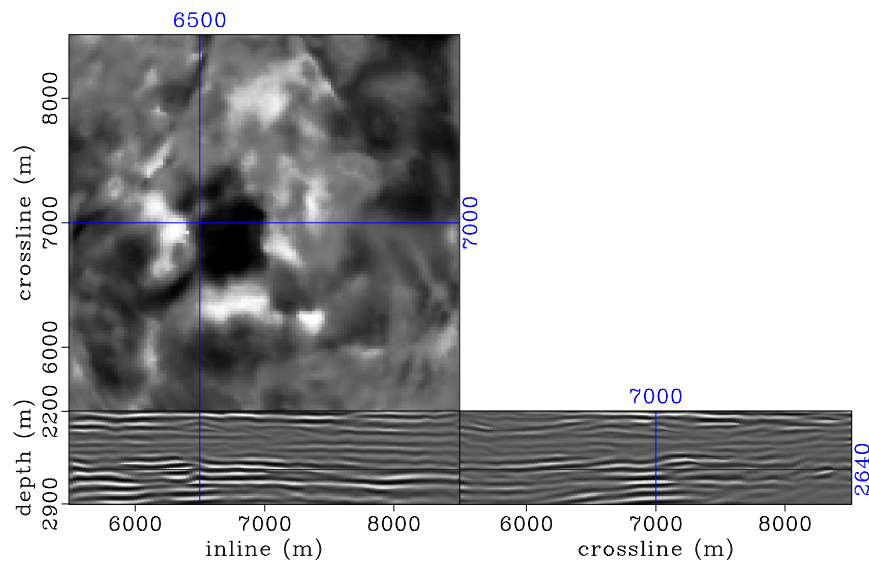


(b)

Figure 6.24: Time-lapse images of the target area obtained from regularized image-domain inversion of the incomplete (a) and complete (b) data sets. Note that these inverted time-lapse images are comparable. In (a), obstruction artifacts in the migrated time-lapse image (Figure 6.22(a)) have been attenuated by inversion. In addition, this inverted time-lapse image shows improved resolution over the migrated time-lapse image. A comparison of the time-lapse amplitudes along the reservoir is presented in Figure 6.26. [CR] chap6/. gap-d-inv, fine-d-inv



(a)



(b)

Figure 6.25: Inverted baseline image (a), and monitor image (b) of the target area obtained from the complete baseline and incomplete monitor data sets. The difference between these images, which are obtained by regularized joint image-domain inversion, is presented in Figure 6.24(a). Compared to the migrated images in Figure 6.18, these images show improved resolution of the subsurface reflectivity. [CR]

chap6/. gap-1,gap-2

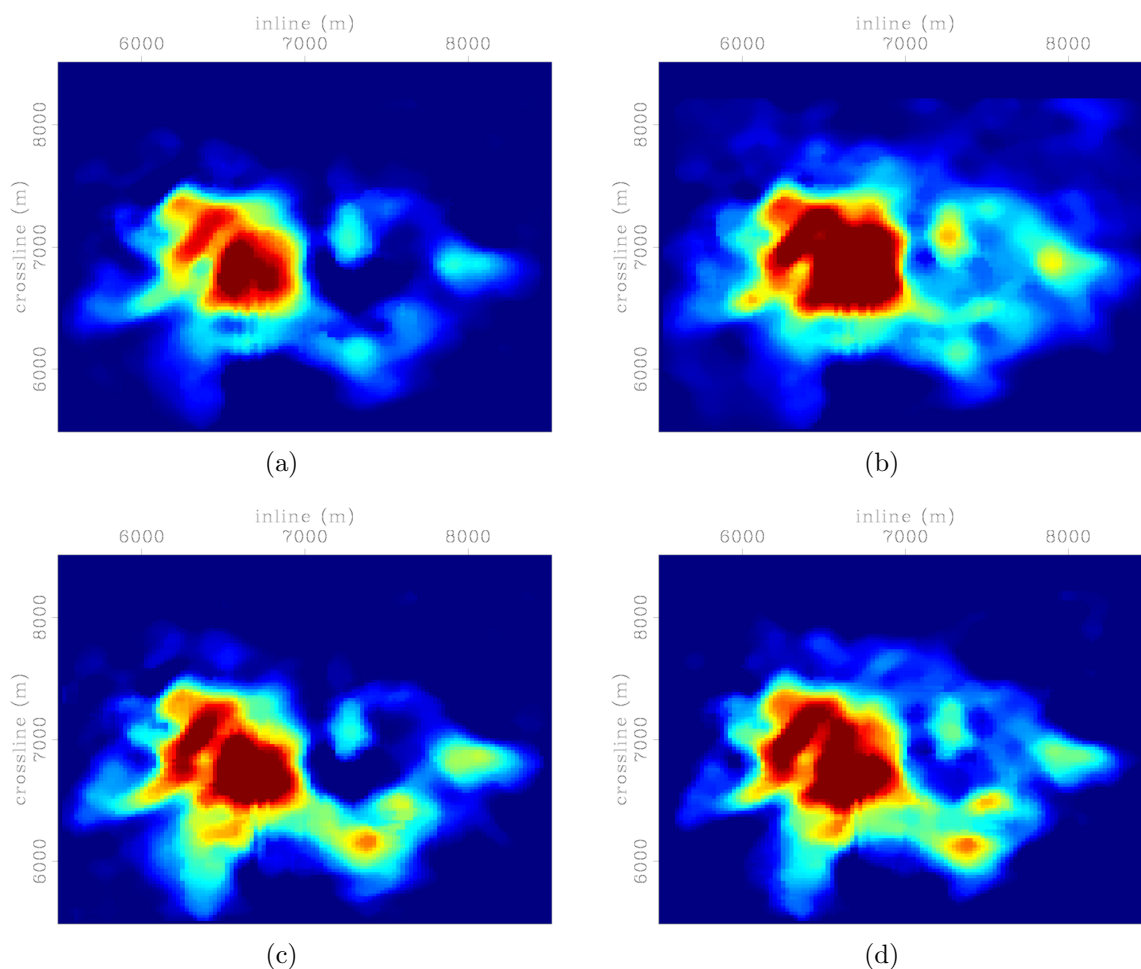


Figure 6.26: Average time-lapse amplitudes within a 60 m window around the reservoir obtained from migration (a) and (b), and from regularized image-domain inversion (c) and (d). Figures (a) and (c) are the reference amplitudes obtained from the complete data, whereas (b) and (d) are obtained from the incomplete data. These amplitude maps are presented at the same clip level relative to the respective baseline and monitor images. Note the discrepancies in the time-lapse amplitude distribution obtained via migration of the complete (a), and incomplete (b) data. This discrepancy has been attenuated via inversion of the same data sets (c) and (d). [CR]

chap6/. hor-4-d3,hor-4-d2,hor-4-d1,hor-4-d

### *Example II: Inversion of multiple data sets*

In this section, using data from the first (LoFS 1), the fifth (LoFS 5), and the ninth (LoFS 9) surveys, I demonstrate an application of joint image-domain inversion to multiple data sets. In this example, LoFS 1 is the baseline survey, LoFS 5 is the first monitor survey, and LoFS 9 is the second monitor survey. As described in example *I*, LoFS 1 and LoFS 9 were acquired in November 2003 and December 2007, respectively. LoFS 5 data set, which was acquired in April 2005, has been preprocessed by the donor using the same parameters as in LoFS 1 and LoFS 9.

In this example, the geometry of the baseline survey is the same as that in example *I*. Furthermore, the geometry of the second monitor survey is the same as the that of the incomplete monitor survey in example *I*. However, to simulate a different geometry for the first monitor survey in this example, I create 1.44 km<sup>2</sup> gap in the source geometry and a 1.0 km<sup>2</sup> gap in the receiver geometry (Figure 6.27). Because of the different sizes of gaps in the geometries of the two monitor surveys, the three surveys in this example have different acquisition geometries.

Using the same parameters as in Example *I*, I compute the diagonal of the Hessian matrices (i.e., the subsurface illumination) corresponding to the three geometries. Figure 6.28 shows the subsurface illumination ratio between the incomplete geometry of the first monitor survey and the complete baseline survey. Recall that in example *I*, the illumination ratio between the incomplete geometry of the second monitor survey and the complete baseline survey was discussed (Figure 6.11(b)). To provide a measure of the differences in illumination along the reservoir that are caused by the differences in survey geometries, I compute the average illumination ratio within a 60 m window around the reservoir. Figures 6.29(a) and 6.29(b) show maps of the illumination ratio between the baseline and the first monitor, and between the baseline and the second monitor, respectively.

I migrate the baseline and monitor data sets using the same parameters as in example *I*. Prior to inversion, as in previous examples, I warp the two monitor images to the baseline using the sequential warping method described in chapter 2.

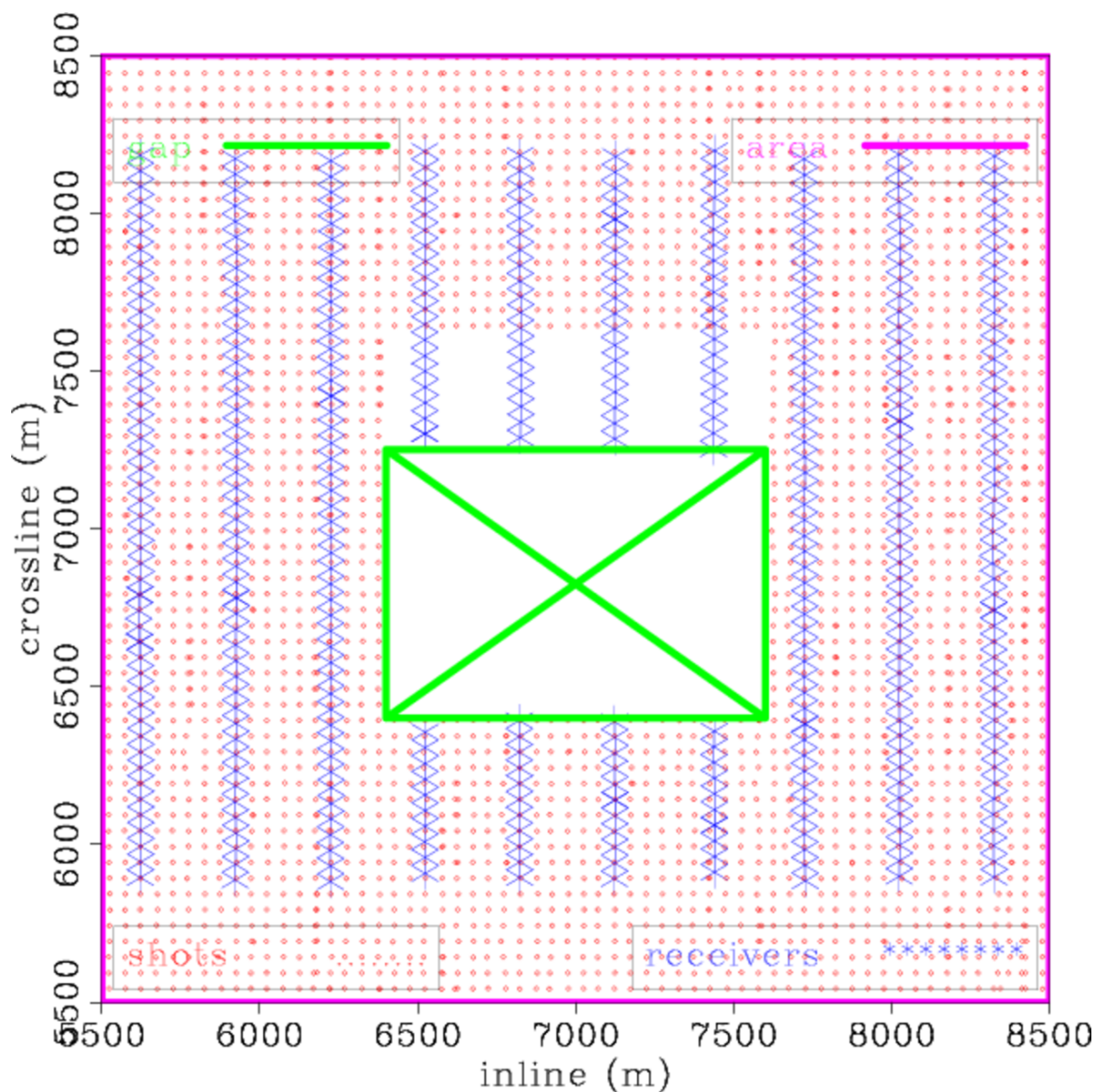


Figure 6.27: An enlarged view of the study area (Figure 6.3) showing the shot and receiver locations within the study area, and the location of the simulated obstruction in the geometry the first monitor (LoFS 5). Note that the gap in the source locations is bigger than the gap in the receiver locations. There are not sources and receivers within the overlap area. Compare this to Figures 6.4 and 6.6, which show the complete baseline geometry and the incomplete geometry of the second monitor.

[ER] chap6/. OOsfull-5-gap

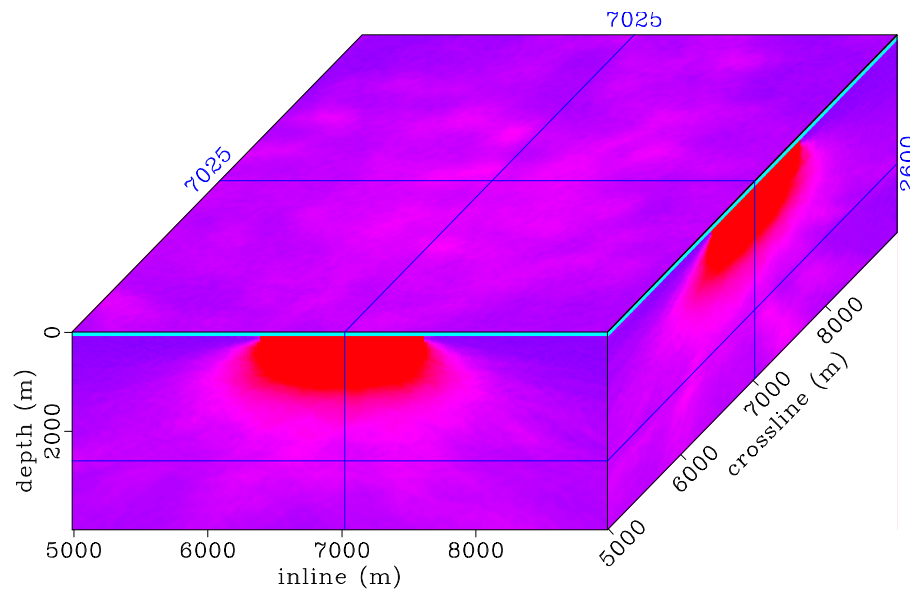


Figure 6.28: Subsurface illumination ratio between the complete baseline survey and the incomplete *first* monitor survey, showing a depth slice through the reservoir. Compare this figure to the illumination ratio between the baseline and the second monitor survey (Figure 6.11(b)). The illumination ratio between the baseline and the two monitor geometries along the reservoir are shown in Figure 6.29. [CR] chap6/. ilumr1-4

For comparison, I apply the same procedure and parameters to the complete baseline and monitor data sets. The time-lapse amplitudes along the reservoir, obtained from the warped migrated images, are presented in Figure 6.30. As shown in Figure 6.30, there are large discrepancies in the time-lapse amplitudes obtained from migration of the complete data and those from the incomplete data.

The inverted reservoir time-lapse amplitude maps are presented in Figure 6.31. A comparison of the inverted maps from the complete data (Figures 6.31(a) and 6.31(c)) and the incomplete data (Figures 6.31(b) and 6.31(d)) show that, compared to the migrated amplitude maps (Figure 6.30), regularized joint image-domain inversion minimizes the discrepancies in time-lapse amplitude information caused by geometry differences between surveys. However, a comparison of Figures 6.31(a) and 6.31(b) shows that this method is not perfect. In particular, where the reflectivity changes are small and the geometry differences are large, although regularized joint inversion

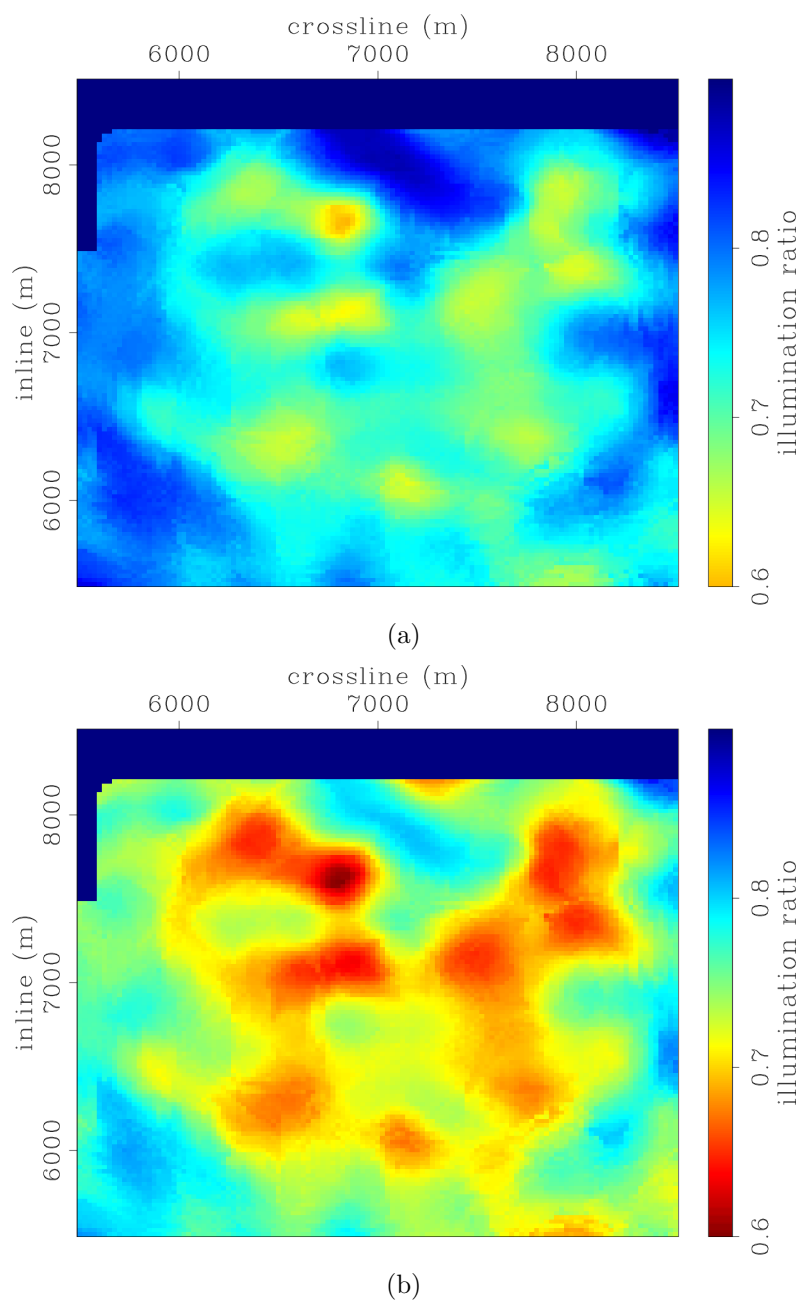


Figure 6.29: Illumination ratio between the baseline and the first monitor (a), and between the baseline and the second monitor (b). In these maps, red indicates regions with the largest illumination disparity, whereas blue indicates regions with the smallest illumination disparity. In both examples, although the geometry difference is caused by a rectangular gap in the monitor geometries, the illumination disparities are complex at depth. [CR] chap6/. ilum-res-1r,illum-res-2r

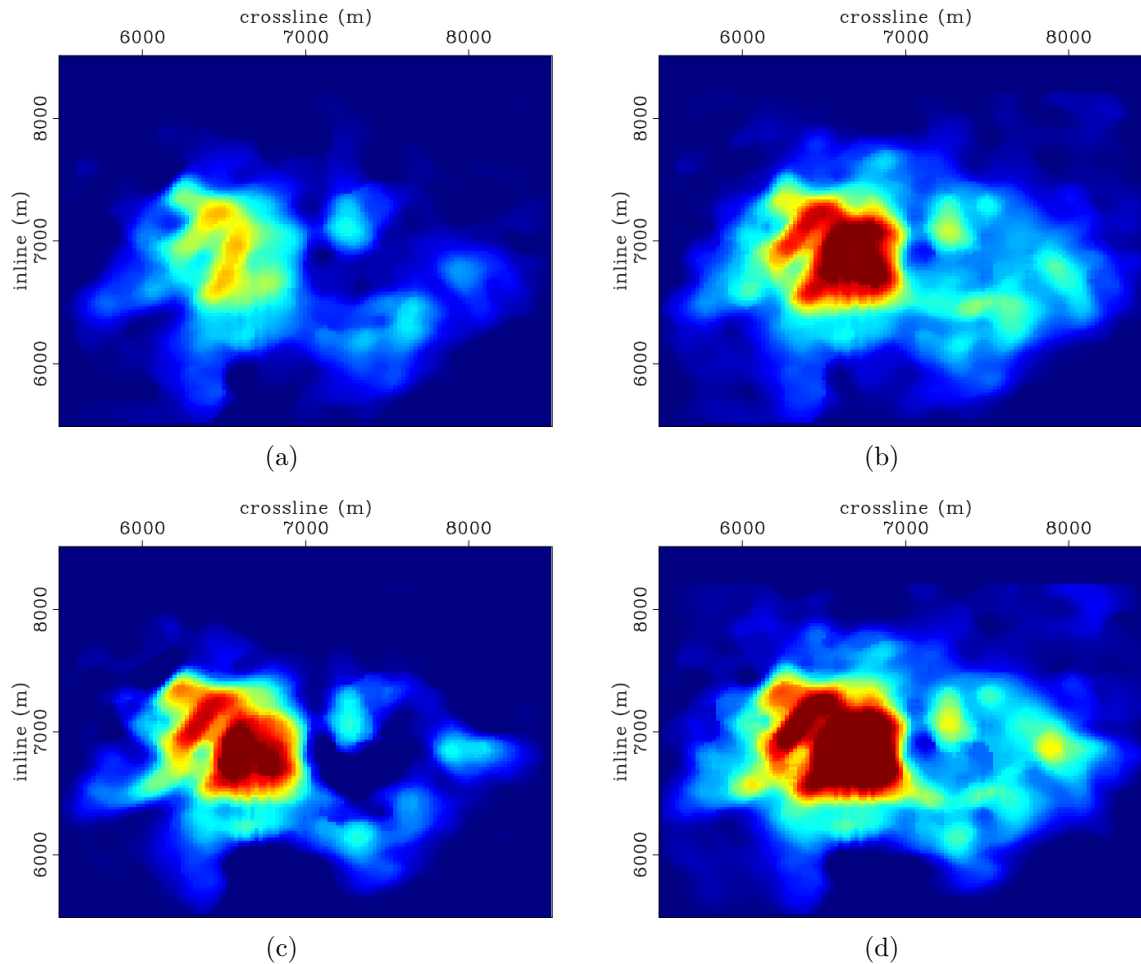


Figure 6.30: Average time-lapse amplitudes within a 60 m window around the reservoir obtained from migration. Panels (a) and (c) are the difference maps between the complete baseline, and the complete first and second monitor, respectively. Panels (b) and (d) are the corresponding results from the complete baseline and the incomplete monitor data. These amplitude maps are presented at the same clip relative to the respective baseline and monitor images. Note that there are large discrepancies in the time-lapse amplitude distribution obtained via migration of the complete and incomplete data sets. [CR]

chap6/. h3-fine-mod-dd1,h3-gap-mod-dd1,h3-fine-mod-dd2,h3-gap-mod-dd2]

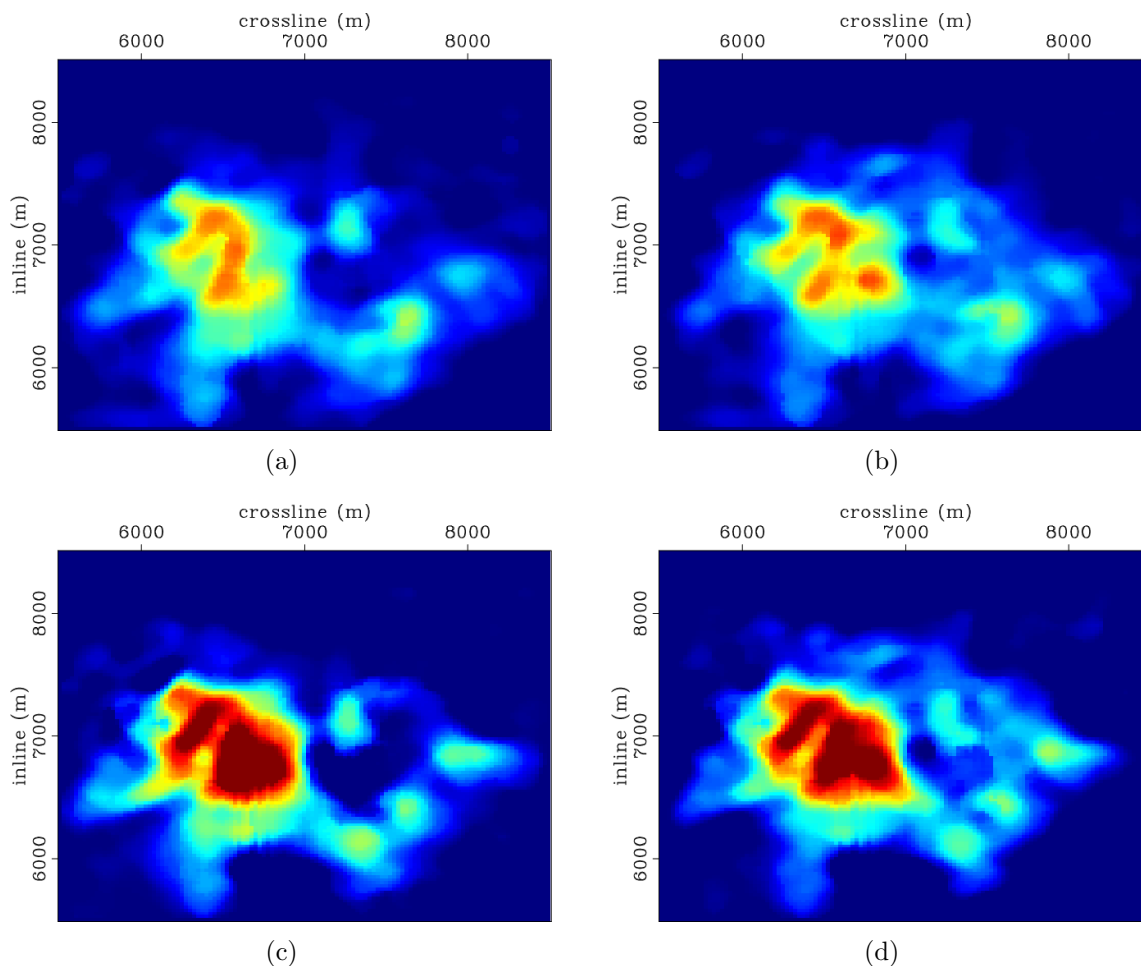


Figure 6.31: Average time-lapse amplitudes within a 60 m window around the reservoir obtained from from regularized joint image-domain inversion. Panels (a) and (c) are the difference maps between the complete baseline, and the complete first and second monitor, respectively. Panels (b) and (d) are the corresponding results from the complete baseline and the incomplete monitor data. These amplitude maps are presented at the same clip relative to the respective baseline and monitor images. Note that discrepancies in the time-lapse amplitude distribution in the migrated results (Figure 6.30) have been reduced. [CR]

chap6/. h3-fine-dd1,h3-gap-dd1,h3-fine-dd2,h3-gap-dd2

will provides more reliable results than migration, it will not fully recover the true reflectivity change.

### *Example III: Multiple realizations of time-lapse images*

In this section, I demonstrate how multiple plausible realizations of the time-lapse image can be obtained from regularized inversion. As noted in chapter 3, one advantage of image-domain inversion is that it allows the linearized inversion problem to be solved in a target-oriented manner. This reduces the size of the computational domain and hence the inversion cost. In addition, as described in previous chapters, each iteration of image-domain inversion requires matrix-vector multiplications, instead of migration and demigration operations required in each iteration of data-domain inversion. Therefore, once the Hessian matrices are computed, regularized joint image-domain inversion is computationally inexpensive, and it is possible to test different constraints in the inversion very rapidly.

Here, I examine how the temporal regularization parameter affects the estimated time-lapse amplitudes. The premise is that, depending on the data quality and the strength of the time-lapse seismic signal, the baseline and monitor images should be similar at most subsurface image positions. The task then is to determine how similar or how different the baseline and monitor images should be. One way to accomplish this is through matched filtering, based on filters derived from non-reservoir parts of the subsurface images. However, as described in chapter 2, matched filtering suffers from several pitfalls. Regularized inversion provides a way to achieve this same requirement by utilizing available information about the subsurface reservoir and expected changes as constraints in the inversion.

In this example, I consider the complete baseline data (LoFS 1), and complete monitor data (LoFS 9). Recall that the geometry of these data sets, along with the preprocessing and migration parameters, and the spatial and temporal regularization operators used in the inversion are described in example *I*.

Figure 6.32 shows the image-fitting residuals as a function of the iteration number, which are obtained with six different regularization parameters. Each curve is scaled by the maximum fitting residual—at the first iteration. As expected, this plot shows that the minimum image-fitting residual increases as a function of the temporal coupling between the images. In general, a high temporal coupling means that the differences between the baseline and monitor images are constrained to be small, whereas a small temporal coupling means that large differences are allowed between the baseline and monitor images. The inverted reservoir time-lapse amplitude maps that correspond to these graphs are presented in Figure 6.33.

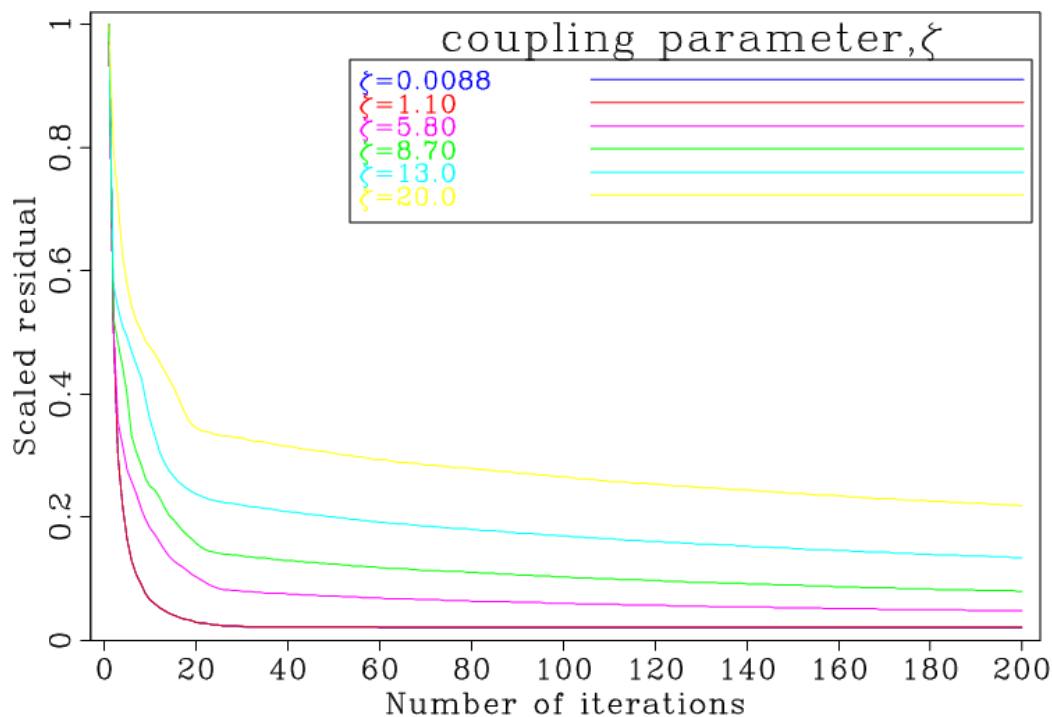


Figure 6.32: Scaled residual for six different regularization parameters. Each graph corresponds to a different temporal regularization parameter, expressed as a percentage of the RMS energy in the migrated baseline image. All the graphs are obtained with the same spatial regularization parameter but different temporal constraints. As expected, large temporal constraints lead to higher residuals. These graphs correspond to the residuals for the amplitude maps in Figure 6.33. [CR]. chap6/. mult-rd

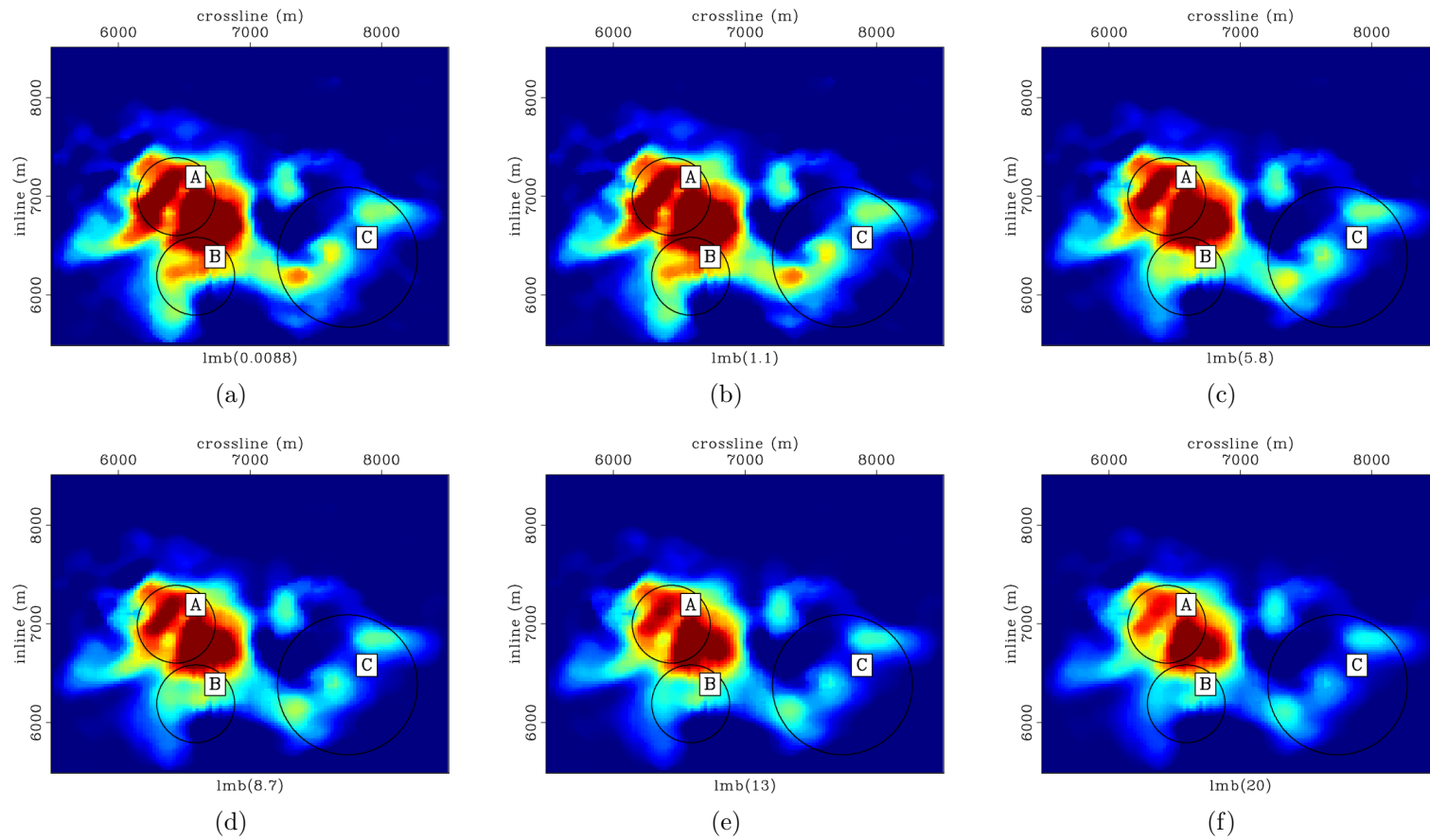


Figure 6.33: Average time-lapse amplitudes within a 60 m window around the reservoir obtained from using different regularization parameters in the image-domain inversion of the complete baseline and monitor data. In these maps, which are presented at the same clip relative to the baseline and monitor images, the temporal (coupling) regularization parameter increases from (a) to (f). These amplitude maps are obtained with the same spatial regularization parameter. Especially within the ovals (labeled A, B and C), note the systematic changes in the time-lapse amplitudes as a function of the coupling strength. [CR] chap6/. mult-1,mult-2,mult-3,mult-4,mult-5,mult-6

As shown in Figure 6.33, there is a systematic change in the reservoir time-lapse amplitudes as a function of the temporal coupling between the baseline and monitor images. In particular, there are significant differences in the time-lapse amplitude map within the ovals (labeled A, B and C). For example, there is a feature in the time-lapse amplitude map within oval B when the temporal coupling is small (e.g., Figure 6.33(a)). This feature disappears as at high temporal coupling (e.g., Figure 6.33(f)).

## DISCUSSION AND CONCLUSIONS

A common problem in many time-lapse seismic monitoring surveys is the presence of obstructions that create gaps in the monitor data. Such obstructions, usually caused by production and drilling facilities, generate artifacts that contaminate production-related seismic amplitudes changes, thereby limiting our ability to accurately interpret observed time-lapse amplitudes. The Valhall LoFS project provides data with high repeatability of both source and receiver locations (Figures 6.2 to ??). Therefore, in this case study, the major sources of time-lapse amplitude contamination are the synthesized gaps in the monitor data. Example *I* shows clearly how inversion can be used to attenuate these contaminating artifacts.

Surface (CMP) folds only provide limited information about geometry differences between surveys (Figure 6.7). Importantly, because surface folds do not provide information about the effects of such geometry differences in the subsurface, information derived from them cannot be used to compensate for the associated subsurface illumination differences. As shown in Figures 6.8 to 6.10, the diagonal of the Hessian matrix provides a good measure of the subsurface illumination for any given geometry. An estimate of the subsurface illumination differences can be obtained from the ratio of the Hessian matrices for the different survey geometries (Figure 6.11).

Although the diagonal of the Hessian matrix provides important information about subsurface illumination and differences, the band-limited wave-propagation effects are provided by the off-diagonals elements of the matrix (Figure 6.12). it is

common practice to correct for subsurface illumination using weights derived from the inverse of the diagonal of the Hessian matrix. However, this approximation assumes that at any subsurface image point, all wavenumbers/dips are illuminated equally. Instead of such approximation, the truncated target-oriented Hessian captures the dip-dependent subsurface illumination (Figure 6.13). Importantly, where time-lapse surveys have different geometries, at any subsurface image point, there are differences in the illumination of different wavenumbers (Figure 6.13(b)). Therefore, as shown in Figure 6.13, the off-diagonal elements of the Hessian matrices provide the information necessary to correctly account for such geometry differences.

An important assumption in the joint inversion method developed in this dissertation is that the velocity is nearly accurate. For this study, the velocity model obtained via full-waveform inversion—and used in several previous studies—satisfies this requirement. As shown in Figures 6.14 to 6.17, using this velocity model, all the key geological horizons in the study area are well imaged. In addition, because the inversion problem is posed in the image domain, I perform inversion only for a small target area around the reservoir (Figures 6.14 to 6.17). Because the target area is small, it is possible to focus efforts to improve results in the region where the most important production- or injection-related changes are expected.

As previously described in this dissertation, prior to inversion, the monitor image is aligned to the baseline image. This multidimensional image alignment is performed efficiently by warping the two images using apparent displacements derived from a one-dimensional sequential warping (Figures 6.20 and 6.21). These apparent displacements are due to a combined effect of deformation and velocity changes associated with hydrocarbon production and water injection in the study area.

Conventional imaging by migration does not account for the geometry differences between the data sets. Because it attenuates artifacts caused by geometry differences between the baseline and monitor images (Figure 6.22(a)), regularized joint image-domain inversion provides time-lapse images with improved quality and more reliable amplitudes (Figure 6.24(a)) compared to migration (Figure 6.22(a)). In addition, because joint inversion accounts for band-limited wave-propagation effects, it provides

subsurface images with improved resolution. Therefore, inverted time-lapse images show improved resolution compared to the migrated time-lapse images (Figure 6.22(a) versus Figure 6.22(a)).

In example *I*, because of the geometry differences between the baseline and monitor surveys, there is a large disparity in the distribution of time-lapse amplitudes for the complete (Figures 6.26(a)) and incomplete (Figure 6.26(b)) data sets. Regularized joint image-domain inversion corrects for this disparity, thereby providing comparable time-lapse amplitude distributions in both the complete and incomplete data examples (Figures 6.26(c) and 6.26(d)).

The regularized joint inversion formulations developed in this dissertation can be applied to any number of surveys. As shown in example *II*, when applied to data sets from three surveys using similar and different geometries, inversion provides more reliable time-lapse amplitude information than does migration. Where multiple surveys have dissimilar geometries, there can be strong dissimilarities in the reservoir illumination (Figure 6.29). These dissimilarities between surveys will affect the reservoir time-lapse amplitudes in different ways (Figure 6.30). Regularized joint inversion provides a framework to account for these differences in an integrated manner, thereby providing more reliable time-lapse amplitude information (Figure 6.31).

From the results in examples *I* and *II*, it is clear that the inverted time-lapse amplitudes derived from the complete data sets and those from the incomplete data are similar. Therefore, I conclude that the regularized joint image-domain inversion method developed in this dissertation can reduce the sensitivity of the time-lapse seismic amplitudes to differences in acquisition geometries.

As discussed in this and in previous chapters, once the approximate Hessian matrices are computed, regularized image-domain inversion is computationally inexpensive. This, combined with the fact that it readily permits inversion of a small target around the reservoir, makes it possible to efficiently test different combinations of regularization parameters. In example *III*, by using different realistic coupling parameters (Figure 6.32), I obtain six possible inverted time-lapse images (Figure 6.33). All these

results, obtained using 200 conjugate iterations, are derived in less than 1 hour on 553 CPU cores. Therefore, depending on the available computer resources, one can quickly test a wide range of realistic constraints in the inversion.

Because regularized joint image-domain inversion is based on the physics of the seismic data acquisition and imaging, it provides a robust way to enforce similarity between the baseline and monitor images without damaging the time-lapse amplitudes of interest. As shown in Figure 6.33, the inverted reservoir time-lapse amplitudes depend on the temporal coupling between the baseline and monitor images. Although not included in this study, the time-lapse amplitudes will also vary as a function of the spatial regularization parameter. By studying the characteristics of the estimated time-lapse amplitudes, and comparing these with other available data, an interpreter can make informed decisions on the time-lapse amplitudes. For example, these results can be used to quantify uncertainties associated with the observed time-lapse amplitude changes. In addition, because any one time-lapse image may not match other geological or engineering data, these multiple realizations can be used as part of an integrated production history matching.

## ACKNOWLEDGMENTS

I thank BP and Valhall partners for donating the time-lapse data sets used in this chapter. In particular, I thank Adeyemi Arogumati and Olav Barkved (both of BP) for their assistance. I thank the Stanford Center for Computational Earth and Environmental Science (CEES) for providing the computer resources used in these studies.

# Chapter 7

## Conclusions

This dissertation introduces novel techniques to overcome some important challenges in current time-lapse seismic imaging practice. Even in difficult circumstances, these techniques provide good-quality time-lapse images—from which we can make reliable deductions about changes in subsurface reservoir properties.

In chapter 2, I discussed two conventional time-lapse *post-imaging* cross-equalization methods. Efficient multidimensional warping by sequential one-dimensional cross-correlation and interpolation (Hale, 2009), overcomes cost limitations of full multidimensional warping, and the inaccuracies in approximate *vertical-only* methods. Optimal matched filtering using an evolutionary algorithm provides more reliable match between the time-lapse data sets. A combination of these two methods provides a robust cross-equalization tool. In addition, the warping method is an important step for the inversion methods developed in this dissertation.

In chapter 3, I discussed the theory of regularized joint inversion of time-lapse seismic data sets. Joint inversion allows the introduction of both spatial and temporal constraints, which stabilize the inversion and provide geologically plausible time-lapse images. Formulations of the regularized joint inversion in both the data and image domains are presented. Although the time-lapse imaging problem can be solved in either domain, an important advantage of image-domain inversion is that it enables

a target-oriented solution of the problem.

I applied the methods developed in chapter 3 to various data sets:

- Chapter 4 – two- and three-dimensional synthetic data sets.
- Chapter 5 – two-dimensional field streamer data sets.
- Chapter 6 – three-dimensional field ocean-bottom-cable (OBC) data sets.

The results of these applications show that:

1. Non-repeated simultaneous-source time-lapse data sets can be imaged adequately by data-domain inversion (Chapter 4).
2. Distortions in time-lapse images, which are caused by complex overburden effects, can be corrected by image-domain inversion (Chapter 4).
3. Artifacts in time-lapse images, which are caused by differences in acquisition geometries, can be attenuated using image-domain inversion (Chapters 4, 5, and 6).
4. Because the image-domain approach is relatively computationally inexpensive, different plausible regularizations can be tested in near real-time—until desirable results are obtained (Chapters 4 and 6).
5. Careful preprocessing is essential in time-lapse seismic imaging, and in particular when imaging by inversion (Chapter 5).
6. A common approximation of subsurface illumination—the diagonal of the Hessian—cannot fully account for the effects of geometry differences between surveys (Chapter 5).

Importantly, the inversion methods developed in this dissertation make the time-lapse image less sensitive to geometry differences and to the overburden complexity.

# Appendix A

## Inverting for the monitor image at the baseline position

Changes in velocity and compaction associated with reservoir production or fluid injection are usually small compared to the background velocity and reservoir depth. In addition, these changes are coupled, and without additional information, it is often difficult to separate them prior to imaging. This makes it difficult to accurately estimate new migration velocities for the monitor data sets without introducing additional errors. Therefore, the baseline and monitor data are often imaged with the baseline velocity. Although this introduces some errors in the migrated monitor image, it is assumed that:

- the imaging errors are negligible compared to the background, and are much smaller than the expected changes associated with production or injection.
- the imaging errors can be adequately removed by kinematic corrections, such as *warping*.

In addition, in order to compute any image of reflectivity change between the baseline and monitor images, all points between the two must be collocated. Therefore, based on the assumptions above, the migrated monitor reflectivity image at the

baseline position  $\tilde{\mathbf{m}}_1^b$  can be approximated as follows:

$$\tilde{\mathbf{m}}_1^b \approx \mathbf{S}^{m+} \tilde{\mathbf{m}}_1 \approx \mathbf{S}^{\alpha+} \tilde{\mathbf{m}}_1^a, \quad (\text{A-1})$$

where  $\tilde{\mathbf{m}}_1$  and  $\tilde{\mathbf{m}}_1^a$  are obtained by migrating the monitor data with the monitor and baseline velocities, respectively. Whereas  $\tilde{\mathbf{m}}_1$  is correctly imaged to the physical *monitor* position,  $\tilde{\mathbf{m}}_1^a$  is imaged to an apparent position  $\alpha$ . The orthogonal warping operators,  $\mathbf{S}^{m+}$  and  $\mathbf{S}^{\alpha+}$ , reposition the monitor images  $\tilde{\mathbf{m}}_1$  and  $\tilde{\mathbf{m}}_1^a$ , respectively, to the baseline position.

Provided the assumptions in equation A-1 hold, we can approximate the monitor data as follows:

$$\mathbf{L}_1 \mathbf{S}^{m-} \mathbf{m}_1^b \approx \mathbf{U}^{m-} \mathbf{L}_1^b \mathbf{m}_1^b \approx \mathbf{L}_1 \mathbf{m}_1 = \mathbf{d}_1, \quad (\text{A-2})$$

where the linear modeling operator  $\mathbf{L}_1$  is a function of both the monitor velocity and geometry, whereas  $\mathbf{L}_1^b$  is a function of the baseline velocity but the monitor geometry. The warping operator  $\mathbf{S}^{m-} = (\mathbf{S}^{m+})^{-1}$  repositions the monitor reflectivity image from the baseline position to the monitor position.  $\mathbf{U}^{m-}$  is an orthogonal operator that translates data due to a reflectivity image at baseline position (modeled with the baseline background velocity), into data due to a reflectivity image at the monitor position (modeled with monitor background velocity). This remapping operator is defined as follows:

$$\mathbf{U}^{m-} \approx \mathbf{L}_1 \mathbf{S}^{m-} \left[ [(\mathbf{L}_1^b)^T \mathbf{L}_1^b]^{-1} (\mathbf{L}_1^b)^T \right]. \quad (\text{A-3})$$

Substituting equation A-3 into equation A-2, we have

$$\mathbf{L}_1 \mathbf{S}^{m-} \mathbf{m}_1^b \approx \mathbf{L}_1 \mathbf{S}^{m-} \left[ [\mathbf{H}_1^b]^{-1} \mathbf{H}_1^b \right] \mathbf{m}_1^b \approx \mathbf{d}_1, \quad (\text{A-4})$$

where  $\mathbf{H}_1^b = (\mathbf{L}_1^b)^T \mathbf{L}_1^b$  is the least-squares imaging Hessian computed using the baseline background velocity but with the monitor geometry.

From equation A-2, we can derive the inverted monitor reflectivity image at the baseline position  $\hat{\mathbf{m}}_1^b$  as follows:

$$(\mathbf{L}_1^b)^T (\mathbf{U}^{m^-})^T \mathbf{U}^{m^-} \mathbf{L}_1^b \hat{\mathbf{m}}_1^b \approx (\mathbf{L}_1^b)^T (\mathbf{U}^{m^-})^T \mathbf{d}_1, \quad (\text{A-5})$$

where

$$(\mathbf{U}^{m^-})^T \mathbf{U}^{m^-} = (\mathbf{U}^{m^-})^{-1} \mathbf{U}^{m^-} = \mathbf{U}^{m^+} \mathbf{U}^{m^-} \approx \mathbf{I}, \quad (\text{A-6})$$

and

$$(\mathbf{L}_1^b)^T (\mathbf{U}^{m^-})^T \approx \mathbf{S}^{m^+} \mathbf{L}_1^T. \quad (\text{A-7})$$

Therefore, the migrated monitor image at the baseline position  $\tilde{\mathbf{m}}_1^b$  (equation A-1) can be derived as follows:

$$\tilde{\mathbf{m}}_1^b \approx \mathbf{H}_1^b \hat{\mathbf{m}}_1^b \approx \mathbf{S}^{m^+} \mathbf{H}_1 \mathbf{S}^{m^-} \hat{\mathbf{m}}_1^b \approx \mathbf{S}^{m^+} \mathbf{L}_1^T \mathbf{d}_1 \approx \mathbf{S}^{\alpha^+} (\mathbf{L}_1^b)^T \mathbf{d}_1. \quad (\text{A-8})$$

# Appendix B

## Joint inversion formulations for multiple surveys

In this Appendix, I derive regularized image-domain joint inversion of time-lapse data sets from multiple surveys.

For  $n$  surveys, spatio-temporally regularized data-domain joint inversion requires a minimization of a cost function of the form

$$S(\mathbf{m}_0, \dots, \mathbf{m}_n) = \sum_{i=0}^n \|\mathbf{L}_i \mathbf{m}_i - \mathbf{d}_i\|^2 + \sum_{i=0}^n \|\epsilon_i \mathbf{A}_i \mathbf{m}_i\|^2 + \sum_{i=1}^n \|\zeta_i \mathbf{\Lambda}_i (\mathbf{m}_{i-1}, \mathbf{m}_i)\|^2, \quad (\text{A-1})$$

where  $\mathbf{d}_i$  is data from the  $i$ th survey, modeled by the linear operator  $\mathbf{L}_i$  from reflectivity mode  $\mathbf{m}_i$ . Regularization parameters  $\epsilon$  and  $\zeta$  determine the strengths of the spatial and temporal regularization operators,  $\mathbf{A}$  and  $\mathbf{\Lambda}$  respectively.

Assuming there are two surveys, and that temporal coupling is achieved with a weighted difference operator, we can write

$$S(\mathbf{m}_0, \mathbf{m}_1) = \left\| \begin{bmatrix} \mathbf{L}_0 & \mathbf{0} \\ \mathbf{0} & \mathbf{L}_1 \end{bmatrix} \begin{bmatrix} \mathbf{m}_0 \\ \mathbf{m}_1 \end{bmatrix} - \begin{bmatrix} \mathbf{d}_0 \\ \mathbf{d}_1 \end{bmatrix} \right\|^2 + \left\| \begin{bmatrix} \epsilon_0 \mathbf{A}_0 & \mathbf{0} \\ \mathbf{0} & \epsilon_1 \mathbf{A}_1 \end{bmatrix} \begin{bmatrix} \mathbf{m}_0 \\ \mathbf{m}_1 \end{bmatrix} \right\|^2 + \left\| \begin{bmatrix} -\zeta_0 \mathbf{\Lambda}_0 & \zeta_1 \mathbf{\Lambda}_1 \end{bmatrix} \begin{bmatrix} \mathbf{m}_0 \\ \mathbf{m}_1 \end{bmatrix} \right\|^2, \quad (\text{A-2})$$

or simply

$$S(\mathbf{m}_0, \mathbf{m}_1) = \left\| \left[ \begin{array}{cc|c} \mathbf{L}_0 & \mathbf{0} & \mathbf{d}_0 \\ \mathbf{0} & \mathbf{L}_1 & \mathbf{d}_1 \\ \hline \epsilon_0 \mathbf{A}_0 & \mathbf{0} & \mathbf{0} \\ \mathbf{0} & \epsilon_1 \mathbf{A}_1 & \mathbf{0} \\ \hline -\zeta_0 \Lambda_0 & \zeta_1 \Lambda_1 & \mathbf{0} \end{array} \right] \begin{bmatrix} \mathbf{m}_0 \\ \mathbf{m}_1 \end{bmatrix} - \begin{bmatrix} \mathbf{d}_0 \\ \mathbf{d}_1 \\ \mathbf{0} \\ \mathbf{0} \\ \mathbf{0} \end{bmatrix} \right\|^2 \approx 0. \quad (\text{A-3})$$

Minimizing this cost function in a least-squares sense gives the solutions  $\hat{\mathbf{m}}_0$  and  $\hat{\mathbf{m}}_1$  which satisfy the following:

$$\left( \begin{bmatrix} \mathbf{H}_0 & \mathbf{0} \\ \mathbf{0} & \mathbf{H}_1 \end{bmatrix} + \begin{bmatrix} \mathbf{A}_{00} & \mathbf{0} \\ \mathbf{0} & \mathbf{A}_{11} \end{bmatrix} + \begin{bmatrix} \mathbf{A}_{00} & -\Lambda_{01} \\ -\Lambda_{10} & \Lambda_{11} \end{bmatrix} \right) \begin{bmatrix} \hat{\mathbf{m}}_0 \\ \hat{\mathbf{m}}_1 \end{bmatrix} \approx \begin{bmatrix} \tilde{\mathbf{m}}_0 \\ \tilde{\mathbf{m}}_1 \end{bmatrix}, \quad (\text{A-4})$$

where  $\mathbf{H}_i = \mathbf{L}_i^T$  is the Hessian matrix,  $\mathbf{A}_{ii} = \epsilon_i^2 \mathbf{A}_i^T \mathbf{A}_i$  and  $\Lambda_{ij} = \zeta_i \mathbf{A}_i^T \zeta_j \mathbf{A}_j$  are the spatial and temporal constraints, respectively. The solution of this *image-domain* formulation is equivalent to the data-domain formulation in equation A-3. However, because the Hessian matrix is not guaranteed to be positive-definite, to solve this system in equation A-4 with a conjugate gradients solver, we can minimize a slightly different cost function given by

$$\tilde{S}(\mathbf{m}_0, \mathbf{m}_1) = \left\| \left[ \begin{array}{cc|c} \mathbf{H}_0 & \mathbf{0} & \tilde{\mathbf{m}}_0 \\ \mathbf{0} & \mathbf{H}_1 & \tilde{\mathbf{m}}_1 \\ \hline \epsilon_0 \mathbf{A}_0 & \mathbf{0} & \mathbf{0} \\ \mathbf{0} & \epsilon_1 \mathbf{A}_1 & \mathbf{0} \\ \hline -\zeta_0 \Lambda_0 & \zeta_1 \Lambda_1 & \mathbf{0} \end{array} \right] \begin{bmatrix} \hat{\mathbf{m}}_0 \\ \hat{\mathbf{m}}_1 \end{bmatrix} - \begin{bmatrix} \tilde{\mathbf{m}}_0 \\ \tilde{\mathbf{m}}_1 \\ \mathbf{0} \\ \mathbf{0} \\ \mathbf{0} \end{bmatrix} \right\|^2 \approx 0, \quad (\text{A-5})$$

which further squares the condition number of the original least-squares problem but guarantees a stable solution is reached. For the synthetic and field data examples considered in this thesis, the squaring the condition number does not cause any significant problems. Furthermore, carefully chosen regularization operators ensure that satisfactory results are achieved at a reasonable number of iterations.

For an arbitrary number of surveys, the generalized inversion problem requires minimization of the cost function of the form

$$\tilde{S} = \left\| \begin{bmatrix} \mathbf{E} \\ \mathfrak{R} \\ \mathbf{\Gamma} \end{bmatrix} \hat{\mathbf{m}} - \begin{bmatrix} \tilde{\mathbf{m}} \\ \mathbf{0} \\ \mathbf{0} \end{bmatrix} \right\|^2 \approx 0, \quad (\text{A-6})$$

where,  $\Xi$ , the image-fitting operator, is a concatenation of the Hessian matrices from different surveys:

$$\Xi = \begin{bmatrix} \mathbf{H}_0 & \mathbf{0} & \mathbf{0} & \dots & \mathbf{0} & \mathbf{0} \\ \mathbf{0} & \mathbf{H}_1 & \mathbf{0} & \dots & \mathbf{0} & \mathbf{0} \\ \vdots & \vdots & \vdots & \vdots & \vdots & \vdots \\ \vdots & \vdots & \vdots & \vdots & \mathbf{H}_{n-1} & \mathbf{0} \\ \mathbf{0} & \mathbf{0} & \mathbf{0} & \dots & \mathbf{0} & \mathbf{H}_n \end{bmatrix}. \quad (\text{A-7})$$

Figure B.1 shows an example of the image fitting operator for three surveys. As seen in Figure B.1, the combined matrix is very sparse. Therefore, with present day storage capacities, it practical to precompute and store the necessary elements to sufficiently approximate the full Hessian.

The spatial and temporal regularization operators,  $\mathfrak{R}$  and  $\mathbf{\Gamma}$  are defined as

$$\mathfrak{R} = \begin{bmatrix} \epsilon_0 \mathbf{R}_0 & \mathbf{0} & \mathbf{0} & \dots & \mathbf{0} & \mathbf{0} \\ \mathbf{0} & \epsilon_1 \mathbf{R}_1 & \mathbf{0} & \dots & \mathbf{0} & \mathbf{0} \\ \vdots & \vdots & \vdots & \vdots & \vdots & \vdots \\ \vdots & \vdots & \vdots & \mathbf{0} & \epsilon_{n-1} \mathbf{R}_{n-1} & \mathbf{0} \\ \mathbf{0} & \mathbf{0} & \mathbf{0} & \mathbf{0} & \mathbf{0} & \epsilon_n \mathbf{R}_n \end{bmatrix}, \quad (\text{A-8})$$

and

$$\mathbf{\Lambda} = \begin{bmatrix} -\zeta_0 \mathbf{\Lambda}_0 & \zeta_1 \mathbf{\Lambda}_1 & \mathbf{0} & \mathbf{0} & \dots & \mathbf{0} \\ \mathbf{0} & -\zeta_1 \mathbf{\Lambda}_1 & \zeta_2 \mathbf{\Lambda}_2 & \mathbf{0} & \dots & \mathbf{0} \\ \vdots & \vdots & \vdots & \vdots & \vdots & \vdots \\ \mathbf{0} & \mathbf{0} & \dots & \mathbf{0} & -\zeta_{n-1} \mathbf{\Lambda}_{n-1} & \zeta_n \mathbf{\Lambda}_n \end{bmatrix}. \quad (\text{A-9})$$

The input and output vectors are defined as follows:

$$\tilde{\mathbf{m}} = \left[ \tilde{\mathbf{m}}_0, \tilde{\mathbf{m}}_1, \tilde{\mathbf{m}}_2, \dots, \tilde{\mathbf{m}}_{n-1}, \tilde{\mathbf{m}}_n \right]^T, \quad (\text{A-10})$$

and

$$\hat{\mathbf{m}} = \left[ \hat{\mathbf{m}}_0, \hat{\mathbf{m}}_1, \hat{\mathbf{m}}_2, \dots, \hat{\mathbf{m}}_{n-1}, \hat{\mathbf{m}}_n \right]^T, \quad (\text{A-11})$$

respectively.

As shown in Appendix A, if the monitor data are imaged with the baseline velocity, the input migrated monitor image must first be warped to the baseline position, and all operators must be referenced to the baseline position. The time-lapse image can

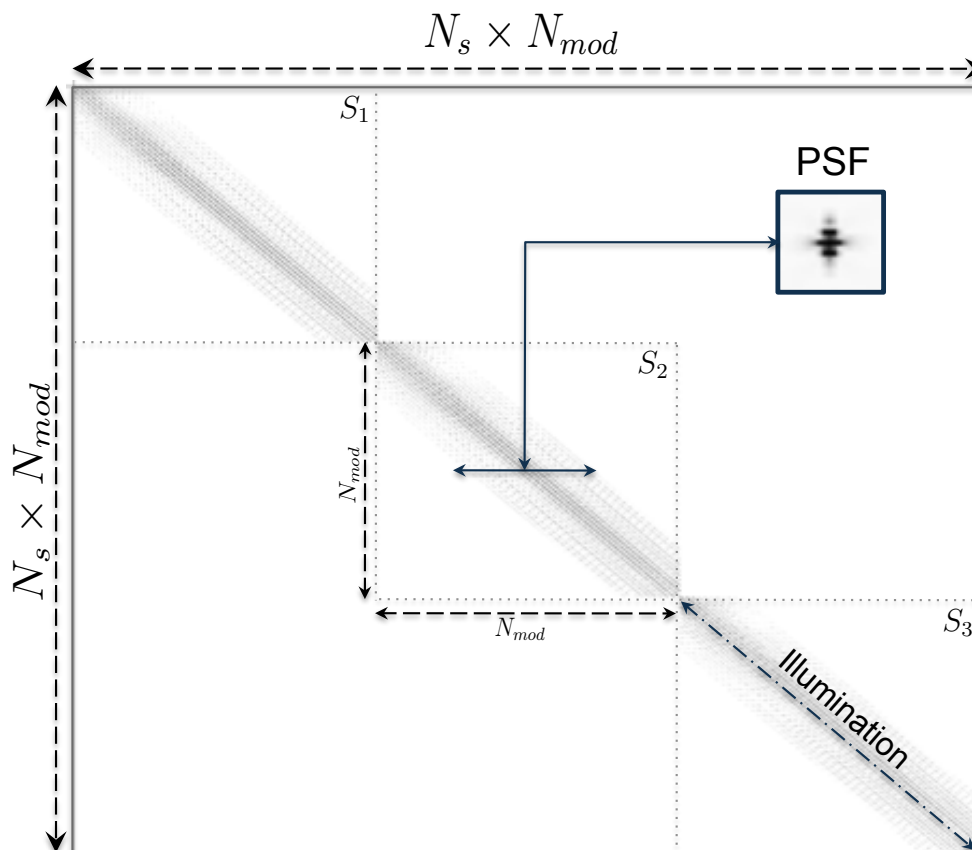


Figure B.1: Concatenated truncated target-oriented Hessian matrices for three surveys. The matrix dimension is  $N_s \times N_{mod}$ , where  $N_s$  is the number of surveys and  $N_{mod}$  is the number of model points in the target area.  $S_i$  denotes the Hessian corresponding to survey  $i$ . Note that because this matrix is sparse and that the absolute values of its coefficients decrease away from its diagonal. As shown, the point-spread-function (PSF) refer to a row of the Hessian matrix, whereas the illumination refers to its diagonal. [CR]. `appendix/. hess`

be computed as a difference between the inverted images.

Instead of computing the time-lapse image from the inverted images, another approach is to compute the time-lapse image directly during inversion. To invert directly for the time-lapse images, I substitute the following into the cost function in

equation A-1:

$$\Delta \mathbf{m}_i = \mathbf{m}_i - \mathbf{m}_{i-1}, \quad (\text{A-12})$$

where  $\Delta \mathbf{m}_i$  is the time-lapse image between  $\mathbf{m}_i$  and  $\mathbf{m}_{i-1}$ . This leads to a new cost function given by

$$\begin{aligned} S(\hat{\mathbf{m}}_0, \Delta \hat{\mathbf{m}}_1, \dots, \Delta \hat{\mathbf{m}}_n) = & \left\| \mathbf{L}_0 \mathbf{m}_0 - \mathbf{d}_0 \right\|^2 + \sum_{i=1}^n \left\| \left( \mathbf{L}_j \mathbf{m}_0^m + \sum_{j=1}^i \mathbf{L}_j \Delta \mathbf{m}_j^m \right) - \mathbf{d}_i \right\|^2 \\ & + \left\| \epsilon_0 \mathbf{A}_0 \mathbf{m}_0 \right\|^2 + \sum_{j=1}^n \left\| \epsilon_j \mathbf{A}_j \Delta \mathbf{m}_j^m \right\|^2 \\ & \sum_{j=1}^n \left\| -\zeta_{j-1} \mathbf{A}_{j-1} \Delta \mathbf{m}_{j-1}^m + \zeta_j \mathbf{A}_j \Delta \mathbf{m}_j^m \right\|^2. \end{aligned} \quad (\text{A-13})$$

One advantage of this approach is that it allows direct regularization of the time-lapse images.

Following the same procedure as above gives an image-fitting operator of the form

$$\Xi = \begin{bmatrix} \mathbf{H}_0 + \dots + \mathbf{H}_n & \mathbf{H}_1 + \dots + \mathbf{H}_n & \dots & \mathbf{H}_{n-1} + \mathbf{H}_n & \mathbf{H}_n \\ \mathbf{H}_1 + \dots + \mathbf{H}_n & \mathbf{H}_1 + \dots + \mathbf{H}_n & \dots & \mathbf{H}_{n-1} + \mathbf{H}_n & \mathbf{H}_n \\ \vdots & \vdots & \vdots & \vdots & \vdots \\ \vdots & \vdots & \vdots & \mathbf{H}_{n-1} + \mathbf{H}_n & \mathbf{H}_n \\ \mathbf{H}_n & \mathbf{H}_n & \dots & \mathbf{H}_{n-1} + \mathbf{H}_n & \mathbf{H}_n \end{bmatrix}. \quad (\text{A-14})$$

The input and output vectors in this case are given by

$$\tilde{\mathbf{m}} = \left[ \tilde{\mathbf{m}}_0 + \dots + \tilde{\mathbf{m}}_n, \tilde{\mathbf{m}}_1 + \dots + \tilde{\mathbf{m}}_n, \tilde{\mathbf{m}}_2 + \dots + \tilde{\mathbf{m}}_n, \dots, \tilde{\mathbf{m}}_{n-1} + \tilde{\mathbf{m}}_n, \tilde{\mathbf{m}}_n \right]^T, \quad (\text{A-15})$$

and

$$\hat{\mathbf{m}} = \left[ \hat{\mathbf{m}}_0, \Delta \hat{\mathbf{m}}_1, \Delta \hat{\mathbf{m}}_2, \dots, \Delta \hat{\mathbf{m}}_{n-1}, \Delta \hat{\mathbf{m}}_n \right]^T, \quad (\text{A-16})$$

respectively.

# Bibliography

- Aarre, V., 2008, On the presence, and possible causes, of apparent lateral shifts below the Nome reservoir: SEG Technical Program Expanded Abstracts, **27**, 3174–3178.
- Ajo-Franklin, J. B., B. J. Minsley, and T. M. Daley, 2007, Applying compactness constraints to differential travelttime tomography: Geophysics, **72**, R67–R75.
- Ajo-Franklin, J. B., J. Urban, and J. M. Harris, 2005, Temporal integration of seismic travelttime tomography: SEG Technical Program Expanded Abstracts, **24**, 2468–2471.
- Albertin, U., P. Sava, J. Etgen, and M. Maharramov, 2006, Adjoint wave-equation velocity analysis: SEG Technical Program Expanded Abstracts, **25**, 3345–3349.
- Ali, N., and T. Alcock, 1994, Valhall Field, Norway - the first ten years: NTH.
- Arogunmati, A., and J. M. Harris, 2009, An approach for quasi-continuous time-lapse seismic monitoring with sparse data: SEG Technical Program Expanded Abstracts, **28**, 3899–3903.
- Ayeni, G., 2011, Cyclic 1D matching of time-lapse seismic data sets: A case study of the Norne field: SEG Technical Program Expanded Abstracts, **30**, 4234–4238.
- Ayeni, G., A. Almomin, and D. Nichols, 2011, On the separation of simultaneous-source data by inversion: SEG Technical Program Expanded Abstracts, **30**, 20–25.
- Ayeni, G., and M. Nasser, 2009, Optimized local matching of time-lapse seismic data: A case study from the Gulf of Mexico: SEG Technical Program Expanded Abstracts, **28**, 3939–3943.
- Ayeni, G., Y. Tang, and B. Biondi, 2009, Joint preconditioned least-squares inversion of simultaneous source time-lapse seismic data sets: SEG Technical Program Expanded Abstracts, **28**, 3914–3918.

- Bäck, T., 1996, *Evolutionary algorithms in theory and practice: evolution strategies, evolutionary programming, genetic algorithms*: Oxford University Press.
- Baek, T., D. Fogel, and Z. Michalewicz, 1997, *Handbook of evolutionary computation*: Taylor and Francis.
- Barkved, O., P. Heavey, R. Kjelstadli, T. Kleppan, and T. G. Kristiansen, 2003, Valhall Field - still on plateau after 20 years of production: *Offshore Europe*, **1**.
- Barkved, O., P. Heavey, J. H. Kommedal, J.-P. van Gestel, R. S. ve, H. Pettersen, C. Kent, and U. Albertin, 2010, Business impact of full waveform inversion at valhall: *SEG Technical Program Expanded Abstracts*, **29**, 925–929.
- Barkved, O. I., 2004, Continuous seismic monitoring: *SEG Technical Program Expanded Abstracts*, **23**, 2537–2540.
- Batzle, M., and Z. Wang, 1992, Seismic properties of pore fluids: *Geophysics*, **57**, 1396–1408.
- Beasley, C. J., 2008, Simultaneous sources: A technology whose time has come: *SEG Technical Program Expanded Abstracts*, **27**, 2796–2800.
- Berkhout, A. J. G., 2008, Changing the mindset in seismic data acquisition: *The Leading Edge*, **27**, 924–938.
- Berkhout, A. J. G., G. Blacquière, and E. Verschuur, 2008, From simultaneous shooting to blended acquisition: *SEG Technical Program Expanded Abstracts*, **27**, 2831–2838.
- Bourgeois, A., M. Bourget, P. Lailly, M. Poulet, P. Ricarte, and R. Versteeg, 1991, Marmousi, model and data:: *Proceedings of 1990 EAEG workshop on practical aspects of seismic data inversion*.
- Calvert, R., 2005, *Insights and methods for 4D reservoir monitoring and characterization: SEG/EAGE DISC (Distinguished Instructor Lecture Course)*.
- Claerbout, J. F., and S. Fomel, 2011, *Image estimation by example: Geophysical soundings image construction: multidimensional autoregression*.
- Clapp, M., and B. Biondi, 2002, Subsalt event regularization with steering filters: *72nd Annual International Meeting, Expanded Abstracts, SEG*, 1176–1179.
- Clapp, M. L., 2005, *Imaging under salt: illumination compensation by regularized inversion*: PhD thesis, Stanford University.

- Clapp, R. G., 2000, Geologically constrained migration velocity analysis: PhD thesis, Stanford University.
- Eiben, A. E., and J. E. Smith, 2003, Introduction to evolutionary computing: Springer. Natural computing series.
- Etgen, J., S. H. Gray, and Y. Zhang, 2009, An overview of depth imaging in exploration geophysics: *Geophysics*, **74**, WCA5–WCA17.
- Fehler, M., and K. Larner, 2008, Seg advanced modeling (seam): Phase i first year update: *The Leading Edge*, **27**, 1006–1007.
- Fomel, S., 2000, Three-dimensional seismic data regularization: PhD thesis, Stanford University.
- , 2002, Applications of plane-wave destruction filters: *Geophysics*, **67**, 1946–1960.
- Fomel, S., P. Sava, J. Rickett, and J. F. Claerbout, 2003, The Wilson–Burg method of spectral factorization with application to helical filtering: *Geophysical Prospecting*, **51**, 409–420.
- Guilton, A., 2004, Amplitude and kinematic corrections of migrated images for nonunitary imaging operators: *Geophysics*, **69**, 1017–1024.
- Guofa, S., M. Jiang, L. Xia, Q. Wei, F. Liu, and S. Crozier, 2006, A comparison of different choices for the regularization parameter in inverse electrocardiography models: *Proceedings of the 28th Annual IEEE Engineering in Medicine and Biology Society Annual International Conference*, **1**, 3903–3906.
- Hale, D., 2007, Local dip filtering with directional Laplacians: *CWP Project Reiew*, **567**, 91–102.
- , 2009, A method for estimating apparent displacement vectors from time-lapse seismic images: *Geophysics*, **74**, V99–V107.
- Hall, S. A., C. MacBeth, O. I. Barkved, and P. Wild, 2005, Cross-matching with interpreted warping of 3d streamer and 3d ocean-bottom-cable data at valhall for time-lapse assessment: *Geophysical Prospecting*, **53**, 283–297.
- Hampson, G., J. Stefani, and F. Herkenhoff, 2008, Acquisition using simultaneous sources: *SEG Technical Program Expanded Abstracts*, **27**, 2816–2820.
- Hatchell, P., and S. Bourne, 2005a, Rocks under strain: Strain-induced time-lapse

- time shifts are observed for depleting reservoirs: *The Leading Edge*, **24**, 1222–1225.
- Hatchell, P., R. Kowar, and A. Savitski, 2005, Integrating 4D seismic, geomechanics and reservoir simulation in the Valhall oil field: 67th EAGE Conference and Exhibition Extended abstract,.
- Hatchell, P. J., and S. J. Bourne, 2005b, Measuring reservoir compaction using time-lapse timeshifts: SEG Technical Program Expanded Abstracts, **24**, 2500–2503.
- Hawkins, K., S. Howe, S. Hollingworth, G. Conroy, L. Ben-Brahim, C. Tindle, N. Taylor, G. Joffroy, and A. Onaisi, 2007, Production-induced stresses from time-lapse time shifts: A geomechanics case study from franklin and elgin fields: *The Leading Edge*, **26**, 655–662.
- Helgerud, M. B., A. C. Miller, D. H. Johnston, M. S. Udoh, B. G. Jardine, C. Harris, and N. Aubuchon, 2011a, 4D in the deepwater gulf of mexico: Hoover, madison, and marshall fields: *The Leading Edge*, **30**, 1008–1018.
- Helgerud, M. B., U. Tiwari, S. Woods, P. Homonko, A. Bucki, B. Laugier, E. Hicks, H. Hoerber, and J. Khan, 2011b, Optimizing seismic repeatability at Ringhorne, Ringhorne East, Balder and Forseti with QC driven time-lapse processing: SEG Technical Program Expanded Abstracts, **30**, 4180–4184.
- Howe, D., M. Foster, T. Allen, I. Jack, D. Buddery, A. Choi, R. Abma, T. Manning, and M. Pfister, 2009, Independent simultaneous sweeping in Libya—full scale implementation and new developments: SEG Technical Program Expanded Abstracts, **28**, 109–111.
- Ikelle, L., 2009, Coding and decoding: Seismic data: The concept of multishooting: Elsevier. Coding and Decoding: Seismic Data.
- Johnston, D., 2005, Time-lapse 4D technology: Reservoir surveillance: AAPG Search and Discovery.
- Kommedal, J. H., O. I. Barkved, J.-P. van Gestel, and R. S. H. Pettersen, 2007, Processing strategies for multiple repeat 4D seismic: SEG Technical Program Expanded Abstracts, **26**, 2908–2913.
- Krebs, J. R., J. E. Anderson, D. Hinkley, R. Neelamani, S. Lee, A. Baumstein, and M.-D. Lacasse, 2009, Fast full-wavefield seismic inversion using encoded sources:

- Geophysics, **74**, WCC177–WCC188.
- Kühl, H., and M. D. Sacchi, 2003, Least-squares wave-equation migration for AVP/AVA inversion: Geophysics, **68**, 262–273.
- Lambaré, G., S. Operto, P. Podvin, and P. Thierry, 2003, 3D ray + Born migration/inversion—Part 1: Theory: Geophysics, **68**, 1348–1356.
- Landro, M., O. A. Solheim, E. Hilde, B. O. Ekren, and L. K. Stronen, 1999, The gullfaks 4d seismic study: Petroleum Geoscience, **5**, 213–226.
- Lefeuvre, F., Y. Kerdraon, J. Peliganga, S. Medina, P. Charrier, R. L'Houtellier, and D. Dubucq, 2003, Improved reservoir understanding through rapid and effective 4D: Girassol field, Angola, West Africa: SEG Technical Program Expanded Abstracts, **22**, 1334–1337.
- Lumley, D., D. C. Adams, M. Meadows, S. Cole, and R. Wright, 2003, 4D seismic data processing issues and examples: SEG Technical Program Expanded Abstracts, **22**, 1394–1397.
- Lumley, D. E., 1995, Seismic time-lapse monitoring of subsurface fluid flow: PhD thesis, Stanford University, <http://sepwww.stanford.edu/public/docs/sep91/>.
- Mavko, G., T. Mukerji, and J. Dvorkin, 2003, The rock physics handbook: Tools for seismic analysis of porous media: Cambridge University Press.
- Messnarz, B., B. Tilg, R. Modre, G. Fischer, and F. Hanser, 2004, A new spatiotemporal regularization approach for reconstruction of cardiac transmembrane potential patterns: IEEE Transactions on Biomedical Engineering, **51**, 273–281.
- Miller, C. R., P. S. Routh, T. R. Brosten, and J. P. McNamara, 2008, Application of time-lapse ert imaging to watershed characterization: Geophysics, **73**, G7–G17.
- Munns, J., 1985, The Valhall field: a geological overview: Marine and Petroleum Geology, **2**, 23 – 43.
- Nemeth, T., C. Wu, and G. T. Schuster, 1999, Least-squares migration of incomplete reflection data: Geophysics, **64**, 208–221.
- Oldenborger, G. A., M. D. Knoll, P. S. Routh, and D. J. LaBrecque, 2007, Time-lapse ERT monitoring of an injection/withdrawal experiment in a shallow unconfined aquifer: Geophysics, **72**, F177–F187.
- Osdal, B., O. Husby, H. A. Aronsen, N. Chen, and T. Alsos, 2006, Mapping the fluid

- front and pressure buildup using 4D data on Norne field: *The Leading Edge*, **25**, 1134–1141.
- Plessix, R.-E., and W. Mulder, 2004, Frequency-domain finite-frequency amplitude-preserving migration: *Geophysical Journal International*, **157**, 975–985.
- Press, W. H., S. A. Teukolsky, W. T. Vetterling, and B. P. Flannery, 1996, *Numerical recipes in fortran 90: the art of parallel scientific computing*: Cambridge University Press. FORTRAN Numerical Recipes.
- Rickett, J., 2003, Illumination-based normalization for wave-equation depth migration: *Geophysics*, **68**, 1371–1379.
- Rickett, J. E., and D. E. Lumley, 2001, Cross-equalization data processing for time-lapse seismic reservoir monitoring: A case study from the Gulf of Mexico: *Geophysics*, **66**, 1015–1025.
- Romero, L. A., D. C. Ghiglia, C. C. Ober, and S. A. Morton, 2000, Phase encoding of shot records in prestack migration: *Geophysics*, **65**, 426–436.
- Røste, T., A. Stovas, and M. Landrø, 2006, Estimation of layer thickness and velocity changes using 4d prestack seismic data: *Geophysics*, **71**, S219–S234.
- Routh, P. S., and P. D. Anno, 2008, Time-lapse noise characterization by inversion: *SEG Technical Program Expanded Abstracts*, **27**, 3143–3147.
- Santosa, F., and W. W. Symes, 1988, Computation of the Hessian for least-squares solutions of inverse problems of reflection seismology: *Inverse Problems*, **4**, 211.
- Sarkar, S., W. P. Gouveia, and D. H. Johnston, 2003, On the inversion of time-lapse seismic data: *SEG Technical Program Expanded Abstracts*, **22**, 1489–1492.
- Schmitt, U., and A. K. Louis, 2002, Efficient algorithms for the regularization of dynamic inverse problems: I. theory: *Inverse Problems*, **18**, 645–658.
- Schmitt, U., A. K. Louis, C. Wolters, and M. Vauhkonen, 2002, Efficient algorithms for the regularization of dynamic inverse problems: II. applications: *Inverse Problems*, **18**, 659–676.
- Schuster, G. T., X. Wang, Y. Huang, W. Dai, and C. Boonyasiriwat, 2011, Theory of multisource crosstalk reduction by phase-encoded statics: *Geophysical Journal International*, **184**, 1289–1303.
- Sharma, A., T. Burch, and G. Murphy, 2011, Low cost 4D using NATS and WATS

- at Europa: SEG Technical Program Expanded Abstracts, **30**, 4185–4189.
- Sirgue, L., O. Barkved, J. Dellinger, J. Etgen, U. Albertin, and J. Kommedal, 2010, Full waveform inversion: the next leap forward in imaging at Valhall: First Break, **28**.
- Spitz, S., G. Hampson, and A. Pica, 2008, Simultaneous source separation: A prediction-subtraction approach: SEG Technical Program Expanded Abstracts, **27**, 2811–2815.
- Stopin, A., P. J. Hatchell, C. Corcoran, E. Beal, C. Gutierrez, and G. Soto, 2011, First OBS to OBS time lapse results in the mars basin: SEG Technical Program Expanded Abstracts, **30**, 4114–4118.
- Symes, W. W., 2008, Approximate linearized inversion by optimal scaling of prestack depth migration: Geophysics, **73**, R23–R35.
- Tang, Y., 2008, Modeling, migration, and inversion in the generalized source and receiver domain: Stanford Exploration Project Report, **136**, 97–112.
- , 2011, Imaging and velocity analysis by target-oriented wavefield inversion: PhD thesis, Stanford University.
- Tang, Y., and B. Biondi, 2009, Least-squares migration/inversion of blended data: SEG Technical Program Expanded Abstracts, **28**, 2859–2863.
- Trad, D., T. Ulrych, and M. Sacchi, 2003, Latest views of the sparse radon transform: Geophysics, **68**, 386–399.
- Valenciano, A., 2008, Imaging by Wave-Equation Inversion: PhD thesis, Stanford University.
- van Gestel, J.-P., K. D. Best, O. I. Barkved, and J. H. Kommedal, 2011, Integration of the life of field seismic data with the reservoir model at the Valhall field: Geophysical Prospecting, **59**, 673–681.
- van Gestel, J.-P., J. H. Kommedal, O. I. Barkved, I. Mundal, R. Bakke, and K. D. Best, 2008, Continuous seismic surveillance of Valhall field: The Leading Edge, **27**, 1616–1621.
- van Mastrigt, P., S. Vaage, M. Dunn, and B. Pramik, 2002, Improvements in 3-D marine acquisition using continuous long offset (clo): The Leading Edge, **21**, 394–399.

- Verschuur, D., and A. Berkhout, 2009, Target-oriented, least-squares imaging of blended data: SEG Technical Program Expanded Abstracts, **28**, 2889–2893.
- Versteeg, R., 1994, The Marmousi experience: Velocity model determination on a synthetic complex data set: The Leading Edge, **13**, 927–936.
- Whitcombe, D. N., J. M. Marsh, P. J. Clifford, M. Dyce, C. J. S. McKenzie, S. Campbell, A. J. Hill, R. S. Parr, C. Pearse, T. A. Ricketts, C. P. Slater, and O. L. Barkved, 2004, The systematic application of 4D in BP's North-West Europe operations — 5 years on: SEG Technical Program Expanded Abstracts, **23**, 2251–2254.
- Womack, J. E., J. R. Cruz, H. K. Rigdon, and G. M. Hoover, 1990, Encoding techniques for multiple source point seismic data acquisition: Geophysics, **55**, 1389–1396.
- Yao, X., Y. Liu, and G. Lin, 1999, Evolutionary programming made faster: Evolutionary Computation, IEEE Transactions on, **3**, 82–102.
- Yu, J., J. Hu, G. T. Schuster, and R. Estill, 2006, Prestack migration deconvolution: Geophysics, **71**, no.2, S53–S62.
- Zou, Y., L. R. Bentley, L. R. Lines, and D. Coombe, 2006, Integration of seismic methods with reservoir simulation, Pikes Peak heavy-oil field, Saskatchewan: The Leading Edge, **25**, 764–781.